Time Domain Boundary Element Method for Room Acoustics

Jonathan A. HARGREAVES

Acoustics Research Centre
School of Computing Science and Engineering
University of Salford, UK

I Table of Contents

II Table of Figures

viii

III Acknowledgements

I've been very lucky to study under the supervision of Professor Trevor Cox. As a supervisor he's been dedicated, supportive and generous with his time. Professionally his energy, enthusiasm and sheer productivity have been an inspiration. I would cite him as being the most definitive academic I have ever met. His efforts have been indispensable and greatly appreciated and I look forward to working under his guidance for another few years.

The Acoustics Research Centre at Salford has been a supportive and welcoming environment in which to study, primarily due to the calibre and good humour of the people who form it. I am indebted to my colleagues for much advice and stimulating debate.

Similar complements are due to my colleagues during my time at Wadham College and Helsby Technology Centre; at the latter I would like to highlight Mike Harrop & Dr. Merrion Edwards who encouraged me greatly, gave me meaningful project work and from whom I learnt much about being a researcher.

I owe a debt of gratitude to the tutors throughout my education whose belief in me has inspired me to better myself. This includes both the study of science and music, which have coalesced in my passion for Acoustics.

I'd like to thank all my family and friends for their support, in particular Dr. Kat, who performed much appreciated proof reading, and Kate, who always tried to encourage me when my motivation was low.

Lastly I pay reverence to my parents. To my father for passing to me his curiosity, hunger to learn, discipline for rigour, humour in the absurd, and confidence in, yet

modest knowledge of, his own capabilities. To my mother for teaching me patience and that respect is earned from within. Much that is good in my character I trace back to them. Their grace and affection are sorely missed.

IV Glossary

IV.i Abbreviations

Acronym:	Meaning:	Defined:
BAD	Binary Amplitude Diffuser	Section 5.5.4
BEM	Boundary Element Method	Section V
BIE	Boundary Integral Equation	Section 2.1
CFIE	Combined Field Integral Equation	Section 2.2.6
CFL	Courant-Friedrich-Levy	Section 2.2.5
DFT	Discrete Fourier Transform	Section 2.2.7
DIFTHIN	Frequency domain BEM for open surfaces	Section 4.3
EFIE	Electric Field Integral Equation	Section 2.2.2
FDTD	Finite Difference Time Domain	Section 1
FFT	Fast Fourier Transform	Section 2.2.7
KIE	Kirchhoff Integral Equation	Section 2.1.1
MFIE	Magnetic Field Integral Equation	Section 2.2.6
MOO	Marching On in Order	Section 2.2.7
MOT	Marching On in Time	Section 2.1.7
PWTD	Plane Wave Time Domain algorithm	Section 2.2.7
QRD	Quadratic Residue Diffuser	Section 4
RADDIFF	Frequency domain BEM for closed surfaces	Section 3.3
Rule7	A 7-point Gaussian rule	Section 3.1.1
SEM	Singularity Expansion Method	Section 2.2.6
TSB	Thin Shape Breakdown.	Section 4.1
Surface reflection response	Inverse Fourier transform of Surface reflection coefficient	Section 5.1

IV.iiSymbols

Conventions:

Vectors are indicated in bold, unit vectors by a hat. Temporal differentiation is indicated by a dot above the quantity. An apostrophe indicates that a term is evaluated at the integration point. Frequency domain quantities are uppercase.

Volumes and Surfaces:

	Description:	**Defined:**
S	The surface of the scatterer.	Figure 2.1
Ω_+	The air surrounding the scatterer.	Figure 2.1
Ω_-	The interior of the scatterer.	Figure 2.2
S_∞	The enclosing boundary of scattering problems.	Figure 2.2
S_m	Element m: usually the testing element.	Section 2.3.4
S_n	Element n: usually the integration element.	Section 2.3.4

Continuous Time and Frequency Terms:

	Description:	**Defined:**
t	Continuous time.	Section 2.1.1
ω	Angular frequency.	Section 2.1.5
k	Wavenumber.	Section 2.2.5
τ	Retarded time.	Section 2.3.4
ς	Normalised time.	Section 2.3.1
ρ_0	Density of air	Section 2.1.1

Vector and Geometric Terms:

	Description:	Defined:
$\mathbf{r}$	A point in space.	Figure 2.1
$\mathbf{r}_m^c$	The centre of element m.	Section 2.1.7
$\hat{\mathbf{n}}$	Surface normal unit vector.	Figure 2.1
$\mathbf{R}$	Vector from $\mathbf{r}'$ to $\mathbf{r}$.	Figure 2.1
$\hat{\mathbf{R}}$	Unit vector in the direction of $\mathbf{R}$.	Section 2.3.4
R	The length of $\mathbf{R}$.	Figure 2.1
θ_{origin}	The angle at the origin enclosed by S_n	Equation 3.18
μ	A unit-less edge position coordinate	Section 3.2.1.2
Δ_x	The greatest separation of two points on an element edge.	Equation 2.35
(v, w, z)	A cartesian coordinate system centred on the projection of $\mathbf{r}$ into the plane of S_n	Figure 3.21
(r, θ, z)	A cylindrical polar coordinate system centred on the projection of $\mathbf{r}$ into the plane of S_n	Figure 3.21

Operators and dyadic functions:

	Description:	Defined:
$\mathrm{L}_p\{\ldots\}$	Pressure operator	Equation 2.63
$\mathrm{L}_c\{\ldots\}$	Combined operator	Equation 2.66
$\mathrm{L}_v\{\ldots\}$	Velocity operator	Equation 2.65
$g(R, t)$	Greens function	Equation 2.7

Scalar and Vector Fields:

	Description:	Defined:
$\varphi^t(\mathbf{r},t)$	Total velocity potential	Section 2.1.1
$\varphi^r(\mathbf{r},t)$	Radiated velocity potential	Section 2.1.1
$\varphi^s(\mathbf{r},t)$	Scattered velocity potential	Section 2.1.2
$\varphi^i(\mathbf{r},t)$	Incident velocity potential	Section 2.1.2
$\varphi^{in}(\mathbf{r},t)$	Incoming velocity potential	Equation 5.6
$\varphi^{out}(\mathbf{r},t)$	Outgoing velocity potential	Equation 5.6
$\tilde{\varphi}^t(\mathbf{r},t)$	Jump in velocity potential across S	Section 4.1
$p(\mathbf{r},t)$	Pressure	Equation 2.1
$\mathbf{v}(\mathbf{r},t)$	Velocity	Equation 2.2
$v_n(\mathbf{r},t)$	Component of velocity normal to S	Section 2.1.1
$Z(\mathbf{r},\omega)$	Surface impedance	Section 5.1
$W(\mathbf{r},\omega)$	Surface reflection coefficient	Section 5.1
$w(\mathbf{r},t)$	Surface reflection response	Section 5.1

Discretisation Terms:

	Description:	Defined:
$f_n(\mathbf{r})$	Spatial basis function	Equation 2.17
$T_i(t)$	Temporal basis function	Equation 2.19
Δ_t	Time-step duration.	Section 2.1.6
t_j	Discretised time.	Section 2.1.7
β	Temporal resolution.	Equation 2.77
N_s	Number of spatial elements	Section 2.1.7
N_t	Number of temporal elements	Section 2.1.7
$\mathbf{Z}_l$	Interaction matrix for retardation l	Equation 2.23
l_{max}	Largest l with non-zero element interactions	Section 2.1.7
$w_{j,n},\ \varphi_{j,n}$	Discretisation Weights	Section 2.1.6
d_n	Well depth of S_n	Section 5.4
r_n	Reflection ratio from S_n	Section 5.4

V Abstract

This thesis is about improving the suitability of the time domain Boundary Element Method (BEM) for predicting the scattering from surface treatments used to improve the acoustics of rooms. The discretised integral equations are typically solved by marching on in time from initial silence; however, this being iterative has potential for divergence. Such instability and high computational cost have prohibited the time domain BEM from widespread use.

The underlying integral equation is known to not possess unique solutions at certain frequencies, physically interpreted as cavity resonances, and these manifest as resonant poles, all excited and potentially divergent due to numerical error. This has been addressed by others using the combined field integral equation; an approach built upon in this thesis.

Accuracy and stability may also be compromised by poor discretisation and integration accuracy. The latter is investigated on real-world surfaces, demonstrating that the popular Gaussian integration schemes are not suitable in some circumstances. Instead a contour integration scheme capable of resolving the integrands' singular nature is developed.

Schroeder diffusers are Room Acoustic treatments which comprise wells separated by thin fins. The algorithm is extended to model such surfaces, applying the combined field integral equation to the body and an open surface model to the fins. It is shown that this improves stability over an all open surface model.

A new model for compliant surfaces is developed, comparable to the surface impedance model used in the frequency domain. This is implemented for surfaces with welled and absorbing sections, permitting modelling of a Schroeder diffuser as a box with surface impedances that simulate the delayed reflections caused by the wells. A Binary Amplitude Diffuser - a partially absorbing diffuser - is also modelled.

These new models achieve good accuracy but not universal stability and avenues of future research are proposed to address the latter issue.

1 Introduction

Numerical modelling is a powerful tool for Acousticians. The overlapping ranges of audible wavelength and typical obstacle dimensions create complex sound fields that do not easily surrender to analytical techniques, except in certain idealised circumstances and geometries. Over recent decades it has gained popularity as the required computational power has become more widely and cheaply available with the increasing capabilities of desktop computers.

The sound that reaches a listener comprises a direct sound from a source and an indirect sound that has been reflected by the environment. This indirect sound has the potential to support or distort the perception of the direct sound. Reflections from a surface may be attenuated by increasing its absorption, or scattered more evenly over a wider range of angles by increasing its diffusion. The latter treatment is particularly useful when sound energy must be maintained, for example in a concert hall, or when envelopment is desired.

A diffusing surface treatment is characterised by the uniformity of its scattering[1]. This may be measured under anechoic conditions, a time consuming and therefore expensive process, particularly for devices that scatter hemispherically. An alternative is to predict this data using a numerical model. The speed and low cost of this approach aid prototyping of new designs, and even allow automated optimisation of treatments to be performed. The Boundary Element Method (BEM) is well suited to this task.

The BEM for Acoustics is derived from the wave equation, the law of how pressure fluctuations propagate through a homogeneous linear media, such as the stationary isothermal air ideally encountered in Room Acoustics. It is known how sound propagates through such a media unobstructed so the problem is converted to one only involving the wave's interaction with obstructions; the media's boundaries. This is stated as a boundary integral equation involving surface pressure and particle velocity perpendicular to the boundary. Particle velocity tangential to the boundary is ignored so it must be assumed that viscous boundary layer losses are small. The BEM is inherently

suited to modelling anechoic conditions: this is equivalent to the air going on forever so there is simply no outer boundary.

The surface quantities are considered to be continuous, but in order to be solved for numerically, a discrete representation is required. To achieve this, the boundary is typically partitioned into elements and upon each the surface quantities are interpolated and thereby described by a few scalars. The resulting model is of each element radiating a scattered wave independently, first due to the incident wave and then due to their mutual interactions.

Most BEMs assume time invariant harmonic excitation so the unknowns are time invariant complex numbers. Whilst this frequency domain analyses is a useful tool, the transient behaviour witnessed in the real world may only be recovered by calculation of many frequency domain models and inverse discrete Fourier transform. An alternative is to drop the time invariant assumption and formulate the BEM in the time domain; this is the algorithm studied in this thesis.

The time domain BEM is capable of modelling transient effects, such as the response of any acoustic treatment that employs lightly damped devices. It may also be coupled to non-linear models; this is not possible for the frequency domain BEM as the assumption of frequency independence breaks down in a non-linear world. It has also been realised during this research that it is easier to comprehend the interaction of scattered waves in a transient scenario than a time invariant one.

Finite Difference Time Domain[2] (FDTD) is a popular competing algorithm to model transient phenomena. It represents the volume of air as a mesh of interconnected nodes, and the differential terms of the wave equation are replaced by finite-difference approximations between nodes in space and time. This creates a great many unknowns, but their interactions are simple and efficient to solve. In contrast, a BEM has a reduced number of unknowns, but solving for them is a comparatively more expensive process. Thus the two algorithms have very different cost trends and the comparison of execution times is very much dependent on implementation and the type of problem to be solved.

1.1 Research Methodology and Project Scope

The original goal of this investigation was naively stated to be application of the time domain BEM to model Room Acoustics surface treatments, under the misconception that the algorithm was sufficiently mature to allow this. Once investigations commenced inadequacies emerged and it became apparent that a deeper understanding was required, so the purpose shifted to developing the algorithm.

The research methodology used was to first replicate a state of the art algorithm and then explore ways of extending it with features either novel or merged from other publications. The replication stage is crucial to algorithm comprehension and provides a working model from which to build and verify. It is also unavoidable as there are few commercial time domain BEM packages and it would not be possible to examine their inner workings or build upon them.

Verification of a new algorithm is imperative, even if it is a replication of a published implementation. This has been performed via Fourier transform against frequency domain BEM codes which have in turn been verified against experimental results.

Unlike many publications of time domain BEM research this investigation has not pursued universal stability as a primary goal. An improvement in stability has been used as supporting evidence for modifications that should be regarded as good practice anyway, but no attempts have been made to eradicate instability by heuristic means. This is in anticipation that future research might tackle solver divergence at its root cause.

Similarly development has not focused on optimisation of implementation. This is partially motivated by the PhD assessment process, which does not offer great rewards for improvements in code efficiency unless they are due to some novel technique. Accordingly implementation has been performed in Matlab to accelerate code development and aid data analysis and debugging. Where a small section of code has been identified as a bottleneck it has been rewritten into a MEX file; a fragment of C code compiled to integrate with Matlab. Despite the scaling trends discussed in section

2.1.8 it has been found that, for the problem sizes modelled herein, greatest computational cost is associated with the integration of interactions coefficients. Clearly computational efficiency is paramount for any commercially released code and any such based on this research would undergo substantial optimisation.

Recently much research has been directed towards acceleration schemes for the time domain BEM to cure its poor computation cost scaling trends. Despite their significance these have not been investigated herein as other issues more important to the primary aims were prioritised.

1.2 Thesis Structure

This thesis is divided into four main chapters, followed by discussions and conclusions. Chapter 2 contains an introduction to the mechanics of the time domain BEM and the literature review. The evolution of the algorithm discussed therein, starting with the earliest publications and then diverging to discuss different strands of development separately. Finally an algorithm is chosen for replication and is described in more detail.

Chapter 3 investigates the effects of integration accuracy on stability and accuracy of solutions. The performance of the integration scheme of the replicated algorithm is shown to be inadequate. In its place a new scheme is derived by conversion to contour integrals and shown to improve stability on real world surfaces.

The scope of the algorithm is extended in chapter 4 to include scatterers with thin fins, such as Schroeder diffusers. The fins must be modelled as rigid air / air interfaces to avoid singular behaviour in the underlying integral equations. However, the replicated algorithm has a unique formulation which fundamentally tackles the stability of models of thick bodies; it is desirable to retain this, so a mixed surface model is developed that supports both surface types. This is verified on some simple surfaces and a Quadratic Residue Diffuser.

Chapter 5 proposes a new model for compliant surfaces, comparable to the surface impedance model used in the frequency domain. This is cast into the time domain BEM framework and requires only one surface quantity to be discretised. The model is implemented for scatterers with welled and absorbing sections and verified on some simple surfaces plus a Quadratic Residue Diffuser and a Binary Amplitude Diffuser.

The contribution to knowledge by the developments of the three preceding chapters is discussed in chapter 6 and many avenues for future research are identified. Finally the conclusions of the thesis are summarised in chapter 7. Some additional proofs follow in the Appendix, followed by the References.

2 Time Domain Boundary Element Methods: concepts and published models

This chapter aims to elucidate to the reader the current state of the art in time domain Boundary Element Method (BEM). It is presented in three sections: section 2.1 outlines the formulation of the time domain BEM and introduces the nomenclature used in this thesis, section 2.2 reviews the contribution made by various authors, and section 2.3 focuses on a specific algorithm that was replicated as a starting point to the research process.

2.1 Introducing Boundary Element Methods

All BEMs begin with a Boundary Integral Equation (BIE). In Room Acoustics the direct time domain BEM begins with the Kirchhoff Integral Equation and this will be introduced in the next section. In this thesis, sound will usually be represented as velocity potential; consequentially it has the symbol φ reserved for it. While this is not a physical quantity, so of limited interest in itself, it has the convenient property that both pressure and velocity may be derived from it according to Equations 2.1 and 2.2. A dot above a quantity indicates temporal differentiation. Both these quantities are not absolute (such as atmospheric pressure) but are small perturbations relative to the equilibrium (silent) state.

$$p(\mathbf{r},t) = -\rho_0 \dot{\varphi}(\mathbf{r},t) \qquad\qquad 2.1$$

$$\mathbf{v}(\mathbf{r},t) = \nabla \varphi(\mathbf{r},t) \qquad\qquad 2.2$$

2.1.1 Kirchhoff Integral Equation

The sound waves considered in this thesis obey the linear acoustic wave equation within an enclosed connected volume of air Ω_+:

$$\nabla^2 \varphi(\mathbf{r},t) = \frac{1}{c^2} \ddot{\varphi}(\mathbf{r},t)$$

2.3

The initial conditions of the problem state that there is silence before time $t = 0$:

$$\varphi(\mathbf{r},t) = 0 \quad \mathbf{r} \in \Omega_+$$

2.4

$$\dot{\varphi}(\mathbf{r},t) = 0 \quad \mathbf{r} \in \Omega_+$$

2.5

These statements, combined with the boundary conditions introduced in section 2.1.2, form an initial boundary value problem. This problem may also be written as a Boundary Integral Equation (BIE); this is known as the Kirchhoff Integral Equation (KIE):

$$\varphi^r(\mathbf{r},t) = \iint_S \left(\varphi(\mathbf{r}',t) * \hat{\mathbf{n}}' \cdot \nabla' g(R,t) - g(R,t) * v_n(\mathbf{r}',t) \right) d\mathbf{r}'$$

2.6

The above may be found by applying Greens Theorem to Ω_+ minus the observation point $\mathbf{r}$ and any point sources present; this is depicted in Figure 2.1. The boundary surface S need not be connected but it must be piecewise smooth enough that a unique normal vector $\hat{\mathbf{n}}$ may be defined everywhere on it, perpendicular to S and directed into Ω_+. For completeness the volume behind S is named Ω_-. Variants on the derivation may be found in Pierce[3] and Groenenboom's 1982 survey article[4].
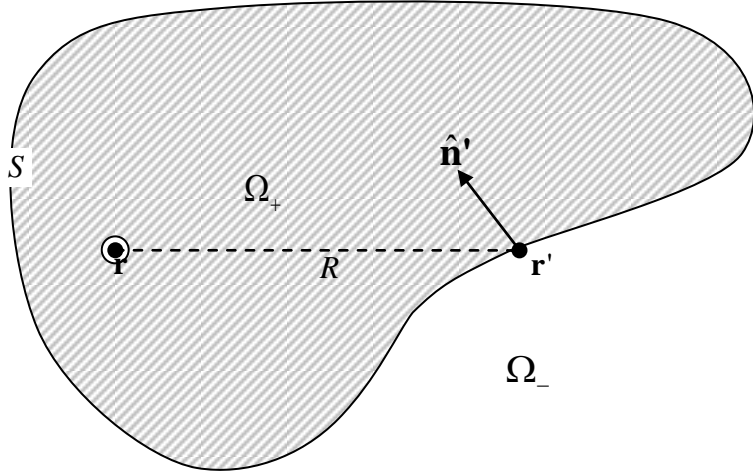
Figure 2.1: The air filled cavity represented by the KIE

In Equation 2.6 $\mathbf{r}$ and $\mathbf{r'}$ are the observation and radiation points respectively and $R = |\mathbf{r} - \mathbf{r'}|$ is the distance between them. $\varphi^r(\mathbf{r},t)$ is the sound that is radiated to point $\mathbf{r}$ due to the pressure and velocity fields on S. $\varphi^t(\mathbf{r'},t)$ is related to the known pressure field on S at $\mathbf{r'}$ by Equation 2.1. $\hat{\mathbf{n}}'$ is the surface normal vector at $\mathbf{r'}$ and $v_n(\mathbf{r'},t)$ is the component of velocity in the direction of $\hat{\mathbf{n}}'$ at $\mathbf{r'}$ and will be referred to as 'normal velocity' for brevity. $*$ denotes temporal convolution; for clarification on the properties of derivatives of the delta function under convolution see sections 8.1 and 8.2. $g(R,t)$ is the time domain Greens function, which describes how sound travels from a point source to a point observer, defined as follows:

$$g(R,t) = \frac{\delta\left(t - R/c\right)}{4\pi R}$$ 2.7

The first term in the KIE is similar to the sound radiated when the boundary exerts a force, a surface pressure, on the air. If a surface section is open, representing a thin plate with air on both sides rather than a boundary, exerting a net force on the air is equivalent to a pressure jump between the two sides of the surface. The radiation characteristics of this term are identical to that of a dipole sources smeared over S with density $\varphi^t(\mathbf{r'},t)$; this hypothetical equivalent is known as a double layer potential since a

8

layer of dipole sources is equivalent to two layers of opposed monopole sources. The radiated sound is discontinuous at surface, limiting to $\pm\frac{1}{2}\varphi^{t}(\mathbf{r}',t)$ depending on the direction of approach.

The second term in the KIE describes the sound radiated by surface vibration. The radiation characteristics of this term are identical to that of monopole sources smeared over S with density $v_{n}(\mathbf{r}',t)$, hence this hypothetical equivalent is known as a single layer potential.

Although the boundary is allowed to possess a non-zero normal velocity, this is considered to be oscillatory and the resulting displacements very small with respect to the dimensions of S. Consequentially the movement of the boundary is negligible, and it is assumed stationary at its mean point so its radiation characteristics are time invariant. Alternatively, if a surface is modelling the boundary of a non-rigid material then the surface may be assumed to be stationary and conformal to the boundary of the material.

The hypothetical equivalent surface sources, the double and single layer potentials, serve as a conceptual tool and illustrate that the KIE is consistent with Huygens principle, which states that a wave-front may be replaced by an equivalent surface of sources. To model this with the KIE, the boundary is chosen along the wave-front and surface pressure and normal velocity values chosen according to what would have been observed there if the incident wave was present; the boundary vibrates and exerts force as if it were the air of the wave-front. The simplest example of this is an infinite flat boundary slicing perpendicularly through a plane wave. Using the coordinate transformation described in section 3.2 it is readily shown analytically that the same plane wave is radiated forwards and nothing is radiated backwards.

2.1.2 Scattering problems

The KIE describes the sound radiated by the known behaviour of a surface: a radiation problem. Conversely this thesis is primarily focused on the sound scattered by a surface

in response to an incident sound wave. This wave could have originated from a point source inside Ω_+, be radiation from another surface segment, just be specified as existing in Ω_+ (such as a plane wave), or be a sum of instances of all three. In order to calculate this scattered sound it must first be known how the boundary reacts to such excitation; this is described by the boundary conditions.

The total sound $\varphi^t(\mathbf{r},t)$ is the summation of sound scattered by the surface $\varphi^s(\mathbf{r},t)$ and incident sound $\varphi^i(\mathbf{r},t)$ originating from other sources. Equation 2.8 describes the total sound arising from a known incident sound and a known surface sound distribution. In a scattering problem the surface sound distribution is unknown and must be found from the incident sound. A relationship between incident sound and surface sound is required; this will be dependent on properties of the surface described by its boundary conditions.

$$
\begin{aligned}
\varphi^t(\mathbf{r},t) &= \varphi^i(\mathbf{r},t) + \varphi^s(\mathbf{r},t) \\
&= \varphi^i(\mathbf{r},t) + \iint_S \left(\varphi^t(\mathbf{r}',t) * \hat{\mathbf{n}}' \cdot \nabla' g(R,t) - g(R,t) * v_n(\mathbf{r}',t) \right) d\mathbf{r}'
\end{aligned}
\qquad 2.8
$$

Boundary conditions place restrictions of the value of $\varphi^t(\mathbf{r},t)$ on S. Examples often encountered in room acoustics include a rigid surface (Neumann problem), where the normal velocity must be zero, and a surface possessing a specific acoustic impedance where the pressure and normal velocity are related by a known transfer function. Surfaces are regarded to be locally reacting, that is behaviour at a point is not affected by neighbouring points (except by propagation through the air), so a boundary condition is a point-wise criterion.

In the direct BEM derivation, a general relationship between incident and surface sound is established for any surface character, and then refined to reflect the surface in question by application of the boundary condition at the integration point. In order to achieve the former, equation 2.8 is examined as the observation point $\mathbf{r}$ approaches S from Ω_+. As was mentioned in section 2.1.1 the two terms in the integrand of the KIE

have known values at the surface; these are substituted, hence the total sound at $\mathbf{r}$ when $\mathbf{r}$ is touching S but still in Ω_+ is given by Equation 2.9.

$$\varphi^i(\mathbf{r},t) = \tfrac{1}{2}\varphi^t(\mathbf{r},t) - \iint\limits_{S\bullet\mathbf{r}'\neq\mathbf{r}} \left(\varphi^t(\mathbf{r}',t)*\hat{\mathbf{n}}'\cdot\nabla' g(R,t) - g(R,t)*v_n(\mathbf{r}',t)\right)d\mathbf{r}' \qquad 2.9$$

Despite the definition that $v_n(\mathbf{r}',t)$ is the normal component of the gradient of $\varphi^t(\mathbf{r}',t)$ they are independent fields on the boundary, so Equation 2.9 has more unknowns than knowns and cannot be solved. This is unsurprising as no information on the characteristics of the boundary has yet been included, apart from its shape. The boundary condition is now applied at the integration point $\mathbf{r}'$.

For example, at a rigid surface $v_n(\mathbf{r}',t) = 0$, hence various terms in 2.9 are zero and the direct BIE is given by Equation 2.10. This equation now possesses only one unknown field so can be solved. It is an integral equation of the second kind as the unknown field also appears outside the integral. The direct BEM is only valid for closed surfaces as it has been assumed that the surface potential is absolute rather than a jump potential.

$$\varphi^i(\mathbf{r},t) = \tfrac{1}{2}\varphi^t(\mathbf{r},t) - \iint\limits_{S\bullet\mathbf{r}'\neq\mathbf{r}} \varphi^t(\mathbf{r}',t)*\hat{\mathbf{n}}'\cdot\nabla' g(R,t)d\mathbf{r}' \qquad 2.10$$

2.1.3 Indirect BEM

The indirect BEM postulates that the solution to the scattering problem may be represented by the summation of the incident sound and sound radiated by single and double layer potentials on a surface. In the acoustics application it so happens that this equation has the same form as the KIE and the densities correspond directly to named quantities, so the indirect and direct BEM appear very similar. However, the single and double layer densities are regarded as hypothetical fields so, instead of application of the boundary condition at the integration point, a solution is found by satisfying the boundary condition at the observation point as it approaches the boundary. This is demonstrated for the case of a rigid surface in Equation 2.11, where $\mathbf{r}$ is assumed to lie on S.

11

$$\hat{\mathbf{n}} \cdot \mathbf{v}^t(\mathbf{r},t) = 0$$

$$\hat{\mathbf{n}} \cdot \mathbf{v}^i(\mathbf{r},t) = -\hat{\mathbf{n}} \cdot \mathbf{v}^s(\mathbf{r},t)$$

$$\hat{\mathbf{n}} \cdot \nabla \varphi^i(\mathbf{r},t) = -\hat{\mathbf{n}} \cdot \nabla \varphi^s(\mathbf{r},t) \qquad \text{2.11}$$

$$\hat{\mathbf{n}} \cdot \nabla \varphi^i(\mathbf{r},t) = -\hat{\mathbf{n}} \cdot \nabla \iint_S \varphi^t(\mathbf{r}',t) * \hat{\mathbf{n}}' \cdot \nabla' g(R,t) d\mathbf{r}' + \hat{\mathbf{n}} \cdot \nabla \iint_S g(R,t) * v_n(\mathbf{r}',t) d\mathbf{r}'$$

Distributions of $v_n(\mathbf{r}',t)$ and $\varphi^t(\mathbf{r}',t)$ are now found that satisfy the boundary condition, using the known behaviour of the normal derivative of the layer potentials. This is rather a trivial example since the boundary condition explicitly sets the single layer potential weights to zero. Less trivial boundary conditions state a relationship between pressure and velocity at the observation point, so there are more terms to solve from. An indirect BEM may be valid on open surfaces if the boundary condition is compatible (as this example is).

2.1.4 External problems

The final piece in the framework for modelling scattering problems is how to deal with the common situation where the air surrounds the boundary (external problem), depicted in Figure 2.2. The KIE was necessarily derived for the interior problem where the boundary surrounds the media, so this must be upheld. The common way of achieving this is to consider there to be an enclosing surface S_∞ at an infinite distance from the scattering body of interest, noting that the derivation of the KIE did not require S or Ω_- to be connected. S_∞ is shown to have no effect on the sound close to the scatterer by using causality for transient problems (the sound scattered from the enclosing boundary never arrives) or by using the Sommerfield Radiation Condition for frequency domain (section 2.1.5) problems.
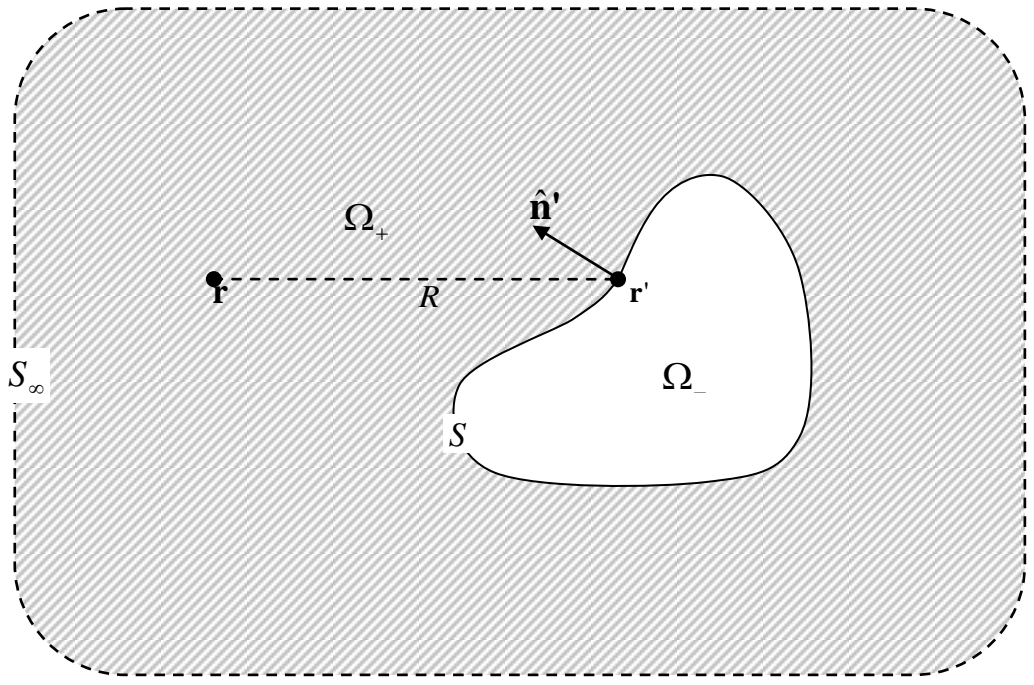
Figure 2.2: In the external problem the air must still be enclosed by surfaces; an outer boundary is imagined that so distant that its effects never arrive.

As was alluded to by the earlier mentions of thin plates and open surfaces, the KIE does not explicitly disallow sound waves to travel through Ω_-. The restriction that air is present on only one side of the boundary was lost in the process of conversion from volume differential equation to BIE. That a wave is propagated outwards rather than inwards from a boundary is merely a property of the interactions of the normal velocity and pressure jump radiation patterns. It is assumed that the $\varphi^i(\mathbf{r},t)$ penetrates the entire media, both Ω_+ and Ω_-. If $\varphi^t(\mathbf{r},t)=0$ in Ω_- this is only because the solution of the boundary condition over S has created an equivalent surface source distribution that radiates a wave $\varphi^s(\mathbf{r},t)$ that cancels out $\varphi^i(\mathbf{r},t)$ in Ω_-. In other words Ω_- is modelled as an air filled cavity; ramifications for BEM performance are discussed in section 2.1.9.

2.1.5 Frequency and Time Domain Models

The time domain KIE discussed so far describes the transient behaviour of sound witnessed in everyday life. A special case of this, albeit a very important one, is when

13

sound of only one frequency is present and always has been and will be, so the system is in steady state. All quantities oscillate in time with angular frequency ω, and are described by $\varphi^t(\mathbf{r},t) = \text{Re}\left[\Phi(\mathbf{r})e^{-i\omega t}\right]$, where $\Phi(\mathbf{r})$ is a time-invariant complex-valued spatial field describing magnitude and phase. This form is valid as sine waves are orthogonal in time hence any excitation describable in the above form will only create steady state oscillations in the media that can be expressed in the same way; solutions for different frequencies are independent and may be evaluated individually provided the acoustic system is linear. Additionally, summation of single frequency responses can represent any transient signal of finite energy, and the Fourier transform provides a gateway between the time domain of $\varphi^t(\mathbf{r},t)$ and the frequency domain of $\Phi(\mathbf{r})$.

$$P(\mathbf{r}) = i\omega\rho_0\Phi(\mathbf{r}) \qquad\qquad 2.12$$

$$\mathbf{V}(\mathbf{r}) = \nabla\Phi(\mathbf{r}) = \frac{\nabla P(\mathbf{r})}{i\omega\rho_o} \qquad\qquad 2.13$$

The relationships between pressure, velocity and velocity potential in the frequency domain are expressed in Equations 2.12 and 2.13. As previously mentioned, the Greens function describes how sound travels from point $\mathbf{r}'$ to point $\mathbf{r}$. The time domain version (Equation 2.7) intuitively comprises a delay term as a numerator and a reduction in magnitude with distance as the denominator. The factor of $(4\pi)^{-1}$ arises from the spherical symmetry of a point source. The frequency domain Greens function (Equation 2.14) is a Fourier transform of the time domain version, where the delay has been converted to a phase change as all variables are oscillating with the same period ω. $k = \frac{\omega}{c}$ is the wavenumber describing phase change as a function of distance $R = |\mathbf{r} - \mathbf{r}'|$.

$$G(R,k) = F\left\{ \frac{\delta\left(t - \frac{R}{c}\right)}{4\pi R} \right\} = \frac{1}{4\pi R}\int_{-\infty}^{\infty} \delta\left(t - \frac{R}{c}\right)e^{i\omega t}dt = \frac{e^{i\omega t}}{4\pi R}\bigg|_{t=\frac{R}{c}} = \frac{e^{ikR}}{4\pi R} \qquad 2.14$$

14

Similarly the frequency domain KIE (Equation 2.15) is the Fourier transform of the time domain version, noting that temporal convolution becomes multiplication under Fourier transform. This has very similar form to the time domain KIE but upon discretisation requires a different solution scheme.

$$
\begin{aligned}
\Phi^s(\mathbf{r},k) &= F\{\varphi^s(\mathbf{r},t)\} \\
&= F\left\{\iint_S \left(\varphi^t(\mathbf{r}',t) * \hat{\mathbf{n}}'\cdot\nabla' g(R,t) - g(R,t) * \hat{\mathbf{n}}'\cdot\nabla'\varphi^t(\mathbf{r}',t)\right)d\mathbf{r}'\right\} \\
&= \iint_S \left(\Phi^t(\mathbf{r}',k)\hat{\mathbf{n}}'\cdot\nabla' G(R,k) - G(R,k)\hat{\mathbf{n}}'\cdot\nabla'\Phi^t(\mathbf{r}',k)\right)d\mathbf{r}'
\end{aligned}
\qquad 2.15
$$

2.1.6 Discretisation

The surface quantities must be discretised in order for a solution to the boundary conditions to be found numerically. The notation for discretisation used in this thesis is that of basis functions; a quantity is approximated by a weighted summation of a family of functions covering its support. For example, the spatial variation of a snapshot of a sound could be written as Equation 2.16 where each $f_n(\mathbf{r})$ is a member of a family of spatial basis functions that cover S and w_n are corresponding scalar weights.

$$
\Phi(\mathbf{r}) = \sum_{\substack{\forall f_n \in \\ \text{spatial basis}}} w_n f_n(\mathbf{r}) \qquad 2.16
$$

This notation improves clarity relative to the definition in prose used in some publications. Generality is not lost; basis functions may be chosen to represent any discretisation scheme mentioned in this thesis. In fact generality is improved as an algorithm may be developed without condition on what the basis functions actually are. Conversely, where a property of a basis function is exploited to allow a certain refinement of an algorithm this must be stated categorically.

Most spatial discretisation schemes require approximation of the surface by elements denoted S_n. These may be flat (usually triangles or quadrilaterals), in which case the surface is approximated by a polyhedron, or possess curvature that is optimised to fit the

surface. Over each element a family of basis functions is defined, usually with the property that the summation of the family is constant everywhere on the element, and zero elsewhere. The simplest family comprises a single basis function that has these properties (Equation 2.17). The spatial discretisation for the entire surface is the weighted summation of all these families of basis functions for all elements.

$$\mathrm{f}_n(\mathbf{r}) = \begin{cases} 1 & \text{if } \mathbf{r} \in \mathrm{S}_\mathrm{n} \\ 0 & \text{otherwise} \end{cases} \qquad 2.17$$

This division of the surface into elements is not strictly necessary, but construction of a bespoke family of basis functions for an arbitrary surface is expensive, certainly more so than meshing into elements. It is generally accepted that using higher order spatial approximations (both element curvature and basis functions) allows larger and hence fewer elements, at the expense of a larger number of unknowns per element.

The temporal variation in the frequency domain problem is described by the complex exponential $e^{-i\omega t}$, which is periodic hence the only time information is phase and that is contained in the complex value of the spatial weight w_n. Consequentially spatial discretisation alone is adequate for the frequency domain discretisation.

By contrast the temporal variation of the time domain problem is unknown. A family of temporal basis functions is required that approximates the temporal variation of the surface sound over the required duration. Spatial discretisation is still required, thus the time domain problem is approximated by a nested summation of spatial basis functions and temporal basis functions as shown in Equation 2.18, where each $\mathrm{T}_i(t)$ is a member of the family of temporal basis functions and each pairing has its own weight $w_{n,i}$.

$$\varphi(\mathbf{r},t) = \sum_{\substack{\forall \mathrm{f_n} \in \\ \text{spatial} \\ \text{basis}}} \sum_{\substack{\forall \mathrm{T}_i \in \\ \text{temporal} \\ \text{basis}}} w_{n,i}\, \mathrm{f}_n(\mathbf{r})\, \mathrm{T}_i(t) \qquad 2.18$$

In order to be suitable for solution using the Marching On in Time solver (defined in section 2.1.7) the temporal basis family should comprise regularly delayed copies of a mother basis function (Equation 2.19), where Δ_t may be thought of as a time-step. Such a family may represent common interpolation schemes such as linear interpolation or zero-order hold, for which the mother basis function is a triangle function or a top-hat function respectively.

$$\mathrm{T}_i(t) = \mathrm{T}_{mother}\left(\frac{t}{\Delta_t} - i \right) \qquad\qquad 2.19$$

2.1.7 Boundary Integral to Boundary Element

The strategy used to create a Boundary Element Method Model from a Boundary Integral Equation is the same in both the frequency and time domains, although the resulting algorithms are different. In both schemes, the surface velocity potential is approximated by a weighted sum of basis functions as described in section 2.1.6 and this is substituted into the integral equation. As the KIE is a linear operator the summations and weights may be moved outside the integrals, creating a weighted sum of integrals that are dependent only on the surface geometry and independent of system excitation. Upon evaluation these integrals become interaction coefficients that can calculate sound radiated from the surface using only the discretisation weights. This is shown in Equations 2.20 and 2.21 for the frequency domain and time domain problems respectively, where the linear operator $L\{\ \}$ represents the KIE, mapping surface velocity potential to radiated velocity potential at $\mathbf{r}$. The discretisation weights will be found by numerical solution of the matrix equations that result from combination of these integral equations with the boundary conditions.

$$\Phi^s(\mathbf{r}) = L\{\Phi^t(\mathbf{r'})\} = L\left\{ \sum_{\substack{\forall f_n \in \\ \text{spatial} \\ \text{basis}}} w_n\, f_n(\mathbf{r'}) \right\} = \sum_{\substack{\forall f_n \in \\ \text{spatial} \\ \text{basis}}} w_n L\{f_n(\mathbf{r'})\} \qquad\qquad 2.20$$

$$\varphi^s(\mathbf{r},t) = L\{\varphi^t(\mathbf{r}',t')\} = L\left\{\sum_{\substack{\forall f_n \in \\ \text{spatial} \\ \text{basis}}} \sum_{\substack{\forall T_i \in \\ \text{temporal} \\ \text{basis}}} w_{n,i}\, f_n(\mathbf{r}')\, T_i(t')\right\} = \sum_{\substack{\forall f_n \in \\ \text{spatial} \\ \text{basis}}} \sum_{\substack{\forall T_i \in \\ \text{temporal} \\ \text{basis}}} w_{n,i}\, L\{f_n(\mathbf{r}')\, T_i(t')\} \qquad 2.21$$

To aid clarity in the remainder of this section the choice of basis functions is assumed to be piecewise constant spatial as Equation 2.17, and time-step based temporal as Equation 2.19. This allows the discussion of the number of unknown weights to use the conventional terms of number of spatial elements N_s and number of time-steps N_t, rather than the product of the size of sets of basis functions used. For higher order discretisation schemes the number of unknowns is still proportional to the number of elements and number of time-steps so the trends discussed hold.

The BIEs derived in sections 2.1.2 and 2.1.3 to calculate surface sound from incident sound are discretised in the same way as the KIE. The frequency domain equation has N_s unknown weights. In order to solve for those weights it must be evaluated at N_s different points on the surface, called collocation points, often chosen to be at the centre of each element. Each collocation point contributes a row to Equation 2.22, comprising a matrix $\mathbf{Z}$ of excitation independent interaction coefficients, a vector of weights $\mathbf{w}$ and an excitation vector $\mathbf{e}$. Once the integrals in each element of $\mathbf{Z}$ have been evaluated, standard linear algebra techniques are used to solve for $\mathbf{w}$. This algorithm may be interpreted as solving for the discretisation weights such that the boundary condition is maintained at all collocation points. $\delta_{m,n}$ is the Kronecker Delta, $\mathbf{r}_m^c$ is the centre of element S_m.

$$\mathbf{Z}\mathbf{w} = \mathbf{e} \quad \text{where} \quad \begin{aligned} \mathbf{Z}_{m,n} &= \tfrac{1}{2}\delta_{m,n} - L\{f_n(\mathbf{r}')\}\big|_{\mathbf{r}=\mathbf{r}_m^c} \\ \mathbf{w}_n &= w_n \\ \mathbf{e}_m &= \varphi^i(\mathbf{r}_m^c) \end{aligned} \qquad 2.22$$

The process is very similar for the time domain, despite the fact that the number of unknowns is multiplied by N_t. Temporal basis function selection combined with causality dictates that past surface sound cannot be changed and future sound is

irrelevant, hence at each time-step $t_j = j\Delta_t$ the algorithm is only solving for the current

unknown weights and N_s collocation points will suffice. Equation 2.23 describes the

time domain problem, comprising matrices $\mathbf{Z}_{j-i}$ of excitation independent interaction

coefficients, vectors of discretisation weights $\mathbf{w}_i$ and excitation vectors $\mathbf{e}_j$.

$$\sum_{i \in time-steps} \mathbf{Z}_{j-i} \mathbf{w}_i = \mathbf{e}_j \quad \text{where} \quad \begin{aligned} \mathbf{Z}_{j-i;m,n} &= \tfrac{1}{2}\delta_{m,n} \, \mathrm{T}_i(j\Delta_t) - L\{\mathrm{f}_n(\mathbf{r})\mathrm{T}_i(j\Delta_t)\}\big|_{\mathbf{r}=\mathbf{r_m^c}} \\ \mathbf{w}_{i;n} &= w_{n,i} \\ \mathbf{e}_{j;m} &= \varphi^i(\mathbf{r_m^c}, j\Delta_t) \end{aligned} \qquad 2.23$$

To emphasise the time and excitation invariant nature of the matrices $\mathbf{Z}_{j-i}$, the

summation index will be changed to retardation $l = j - i$ in Equation 2.24. If the mesh

is finite and the temporal basis functions compact then there will be an upper limit on

retardation time across the mesh, hence $\mathbf{Z}_l$ will be zero for l greater than some constant

l_{max}. Future surface sound cannot contribute to current sound so l must be also greater

than or equal to zero.

$$\sum_{l \geq 0}^{l \leq l_{max}} \mathbf{Z}_l \mathbf{w}_{j-l} = \mathbf{e}_j \qquad 2.24$$

Known terms are gathered together on the right hand side in Equation 2.25, revealing

that this equation, like that of the frequency domain, may be interpreted as solving for

the approximation weights such that the boundary condition is maintained at each

collocation point at each time-step. The resulting algorithm is commonly referred to as

the Marching On in Time (MOT) or 'Retarded Potential' algorithm, and intuitively

possesses an iterative structure with sound travelling from element to element with a

finite speed.

$$\mathbf{Z}_0 \mathbf{w}_j = \mathbf{e}_j - \sum_{l > 0}^{l \leq l_{max}} \mathbf{Z}_l \mathbf{w}_{j-l} \qquad 2.25$$

2.1.8 Computational Cost

The first stage of both these algorithms is to populate the interaction matrices by numerical integration. In the frequency domain, both computational and storage requirements for this scale $O(N_s^2)$. In the time domain, a pair of elements may have multiple non-zero interactions, but for the time-step values typically used the number of these turns out to be roughly constant. Hence both computational and storage requirements for the time domain interaction matrices also scale $O(N_s^2)$. In both algorithms the matrix population stage can be easily parallelised (fine-grained) to accelerate larger problems.

The solution stage differs, and both are not easily parallelisable so their computational cost is paramount. In the frequency domain, a dense matrix equation must be solved. The cost of performing this with traditional methods such as Gaussian Elimination is $O(N_s^3)$. Modern iterative solution methods scale substantially better than this; $O(N_s^2)$. In the time domain a sequence of matrix multiplications must be performed. This appears from Equation 2.25 to be cost $O(N_s^2 l_{max})$, but the predictable and sparse structure of the interaction matrices may be exploited to give a cost $O(N_s^2)$. A sparse matrix equation must then be solved, but as the previous time-step's weights are available as a seed an iterative solver will converge rapidly with cost $O(N_s)$. This must all be done N_t times, so the overall cost is $O(N_s^2 N_t)$. The storage for the surface sound history requires $O(N_s N_t)$, though can be reduced by only storing contributing weights in a buffer size $O(N_s l_{max})$ and streaming older results to disk.

For both algorithms the number of spatial elements required to mesh a given body is proportional to maximum frequency squared. Additionally for fixed model duration the number of time-steps required by the time domain algorithm is proportional to maximum frequency of the excitation signal. Hence the cost of the frequency domain algorithm is $O(frequency^4)$ and the cost of the time domain algorithm $O(frequency^5)$.

This analysis makes the cost of the time domain algorithm look not unreasonable compared to the frequency domain algorithm, especially when excitation is short, system reverberation is brief and solutions over a broad bandwidth are required,. However, the cost of both algorithms increases extremely rapidly with frequency restricting them to low frequency applications.

2.1.9 Non-uniqueness and Stability

It is well known that matrix equations such as Equation 2.15 may not possess a unique solution. In scattering problems these correspond to non-physical resonances of the air filled cavity created inside the surface on conversion to a BIE; the phenomenon is fundamental to the BIE rather than being caused by the discretisation scheme, although the latter may aggravate the problem. If the frequency of excitation is close to a resonance of the cavity accuracy will be poor or the numerical solver may fail to converge at all. This problem is commonly addressed in the frequency domain by using either the CHIEF[5] method, where internal points are used to create an over-determined system of equations, or the Burton-Miller[6] method, which uses a linear combination of the KIE and its surface normal derivative that only possesses unique solutions.

The same issue affects the time domain BEM, unsurprising as it is derived from an equivalent BIE. As the algorithm iteratively models sound at the surface, cavity resonances appear as oscillations in the surface fields; the MOT equation may be considered to be a discrete multi-variant infinite-impulse-response filter, and the cavity resonances are its poles. Error introduced in the discretisation process may corrupt a pole so that its response now grows exponentially, and as all resonances will be excited to some extent by any excitation signal this will dominate in long duration problems. This relationship between discretisation and stability masks the true origin of the oscillations and is responsible for the many publications that propose stability criteria based on an observed correlation with some aspect of discretisation. Section 2.2.6 discusses the development of these conclusions in detail.

2.2 Literature Review

Very similar integral equations to the KIE appear in disciplines other than Room Acoustics, primarily Underwater Acoustics, Electromagnetics and Elastodynamics; hence the appearance of such publications in what follows. While the latter two of these differ in that their unknown fields are vector rather than scalar, they share many characteristics, not least the resulting solution algorithm, since they are all concerned with the propagation of a wave of finite speed through a linear media.

2.2.1 Early algorithms

The earliest algorithms created to solve the transient scattering problem fell into the class of boundary integral solvers rather than BEMs. Examples of these include Keller and Blank's[7] 1951 model of scattering from an infinite wedge using conformal mapping, Mindlin and Bleich's[8] 1953 model of scattering from a circular cylinder using separation of variables, and Barakat's[9] 1960 model of scattering by a sphere using a temporal Laplace transform and spherical spatial modal functions. These models used boundary conditions and approximations of the surface quantities; however space and time were not discretised into elements and they lack the characteristic numerical solution stage hence are not classed as BEM models.

Friedman and Shaw's[10] 1962 algorithm was the first to discretise the surface and form a time domain BEM. It modelled arbitrary rigid cylindrical objects subject to shockwaves using two-dimensional elements assuming constant velocity potential within an element in a time-step. It used an unusual Greens function, but after manipulation the end result was the characteristic MOT equation, albeit referred to as solution of "*successive algebraic non-simultaneous equations*".

Shaw's research interests appear to have been motivated by tsunami research in underwater acoustics. In 1966[11] he tackled scattering by cylindrical obstacles that exhibited inertial but not elastic resistance and in 1972 he and English[12] published an algorithm for transient scattering by a pressure-release sphere (bubble). Finally in 1975 Shaw[13] published an algorithm for transient scattering by a circular cylinder. This

ruthlessly exploited the problem symmetry; using regularly spaced elements created repetition in the interaction matrices reducing storage and set-up cost from $O(N_s^2)$ to $O(N_s)$. Some late time instability can be observed in the results from this algorithm.

The first algorithm for surfaces of completely arbitrary shape was by Mitzner[14] in 1967. Although criticised by Shaw[15] for not supporting discontinuous excitation waves it may still have influenced him as his 1975 paper had the same restriction. Surface quantity discretisation was still constant in time and space, but a novel integration routine supported curvilinear elements and elements of revolution; velocity potential terms were brought outside the surface integral using a Taylor expansion, then the remaining term was recognised as being the negative solid angle and approximated using a procedure by Kellogg[16]. Temporal derivatives were evaluated using a three-point backward difference rule that Groenenboom[4] later describes as equivalent to the use of a quadratic interpolation scheme.

Neilson, Lu and Wang[17] combined the approaches of Shaw and Mitzner in 1978 by tracking a discontinuous wave front across a surface of revolution. Discontinuities are of interest because a pressure impulse excitation creates a discontinuity in velocity potential. This is an issue in Mitzner's scheme because the numerical temporal differentiation method used is only suitable for continuous excitation. To circumvent this, Neilson *et al* divide the surface into the silent part ahead of the wave front, the discontinuous part around the intersection of the wave front with the surface, and the continuous part behind the wave front. The thickness of the wave front region is shrunk so that it becomes a line integral. The fact that this region is seeing its first excitation (no other sound has previously arrived) justifies use of the Kirchhoff (infinite plane) boundary condition on this region, which gives surface pressure directly as twice that of the incident wave without use of temporal derivatives. This expression is substituted into the right-hand side of the KIE, allowing pressure in the continuous region behind the wave front to be handled conventionally. The resulting algorithm is complicated, not least because the wave front's intersection with the surface must be calculated at each time-step and the elements are treated differently depending on which region they are in. Ironically Neilson *et al* comment that Mitzner's scheme actually performs

surprisingly well on such discontinuous excitation as the temporal difference scheme acts as a smoothing filter.

Kawai and Terai's[18] 1990 scheme for scattering from thin rigid plates is mentioned here as it does not fit comfortably into any of the following sections. The discretisation scheme in this algorithm is simplistic for its time, comprising flat elements with constant quantities in a time-step and temporal derivatives by finite difference. It is also slightly inconsistent due to the occasional use of temporal interpolation. What this paper does contribute is the conversion of the spatial double integral to a contour integral, and the ability to model arbitrary thin surfaces. This algorithm's integration routine is the foundation of that detailed in section 3.2, and its formulation for thin surfaces is detailed in section 4.1.

2.2.2 Discretisation

All the BEM models mentioned in the previous section feature elementary discretisation specified in prose, complicating distinction of the algorithm from the discretisation scheme. This section describes the migration towards the more accurate and concise description using basis functions.

In 1983 Groenenboom[4] contributed a book chapter which aimed to review and discuss all time domain BEM for all applications through discussion of the acoustic (scalar) version. In this publication he uses interpolating temporal basis functions and finds spatial derivatives from these and his spatial basis analytically rather than by using the finite-difference approach he took in his 1982 paper[19]. High order isoparametric spatial elements are also used, which can mimic curved surfaces and represent quantities by a small family of basis spatial functions each with their own weight. These were originally developed for Finite Element Method (FEM) models, so some have characteristics more suitable for FEM than BEM. The eight-node compatible quadrangle element (Figure 2.3a) is an example of this; it is missing the ninth (central) basis function necessary for complete surface quantity approximation as it is insignificant to FEM models due to it being zero valued around the edges of the element. Similarly compatible elements are favoured by FEM models as they have

24

nodes on the edge that can be shared between elements; for BEM this causes complications as nodes are used as collocation points and these are not guaranteed to be on a smooth part of the surface. Groenenboom advocates the use of nine-node non-compatible quadrangle elements (Figure 2.3b) which posses the full family of basis functions and do not have collocation points on their edges. Seven-node non-compatible triangular elements (Figure 2.3c) are also ideal for BEM discretisation.

| (a) | (b) | (c) |
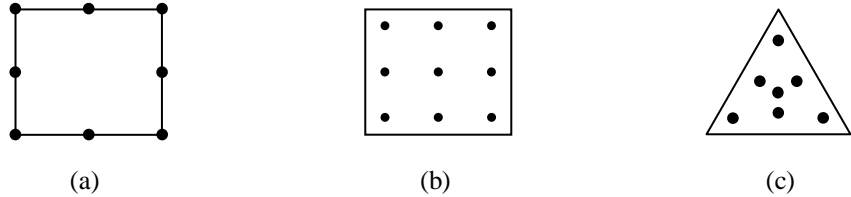
Figure 2.3: Some high order isoparametric elements

Bluck and Walker's[20] 1996 algorithm uses isoparametric spatial elements; these are the eight-node type derided by Groenenboom thirteen years earlier. They argue the generally accepted point that use of higher order elements such as these reduces the number of unknowns, a critical factor in reducing the cost of the MOT algorithm. An unusual temporal interpolation scheme is used: quadratic temporal elements (probably Lagrange polynomial basis functions) each length $2\Delta_t$, creating three unknowns for each two time-steps. Temporal derivatives are evaluated analytically.

Manara, Monorchio and Regginannini's[21] 1997 algorithm for the Electric Field Integral Equation (EFIE) returns to piecewise constant spatial basis on a flat triangular patch geometry but with a piecewise quadratic temporal basis function. The exact motivation for this function is unknown, but multiple delayed copies sum to one as desired and the authors consider significant that the middle piece is part of a parabola interpolating $(-\Delta_t, 0), (0, 1), (\Delta_t, 0)$. Ergin, Shanker and Michielssen's[22] 1999 paper uses the same spatial discretisation scheme and a piecewise cubic temporal basis function inspired by that of Manara *et al.* Both these temporal basis functions are attributed stabilizing properties. Ergin *et al* comment on their spatial discretisation scheme that "*Numerical*

schemes employing more sophisticated spatial basis functions (e.g. isoparametric elements) are expected to behave similarly to the present scheme".

Continuing the idea that the temporal basis function is pivotal in creating stability in the MOT algorithm, Hu, Chan and Xu[23,24] have published temporal basis functions that have been numerically optimized to maximize stability. Unfortunately these basis functions are symmetrical so unsuitable for evaluation with the model described in section 2.3; the temporal derivative of the basis function at $t = 0$ appears in the self-interaction equation, hence a symmetrical temporal basis function creates an all zero diagonal of the matrix $\mathbf{Z}_0$ potentially resulting in a non-unique solution.

In Ha-Duong, Ludwig and Terrasse's[25] 2003 paper basis functions are chosen according to the assumed variation of the quantity to be represented. For example, pressure jump is assumed to possess a square integrable first derivative so a piecewise constant discretisation is inadequate and piecewise linear must be used. Temporal discretisation is also piecewise linear.

A recent approach to discretisation is to use a family of hierarchical basis functions such as wavelets. Such a temporal family could be used with a conventional element-based spatial discretisation scheme, or could be combined with a hierarchical family of spatial basis functions that supports the entire scatterer, moving away from the surface elements concept entirely. The latter approach is attracting interest in the solution of the Laplace and Helmholtz equations, such as the 2006 algorithm of Amini and Nixon[26], and is considered attractive as the basis families may be chosen such that they exhibit orthogonality properties that can be exploited to reduce the cost scaling of the algorithm. These approaches are discussed further in section 2.2.7

2.2.3 Two Dimensions

A potential computational cost saving may be made by considering the two-dimensional version of a problem, as was done by Shaw in his 1962[10] and 1975[13] papers. Groenenboom[4] also used the two-dimensional time domain BEM in the context of modelling the behaviour of liquid sodium in a nuclear reactor heat-transfer system.

In 1994 Cox[27] found that a two-dimensional frequency domain BEM model is a good approximation for the scattering behaviour of diffusers that are of constant cross-section so long as a correction factor is used to account for their non-infinite length. This factor could be calculated from a two-dimensional BEM model of a plate of suitable length or by Fresnel diffraction theory - both methods assume that vertical and horizontal scattering mechanisms are independent. It follows that a two-dimensional time domain BEM may be expected to perform well with the same caveats.

In room acoustics the two-dimensional world is considered to be a slice through a three-dimensional world where all quantities and geometries are invariant with the third dimension z. An element is a small section of the line of intersection of the surface and a plane of constant z, but radiation implicitly includes the corresponding part of the surface stretching to infinity in the z direction so point sources are now line sources. Spherical radius R is replaced with cylindrical radius r. The number of elements required is now $O(frequency)$ and collocation points are chosen at the centre of the line elements. This is depicted in Figure 2.4.
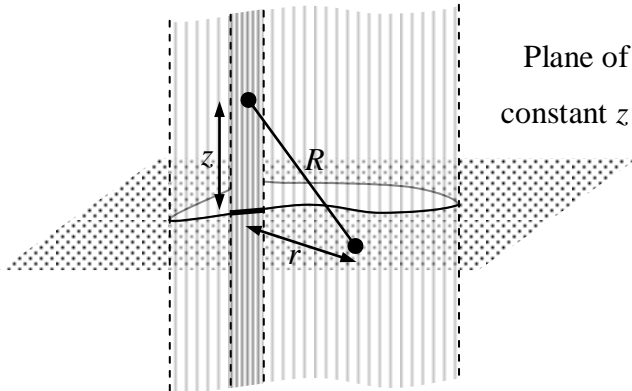
Figure 2.4: Two-dimensional BEM element interaction geometry

This is the geometry used by Shaw and in justification he writes "*The form of the fundamental solution requires that the problem be considered as three-dimensional rather than two*". However, two-dimensional Greens functions do exist for both the frequency and time domains. The surface integral can be decomposed into a contour integral along the line of intersection of the surface and the slice, and an integral in z.

27

All quantities (pressure, velocity, velocity potential and geometry) are invariant in z, so the integrals can be rearranged so that the z integral only contains the Greens function. This is shown in Equation 2.26 for the time domain and the same applies for the frequency domain.

$$\varphi^s(\mathbf{r},t) = \int\limits_{-\infty}^{\infty} \oint\limits_{S \cap (z=0)} (\varphi(\mathbf{r}',t) * \hat{\mathbf{n}}' \cdot \nabla' g(R,t) - g(R,t) * \hat{\mathbf{n}}' \cdot \nabla' \varphi(\mathbf{r}',t)) dl dz$$

$$= \oint\limits_{S \cap (z=0)} \left(\varphi(\mathbf{r}',t) * \hat{\mathbf{n}}' \cdot \nabla' \int\limits_{-\infty}^{\infty} g\left(\sqrt{r^2+z^2},t\right) dz - \int\limits_{-\infty}^{\infty} g\left(\sqrt{r^2+z^2},t\right) dz * \hat{\mathbf{n}}' \cdot \nabla' \varphi(\mathbf{r}',t) \right) dl \quad 2.26$$

$$= \oint\limits_{S \cap (z=0)} (\varphi(\mathbf{r}',t) * \hat{\mathbf{n}}' \cdot \nabla' g_{2D}(r,t) - g_{2D}(r,t) * \hat{\mathbf{n}}' \cdot \nabla' \varphi(\mathbf{r}',t)) dl$$

Here a two-dimensional Greens function has been introduced that encapsulates two-dimensional behaviour; it is given explicitly in Equation 2.27 where $h(...)$ is the heavy-side function. Importantly it is no longer compact in time, but has an infinite decaying tail. This agrees with the view of Morse and Ingard[28] who write "...*circular waves have a more complicated shape than plane or spherical waves; they leave a 'wake' behind them as they spread out*". As a result the sequence of interaction matrices is now endless, requiring truncation, and they are mostly full. The computational cost is now $O(N_s^2 N_t^2)$. The number of elements and time-steps both scale $O(frequency)$, so the cost of the 2D problem is $O(frequency^4)$, which versus the 3D problem's $O(frequency^5)$ is not a great saving. Consistently Groenenboom[4] writes that "*the expected advantage of treating 3D problems in 2D symmetry is partly lost*".

$$g_{2D}(r,t) = \frac{h\left(t - r/c\right)}{2\pi\sqrt{t^2 - \left(r/c\right)^2}} \quad\quad 2.27$$

In the frequency domain the computational saving is greater. By virtue of the system's time-invariant nature, the frequency domain two-dimensional Greens functions (Equation 2.28) is still a complex valued scalar, so the matrix equation is still full but with a reduction in the number of elements. The computational and storage cost is still

$\mathrm{O}\!\left(N_s^2\right)$, but due to the reduced number of elements this is $\mathrm{O}\!\left(frequency^2\right)$, substantially faster than the 3D problem's $\mathrm{O}\!\left(frequency^4\right)$. $H_0^{(1)}(...)$ is the Hankel function, the outgoing-wave solution of the Bessel equation.

$$G_{2D}(r,k) = \frac{i}{4} H_0^{(1)}(kr)$$
<div align="right">2.28</div>

In 2000 Lu, Wang, Ergin, and Michielssen[29] published a paper applying their Plane-Wave Time Domain algorithm (section 2.2.7) to two-dimensional electromagnetic scattering. This significantly reduces the computational cost from $\mathrm{O}\!\left(N_s^2 N_t^2\right)$ to $\mathrm{O}\!\left(N_s \log(N_s) N_t \log(N_t)\right)$. This breakthrough may make two-dimensional time domain BEM attractive.

In conclusion, great computational savings may be made by considering frequency domain problems in two-dimensions. Traditionally these savings do not translate to the time domain except for short model durations, so the two-dimensional time domain BEM is of less interest. Use of the Plane-Wave Time Domain algorithm may redress this.

2.2.4 Galerkin Schemes

Both collocation and Galerkin testing schemes are approaches to converting an equality between fields on a domain into a matrix equality suitable for numerical solution. This is illustrated for two hypothetical spatially and temporally varying fields ψ and φ as follows, where the domain of equality is the product of the spatial domain Γ and the temporal domain $t_{min} \leq t \leq t_{max}$:

$$\psi(\mathbf{r},t) = \varphi(\mathbf{r},t)\big|_{\mathbf{r}\in\Gamma,\,t_{min}\leq t\leq t_{max}} \quad \rightarrow \quad \mathbf{\Psi} = \mathbf{\Phi}$$
<div align="right">2.29</div>

In the case of time domain BEM, the KIE and the boundary conditions have created a relationship between incident and surface sound and upon discretisation this yields the MOT equation. All schemes discussed so far have used collocation; the relationship

between incident and surface sound is considered at (and hence the integral equation is evaluated at) the centre of each element at each time-step. Accordingly the elements of the matrices in Equation 2.29 would be defined:

$$\mathbf{\Psi}_{m,j} = \psi\left(\mathbf{r}_m^c, t_j\right)$$

$$\mathbf{\Phi}_{m,j} = \varphi\left(\mathbf{r}_m^c, t_j\right) \qquad\qquad 2.30$$

A Galerkin testing scheme is more sophisticated than collocation; where collocation only evaluates the fields to be tested at a set of points in space-time, a Galerkin scheme integrates them over all space-time with significance weighting functions, referred to as testing functions (indicated by a tilde). If a Galerkin testing scheme was applied to the field equality of Equation 2.29 then the matrix elements would be defined:

$$\mathbf{\Psi}_{m,j} = \int_{-\infty}^{\infty}\iiint_\Gamma \psi(\mathbf{r},t)\tilde{\mathrm{f}}_m(\mathbf{r})\tilde{\mathrm{T}}_j(t)d\mathbf{r}dt$$

$$\mathbf{\Phi}_{m,j} = \int_{-\infty}^{\infty}\iiint_\Gamma \varphi(\mathbf{r},t)\tilde{\mathrm{f}}_m(\mathbf{r})\tilde{\mathrm{T}}_j(t)d\mathbf{r}dt \qquad\qquad 2.31$$

The testing functions must be non-zero only in the domain of equality (Equation 2.32). If the support of each testing function is known then the integration domain may be reduced. If, as in the BEM case, the domain of equality Γ is a surface then the order of integration may be reduced.

$$\begin{aligned} &\forall_m \left\{\sup\left(\tilde{\mathrm{f}}_m(\mathbf{r})\right)\subset \Gamma\right\} \\ &\forall_j \left\{t_{\min} \le \sup\left(\tilde{\mathrm{T}}_j(t)\right) \le t_{\max}\right\} \end{aligned} \qquad\qquad 2.32$$

It is common in Galerkin BEM to find the basis functions being used as testing functions firstly because they are already defined appropriately over the surface, and secondly because when used with symmetrical integrands the interaction matrices become symmetric which may be exploited to reduce storage. The schemes are

interchangeable, and in addition to matched testing schemes the combinations of spatial collocation with Galerkin temporal testing and vice-versa appear in the literature. This flexibility is unsurprising as collocation is a special case of the Galerkin method where the testing functions are delta functions:

$$
\begin{aligned}
\tilde{f}_m(\mathbf{r}) &= \delta\left(\left|\mathbf{r} - \mathbf{r}_m^c\right|\right) \\
\tilde{T}_j(t) &= \delta\left(t - t_j\right)
\end{aligned}
$$

2.33

The flourishing use of Galerkin testing schemes in time domain BEM models is a relatively recent phenomenon, although Shaw[13] proposed it in the future work section of his 1975 paper. In the field of Electromagnetics Vechinski and Rao[30] used spatial Galerkin testing with temporal collocation in 1992, and Manara, Monorchio and Regginannini[21] allegedly use a Gallerkin testing scheme in 1997 although details are omitted. Ergin's 2000 Thesis[31] uses spatial Galerkin testing with temporal collocation, but in all but one special case he evaluates the testing integral (over the observer element S_m) using a one-point Gaussian rule, resulting in almost the same implementation produced by collocation in his 1999 paper[22].

Galerkin schemes are preferred by the more mathematically inclined authors perhaps because their properties are better understood and surrender more readily to rigorous theoretical analysis. A Galerkin scheme is more accurate, and hence more stable, than a collocation scheme; for example Ding, Forestier and Ha-Duong[32] concluded in 1989 that use of Galerkin testing with piecewise constant basis gave better results than collocation with a quadratic basis. This is believable from a physical perspective as a Galerkin scheme maintains the boundary condition across the whole surface rather than just at the collocation points.

Philosophical comments also appear, such as Bonnet, Maier and Polizzotto's [33] in 1998 that the symmetric Galerkin BEM has "*harmony*". An energy meaning is also attributed to the procedure, due to Equation 2.31 having the form of an inner-product. There are many publications discussing the mathematical properties of the time domain BEM, a

substantial proportion of which are in French. Ha-Duong's [34] comprehensive 2003 survey article references the bulk of these.

However all this is at the expense of additional integration effort and additional complication because the collocation point can no longer be guaranteed to be on a smooth region of the scattering surface. Ding, Forestier and Ha-Duong [32] circumvent this issue in 1989 by using a one-point Gaussian rule to evaluate their testing integral. In light of this, their comments in the previous paragraph on improved accuracy must be solely attributed to the use of temporal Galerkin testing, which perhaps is more critical. In 2003 Ha-Duong, Ludwig and Terrasse [25] do integrate over the entire testing element, but the jump property is considered to be ½ everywhere, even on element edges, on the reasoning that they have infinitesimal thickness and therefore contribute negligibly to the integral. Bonnet, Maier and Polizzotto [33] consider the singularity occurring on a common edge or vertex of adjacent elements separately from the contribution of the rest of each element.

In the hierarchical basis function schemes mentioned in section 2.2.2 and discussed further in section 2.2.7 Galerkin testing plays a pivotal role. Basis and testing functions are chosen such that they exhibit orthogonality properties, meaning they have a zero non-self inner-product with respect to space or time. The cost savings associated with these algorithms are achieved by using Galerkin testing and exploiting the pattern of zero interactions that arises.

2.2.5 Implicitness

The word implicitness refers to the existence of off-diagonal terms in the current-interaction matrix $\mathbf{Z}_0$, meaning a matrix equation must be solved to find the current discretisation weights to satisfy the boundary condition. Conversely explicitness is the inexistence of these terms, so each discretisation weight is found by division by a scalar. The physical interpretation is that an explicit algorithm solves to maintain the boundary condition at each collocation point *individually*, while an implicit scheme allows elements to interact within the current time-step and its solution maintains the boundary condition at *all* collocation points *simultaneously*. Implicit iterative algorithms are

generally considered to be more stable than their explicit counterparts, as local errors are damped by the effect of their neighbours.

In many time domain BEM implementations sound radiated in the current time-step and that from past time-steps cannot be distinguished, often ultimately due to imprecise specification of the temporal discretisation scheme in prose. Instead all self interactions are considered current and all non-self interactions are considered past, forcing $\mathbf{Z}_0$ to be diagonal and solution explicit. Many algorithms do not even have a $\mathbf{Z}_0$ matrix, its diagonal terms appearing directly in the equation for each collocation point, hence explicitness is embedded. This restriction forces an upper limit to be placed on the time-step duration such that sound from other elements cannot contribute to the current-interaction. This is the Courant-Friedrich-Levy (CFL) condition defined:

$$\mathrm{CFL}(mesh) = \frac{c\Delta_t}{\min_{S_n \in elements} \min_{\mathbf{r} \in \partial S_n} \left| \mathbf{r} - \mathbf{r_n^c} \right|} < 1 \qquad\qquad 2.34$$

If an implicit scheme is used Δ_t may be chosen freely instead of being limited by the smallest element according to the CFL condition. This can make a particular difference in situations where a few small elements are required to describe a small surface feature rather than to model rapid spatial variation in the surface fields. An explicit model would be tied to the short Δ_t prescribed by the CFL condition for the smallest element, hence would require more time-steps to model the problem duration with increased numerical cost. Dodson, Bluck and Walker [35] suggest a typical ratio of $\Delta_x \approx c\Delta_t$ (cubic elements in space-time) when similar order spatial and temporal basis are used, which is logical as temporal and spatial variation is represented with similar accuracy for each frequency component. Δ_x is the maximum element vertex separation defined as:

$$\Delta_x = \max_{S_n \in elements} \max_{\substack{\mathbf{r} \in S_n \\ \mathbf{r}' \in S_n}} |\mathbf{r} - \mathbf{r}'| \qquad\qquad 2.35$$

In their 1996 paper, Bluck and Walker [20] published an implicit time domain BEM for acoustic scattering. Gaussian (point-wise) numerical integration was used (more details on numerical integration follow in chapter 3) and points lying within a sphere radius $c\Delta_t$ were flagged as 'current' and moved to the left hand side of the MOT equation. Ergin, Shanker and Michielssen's [22] 1999 method achieved greater elegance than this; their summation of temporal basis functions was brought outside the integrals and the implicit structure follows naturally.

Both these algorithms efficiently addressed the issue of solution of the matrix equation that had previously been considered a major disadvantage of the implicit scheme. If Gaussian elimination were used, at a cost of $O(N_s^3)$, this stage would dominate the cost of the MOT process. By exploiting the time-invariant of $\mathbf{Z}_0$ and using LU decomposition or multiplication by $\mathbf{Z}_0^{-1}$ the cost can be reduced to $O(N_s^2)$, the same order as the right hand side of the MOT equation, but the real cost is still substantial. The most efficient method is to use an iterative matrix solver, such as the conjugate-gradient algorithm. The two reasons this is so efficient are that $\mathbf{Z}_0$ is extremely sparse and that the previous time-step's solution is an excellent solution seed; cost is the order of the number of non-zeros in $\mathbf{Z}_0$ which is $O(N_s)$. Consequentially the implicit algorithm has the same cost trends as the explicit algorithm but with fewer time-steps, possibly making it more efficient overall.

Many authors have put a stronger (lower) limit on Δ_t than the CFL condition as it is considered that a smaller time-step improves stability, an argument clearly against implicit schemes. However, there is also published evidence to the contrary. Dodson, Bluck and Walker [35] found a trend of increased instability at smaller (less implicit) time-steps. Herman and van den Berg [36] found that an implicit time-step gave the most accurate results for their steepest-descent scheme (described in section 2.2.7). In 1998 Dyka and Ingel [37] wrote "*More importantly, but less widely known, is the fact that the*

standard retarded potential formulation is unstable for time-steps below a critical value"; Groenenboom's [19] 1982 paper is cited as justification for this statement, though the only relevant evidence contained there is a pair of numerical examples where the one with the smaller time-step shows instability, so the evidence is not extensive. A further argument in favour of implicitness is that, if a primary concern is instability that occurs after a large number of time-steps, then surely fewer time-steps are favourable to more.

The use of CFL as an accuracy criterion is also anti-intuitive. In the frequency domain, spatial variation is described by the wavenumber $k = \omega c^{-1}$. The largest phase variation over an element's area is expected to be k multiplied by its maximum vertex separation Δ_x. For the entire mesh, spatial discretisation error will likely be defined by the size of the largest element, not the smallest as with the CFL condition. For a given mesh, CFL is likely to be proportional to temporal discretisation error, as it is proportional to Δ_t. However, the same proportionality factor would unlikely transfer to a different mesh. Assuming similar order spatial and temporal discretisation, a more appropriate accuracy measure for the time domain BEM is the phase variation permitted by the discretisation scheme (Equation 2.36), where ω_{max} is the maximum angular frequency and a small value indicates high accuracy.

$$\omega_{max}\left(\Delta_t + \Delta_x c^{-1}\right) \qquad\qquad 2.36$$

Ha-Duong is less positive about implicitness. In his 2003 book chapter [34] he writes "*Actually various methods are proposed to improve the stability of these schemes: techniques of time-averaging, of shifted time-steps or by having recourse to some implicitness. The main idea is to manage to kill the high frequencies of the algebraic systems obtained in the discretisation process*". By this he groups together implicitness with engineered stabilization schemes, when it is rather an improvement in generality of formulation. His 1989 algorithm [32] enforces the CFL condition, creating an explicit matrix equation as delta functions are used as Galerkin spatial testing functions. By contrast his 2003 paper [25] uses the spatial basis functions as Galerkin testing functions,

so even when the (now meaningless) CFL condition is enforced, $\mathbf{Z}_0$ contains non-zero off-diagonal terms. However, rather than acknowledge that this algorithm is 'implicit', the authors choose to designate it 'semi-explicit', claiming in justification that CFL > 1 would violate the causality condition. In contrast, this thesis asserts that the CFL value characterises only the discretisation scheme and causality is ensured by the time domain Greens function, a stance reinforced by the existence of non-MOT simultaneous solvers and non-time-step based temporal discretisation (e.g. hierarchical) as described in section 2.2.7.

Explicitness is merely a special case of implicitness. The elegance of formulations such as Ergin *et al's* [22] should improve the popularity of implicit MOT based schemes. Simultaneously the introduction of hierarchical temporal basis functions renders the notion of time-step, and consequently the CFL condition, redundant.

2.2.6 Stability

Stability is a crucial issue for the time domain BEM and it, along with high computational cost, is a key reason for its lack of widespread use. The vast majority of publications touch upon stability issues, and many propose conditions (often heuristic) that if met guarantee stability of the corresponding algorithm. However it was not until 1986 that the source of the instabilities was addressed directly.

Rynne [38] observed that similar instabilities affect all time domain BEM models regardless of the application or discretisation, implying that this behaviour is fundamental to the method rather than the problem considered. Additionally, these instabilities commonly take the form of an exponentially increasing oscillation that alternates in sign at each time-step. He proposed that the instabilities are solutions of Equation 2.37 with the form of Equation 2.38. This contradicts the initial conditions so the instability must be initiated by numerical errors, explaining the apparent dependency on discretisation scheme. It also allows multiple instabilities to exist but, due to their exponential increase, the one with the largest α will ultimately dominate. From this model of the instabilities, he concluded that the backward finite-difference formula used to evaluate temporal derivatives is a prime culprit for promoting instability, as it

magnifies errors with alternating sign. Use of a central-difference formula produces better results as alternating sign errors cancel out.

$$\sum_{l \geq 0}^{l \leq l_{\max}} \mathbf{Z}_l \mathbf{\Phi}_{j-l} = 0 \qquad\qquad 2.37$$

$$\mathbf{\Phi}_j = (-1)^j e^{\alpha j} \mathbf{\Phi}_0^e \qquad\qquad 2.38$$

Additionally to this, he suggested that instabilities are associated with the harmonic solutions (resonances) of the equivalent frequency domain problem. He executed low frequency models with long time-steps and correlated the frequency of the resulting non-physical oscillations with the internal resonances of the scatterer. This evidence supported the resonance association and proved that solutions excluded by the initial conditions can exist. At higher frequencies there was no obvious correlation between the growing instabilities and resonant frequencies, but this was attributed to poor representation of high frequency components combined with the destabilizing effect of the finite-difference formula.

In 1990 Rynne and Smith[39] re-examined these high frequency instabilities. Rynne's instability model was superseded by the use of Singularity Expansion Method (SEM) poles, combining the $(-1)^j e^{\alpha j}$ terms into a pole term λ_n^j. The continuous system response is given in Equation 2.39 in terms of poles and corresponding modes denoted s_n and $\mathbf{\Phi}_n$ respectively. The real part of s_n represents a damping coefficient and the imaginary part an oscillatory component. The discrete time version of this model is given in Equation 2.40 and is related to the continuous time version by Equation 2.41. A stable continuous time pole s_n will lie in the left-hand complex half plane of an Argand diagram, and corresponds to a discrete time pole λ_n inside the unit circle, as depicted in Figure 2.5.

$$\mathbf{\Phi}^t(t) = \sum_n \mathbf{\Phi}_n \left[\mathrm{Re}\left(e^{s_n t}\right) \underset{t}{*} \mathbf{\Phi}_n \cdot \mathbf{\Phi}^i(t) \right] \qquad\qquad 2.39$$

37

$$\Phi_{j}^{t} = \sum_{n} \Phi_{n}\left[\mathrm{Re}\!\left(\lambda_{n}^{j}\right)\underset{j}{*}\,\Phi_{n}\cdot\Phi_{j}^{i}\right]\qquad\qquad 2.40$$

$$\lambda_{n} = e^{s_{n}\Delta_{t}};\quad \mathrm{Re}[s_{n}] = \frac{\ln\!\left|\lambda_{n}\right|}{\Delta_{t}};\quad \mathrm{Im}[s_{n}] = \frac{\angle\lambda_{n}}{\Delta_{t}}\qquad\qquad 2.41$$
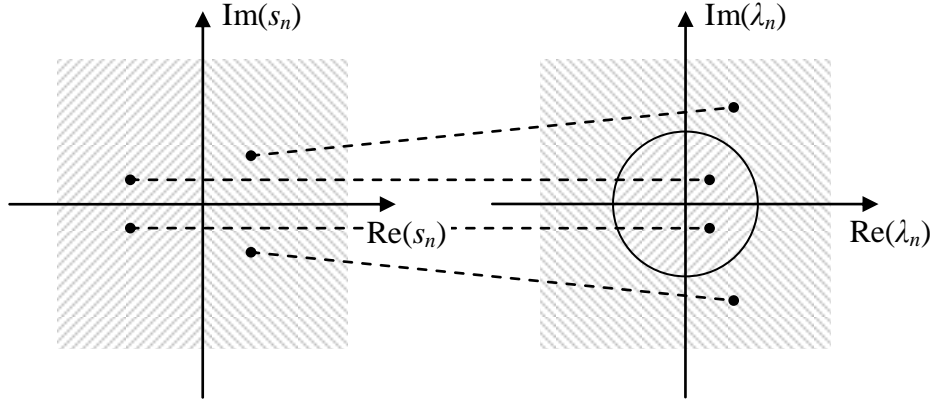
Figure 2.5: The equivalent poles of continuous and discrete time models

Rynne and Smith write "*The inaccuracies induced by the numerical discretisation of the integral equation causes some SEM poles, which theoretically should lie on the imaginary axis, to move into the right half plane. Their corresponding solutions are then excited by the incident sound, at a low level initially, and then proceed to grow exponentially due to the positive real part of the pole.*" Additionally they note that open but lightly damped structures such as parallel plates may have poles close to the imaginary axis. Again numerical inaccuracies may cause them to move into the right half plane and become unstable.

Smith [40] goes on to argue that any body with many resonances is likely to have a troublesome pole near -1, as resonances near the Nyquist frequency are most poorly represented. Reducing the time-step extends the frequency range of possible resonances, and they will have coarse spatial representation so are more likely to stray unstable. She also states that if a body has a multiple pole, the corresponding solution will grow like $\mathrm{p}(j)\lambda^{j}$, where $\mathrm{p}(\ldots)$ is a polynomial of order equal to the multiplicity of λ, hence if $|\lambda| = 1$ this will still grow like a polynomial in j.

Any numerical analysis of stability requires a measure of stability such that algorithms may be ranked and the effectiveness of modifications evaluated. Dodson, Walker and Bluck [35] wrote: "*There are two coupled aspects to instability; the time till the field begins its oscillatory exponential increases, and the rate of this increase*." From this they propose a measure of stability being the reciprocal of the time required for the surface sound to reach again the intensity of the incident sound. But this measure is dependent on the spectral content of the excitation signal which is undesirable. Based on the preceding discussion, a possible measure independent of the excitation spectrum would be the rate of the exponential increase, as this tends to the magnitude of the largest pole.

SEM poles may be found numerically using the state-transition matrix method used by Smith [40] in 1990 and Dodson, Walker and Bluck [35] in 1998. The definition begins with the MOT equation without excitation (homogeneous), as it has been established that instabilities are excitation independent:

$$\mathbf{Z}_0 \mathbf{\Phi}_j = -\sum_{l=1}^{l_{max}} \mathbf{Z}_l \mathbf{\Phi}_{j-l} \qquad\qquad 2.42$$

The state includes the current surface sound and sound that is en route between parts of the surface. In a BEM model this travelling sound is computed as retarded potential, radiated by a surface element at some point in history, so the state vector must include the surface sound for all time that is still contributing to the current observed sound. This is represented by a vector $\mathbf{h}_{j-1}$ created by stacking all the surface sound vectors that contribute to the right-hand side of the MOT equation. The retardation limit, l_{max}, is easily found as the largest l for which $\mathbf{Z}_l$ is non-zero. Equation 2.44 represents a MOT iteration through multiplication of $\mathbf{h}_j$ by the state-transition matrix $\mathbf{M}$. Both $\mathbf{h}_{j-1}$ and $\mathbf{M}$ are defined in Equation 2.43 where $\mathbf{M}_l = -\mathbf{Z}_0^{-1}\mathbf{Z}_l$. For a typical mesh $\mathbf{M}$ is very large and sparse with $(N_s l_{max})^2$ elements and $N_s^2 l_{max} + N_s (l_{max} - 1)$ non-zeros.

$$\mathbf{h}_{j-1} = \begin{bmatrix} \boldsymbol{\Phi}_{j-1} \\ \boldsymbol{\Phi}_{j-2} \\ \vdots \\ \boldsymbol{\Phi}_{j-l_{\max}} \end{bmatrix} \quad \mathbf{M} = \begin{bmatrix} \mathbf{M}_1 & \mathbf{M}_2 & \cdots & \mathbf{M}_{l_{\max}-1} & \mathbf{M}_{l_{\max}} \\ \mathbf{I} & & & & \\ & \mathbf{I} & & & \\ & & \ddots & & \\ & & & \mathbf{I} & \end{bmatrix} \qquad 2.43$$

$$\mathbf{h}_j = \mathbf{M}\mathbf{h}_{j-1} \qquad\qquad 2.44$$

The significance of $\mathbf{M}$ is that the SEM poles discussed above are found by its eigenvalue decomposition; each eigenvector eigenvalue pair describes a state that is unchanged by a MOT iteration except for a multiplication by a scalar. These eigenvalues (and eigenvectors if desired) are easily computed using a sparse matrix eigenvalue decomposition algorithm. This can be verified by reconstructing a system state from an eigenvector, then iterating it through the MOT algorithm and confirming that future states are indeed the initial state multiplied by powers of the eigenvalue. Unfortunately, due to the size of $\mathbf{M}$, meshes with a large number of elements or long interaction history quickly reach memory limits, so only small meshes (e.g. <300 elements for the MATLAB function eigs.m) may be subjected to this technique.

Manara, Monorchio and Regginannini [21] proposed a different model in 1997. The MOT algorithm is a multi-variable Infinite Impulse Response (IIR) filter calculating surface sound from excitation sound, so its inverse is a Finite Impulse Response (FIR) transfer function from surface to excitation sound. The zeros of the latter are found by standard filter design techniques and correspond to the poles of the former, and the largest in magnitude of these characterises stability. However, they concluded that this approach was prohibitively costly and instead focused their efforts on creation of an algorithm-specific heuristic stability condition based on time-step and geometric properties.

Once the mechanism causing the instabilities was understood, methods were created to suppress them. In his 1986 paper Rynne [38] proposed two different methods. The first was a system of spatial smoothing where the effect of the unstable mode $\boldsymbol{\Phi}^e$ was

subtracted at each time-step, as described in Equation 2.45. $\mathbf{\Phi}^e$ was not found by eigenvector decomposition of the state-transition matrix, but by running the MOT algorithm normally, isolating any stability that became dominant, and then re-running with the spatial smoothing applied. To automate this process Rynne also proposed a method of detecting instability given in Equation 2.46. This coefficient remains close to one for a stable solution, but is consistently close to minus one once an unstable solution is dominant. Spatial smoothing was found to be very effective, with minimal effect on accuracy; however the method of finding $\mathbf{\Phi}^e$ is computationally expensive and prone to error if two poles of similar magnitude exist.

$$\mathbf{\Phi}_j = \mathbf{\Phi}_j - \left(\mathbf{\Phi}_j \cdot \mathbf{\Phi}^e\right)\mathbf{\Phi}^e \qquad 2.45$$

$$\gamma_j = \frac{\mathbf{\Phi}_j \cdot \mathbf{\Phi}_{j-1}}{\left|\mathbf{\Phi}_j\right|\left|\mathbf{\Phi}_{j-1}\right|} \qquad 2.46$$

Rynne's second proposition was a temporal smoothing scheme, which has the advantage of being instability independent so applicable immediately for any problem. At each iteration two MOT steps are calculated, then these and the previous surface sound vector are averaged according to Equation 2.47. This does not create the doubling in computational cost that it first appears, as much of the assembly of the right hand side of the MOT equation used to calculate $\mathbf{\Phi}_{j+1}$ may be stored and used again at the next iteration. However it does cause some loss of accuracy, proportional to the second derivative of the true solution multiplied by the time-step squared.

$$\mathbf{\Phi}_j = \tfrac{1}{4}\left(\mathbf{\Phi}_{j+1} + 2\mathbf{\Phi}_j + \mathbf{\Phi}_{j-1}\right) \qquad 2.47$$

In 1990 Rynne and Smith [39] further examined the temporal smoothing approach, showing that such schemes alter the stability condition to be that the magnitude of a polynomial in the pole must be less than one (Equation 2.48). Relative to Rynne's 1986 scheme (Equation 2.47) this replaces the unit circle region of stability with a circle radius two centred on minus one (Equation 2.49). Other similar and higher order schemes were also proposed and the stability regions identified. In the same year Smith

[40] also investigated the stability region created by application of Equation 2.47 once every k iterations. This was an efficient approach but created peculiar, non-physical 'saw-tooth' graphs in log pressure, as instabilities periodically grew and were suppressed.

$$\Phi_j = \left(\alpha \Phi_{j+1} + \beta \Phi_j + \gamma \Phi_{j-1}\right)$$
$$\Phi_j^e = \left(\alpha \lambda^2 + \beta \lambda + \gamma\right)\Phi_{j-1}^e \qquad\qquad 2.48$$
$$\Phi_j^e = p(\lambda)\Phi_{j-1}^e \qquad \Rightarrow \qquad \left|p(\lambda)\right| < 1$$

$$p(\lambda) = \tfrac{1}{4}\left(\lambda^2 + 2\lambda + 1\right)$$
$$= \tfrac{1}{4}\left(\lambda + 1\right)^2 \qquad\qquad 2.49$$
$$\left|p(\lambda)\right| < 1 \Rightarrow \left|\lambda + 1\right| < 2$$

In contrast to the preceding methods that modify the discretisation weights, Harris, Wang, Chakrabarti and Henwood [41] proposed in 2005 a stabilisation method based on modifying the state-transition matrix $\mathbf{M}$ such that the magnitudes of all eigenvalues are less than or equal to one. This approximation is considered reasonable as unstable eigenvalues are typically only 1% larger than one. $\mathbf{M}$ is decomposed according to $\mathbf{M} = \mathbf{PDP}^{-1}$, where $\mathbf{D}$ is a diagonal matrix containing the eigenvalues of $\mathbf{M}$. $\mathbf{D}$ is replaced by $\tilde{\mathbf{D}}$ (Equation 2.50), capping the magnitude of each eigenvalue to one, and a modified state transition matrix $\tilde{\mathbf{M}}$ is calculated by $\tilde{\mathbf{M}} = \mathbf{P}\tilde{\mathbf{D}}\mathbf{P}^{-1}$ to be used in place of $\mathbf{M}$. It is unclear whether the modified system of equations may be solved by the classical MOT algorithm, or if repeated multiplication of $\mathbf{h}_j$ by $\tilde{\mathbf{M}}$ must be used, but the end result would be the same. $\mathbf{P}$ may be rank deficient due to $\mathbf{M}$ possessing repeated eigenvalues, however in practice these are always zero so contribute nothing to the iterative process; the generalised inverse of $\mathbf{P}$ may be used as the rank deficient sections are multiplied by zero. Unfortunately this stabilisation technique is expensive to implement. This paper also showed evidence that more accurate integration can tame instabilities.

$$
\tilde{\mathbf{D}}_{i,j} = \begin{cases} \mathbf{D}_{i,j} & \mathbf{D}_{i,j} \leq 1 \\ \dfrac{\mathbf{D}_{i,j}}{\left|\mathbf{D}_{i,j}\right|} & \mathbf{D}_{i,j} > 1 \end{cases} \qquad\qquad 2.50
$$

Ha-Duong *et al's* [25, 32, 34] approach to stability analysis is that of mathematical analysis of the integral equations in question. No attempt is made here to précis his arguments; however his thoughts on the above temporal smoothing schemes are clear from the quotation in section 2.2.5. This comment is justifiable when targeted at temporal smoothing schemes as they do indeed suppress high-frequency components producing inaccuracy. He goes on to write that such techniques are "*insufficiently well grounded*" in mathematical analysis.

The association of the bulk of instabilities with cavity resonances suggests examination of the well established techniques of eliminating these in the frequency domain BEM. One popular method is CHIEF [5,] where silent observation points are chosen inside the scatterer and used to form an over-determined system of equations. This method has the weakness that if all points happen to be chosen on nodes of the resonance, then the matrix will still be ill-conditioned and the solution non-unique. It is also unsuitable for time domain application due to the finite-velocity of propagation between surface and observer.

The alternative method is that of Burton and Miller [6]. They show that the complementary cavity problems of the standard BIE and its surface normal derivative never both have resonances at the same frequency. Consequentially a matrix equation created from a weighted sum of the two will never be ill-conditioned and always possess a unique solution. In 1999 Ergin, Shanker and Michielssen [22] published such an algorithm for the time domain and demonstrated its effectiveness. Additionally they, plus Aygün [42], published a similar algorithm in 2000 for electromagnetics applications. This was a linear combination of the Magnetic Field Integral Equation (MFIE) and EFIE, referred to as the Combined Field Integral Equation (CFIE), a name they transferred to its acoustic equivalent. This was not the first time the CFIE had been

investigated in a time domain context. In 1992 Vechinski and Rao[32] compared the MFIE, EFIE and CFIE in the application of modelling scattering from a dielectric cylinder and experienced some, but not significant, improvement in accuracy by using the CFIE. Ergin *et al* attribute the inconclusiveness of Vechinski and Rao's results to general numerical inaccuracies masking the improved stability granted by the CFIE. In particular, low accuracy spatial integration and finite-difference temporal differentiation were used and sound retardation over an element was assumed constant.

In 2006 Harris, Chappell, Henwood and Chakrabarti[43] published work using the CFIE to model sound radiated from vibrating surfaces. Their algorithm was based on Ergin *et al's*, with the additional inclusion of terms for non-zero surface-velocity and an integration method for axisymmetric surfaces based on a Taylor Series expansion of the integrands.

A final perspective on cavity resonances is Groenenboom's[4] 1983 line of sight argument. Based on the derivation of the BIE from the application of Greens theorem to the domain Ω_+ that supports acoustic wave propagation, he argues that influence between points that do not have 'line of sight' should be excluded, the intention being to restore the restriction that sound may only propagate through Ω_+. He does not give implementation details, but it seems this must eliminate any interaction that propagates through Ω_-, including all cavity resonances. There remain implementation questions such as whether the same shadows are applied to the incident sound (does $\varphi^i(\mathbf{r}) = 0$ if $\mathbf{r} \in \Omega_-$?) and how a convex surface can support tangential waves when the interaction from element to collocation point must pass through Ω_-; perhaps the solution to this later point is use of a Galerkin testing scheme. However, it seems this approach possesses a unique advantage of simultaneously removing cavity resonances and reducing the cost of the MOT routine (possibly at increased, though parallelisable, integration cost) through reduction in the number of non-zero interaction coefficients. For example, a convex scatterer would normally be expected to possess $O(N_s^2)$ interactions, but with Groenenboom's argument this would be reduced to neighbouring elements only being $O(N_s)$ interactions, a vast computational saving.

2.2.7 MOT Alternatives and Acceleration

As the size of the problem and the number of elements increases, the bottleneck in the algorithm becomes the MOT process. The integration stage may be fine-grain parallelised so can take as much or little time as the user chooses depending on the computational resources applied to it. By comparison the MOT algorithm is not easily parallelised as each element interacts with every other element at every iteration. Granted, elements in proximity of each other will interact more imminently than those further away but a scheme for subdividing the surface among processors is not straightforward.

This section describes methods proposed to accelerate or replace the MOT solver. The methods that retain the Marching on in Time iterative process will be described first, and those that function by solving for all time simultaneously described second.

In 1998 Walker and Vartiainen [44] proposed the use of the Kirchhoff boundary condition (surface velocity potential is double the incident) on parts of a surface that are large with respect to the largest wavelength present in the excitation signal. Regions of complex geometry continue to be solved using the KIE and the MOT algorithm, but the numerical cost is reduced as the sound at much of the surface is already known. Let x be the fraction of surface elements with complex geometry for which the KIE continues to be used. Interaction matrices storage cost is reduced to $O(xN_s^2)$, cost of assembling the right-hand side of the MOT equation is $O(xN_s^2 + N_s)$, and the naive implicit matrix solution used costs $O(x^3 N_s^3)$ though this could be reduced to $O(xN_s)$ by using an iterative solver, giving a total algorithm cost of $O(xN_s^2 N_t)$. This does not change the frequency scaling of the cost of the time domain BEM algorithm, unless x is considered to be a function of frequency. However, the real cost of any suitable problem is reduced. Walker and Vartiainen demonstrate the algorithms accuracy and efficiency on the problem of a rigid sphere close to a flat rigid plate.

Another approach to accelerating the MOT directly is to perform convolutions using the Fast Fourier Transform (FFT). Yilmaz, Jin and Michielssen's [45] 2001 MOT-FFT

algorithm computes spatial convolutions in this manner for electromagnetic scattering from a rectangular plate. Features of the geometry are exploited to increase efficiency; in particular the plate must be meshed regularly, although some elements in the mesh may be holes rather than plate if desired. As a result all element interactions for a given retardation are equal except for translation so form a two-dimensional spatial convolution; this is depicted in Figure 2.6. All quantities are stored in their Discrete Fourier Transformed (DFT) form, and an inverse DFT is only taken of them for the MOT equation to be summed and solved before a DFT is applied to the solution Noting that for a regular rectangular mesh $l_{max} \propto \sqrt{N_s}$ and that the cost of carrying out a DFT sequence of length n using an FFT algorithm is $n \log(n)$, the setup cost is $O(N_s^{1.5} \log(N_s))$, the storage cost is $O(N_s^{1.5})$ and the MOT cost is $O(N_s^{1.5} N_t)$. These cost trends are not as low as the Plane Wave Time Domain (PWTD) algorithm (introduced below) but this algorithm has a low complexity constant; the authors' implementation is faster than conventional MOT for 100 plus unknowns, and faster than PWTD for up to 100,000 unknowns, albeit for a limited application. This algorithm could be readily transferred to acoustics. In addition to a plate, the MOT-FFT method could be used to accelerate Shaw's [13] 1975 cylinder model by one-dimensional spatial convolution. No attempt appears to have been made to accelerate temporal convolution using the FFT, perhaps because temporal convolutions in three-dimensions are usually quite compact. However, two-dimensional models require non-compact temporal convolutions so the FFT may be an efficient approach.
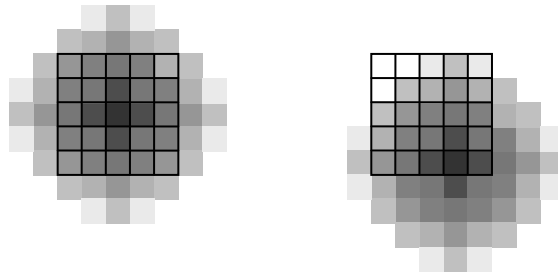
Figure 2.6: Interactions on a regular grid of elements form a spatial convolution

Ergin, Shanker and Michielssen published their two-level [46] and multi-level [47] Plane Wave Time Domain (PWTD) algorithms for acoustics in 1999 and 2000 respectively.

They write that they "*can be considered the time domain counterpart of the frequency domain fast multipole method*", some versions of which [48, 49, 50] are based on similar principles. The algorithms function by projecting the aggregate sound radiated by a portion of the scatterer (sub-scatterer) onto a number of time-dependent plane waves. These are readily propagated and the sound at an observer sub-scatterer is constructed from the plane waves arriving from all adequately distant sub-scatterers; MOT is used for adjacent sub-scatterers and self-interaction. The number of plane waves required and their permitted duration are functions of sub-scatterer size and separation respectively. The latter limit exists due to the presence of non-casual 'ghost' signals in the plane wave transform that must be removed by temporal gating.

In the two-level algorithm all sub-scatterers are similar size and periodically the plane wave transform is used to calculate retarded interaction between all non-adjacent sub-scatterer pairs. The implicit matrix equation is solved simultaneously over the whole surface using an iterative solver. Computational cost is improved from $O(N_t N_s^2)$ for MOT to $O(N_t N_s^{1.5} \log(N_s))$.

The multi-level algorithm uses the same plane wave transform but exploits the relationship between sub-scatterer separation and plane wave duration more fully. Sub-scatterers are grouped hierarchically according to location, so distant regions can be aggregated and interact on mass. These interactions between these larger, more distant sub-scatterers can occur less frequently but require a larger number of plane waves to achieve acceptable accuracy. In order to achieve this efficiently in a multi-level setting processes of 'interpolating' and 'splicing' are developed that construct the plane wave transform of a parent sub-scatterer from those of its children. The inverse operations of 'resection' and 'anterpolation' convert long duration plane waves arriving at a parent observer sub-scatterer into a shorter duration representation suitable for its children. Again MOT is used for close elements and iterative implicit matrix solution is applied at each time-step. Plane wave terms dominate memory usage at a cost of $O(N_t N_s)$. The computational cost is reduced to an attractive $O(N_t N_s \log^2(N_s))$ and the authors' implementation is more efficient than MOT for 1600 plus unknowns.

An entirely different approach to solving a time domain BEM matrix equation is to solve for all time simultaneously. This approach is given by in Equation 2.51; all surface sound and excitation vectors are stacked and the interaction matrix $\mathbf{Z}$ exhibits a clear pattern in terms of the MOT interaction matrices. In this context the MOT algorithm may simply be considered a matrix solver for any problem where $\mathbf{Z}$ is lower-block-triangular, but standard matrix solution techniques may also be used.

$$\mathbf{Z}\mathbf{\Phi} = \mathbf{e} \qquad \text{where:} \qquad\qquad 2.51$$

$$\mathbf{Z} = \begin{bmatrix} \mathbf{Z_0} & & & & & & \\ \mathbf{Z}_1 & \mathbf{Z_0} & & & & & \\ \cdot^{\cdot\cdot} & \mathbf{Z}_1 & \mathbf{Z_0} & & & & \\ \cdot^{\cdot\cdot} & \cdot^{\cdot\cdot} & \mathbf{Z}_1 & \ddots & & & \\ \mathbf{Z}_{l_{max}} & \cdot^{\cdot\cdot} & \ddots & \mathbf{Z}_1 & \mathbf{Z_0} & & \\ & \ddots & \cdot^{\cdot\cdot} & \cdot^{\cdot\cdot} & \mathbf{Z}_1 & \mathbf{Z_0} & \\ & & \mathbf{Z}_{l_{max}} & \cdot^{\cdot\cdot} & \cdot^{\cdot\cdot} & \mathbf{Z}_1 & \mathbf{Z_0} \end{bmatrix}$$

$$\mathbf{\Phi} = \begin{bmatrix} \mathbf{\Phi}_0 \\ \mathbf{\Phi}_1 \\ \vdots \\ \mathbf{\Phi}_{N_t} \end{bmatrix} \qquad\qquad \mathbf{e} = \begin{bmatrix} \mathbf{e}_0 \\ \mathbf{e}_1 \\ \vdots \\ \mathbf{e}_{N_t} \end{bmatrix}$$

Due to the size of $\mathbf{Z}$ ($N_t^2 N_s^2$ elements) a very efficient solution strategy is required. Herman and van den Berg's [36] 1982 algorithm was defined as a steepest-descent algorithm but in integral equation terms rather than matrix terms. Starting with the incident sound as an estimated solution, the square of the residual from the KIE integrated over the surface and time was iteratively minimised. They achieved similar computational cost to the MOT process, and better accuracy in terms of the residual criteria. Additionally Rynne [38] commented that such methods tend not to exhibit

instability; steepest-descent solvers typically disregard components of homogeneous solutions which do not affect the residual that they aim to minimise.

Although Equation 2.51 can be extremely memory inefficient, some restrictions imposed by the MOT equation are lifted. As the solution is performed simultaneously for all time, a time domain version of the CHIEF[5] algorithm could be used to tackle cavity resonances. The notion of time-steps is not required so temporal basis functions may be chosen to be something other than delayed copies of a mother basis function; for example a hierarchical scheme such as a wavelet family.

One approach to improving the computational efficiency of matrix solution is to choose basis functions that exhibit orthogonality under Galerkin testing such that the majority of coefficients in $\mathbf{Z}$ are zero and a compressed version of Equation 2.51 may be solved. This is attracting significant attention in the solution of the Laplace and Helmholtz equations such as Amini and Nixon's[26] 2006 two-dimensional algorithm that achieves $O(N_s \log(N_s))$ computational cost. Shifman and Leviatan's[51] 2001 publication uses this approach in the time domain Electromagnetics application for a one-dimensional dielectric slab. In their implementation interactions are evaluated for a standard basis function representation, but subsequently transformed to a Haar wavelet basis using a basis transformation matrix. A compressed matrix equation is solved, iteratively including dominant wavelets until an error criterion is satisfied. Optimisations include tailoring the wavelet library to include appropriate basis, such as periodic or semi-periodic functions to model quasi-periodic behaviour. This approach appears to have the potential to achieve excellent cost scaling and emphasises the equivalence of the frequency and time domain problems.

The final algorithm in this section exploits the orthogonality of Laguerre polynomials with respect to e^{-t} (Equation 2.52). This suggests Equation 2.53 for use as temporal basis and Gallerkin testing functions, where s is a scaling value, with the orthogonality property given in Equation 2.54. The Laguerre polynomials are defined recursively according to Equation 2.55. The definition of these temporal basis functions also has

the convenient property of not supporting un-physical exponentially growing oscillations.

$$\int_0^\infty e^{-t} L_u(t) L_v(t) dt = \delta_{uv} \qquad\qquad 2.52$$

$$T_u(t,s) = e^{-\frac{st}{2}} L_u(st) \qquad\qquad 2.53$$

$$\int_0^\infty T_u(t) T_v(t) dt = \delta_{uv} \qquad\qquad 2.54$$

$$L_u(t) = \begin{cases} 1 & u = 0 \\ 1-t & u = 1 \\ \dfrac{1}{u}\left[\begin{array}{c}(2u-1-t)L_{u-1}(t)\\ -(2u-1)L_{u-2}(t)\end{array}\right] & u \geq 2 \end{cases} \qquad\qquad 2.55$$

This approach was published for electromagnetic applications by Chung, Sarkar, Jung, Salazar-Palma, Ji, Jang and Kim[52] in 2004, and an updated algorithm with improved integration by Ji, Sarkar, Jung, Yuan and Salazar-Palma[53] in 2006. The algorithm solves for all time simultaneously, but due to the recursive definition of the temporal basis functions, takes on a Marching On in Order (MOO) representation. This process requires a matrix equation solution at each iteration, but the matrix in question is spatially dependent only so LU factorisation need be performed only once. This method has the benefit that the same temporal basis is used for all bandwidth excitation sound, suffice that the MOO process is truncated at an appropriate order.

2.2.8 Boundary Conditions

Most surfaces studied using time domain BEM are rigid but a few exceptions have been published. Shaw and English's[12] 1972 publication of an algorithm for a pressure release sphere contained a zero pressure boundary condition, but this is realised by

discretising normal velocity and remains a simple implementation. Groenenboom [19] used a radiation condition (Equation 2.56) to model pipes leaving a pressure vessel. The same boundary condition was used by Ha-Duong, Ludwig and Terrasse [25] in their 2003 model of absorbing boundary conditions using a real absorption coefficient a. A Robin boundary condition (Equation 2.57) is equivalent to a surface that offers inertial but no elastic resistance. This was modelled by Shaw [11] in his 1967 paper, with differing algorithms for heavy surfaces (discretised pressure) and light surfaces (discretised normal velocity) with respect to the weight of the fluid. Herman [54], and Herman and van den Berg [36] modelled scattering by inhomogeneous and homogeneous obstacles respectively.

$$\hat{\mathbf{n}} \cdot \nabla \varphi - \frac{a}{c} \frac{\partial \varphi}{\partial t} = 0 \qquad\qquad 2.56$$

$$\hat{\mathbf{n}} \cdot \nabla \varphi - K \varphi = 0 \qquad\qquad 2.57$$

Boundary conditions in the form of Equation 2.56 are used in the frequency domain to represent reflection from arbitrary surfaces except αc^{-1} is replaced by specific acoustic impedance, a frequency dependent complex quantity. Such a multiplication in the frequency domain is equivalent to a convolution in the time domain, as shown in Equation 2.58. Unfortunately a $\beta(t)$ found by inverse Fourier transform of measured and extrapolated frequency domain data is not necessarily casual. Publications addressing this issue include 1996 Tam and Auriault [55], 2000 Fung, Ju and Tallapragada [56], 2001 and 2004 Fung and Ju [57, 58]. Their discussion of obtaining time domain versions of frequency domain impedance data is not considered in this thesis, however their conclusion that reflectance is a more reliable quantity to use is exploited in chapter 5.

$$\hat{\mathbf{n}} \cdot \nabla \varphi - \beta(\omega)\frac{\partial \varphi}{\partial t} = 0 \quad \rightarrow \quad \hat{\mathbf{n}} \cdot \nabla \varphi - \beta(t) * \frac{\partial \varphi}{\partial t} = 0 \qquad\qquad 2.58$$

2.2.9 Conclusions

Many ideas and implementation approaches have been précised in this chapter, presenting a wealth of research questions to be answered. However, what is initially required by the research methodology is an algorithm that occupies the middle ground of the state-of-the-art and is accurately described so as to be readily replicated. The various sections of this literature review have identified that such an algorithm should use the classical MOT process but support implicit time stepping, use a basis function representation so that the discretisation scheme may be readily altered, and address stability, preferably by considering its origins rather than applying averaging.

Of the algorithms referenced the one that most closely fits these criteria is Ergin *et al*'s [22] 1999 publication. In addition to these properties, it is an ideal candidate for acceleration, proven as it is the basis for the group's PWTD algorithms, and suitable for application of a Galerkin testing scheme rather than collocation. In addition, there is a wealth of implementation detail present in the paper that allows the following section to describe the algorithm with authority. This algorithm will form the algorithmic foundation of this thesis, with concepts and implementation approaches being introduced from other publications as necessary.

2.3 "Analysis of transient wave scattering from rigid bodies using a Burton-Miller approach"

This section describes the algorithm published by the group at the University of Illinois [22] in 1999. The structure of the algorithm and its transparent nomenclature matches that used in this thesis, which in turn bears great similarity to the nomenclature of Pierce [3]. Because much of this has already been discussed in section 2.1 the key features of this algorithm and their significance will here be outlined individually. The algorithm also appears in Ergin's thesis [31], and there are slight discrepancies between the two that will be highlighted in what follows.

2.3.1 Basis functions

The scattering surface S is approximated by flat triangular surface elements. Velocity potential is assumed to have no spatial variation over each of these elements so may be approximated by a single time dependent scalar; the basis function used is by Equation 2.17.

This is a MOT style algorithm, so the temporal discretisation comprises regularly delayed copies of a mother basis function as Equation 2.19; the mother basis function used is a piecewise polynomial given in Equation 2.60 and shown in Figure 2.7 and has the important advantage that temporal derivatives may be found analytically. The piecewise polynomial chosen is stated to be an extension of that used by Manara *et al* [21] in electromagnetic applications. It is continuous but does not possess continuous derivatives. It is compact in time and its integral with respect to time is unity. It is asymmetrical, with a non-zero derivative at zero time, and supports less than Δ_t into negative time, hence is suitable for solution by the MOT algorithm.

The full discretisation scheme may be written as Equation 2.59. The weights $w_{j,n}$ have been renamed $\varphi_{j,n}$ in response to the fact that, because of the choice of the basis functions, each set of weights $\mathbf{\Phi}_j$ is equal to the instantaneous surface velocity potential at time $t_j = j\Delta_t$.

$$\varphi^t(\mathbf{r},t) = \sum_{n=1}^{N_s}\sum_{j=1}^{N_t} \varphi_{j,n}\, \mathrm{f}_n(\mathbf{r})\mathrm{T}_j(t) \qquad\qquad 2.59$$

$$\mathrm{T}_{mother}(\varsigma) = \begin{cases} 1 + \dfrac{11}{6}\varsigma + \varsigma^2 + \dfrac{1}{6}\varsigma^3 & -1 \le \varsigma \le 0 \\[2mm] 1 + \dfrac{1}{2}\varsigma - \varsigma^2 - \dfrac{1}{2}\varsigma^3 & 0 \le \varsigma \le 1 \\[2mm] 1 - \dfrac{1}{2}\varsigma - \varsigma^2 + \dfrac{1}{2}\varsigma^3 & 1 \le \varsigma \le 2 \\[2mm] 1 - \dfrac{11}{6}\varsigma + \varsigma^2 - \dfrac{1}{6}\varsigma^3 & 2 \le \varsigma \le 3 \\[2mm] 0 & \text{otherwise} \end{cases} \qquad\qquad 2.60$$
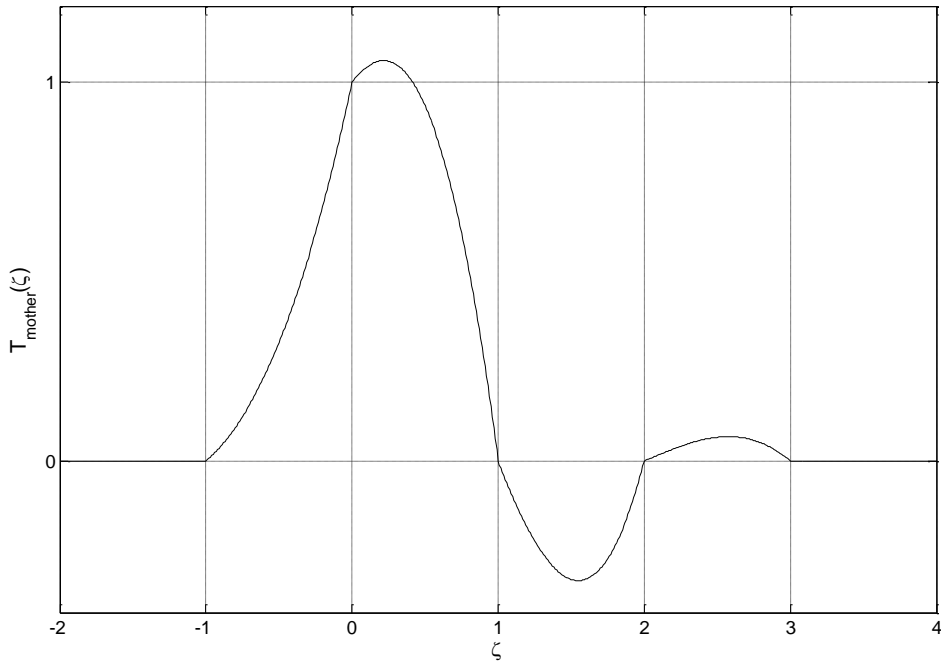
Figure 2.7: The mother temporal basis function

2.3.2 Integral operators

All the operators are derived from the KIE for a rigid surface, given in Equation 2.61; here the time domain Greens function has been written explicitly in the integral equation. The primed surface normal vector and gradient operator are evaluated at the integration point $\mathbf{r}'$.

$$\varphi^s(\mathbf{r},t) = \iint_S \varphi^t(\mathbf{r}',t) * \hat{\mathbf{n}}' \cdot \nabla' \frac{\delta\left(t - R/c\right)}{4\pi R} d\mathbf{r}' \qquad 2.61$$

The pressure operator is created by substituting Equation 2.61 into the boundary condition that no pressure field may exist inside the scatterer (Ω_-), hence incident and scattered fields must annihilate (Equation 2.62). Substituting in Equations 2.1 and 2.61 and taking the limit as $\mathbf{r}$ approaches S from the inside results in the familiar double layer potential jump property and definition of the pressure operator $L_p\{...\}$ (Equation 2.63).

54

$$p^i(\mathbf{r},t) = -p^s(\mathbf{r},t) \quad \text{if } \mathbf{r} \in \Omega_- \qquad\qquad 2.62$$

$$-\dot{\varphi}^i(\mathbf{r},t) = \mathrm{L}_p\{\varphi^t(\mathbf{r},t)\}$$
$$= -\frac{1}{2}\dot{\varphi}^t(\mathbf{r},t) + \iint\limits_{\forall S|\mathbf{r}\neq\mathbf{r}'} \dot{\varphi}^t(\mathbf{r}',t) * \hat{\mathbf{n}}'\cdot\nabla'\frac{\delta\left(t - R/c\right)}{4\pi R}d\mathbf{r}' \quad \text{if } \mathbf{r} \in S \qquad 2.63$$

The velocity operator $\mathrm{L}_v\{...\}$ is created by specifying that surface normal velocity through a rigid surface must be zero, so components of velocity must cancel at S (Equation 2.64). Note that this un-primed normal derivative is carried out at the collocation point $\mathbf{r}$. The integral is smooth everywhere except the singularity $\mathbf{r} = \mathbf{r}'$, so the normal derivative operation may be moved inside the integral everywhere apart from there. However, the integral is spherically symmetric so the gradient at the singularity must be zero. Hence the integral with the normal derivative moved inside is simply evaluated in the finite part sense with no other term (Equation 2.65).

$$\hat{\mathbf{n}}\cdot\mathbf{v}^i(\mathbf{r},t) = -\hat{\mathbf{n}}\cdot\mathbf{v}^s(\mathbf{r},t) \quad \text{if } \mathbf{r} \in S \qquad\qquad 2.64$$

$$\hat{\mathbf{n}}\cdot\nabla\varphi^i(\mathbf{r},t) = \mathrm{L}_v\{\varphi^t(\mathbf{r},t)\}$$
$$= -\iint\limits_{\forall S|\mathbf{r}\neq\mathbf{r}'} \varphi^t(\mathbf{r}',t) * \hat{\mathbf{n}}\cdot\nabla\hat{\mathbf{n}}'\cdot\nabla'\frac{\delta\left(t - R/c\right)}{4\pi R}d\mathbf{r}' \quad \text{if } \mathbf{r} \in S \qquad 2.65$$

The combined operator is defined as a linear sum of the pressure and velocity operators, where α is a parameter between 0 and 1 that defines the weighting of the two constituent operators; if $\alpha = 0$ then $\mathrm{L}_c = -\mathrm{L}_p$, if $\alpha = 1$ then $\mathrm{L}_c = c\mathrm{L}_v$. The wave speed c normalises the magnitude of the self-interaction terms. The complete acoustic CFIE is defined from the linear sum of the respective boundary conditions:

$$(1-\alpha)\dot{\varphi}^i(\mathbf{r},t)+\alpha c\hat{\mathbf{n}}\cdot\nabla\varphi^i(\mathbf{r},t)=\mathrm{L}_c\left\{\varphi^t(\mathbf{r},t)\right\}$$
$$=-(1-\alpha)\mathrm{L}_p\left\{\varphi^t(\mathbf{r},t)\right\}+\alpha c\,\mathrm{L}_v\left\{\varphi^t(\mathbf{r},t)\right\}$$

2.66

Ergin *et al* present numerical examples plus an argument based on conservation of energy to strengthen the case that this combined operator is fundamentally more stable than either of its constituent operators. This argument states that only the combined operator provides a means for energy trapped in the cavity to escape. Although in principle the initial conditions (silence) combined with the rigidity of S should prevent energy from being present in the cavity, numerical inaccuracies allow leakage and, without a means to escape, this accumulates into growing oscillations at resonant frequencies of the cavity. Hence the CFIE circumvents instabilities inherent in its constituent operators and any remaining instability is attributed to numerical inaccuracy, be its origin discretisation approximation or finite machine precision.

2.3.3 Implicitness

An implicit algorithm structure follows naturally from the summation of temporal basis functions being brought outside the integrals. In addition to this improvement in elegance Ergin *et al* propose an efficient approach to address the issue of solution of the current-interaction matrix. This exploits the fact that it is usually diagonally dominant and extremely sparse, making it an ideal candidate for iterative solution. Additionally, in their implementation the previous time-step's solution is used as a seed so convergence is rapid; the authors write "*a relative residual error of 10^{-6} was obtained in less than 15 iterations for all cases presented*".

2.3.4 Integration

Numerical integration is addressed differently in the paper and Ergin's thesis; the latter implements a spatial Galerkin scheme and the former spatial collocation, both use temporal collocation. However, due to the numerical integration methods chosen for the Galerkin testing the resulting implementations are extremely similar. It appears that the Galerkin scheme existed first and was replaced by collocation for journal publication. (Evidence for this sequence of events lies in a typographical error in the

appendix of the paper where an expression from the Galerkin scheme mistakenly appears.)

In the paper spatial testing is performed with delta functions to form a collocation scheme, where $\mathbf{r}_m^c$ is a collocation point:

$$\iint_S \delta\left(\left|\mathbf{r}-\mathbf{r}_m^c\right|\right)\left[(1-\alpha)\dot{\varphi}^i(\mathbf{r},t)_{t=t_j} + \alpha c\hat{\mathbf{n}}\cdot\nabla\varphi^i(\mathbf{r},t_j)\right]d\mathbf{r}$$
$$= \sum_{i=1}^{N_t}\sum_{n=1}^{N_s}\varphi_{i,n}\iint_S \delta\left(\left|\mathbf{r}-\mathbf{r}_m^c\right|\right)L_c\left\{f_n(\mathbf{r})T_i(t)\right\}_{t=t_j}d\mathbf{r}$$

2.67

In the thesis testing is performed with the spatial basis functions to form a Galerkin method:

$$\iint_S f_m(\mathbf{r})\left[(1-\alpha)\dot{\varphi}^i(\mathbf{r},t)_{t=t_j} + \alpha c\hat{\mathbf{n}}\cdot\nabla\varphi^i(\mathbf{r},t_j)\right]d\mathbf{r}$$
$$= \sum_{i=1}^{N_t}\sum_{n=1}^{N_s}\varphi_{i,n}\iint_S f_m(\mathbf{r})L_c\left\{f_n(\mathbf{r})T_i(t)\right\}_{t=t_j}d\mathbf{r}$$

2.68

Testing for all surface elements produces a matrix equation that is rearranged to form the familiar MOT equation (Equation 2.25). In the paper the excitation vector $\mathbf{e}_j$ is evaluated at the collocation points (Equation 2.69) but in the thesis it is integrated over the observer element S_m using a one point Gaussian rule (Equation 2.70). Consequentially the only difference between the schemes in implementation is a scaling by A_m, the area of element S_m.

$$\mathbf{e}_{j;m} = \iint_S \delta\left(\left|\mathbf{r}-\mathbf{r}_\mathbf{m}^\mathbf{c}\right|\right)\left[(1-\alpha)\dot{\varphi}^i(\mathbf{r},t)\right|_{t=t_j} + \alpha c\hat{\mathbf{n}}\cdot\nabla\varphi^i(\mathbf{r},t_j)\right]d\mathbf{r}$$
$$= (1-\alpha)\dot{\varphi}^i\left(\mathbf{r}_\mathbf{m}^\mathbf{c},t\right)\Big|_{t=t_j} + \alpha c\hat{\mathbf{n}}\cdot\nabla\varphi^i\left(\mathbf{r}_\mathbf{m}^\mathbf{c},t_j\right)$$

2.69

$$\mathbf{e}_{j;m} = \iint_S \mathrm{f}_m(\mathbf{r})\left[(1-\alpha)\dot{\varphi}^i(\mathbf{r},t)\big|_{t=t_j} + \alpha c\hat{\mathbf{n}}\cdot\nabla\varphi^i(\mathbf{r},t_j)\right]d\mathbf{r}$$

$$= A_m\left[(1-\alpha)\dot{\varphi}^i(\mathbf{r_m^c},t)\big|_{t=t_j} + \alpha c\hat{\mathbf{n}}\cdot\nabla\varphi^i(\mathbf{r_m^c},t_j)\right]$$

2.70

To calculate the elements of $\mathbf{Z}_l$ the testing schemes are carried through to the pressure and velocity operators as shown in Equations 2.71 and 2.72.

$$\mathbf{Z}_{l;m,n} = \iint_S \delta\big(\big|\mathbf{r}-\mathbf{r_m^c}\big|\big)L_c\big\{\mathrm{f}_n(\mathbf{r})\mathrm{T}_{j-l}(t)\big\}\big|_{t=t_j}d\mathbf{r}$$

$$= L_c\big\{\mathrm{f}_n(\mathbf{r})\mathrm{T}_{j-l}(t)\big\}\big|_{t=t_j;\mathbf{r}=\mathbf{r_m^c}}$$

2.71

$$= -(1-\alpha)L_p\big\{\mathrm{f}_n(\mathbf{r})\mathrm{T}_{j-l}(t)\big\}\big|_{t=t_j;\mathbf{r}=\mathbf{r_m^c}} + \alpha c L_v\big\{\mathrm{f}_n(\mathbf{r})\mathrm{T}_{j-l}(t)\big\}\big|_{t=t_j;\mathbf{r}=\mathbf{r_m^c}}$$

$$\mathbf{Z}_{l;m,n} = \iint_S \mathrm{f}_m(\mathbf{r})L_c\big\{\mathrm{f}_n(\mathbf{r})\mathrm{T}_{j-l}(t)\big\}\big|_{t=t_j}d\mathbf{r}$$

$$= \iint_S L_c\big\{\mathrm{f}_n(\mathbf{r})\mathrm{T}_{j-l}(t)\big\}\big|_{t=t_j}d\mathbf{r}$$

2.72

$$= -(1-\alpha)\iint_{S_m} L_p\big\{\mathrm{f}_n(\mathbf{r})\mathrm{T}_{j-l}(t)\big\}\big|_{t=t_j}d\mathbf{r} + \alpha c\iint_{S_m} L_v\big\{\mathrm{f}_n(\mathbf{r})\mathrm{T}_{j-l}(t)\big\}\big|_{t=t_j}d\mathbf{r}$$

$L_p\{..\}$ is first evaluated analytically converting all spatial differentiation into temporal differentiation of the temporal basis function. This is given below, except that Ergin *et al* omit the $(4\pi)^{-1}$ from the integrand; this is a typographical error. $\tau = t_j - Rc^{-1}$ is retarded time.

$$L_p\big\{\mathrm{f}_n(\mathbf{r})\mathrm{T}_{j-l}(t)\big\}\big|_{t=t_j} = \begin{cases} -\dfrac{1}{2}\dot{\mathrm{T}}_{j-l}(t)\big|_{t=t_j} & \mathrm{f}_n(\mathbf{r})=1 \\[2ex] \displaystyle\iint_{S_n} \dfrac{\hat{\mathbf{n}}'\cdot\widehat{\mathbf{R}}}{4\pi}\left[\dfrac{\ddot{\mathrm{T}}_{j-l}(\tau)}{cR} + \dfrac{\dot{\mathrm{T}}_{j-l}(\tau)}{R^2}\right]d\mathbf{r}' & \mathrm{f}_n(\mathbf{r})=0 \end{cases}$$

2.73

The same process is performed for $L_v\{...\}$:

$$L_v\left\{f_n(\mathbf{r})T_{j-l}(t)\right\}\Big|_{t=t_j} = -\iint_{Sn}\left[\begin{array}{c}\dfrac{\hat{\mathbf{n}}\cdot\hat{\mathbf{n}}'}{4\pi}\left[\dfrac{\dot{T}_{j-l}(\tau)}{cR^2}+\dfrac{T_{j-l}(\tau)}{R^3}\right]\\[2em]-\dfrac{\hat{\mathbf{n}}'\cdot\hat{\mathbf{R}}\hat{\mathbf{n}}\cdot\hat{\mathbf{R}}}{4\pi}\left[\dfrac{\ddot{T}_{j-l}(\tau)}{c^2R}+3\dfrac{\dot{T}_{j-l}(\tau)}{cR^2}+3\dfrac{T_{j-l}(\tau)}{R^3}\right]\end{array}\right]d\mathbf{r}' \qquad 2.74$$

In the self interaction case, this integral becomes hyper-singular so it is regularized by conversion to a polar integral. Equation 2.75 is correct for the paper, and Equation 2.76 for the thesis, where a one-point Gaussian rule is used to evaluate the testing integral. (typographical errors corrected):

$$L_v\left\{f_m(\mathbf{r})T_{j-l}(t)\right\}\Big|_{t=t_j;\mathbf{r}=\mathbf{r_m^c}} = \frac{1}{4\pi}\int_0^{2\pi}\frac{T_{j-l}\left(t_j - {R(\theta)}/{c}\right)}{R(\theta)}d\theta + \frac{1}{2c}\dot{T}_{j-l}(t)\Big|_{t=t_j} \qquad 2.75$$

$$\iint_{S_m}L_v\left\{f_m(\mathbf{r})T_{j-l}(t)\right\}d\mathbf{r}\Bigg|_{t=t_j} = A_m\left[\frac{1}{4\pi}\int_0^{2\pi}\frac{T_{j-l}\left(t_j - {R(\theta)}/{c}\right)}{R(\theta)}d\theta + \frac{1}{2c}\dot{T}_{j-l}(t)\Big|_{t=t_j}\right] \qquad 2.76$$

2.3.5 Choosing time-step duration

Ergin *et al* recommend that an appropriate value for Δ_t may be found by solely considering the frequency content of the excitation signal. They introduce a parameter β to represent temporal resolution and suggest Δ_t is chosen according to Equation 2.77, where for all the examples they present "$\beta = 10$ yielded reliable results". Rearrangement of this equation shows that β is inversely proportional to the CFL coefficient for a given problem (mesh and excitation). While numerical examples later in this thesis show that error does increase as β is reduced, results will also reveal that in practice the choice of Δ_t is very critical for stability of certain meshes.

$$\beta = \frac{2\pi}{\omega_{max}\Delta_t}$$

2.77

2.3.6 Verification

Ergin *et al* verified their algorithm against a Mie series scattering model on a sphere and against a frequency domain BEM model on a cube and an almond. The verification was run with differing values of α and the instabilities that occurred when $\alpha = 0$ or $\alpha = 1$ reinforced the effectiveness of the CFIE formulation.

2.3.7 Weaknesses

Ergin *et al's* algorithm only calculates surface velocity potential for rigid polyhedral surfaces devoid of thin appendages. It does not calculate the scattered sound in Ω_+ but this is trivial to implement. More significantly, it will be seen in chapter 3 that the numerical integration techniques employed are incompatible with the temporal basis function used, although this has surprisingly little effect on the solution. Chapter 4 demonstrates a simple way to extend the algorithm to model surfaces with thin appendages. Chapter 5 extends the algorithm to model absorbing and welled surfaces.

2.4 Conclusions

The time domain Boundary Element Method has been presented. Its likenesses to its frequency domain counterpart have been highlighted and the computational costs have compared. The current state-of-the-art has been listed, précised where appropriate, and the foundations of this thesis laid. An algorithm has been selected for replication and its implementation described.

In the next chapter the effect of integration accuracy on solution accuracy and system stability will be investigated. A numerical integration scheme based on conversion of the surface integral to a contour integral is proposed and shown to be superior to the implementation used by Ergin *et al*.

3 Integration accuracy and real-world surfaces

Typically, the problems used for verification of time domain BEMs are extremely simple. In contrast most surfaces of interest in Acoustics, such as diffusers, are extremely complex. This has a two-fold effect; first the sound field at the surface may be expected to exhibit more rapid spatial variation than for a simple surface, resulting in greater discretisation error. Secondly, quirks of the geometry may cause the integrals to become more singular, hence more difficult to evaluate accurately.

As the MOT solver is an iterative process any errors in the interaction coefficients can affect not only accuracy but also stability. Ergin *et al* [22] claim their combined operator is inherently stable, unlike the pressure and velocity operators alone, so any additional instability must result from discretisation and integration errors. Within the current discretisation scheme, error can only be reduced by increasing the number of elements and reducing the time-step, both of which significantly increase numerical cost. It therefore seems logical to investigate the numerical integration algorithm, to discover if accuracy can be improved without a major increase in computing overhead. In 2005 Harris, Wang, Chakrabarti and Henwood [41] applied Ergin *et al's* algorithm to radiation problems, and published evidence in support of this stance.

As was concluded in chapter 2, the Combiner Field Integral Equation (CFIE) will be implemented due to its absence of cavity resonances; accordingly this chapter must study numerical integration performance on both the pressure and velocity operators that comprise the CFIE. The discretisation scheme is chosen to match that of Ergin *et al*; some ramifications of temporal basis function choice will be discussed in chapter 6. The MOT solver will be used as, although inefficient, it forms the basis of acceleration schemes such as PWTD and it is anticipated that meshes need not be large for the effect of integration accuracy to be assessed.

In this chapter two candidate integration schemes will be contrasted: Gaussian and contour. The former will be examined in section 3.1, where the scheme used by Ergin *et al* is adopted as a typifying example. The integrands of this scheme will be seen to be

discontinuous, due to the choice of the temporal basis function, and accuracy poor where a discontinuity intersects the integration element of an interacting pair. Monte Carlo integration [59] is used as a verification tool to assess numerical accuracy.

In section 3.2 the contour integration scheme is derived, based on the same integral transformation used by Kawai & Terai [18] (1990). This is compared with the Gaussian integrands, again by Monte Carlo integration, and seen to disagree when a discontinuity intersects the integration element. Modifications are made to the contour scheme to compensate and the resulting implementation achieves excellent agreement with the Gaussian integrands. The origin of these changes is explored and it is found to be the Gaussian scheme that is deficient; the un-modified contour integration scheme is embraced as correct.

Section 3.3 provides numerical examples, contrasting performance of the three integration implementations on a simple idealised surface (a sphere) and a complex diffusing surface typical to Room Acoustics. Significant integration error is observed for both meshes, but the MOT results are largely unaffected; accordingly a mechanism is identified by which integration errors arsing from the temporal basis function largely cancelled out. However, on the diffuser mesh the MOT solver is unstable with Gaussian integration, while the contour integration schemes both result in stable solutions. It is concluded that spatial singularity terms are responsible for the latter result.

3.1 Gaussian Integration
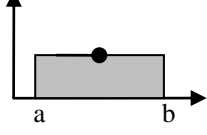
Ergin *et al's* integrands were briefly introduced in section 2.3.4. This section examines the behaviour of those integrands, describes the numerical integration strategy used and reviews their appropriateness. Symmetric Gaussian integration rules for triangular domains will be introduced, some suitable for polynomial integrands of a very high order. The convergence of Monte Carlo integration on the real integrands will be examined to show the significant factors which affect accuracy.

3.1.1 Gauss-Legendre Rules

Gaussian integration is a fixed precision numerical integration scheme which operates by evaluating the integrand at a set of abscissa (locations), multiplying those results by a corresponding set of weighting coefficients, and summing to obtain an approximation to the integral. The corresponding sets of abscissa and weights are referred to as a rule, and may be optimised for different types of integrand. In this chapter all Gaussian rules fall into the subcategory of Gauss-Legendre rules, and are optimised to give zero error for polynomials of up to a given order, referred to as the order of the rule. This is easiest to visualise for a one-dimensional integral; the approximation equation and a few simple examples are shown below where $f(\ldots)$ is the integrand to be approximated, and w_i and x_i are the weights and abscissa respectively which are scaled according to the integration domain $[a, b]$:

$$\int_a^b f(x)dx \approx \sum_{x_i \in abscissa} w_i\, f(x_i) \qquad\qquad 3.1$$

Table 3.1: Examples of low order Gauss-Legendre rules.

Order	Polynomial		Abscissa	Weights
0	$f(x) = a_0$		anywhere	$b - a$
1	$f(x) = a_0 + a_1 x$		$\dfrac{a+b}{2}$	$b - a$
2	$f(x) = a_0 + a_1 x + a_2 x^2$		$\dfrac{a+b}{2} \pm \dfrac{b-a}{2\sqrt{3}}$	$\dfrac{b-a}{2}$

Gaussian rules for double integrals (surfaces) are more difficult to optimise for a given polynomial order than those for single integrals (lines). They still have the same form as the one-dimensional integral approximation with only a single summation despite the double integral:

$$\iint\limits_{S_n} f(\mathbf{r'})d\mathbf{r'} \approx \sum_{\mathbf{r}_j \in abscissa} w_i\, f(\mathbf{r}_j) \qquad 3.2$$

Rules for quadrangle integration domains are often created from two nested single integral rules and may be condensed into the above single summation form. These rules are usually termed "Gaussian Product Rules", and the number of abscissa possessed is the product of the numbers in the constituent rules:

$$\iint\limits_{S_n} f(\mathbf{r'})d\mathbf{r'} = \iint\limits_{S_n} f(x, y)dxdy$$
$$\approx \sum_{x_i \in abscissa}\; \sum_{y_j \in abscissa} w_i w_j\, f(x_i, y_j) \qquad 3.3$$
$$= \sum_{\mathbf{r}_k \in abscissa} w_k\, f(\mathbf{r}_k)$$

This chapter will deal solely with triangular elements in accordance with the example Gaussian implementation chosen, so it is triangular integration domains that are of interest. Gaussian product rules may be used for triangular domains, but many abscissa become clustered in one corner, an inefficient distribution. Symmetric rules are evenly spaced so more efficient in their use of abscissa. The seven-point symmetric 6th order rule [60] used by the Gaussian implementation is given in Table 3.2 and the location of the abscissa is depicted in Figure 3.1; this will be referred to as 'Rule7'. Wandzura and Xiao [61] have published very high order rules found by numerical optimization. Many of these can be downloaded as Matlab m-files from a useful online resource created by John Burkardt [62].

Table 3.2: Rule7 abscissa and weights

Abscissa	Weights
$(0,0)$	$\frac{270}{1200}$
$\left(\frac{\sqrt{15}+1}{7},0\right),\quad\left(-\frac{\sqrt{15}+1}{14},\pm\sqrt{3}\,\frac{\sqrt{15}+1}{14}\right)$	$\frac{155-\sqrt{15}}{1200}$
$\left(-\frac{\sqrt{15}-1}{7},0\right),\quad\left(\frac{\sqrt{15}-1}{14},\pm\sqrt{3}\,\frac{\sqrt{15}-1}{14}\right)$	$\frac{155+\sqrt{15}}{1200}$
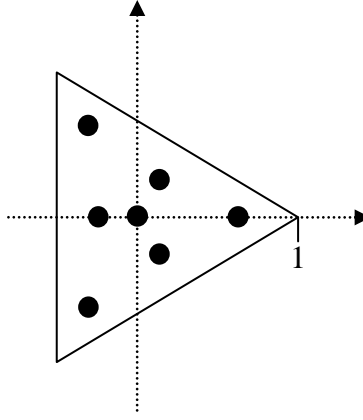
Figure 3.1: Locations of the abscissa of Rule7

To grasp the meaning of the "order" of a Gaussian integration rule it will be applied to an analytically integrable integrand and the error examined. This shall be the product of powers of two orthogonal variables, intended to represent any term arising from the product of two one-dimensional polynomials. The integration domain shall be the triangle bounded by the lines $y = 0$, $y = x$ and $x = 1$. The analytical result and the vectorised integrand are given in Equations 3.4 and 3.5 respectively. Figure 3.2 shows isograms of relative error (the magnitude of the error divided by the magnitude of the correct result) as a percentage for varying powers m and n as evaluated with Rule7.

$$\int_0^1 \int_0^x x^m y^n \, dydx = \left[(n+1)(m+n+2)\right]^{-1} \qquad\qquad 3.4$$

$$f(\mathbf{r'}) = (\mathbf{r'} \cdot \hat{\mathbf{x}})^m (\mathbf{r'} \cdot \hat{\mathbf{y}})^n \qquad\qquad 3.5$$
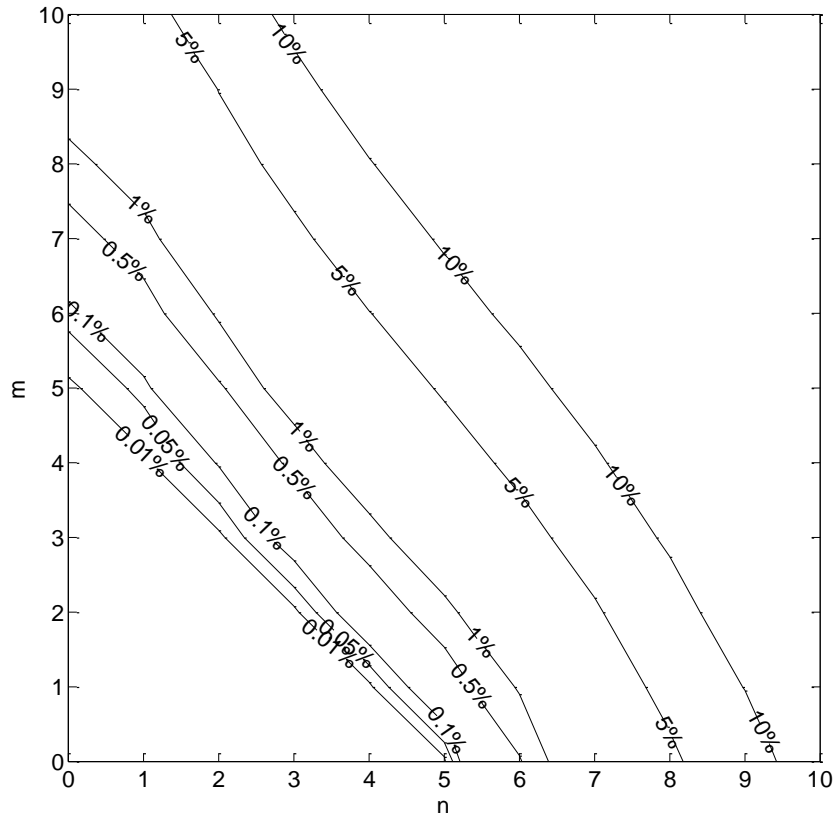
Figure 3.2: Error in integrating the product of two polynomial terms using Rule7

It is concluded from Figure 3.2 that small relative errors are a function of $m+n$, the combined order of orthogonal polynomials, meaning the orientation of the polynomial is irrelevant. This assumption allows n to be set to zero and m varied; Equations 3.4 and 3.5 are replaced by 3.6 and 3.7 respectively.

$$\int\limits_{0}^{1}\int\limits_{0}^{x} x^{m} dy dx = (m+2)^{-1} \qquad\qquad 3.6$$

$$f(\mathbf{r'}) = (\mathbf{r'} \cdot \hat{\mathbf{x}})^{m} \qquad\qquad 3.7$$
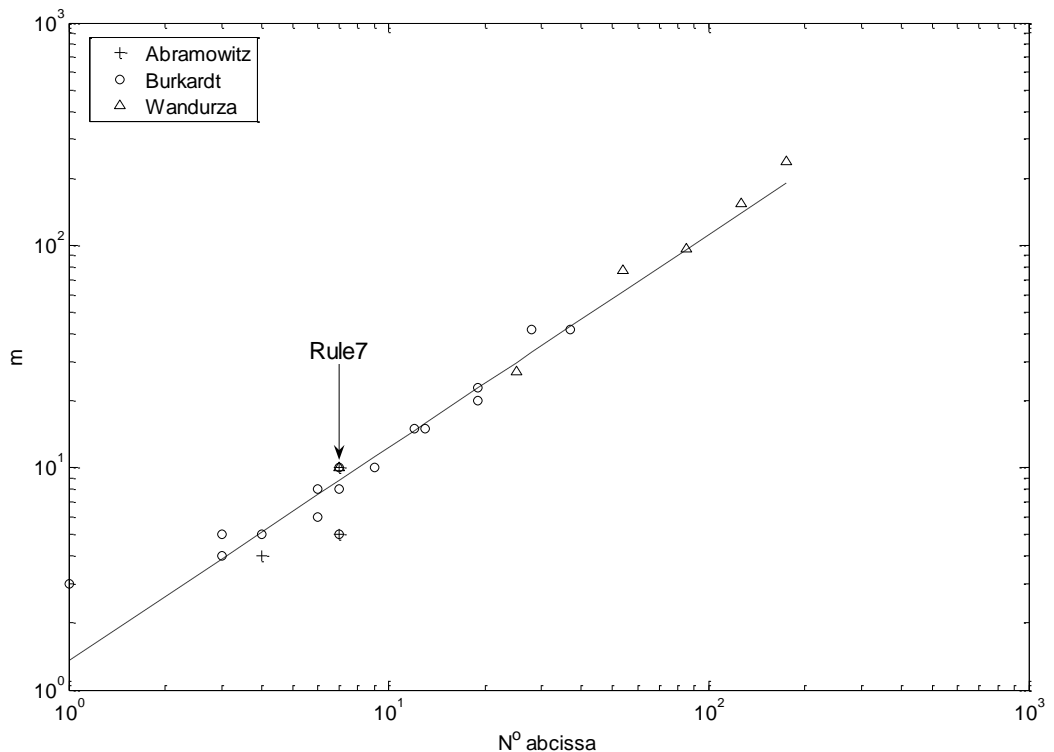
Figure 3.3: Performance of symmetric Gaussian integration rules: Lowest polynomial order giving greater than 1% error versus number of abscissa

Figure 3.3 shows the lowest polynomial order giving greater than 1% error versus the number of abscissa (the cost of the rule) for a variety of symmetric rules. The trend is that the number of abscissa is roughly equal to the order of polynomial that creates 1% error. Rule7 is indicated and can be seen to perform slightly better than the trend; from this result and its cited order it is expected to give less than 1% error and zero error when integrating polynomials of order nine and six respectively.

The Gaussian integration implementation tested replicates that in the 1999 paper of Ergin *et al*. Rule7 is utilised for elements pairs that are non-adjacent (do not share a

vertex). Where elements share vertices the integral is expected to be more singular and the integration element is first subdivided into four sub-triangles then Rule7 applied to each. Self-interaction in the case of the pressure operator $L_p\{...\}$ is a special case that only involves the collocation point so no numerical integration is necessary. The self-interaction integral occurring for the velocity operator $L_v\{...\}$ is converted to a contour integral, as was described in section 2.3.4, and one-dimensional numerical integration is applied to each contour.

3.1.2 Integrands

The temporal basis function is defined from a piecewise polynomial and was introduced in Equation 2.19, Equation 2.60 and Figure 2.7. Each piece of the polynomial is readily differentiated, the results are given in Equations 3.8, 3.9, 3.10 and 3.11, but Figure 3.4 and Figure 3.5 show that there is ambiguity, as there are two possible values for the differential at each integer time-step.

The choice of differential at integer time-steps is critical as $\dot{T}_{j-l}(t_j)$ appears in the element self-interaction term for all operators. Which piece is chosen (or perhaps the average of the two) has a major effect on the result of the MOT solver.

$$\dot{T}_i(t) = \frac{1}{\Delta_t} T'_{mother}\left(\frac{t}{\Delta_t} - i\right)$$

3.8

$$T'_{mother}(\varsigma) = \begin{cases} \dfrac{11}{6} + 2\varsigma + \dfrac{1}{2}\varsigma^2 & -1 \le \varsigma \le 0 \\[2mm] \dfrac{1}{2} - 2\varsigma - \dfrac{3}{2}\varsigma^2 & 0 \le \varsigma \le 1 \\[2mm] -\dfrac{1}{2} - 2\varsigma + \dfrac{3}{2}\varsigma^2 & 1 \le \varsigma \le 2 \\[2mm] -\dfrac{11}{6} + 2\varsigma - \dfrac{1}{2}\varsigma^2 & 2 \le \varsigma \le 3 \\[2mm] 0 & \text{elsewhere} \end{cases}$$

3.9
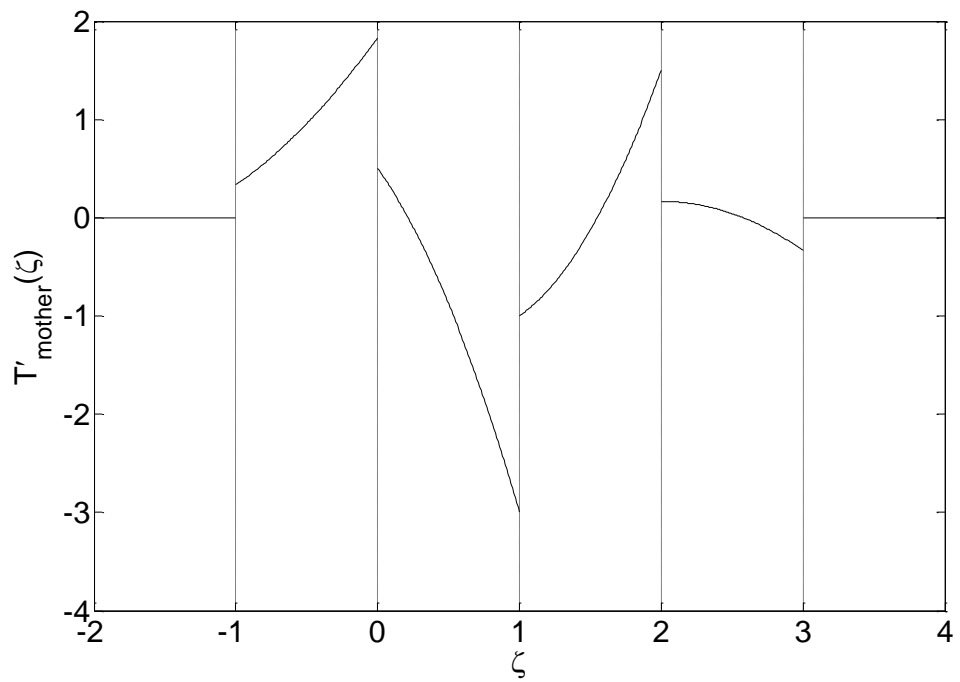
Figure 3.4: The first derivative of $\mathrm{T}_{mother}\left(\ldots\right)$
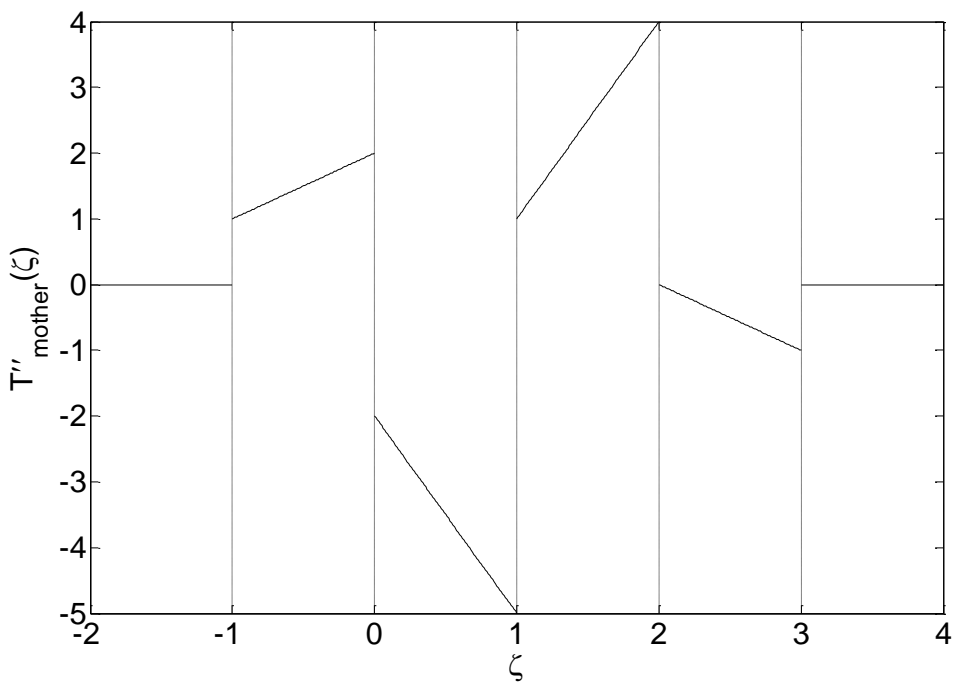
Figure 3.5: The second derivative of $\mathrm{T}_{mother}\left(\ldots\right)$

69

$$\ddot{\mathrm{T}}_i(t) = \frac{1}{\Delta_t^2} \mathrm{T}''_{mother}\left(\frac{t}{\Delta_t} - i\right) \tag{3.10}$$

$$\mathrm{T}''_{mother}(\varsigma) = \begin{cases} 2 + \varsigma & -1 \le \varsigma \le 0 \\ -2 - 3\varsigma & 0 \le \varsigma \le 1 \\ -2 + 3\varsigma & 1 \le \varsigma \le 2 \\ 2 - \varsigma & 2 \le \varsigma \le 3 \\ 0 & \text{elsewhere} \end{cases} \tag{3.11}$$

Section 3.2.1 shows that these terms appear in the self-interaction equations as lower limits in integrals in R, hence should be considered as upper limits in $\tau = t_j - Rc^{-1}$, so the lower piece with respect to τ should be chosen. This is easily achieved by changing the lower limits in the mother basis piece criteria from $\le$ to $<$; the revised first and second derivative definitions are given in Equations 3.12 and 3.13, and shown in Figure 3.6 and Figure 3.7 where the values at integer time-steps are marked with a dot.

$$\mathrm{T}'_{mother}(\varsigma) = \begin{cases} \dfrac{11}{6} + 2\varsigma + \dfrac{1}{2}\varsigma^2 & -1 < \varsigma \le 0 \\ \dfrac{1}{2} - 2\varsigma - \dfrac{3}{2}\varsigma^2 & 0 < \varsigma \le 1 \\ -\dfrac{1}{2} - 2\varsigma + \dfrac{3}{2}\varsigma^2 & 1 < \varsigma \le 2 \\ -\dfrac{11}{6} + 2\varsigma - \dfrac{1}{2}\varsigma^2 & 2 < \varsigma \le 3 \\ 0 & \text{elsewhere} \end{cases} \tag{3.12}$$

$$\mathrm{T}''_{mother}(\varsigma) = \begin{cases} 2 + \varsigma & -1 < \varsigma \le 0 \\ -2 - 3\varsigma & 0 < \varsigma \le 1 \\ -2 + 3\varsigma & 1 < \varsigma \le 2 \\ 2 - \varsigma & 2 < \varsigma \le 3 \\ 0 & \text{elsewhere} \end{cases} \tag{3.13}$$
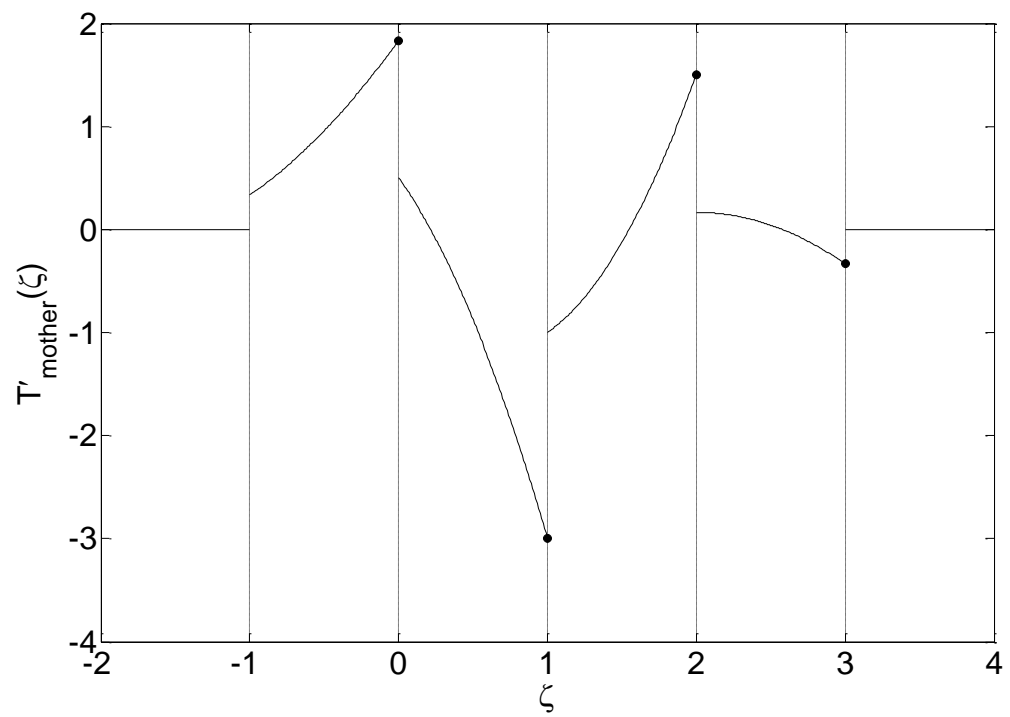
Figure 3.6: The clarified first derivative of $T_{mother}(...)$
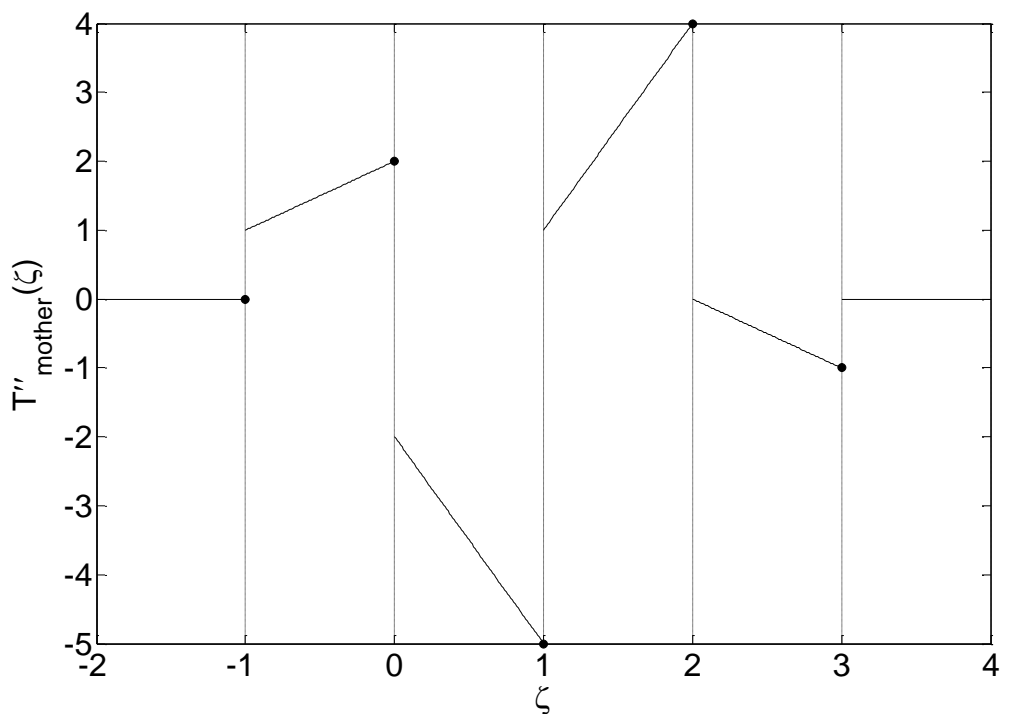
Figure 3.7: The clarified second derivative of $T_{mother}(...)$

71

Now the values of the derivatives at integer time-steps are clarified the self-interaction equations require no further attention as they are already implemented in an accurate and efficient manner. The rest of this section focuses on non-self-interactions.

Both the $L_p\{...\}$ and $L_v\{...\}$ integrands (Equations 2.73 and 2.74) contain the first and second derivatives of the temporal basis function. These operate on retarded time $\tau = t_j - R c^{-1}$ so their temporal discontinuities are converted into spatial discontinuities that lie on spherical shells at radii $lc\Delta_t$ centred on $\mathbf{r}$ as depicted in Figure 3.8, where retardation index l is a non-negative integer. Their intersection with the plane of S_n forms irregularly spaced circular arcs, whose radii may be calculated by Pythagoras' rule, centred on the projection of $\mathbf{r}$ into the plane, as depicted in Figure 3.9. The presence of these discontinuities due to the choice of temporal basis function will be seen to be fundamental to the performance of the integration strategy.

Figure 3.9: Discontinuities in the plane of S_n

Figure 3.8: Spherical discontinuity geometry

3.1.3 Monte Carlo Convergence to Gaussian Integration

Monte Carlo integration[59] is a "blind" numerical integration strategy, usually chosen as a last resort when nothing is known about the integrand. Unlike the Gaussian schemes above, which are optimised for a polynomial of a given order, Monte Carlo integration is not optimised for any integrand, yet will converge as the number of integration points is increased. The algorithm is very simple: pick a given number N abscissa randomly over the integration domain and then take the mean of the integrand value at these points; this amounts to using a uniform weighting of N^{-1}. Abscissa are chosen randomly to avoid the pitfall that if using uniformly spaced abscissa, periodic variations with a period equal to the grid spacing do not contribute to the scheme's result.

Monte Carlo integration has been chosen as a verification tool as, although inefficient, it is guaranteed to converge to the true integral with the general trend that error is inversely proportional to number of abscissa. If this trend is plotted on a log-log axis it appears as a straight downward sloping line. Figure 3.10 shows its convergence to the analytical solution of the integral given in Equation 3.6, used to evaluate order of Gaussian integration rules in section 3.1.1. The y-axis displays normalised disagreement, the magnitude of the difference between the Monte Carlo solution and the analytic solution divided by the magnitude of the analytic solution. This has been termed disagreement rather than error as in forthcoming sections both the Monte Carlo result and the comparison solution will have inherent error.

In Figure 3.11 a 1% error has been artificially introduced into the analytical solution by multiplying it by 1.01. The Monte Carlo scheme still converges to the correct solution, so the normalised disagreement converges to the error, indicated by the dashed horizontal line. This demonstrates how it will be used as a means of estimating the accuracy of a numerical integral.
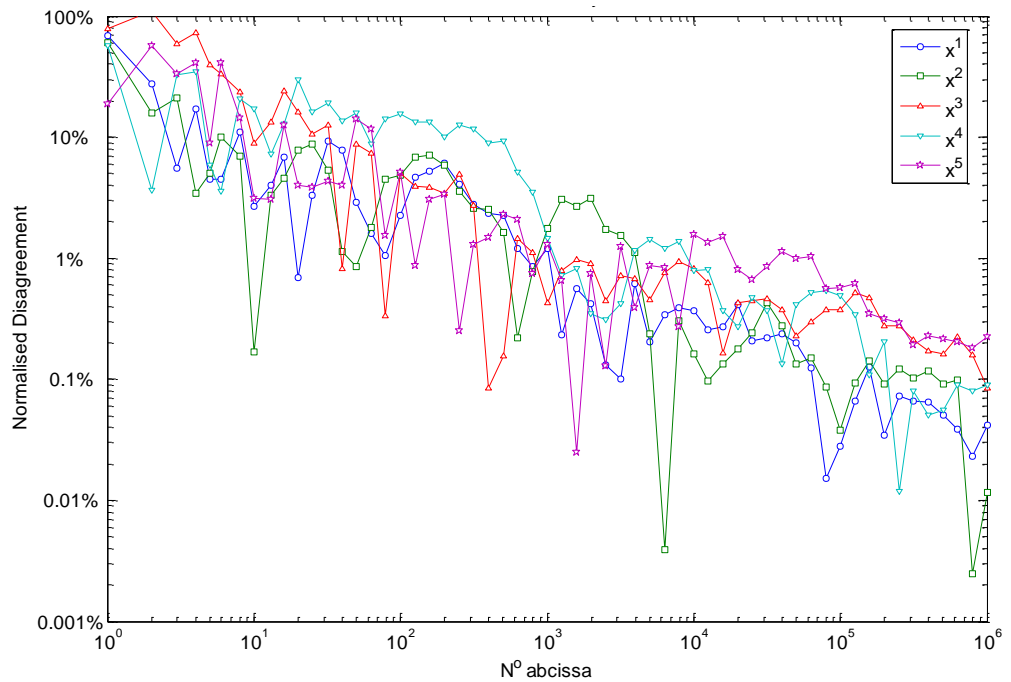
Figure 3.10: Monte Carlo convergence to the analytic result of Equation 3.6
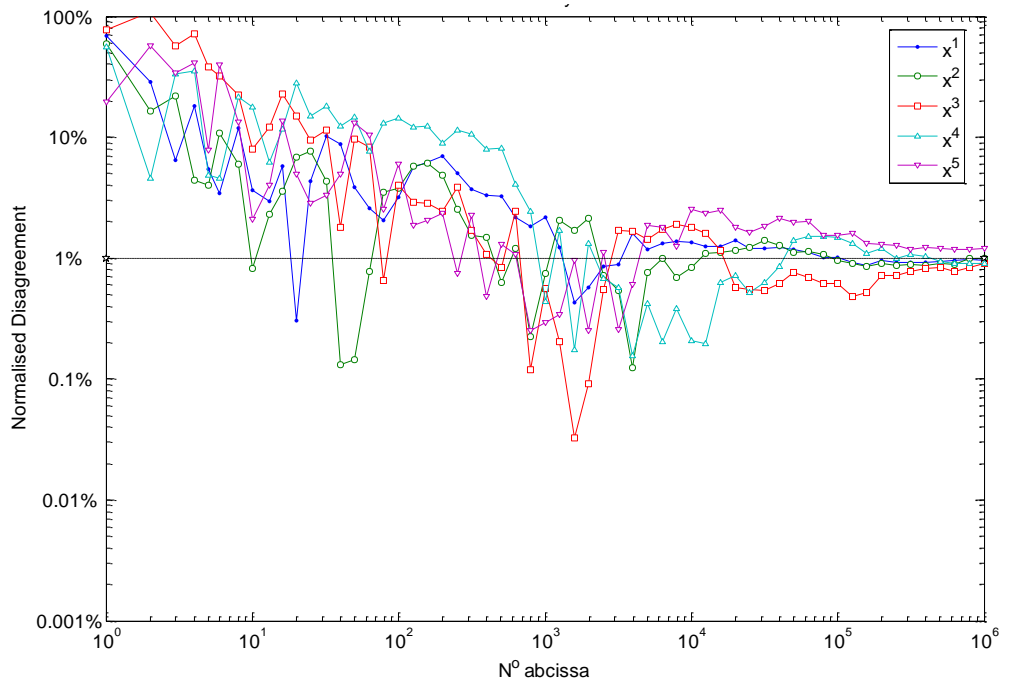
Figure 3.11: Monte Carlo disagreement convergence on Equation 3.6 when 1% error has been added to the analytical solution

The Monte Carlo implementation that produced the convergences shown here reuses abscissas; 10^6 abscissa were chosen and the integrand evaluated at each; results for smaller N are found from subsets of these evaluations. This is permissible since the abscissa were randomly chosen, plus it is more efficient and produces clearer convergence trends than picking a new set of abscissa for every N. 10^6 was roughly the maximum number of abscissa the hardware could handle without optimisations in integrand coding.

Ideally the above convergence test would be performed for every element pair in a mesh. However this would have a prohibitive duration, plus the convergence is not always very clear hence automatic detection is unreliable. Here instead the worst case scenario will be investigated, depicted below. Two elements have been created that share an edge (adjacent) and are inclined relative to one another such that all scalar product terms in the integrands are non-zero. The black cones represent their normal vectors and the black dots the vertices, which lie on the corners of a 0.1m cube; these are clearly uncharacteristically large elements, but since errors and time-step durations are normalised this is of no consequence. The lighter grey element is the integration element S_n.
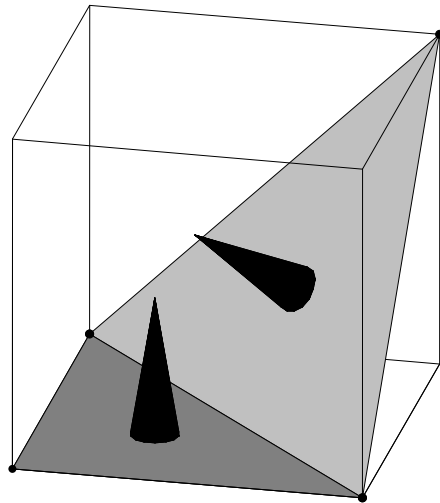
Figure 3.12: Element pair used for Monte Carlo convergence testing

The following figures show Monte Carlo disagreement with the Gaussian scheme's result (elements are adjacent so S_n is subdivided into four triangles and Rule7 applied to each) on both $L_p\{...\}$ and $L_v\{...\}$ integrands for all l (retardations) that yield non-zero interaction. In Figure 3.13 and Figure 3.14 the time-step has been chosen such that $c\Delta_t = 0.16m$ therefore no discontinuity intersects S_n. The disagreement with Monte Carlo integration either does not converge clearly so the error is very small, or converges to an error smaller than 1%. The only exception to this is the $l = 0$ line for the $L_v\{...\}$ integrand which converges to an error of approximately 2.5%. This error is due to the more complex spatial variation of $L_v\{...\}$; the $l = 0$ $L_p\{...\}$ and $L_v\{...\}$ integrands are shown in Figure 3.15 and Figure 3.16 for comparison. The $L_p\{...\}$ integrand shows better than 1% error for all retardations, but the $L_v\{...\}$ integrand evidently can be too singular to be integrated accurately on adjacent elements by the Gaussian scheme.
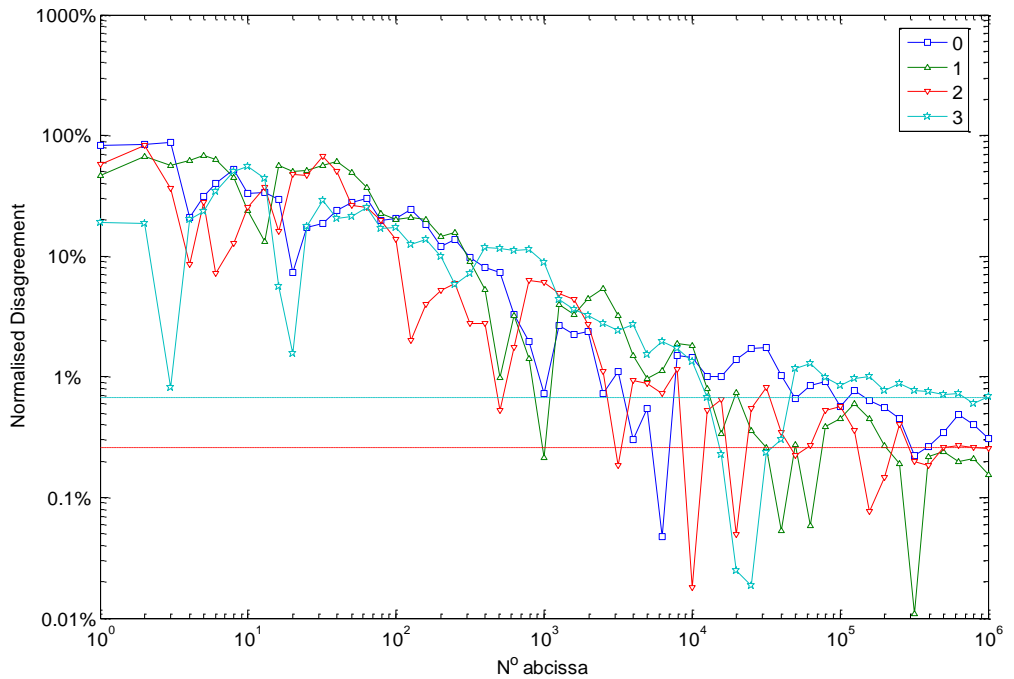
Figure 3.13: $L_p\{...\}$ Monte Carlo convergence to Gaussian result, $c\Delta_t = 0.16m$
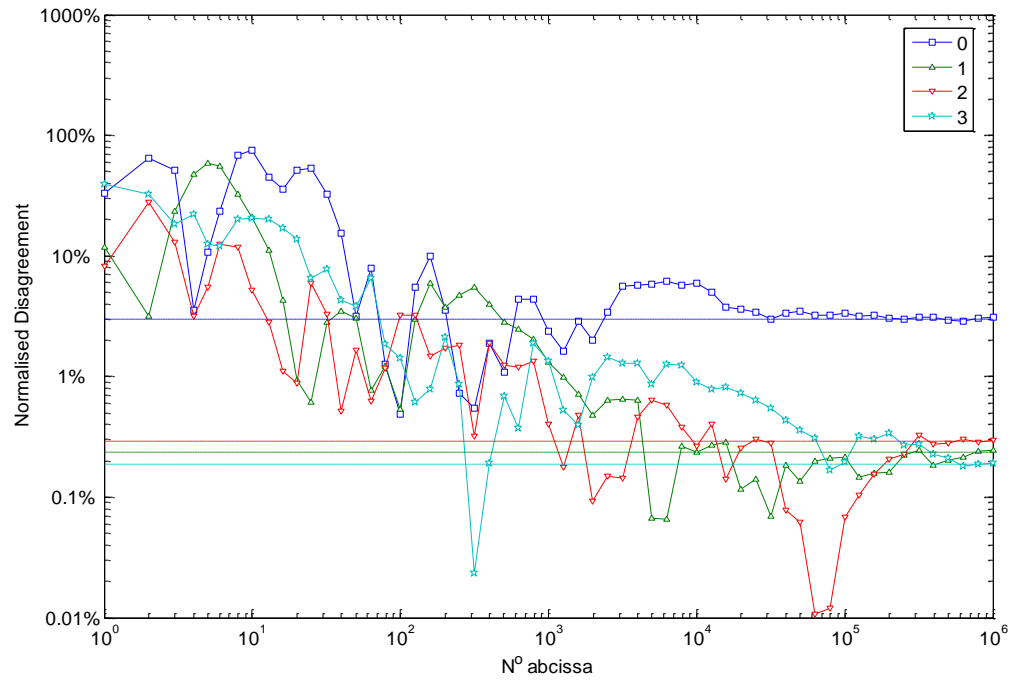
Figure 3.14: $L_v\{\ldots\}$ Monte Carlo convergence to Gaussian result, $c\Delta_t = 0.16\text{m}$
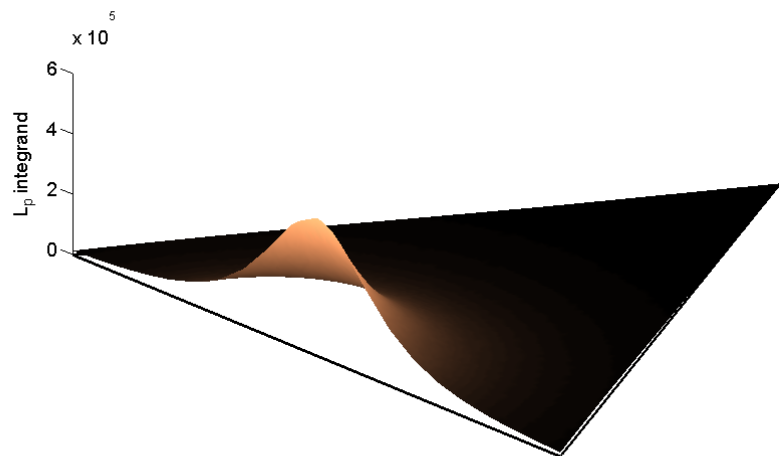
Figure 3.15: $l = 0$ $L_p\{\ldots\}$ integrand where $c\Delta_t = 0.16\text{m}$
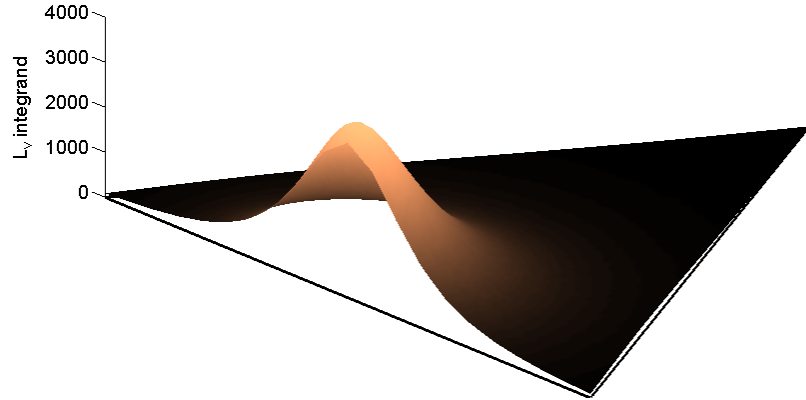
Figure 3.16: $l = 0$ $\mathrm{L}_v\{\ldots\}$ integrand where $c\Delta_t = 0.16\text{m}$

If the time-step is adjusted such that $c\Delta_t = 0.08\text{m}$ then a discontinuity does intersect S_n and different results appear. Figure 3.17 shows Monte Carlo convergence on the $\mathrm{L}_p\{\ldots\}$ integrand. Typically the Gaussian scheme still achieves accuracy of 2% or better, but when $l = 3$ error is worse than 10%. Figure 3.19 and Figure 3.20 show the $l = 3$ integrand and $l = 1$ integrands respectively; the larger $l = 3$ error is associated with a larger discontinuity jump. Figure 3.18 shows Monte Carlo convergence on the $\mathrm{L}_v\{\ldots\}$ integrand. In this example the discontinuities do not appear to significantly affect the accuracy relative to Figure 3.14.
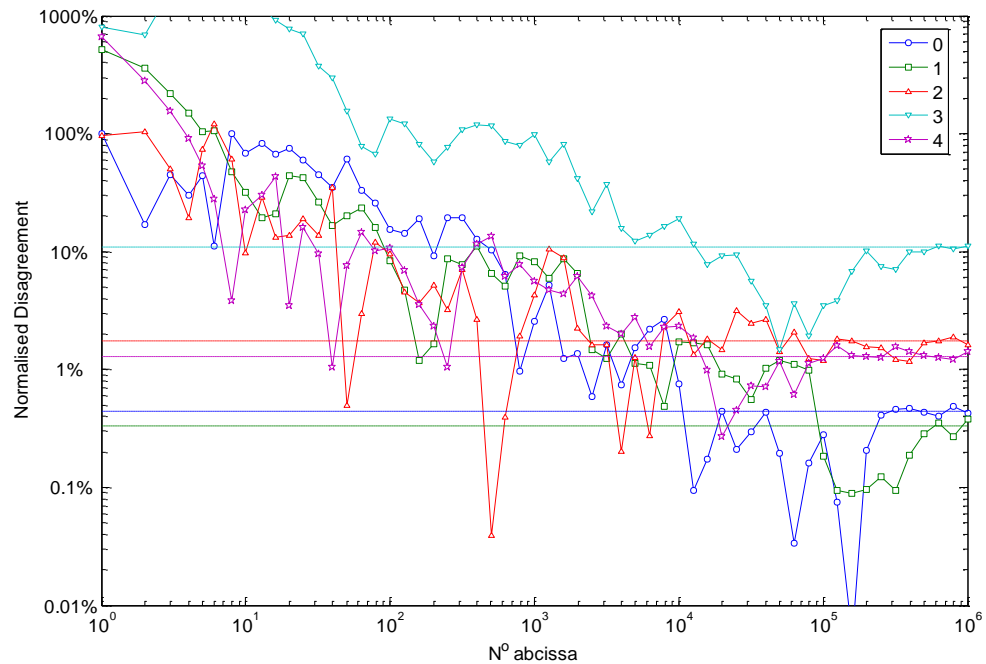
Figure 3.17: $L_p\{\ldots\}$ Monte Carlo convergence to Gaussian result, $c\Delta_t = 0.08\text{m}$
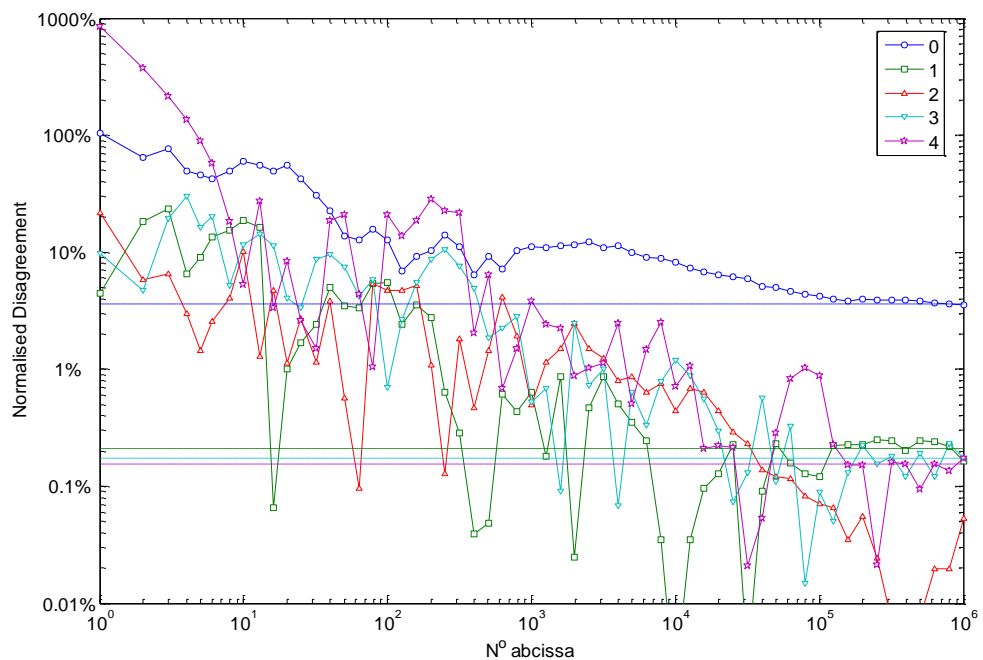
Figure 3.18: $L_v\{\ldots\}$ Monte Carlo convergence to Gaussian result, $c\Delta_t = 0.08\text{m}$
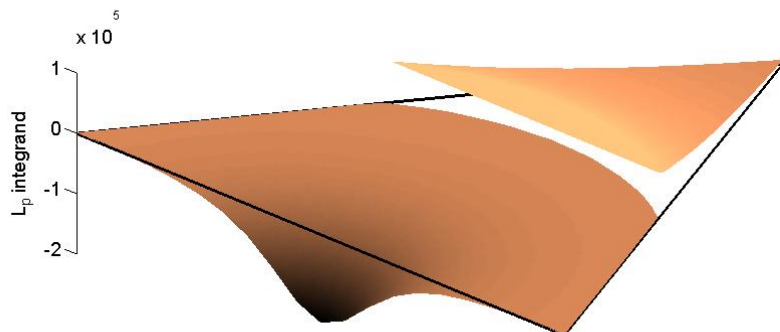
Figure 3.19: $l = 3$ $L_p\{\ldots\}$ integrand where $c\Delta_t = 0.08$m
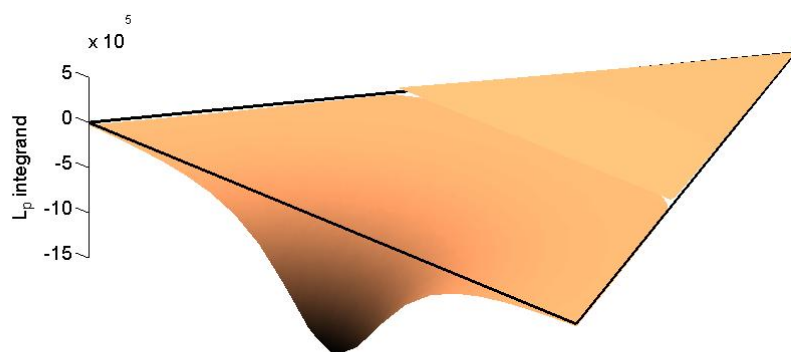
Figure 3.20: $l = 1$ $L_p\{\ldots\}$ integrand where $c\Delta_t = 0.08$m

In conclusion, the singularity of the integrand does not appear to be a significant source of error for the Gaussian scheme. However, accuracy does suffer when discontinuities are present in the integrand, and they will occur for many element pairs if $c\Delta_t$ is of the order of Δ_x. A point-wise integration rule is inherently unsuitable for a discontinuous integrand as its result will be significantly affected by the location of the abscissa relative to the discontinuity. Either these discontinuities must be removed or a new integration technique that respects their existence created.

3.2 Contour Integration

As was alluded to in the definition of the Gaussian product rules mentioned in section 3.1.1, the cost associated with evaluating a surface integral over an element using a given spatial resolution scales with the element's area. By contrast, the cost of evaluating a contour integral around the edge of an element with constant spatial resolution scales only with cumulative edge length. If a surface integral is converted to an equivalent contour integral then the cost scaling of achieving a given accuracy is reduced, so long as the contour integrand is no worse behaved than the surface integrand it replaces. In addition, a wider palette of numerical integration methods is available for one-dimensional integrals.

A common approach to conversion between surface and contour integrals is use of Stokes' theorem [63] below. This is valid for any bounded surface, including curvilinear elements and surfaces of revolution. Unfortunately its use in this application amounts to guessing a vector field $\mathbf{F}$ with curl equal to either the $L_p\{...\}$ or $L_v\{...\}$ surface integrand, a feat this author has attempted with limited success.

$$\iint_S \hat{\mathbf{n}} \cdot \nabla \times \mathbf{F} dS = \oint_{\partial S} \mathbf{F} \cdot \mathbf{l} dl \qquad\qquad 3.14$$

An alternative approach is to use a change of coordinate system. Bonnet, Maier and Polizzotto [33] mention various in the context of self-interaction singularity evaluation in their 1998 Elastodynamics survey paper. For flat elements, such as used in this thesis, conversion to cylindrical coordinates proves very convenient. Stokes' theorem is not applied; instead the radial component of the integration is performed analytically leaving just the angular component to be evaluated as a contour integral. This coordinate system transform was used by Ding, Forestier and Ha-Duong [25] in 1989 for their Galerkin scheme, and by Terai and Kawai [18] in 1990 for their thin surfaces algorithm, creating an implementation equivalent to the $L_v\{...\}$ operator in section 3.2.1.8.

3.2.1 Derivation of contour integration

In this section the contour integration scheme will be derived. First the coordinate system will be defined, followed by derivation of the process to convert polar and cartesian integrals to edge integrals, and finally the derivation of scattered quantities themselves. The new numerical integration scheme will be seen to have the desirable property that, on calculating element self-interaction, it reduces to the special schemes used by Ergin *et al* in this context. Although this integral coordinate transformation has been exploited before, this derivation is more general as it is followed without refinement specific to any basis function – it is valid for any quantity discretisation on a polyhedron. The implementation is valid not only for triangular elements, but for polygonal ones with any number of straight sides.

Following this section the new integration scheme will be contrasted with the Gaussian integration strategies discussed in section 3.1 and discrepancies highlighted and justified.

3.2.1.1   Coordinate system

In order to clarify the conversion of the surface integral over S_n into nested integrals two new coordinate systems will be used; one is a cartesian system (v, w, z) and one a cylindrical polar system (r, θ, z), both shown in Figure 3.21. The origin and positive z direction are the same in both coordinate systems. The origin is defined as the projection of the collocation point $\mathbf{r}$ into the plane of S_n and the positive z direction is specified by $\hat{\mathbf{n}}'$. The positive v direction is defined as the projection of $\hat{\mathbf{n}}$ into the plane of S_n. In practice the unit vectors of the cartesian system are found according to Equation 3.15 such that $\hat{\mathbf{w}} \cdot \hat{\mathbf{n}} = 0$. If the normal vectors of the two elements are parallel, or velocity scattered to an off-body point is being evaluated, then $\mathbf{v}$ and $\mathbf{w}$ may be chosen arbitrarily; an easy choice is for $\hat{\mathbf{v}}$ or $\hat{\mathbf{w}}$ to be parallel to an edge vector as these are known to lie in the plane of S_n. The positive theta direction is defined such that $v = r\cos(\theta)$ and $w = r\sin(\theta)$ in the conventional way. As the collocation point $\mathbf{r}$ is the only point with a non-zero z coordinate, the variable z will be used to refer to

that and equally the z component of R. Similarly, any reference to v, w, r or θ implies the integration point $\mathbf{r'}$ or the appropriate component of R.
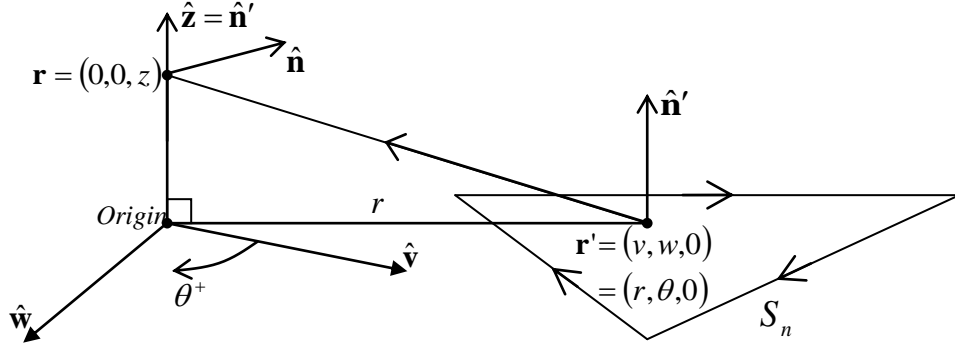
Figure 3.21: Problem geometry and coordinate systems

$$\hat{\mathbf{w}} = \frac{\hat{\mathbf{n}} \times \hat{\mathbf{n}}'}{\left|\hat{\mathbf{n}} \times \hat{\mathbf{n}}'\right|}, \quad \hat{\mathbf{v}} = \frac{\hat{\mathbf{w}} \times \hat{\mathbf{n}}'}{\left|\hat{\mathbf{w}} \times \hat{\mathbf{n}}'\right|} \qquad 3.15$$

The contour integration path shall be the edge vectors, the directions of which are defined by the order of the vertices in the definition of S_n. Because the new coordinate systems are defined from $\hat{\mathbf{n}}'$ (which is in turn also defined by the order of the vertices), the edge vectors always travel around the centre of S_n in the same direction that θ increases around the origin. This property will be exploited in subsequent sections.

3.2.1.2 Transforming polar integrals into edge integrals

The polar integrals requiring evaluation have the form shown in Equation 3.16. How this is evaluated depends on whether the cylindrical origin is contained by S_n; the two scenarios are depicted in Figure 3.22.

$$\int_{\theta_{\min}}^{\theta_{\max}} f(R_{\max}(\theta))d\theta - \int_{\theta_{\min}}^{\theta_{\max}} f(R_{\min}(\theta))d\theta \qquad 3.16$$
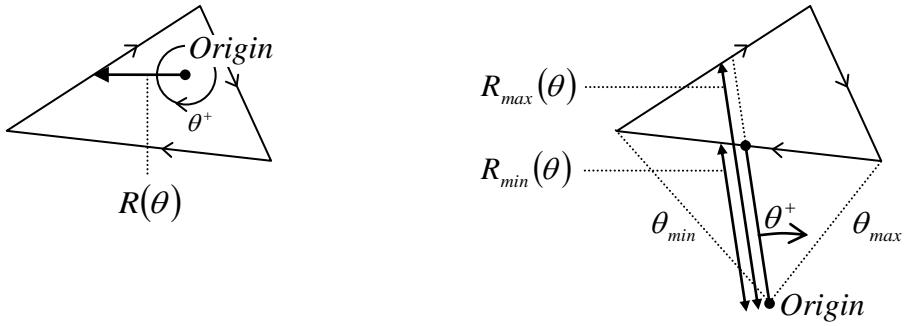
Figure 3.22: Polar origin interior and exterior to S_n

In the case where S_n contains the origin, $R_{min} = |z|$ so the first integral is an integral around the edge and the second integral is evaluated at the origin; this takes the form of Equation 3.17 where $\theta_{origin} = 2\pi$. If the origin lies on the edge of S_n θ_{origin} will equal the enclosed angle; intersection of one edge implies $\theta_{origin} = \pi$, intersection of a corner implies θ_{origin} will equal the acute angle between the adjoining edges.

In the case where the origin is outside S_n, each integral is around an exclusive segment of the edge. If written as a contour integral those edge segments that correspond to R_{min} automatically have a negative contribution as they travel in a negative direction with respect to θ. If θ_{origin} is defined to equal zero if the origin is outside S_n then, regardless of the position of the origin, the integral may always be expressed as:

$$\int_{\theta_{\min}}^{\theta_{\max}} f(R_{\max}(\theta))d\theta - \int_{\theta_{\min}}^{\theta_{\max}} f(R_{\min}(\theta))d\theta = \oint_{S_n} f(R(\theta))d\theta - \theta_{origin} f(|z|) \qquad 3.17$$

$$\theta_{origin} = \begin{cases} 0 \text{ if origin is external to } S_n \\ 2\pi \text{ if } S_n \text{ contains origin} \\ \pi \text{ if one edge passes through the origin} \\ \cos^{-1}|\hat{\mathbf{e}}_{before} \cdot \hat{\mathbf{e}}_{after}| \text{ if a vertex lies on the origin} \end{cases} \qquad 3.18$$

This contour integral around S_n is with respect to θ. Numerical integration implementation would be simpler if the integral were with respect to a parameter that reflects position along an edge. Hence μ is introduced as the edge coordinate; $\mu = 0$ represents the start vertex of the edge, $\mu = 1$ the end vertex. A relationship must be found between μ and θ so that the contour integral with respect to θ can be transformed into a summation of edge integrals with respect to μ.

$\mu_\perp$ is defined as the line coordinate of the projection of the origin into the line of edge $\mathbf{e}$ as depicted in Figure 3.23. It is found by solving Equation 3.19, observing that the shortest distance from a point to a line is perpendicular to the line. As drawn it would take a negative value. ϕ may be found from μ by Equation 3.20.
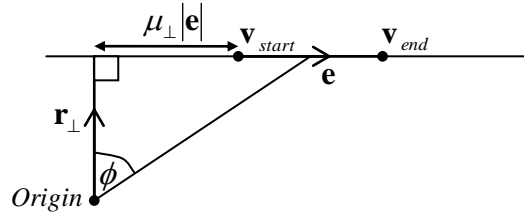
Figure 3.23: Converting polar coordinates to edge coordinates

$$\mathbf{r}_\perp = \left(\mathbf{v}_{start} - Origin\right) + \mu_\perp \mathbf{e}$$
$$\mathbf{e} \cdot \mathbf{r}_\perp = \mathbf{e} \cdot \left(\mathbf{v}_{start} - Origin\right) + \mu_\perp \mathbf{e} \cdot \mathbf{e} = 0 \qquad 3.19$$
$$\mu_\perp = -\frac{\mathbf{e} \cdot \left(\mathbf{v}_{start} - Origin\right)}{\mathbf{e} \cdot \mathbf{e}}$$

$$\phi = \tan^{-1}\left(\frac{\left(\mu - \mu_\perp\right)\left|\mathbf{e}\right|}{\left|\mathbf{r}_\perp\right|}\right) \qquad 3.20$$

θ is equal to some constant plus or minus ϕ depending on the direction of the edge with respect to θ (Equation 3.21). The sought differential of θ with respect to μ may be evaluated by Equation 3.22. $\text{sign}\left(\hat{\mathbf{e}} \cdot \hat{\boldsymbol{\theta}}\right)$ is constant along the length of $\mathbf{e}$ and is

evaluated according to Equation 3.23. If an edge intersects the origin, that edge's contribution to the contour integral will be zero as $\hat{\mathbf{e}} \cdot \hat{\mathbf{\theta}} = 0$ and $|\mathbf{r}_\perp| = 0$.

$$\theta = \text{sign}(\hat{\mathbf{e}} \cdot \hat{\mathbf{\theta}})\phi + constant \qquad\qquad 3.21$$

$$\begin{aligned}
\frac{d\theta}{d\mu} &= \frac{d\phi}{d\mu}\text{sign}(\hat{\mathbf{e}} \cdot \hat{\mathbf{\theta}}) \\
&= \frac{|\mathbf{e}||\mathbf{r}_\perp|}{|\mathbf{r}_\perp|^2 + (\mu - v)^2|\mathbf{e}|^2}\text{sign}(\hat{\mathbf{e}} \cdot \hat{\mathbf{\theta}}) \\
&= r^{-2}|\mathbf{e}||\mathbf{r}_\perp|\text{sign}(\hat{\mathbf{e}} \cdot \hat{\mathbf{\theta}})
\end{aligned} \qquad\qquad 3.22$$

$$\text{sign}(\hat{\mathbf{e}} \cdot \hat{\mathbf{\theta}}) = \text{sign}(\mathbf{e} \cdot (\hat{\mathbf{n}}' \times (\mathbf{v}_{start} - Origin))) \qquad\qquad 3.23$$

Combining Equations 3.17 and Equation 3.18 with the above expressions completes the transform from polar integral to summation of edge integrals with respect to μ.

3.2.1.3 Transforming Cartesian integrals into edge integrals

The Cartesian integral requiring evaluation over each smooth region has the form shown in Equation 3.24. As with the polar integral this would be most convenient to integrate if transformed to a summation of edge integrals. To achieve this requires the derivative of w with respect to μ; this is easily found in Equation 3.25 from the definition of w for a point on $\mathbf{e}$ and is constant along the length of an edge.

$$\int_{w_{min}}^{w_{max}} f(R(v_{max}(w)))dw - \int_{w_{min}}^{w_{max}} f(R(v_{min}(w)))dw \qquad\qquad 3.24$$

$$\begin{aligned}
w &= \hat{\mathbf{w}} \cdot (\mathbf{v}_{start} + \mu\mathbf{e}) \\
\frac{dw}{d\mu} &= \hat{\mathbf{w}} \cdot \mathbf{e}
\end{aligned} \qquad\qquad 3.25$$

As mentioned in section 3.2.1.1, the (v, w, z) coordinate system is derived from the normal vector of S_n, so the edges have the convenient property of always travelling clockwise when viewed in the (v, w) axes as shown in Figure 3.24. Consequentially the derivative of w with respect to μ will always be positive for edges contributing to the v_{max} integral and negative for edges contributing to the v_{min} integral. There is no contribution from the origin, even if it is within S_n. Hence the Cartesian integral may be written in edge integral form as Equation 3.26. Similarly Equation 3.27 holds with Equation 3.28.
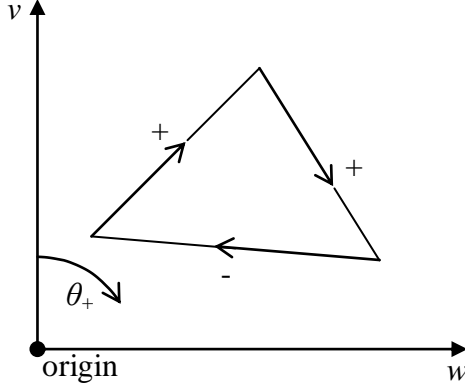
Figure 3.24: Edge directions in the (v, w) plane

$$\int_{w_{min}}^{w_{max}} f(R(v_{max}(w)))dw - \int_{w_{min}}^{w_{max}} f(R(v_{min}(w)))dw = \oint_{S_n} f(R)dw = \sum_{edges} \int_0^1 f(R(v(\mu)))\frac{dw}{d\mu}d\mu \qquad 3.26$$

$$\int_{v_{min}}^{v_{max}} f(R(w_{max}(v)))dv - \int_{v_{min}}^{v_{max}} f(R(w_{min}(v)))dv = \oint_{S_n} f(R)dv = \sum_{edges} \int_0^1 f(R(w(\mu)))\frac{dv}{d\mu}d\mu \qquad 3.27$$

$$\frac{dv}{d\mu} = -\hat{\mathbf{v}} \cdot \mathbf{e} \qquad 3.28$$

3.2.1.4 Scattered velocity potential

Scattered velocity potential is described by the KIE for a rigid surface. The Greens function term is a function solely in R and t hence its spatial gradient may be expressed as a derivative with respect to R. Convolution with retarded derivatives of the delta function has the effect of applying its derivatives and retardation onto the convolved field. This identity is proved in section 8.1.

$$
\begin{aligned}
\varphi^s(\mathbf{r},t) &= \iint_S \varphi^t(\mathbf{r}',t) * \hat{\mathbf{n}}'\cdot\nabla' \frac{\delta\left(t - R/c\right)}{4\pi R} d\mathbf{r}' \\
&= -\iint_S \hat{\mathbf{n}}'\cdot\hat{\mathbf{R}} \frac{\partial}{\partial R} \frac{\varphi^t\left(\mathbf{r}', t - R/c\right)}{4\pi R} d\mathbf{r}'
\end{aligned}
\tag{3.29}
$$

It can be observed from Figure 3.21 that for a flat surface section Equation 3.30 holds. Equation 3.31 results from substitution of Equation 3.30 into Equation 3.29, then conversion of the surface integral to a polar integral.

$$
\hat{\mathbf{n}}'\cdot\hat{\mathbf{R}} = \frac{\hat{\mathbf{n}}'\cdot\mathbf{R}}{R} = \frac{z}{R}
\tag{3.30}
$$

$$
\begin{aligned}
\varphi^s(\mathbf{r},t) &= -\sum_{\text{elements}} \iint_{S_n} \frac{z}{R} \frac{\partial}{\partial R}\left(\frac{\varphi^t\left(\mathbf{r}', t - R/c\right)}{4\pi R} \right) d\mathbf{r}' \\
&= -\sum_{\text{elements}} z \int_{\theta_{\min}}^{\theta_{\max}} \int_{r_{\min}(\theta)}^{r_{\max}(\theta)} \frac{r}{R} \frac{\partial}{\partial R}\left(\frac{\varphi^t\left(\mathbf{r}', t - R/c\right)}{4\pi R} \right) dr d\theta
\end{aligned}
\tag{3.31}
$$

This integral in cylindrical radius r is converted to an integral in spherical radius R by substituting Equation 3.32, and is integrated analytically in Equation 3.33. The resulting polar integral is converted into a contour integral using the identities derived in section 3.2.1.2.

$$\frac{dr}{dR} = \frac{2R}{2\sqrt{R^2 - z^2}} = \frac{R}{r}$$

<div align="right">3.32</div>

$$
\begin{aligned}
\varphi^s(\mathbf{r},t) &= -\sum_{elements} z \int_{\theta_{min}}^{\theta_{max}} \int_{R_{min}(\theta)}^{R_{max}(\theta)} \frac{\partial}{\partial R}\left(\frac{\varphi^t\left(\mathbf{r}',t - R\!\big/\!c\right)}{4\pi R}\right) dR\, d\theta \\
&= -\sum_{elements} z \int_{\theta_{min}}^{\theta_{max}} \left[\frac{\varphi^t\left(\mathbf{r}',t - R\!\big/\!c\right)}{4\pi R}\right]_{R_{min}(\theta)}^{R_{max}(\theta)} d\theta \\
&= \sum_{elements} \left[\frac{\theta_{origin}}{4\pi}\frac{z}{|z|}\varphi^t\left(\mathbf{r}_{origin}, t - |z|\!\big/\!c\right) - z\oint_{S_n} \frac{\varphi^t\left(\mathbf{r}',t - R\!\big/\!c\right)}{4\pi R} d\theta\right]
\end{aligned}
$$

<div align="right">3.33</div>

Importantly this identity is valid for any piecewise flat surface (polyhedron), regardless of the discretisation scheme for $\varphi^t(\mathbf{r}',t)$. The situation where $z = 0$ and $\theta_{origin} \neq 0$ is ambiguous (dual-valued as expected of the double layer potential), but only occurs in the case of element self-interaction where it is resolved by the boundary condition.

3.2.1.5 Scattered pressure

Scattered pressure is easily found by temporal differentiation of Equation 3.33, and again this statement is valid for ~~any $\varphi^t(\mathbf{r}',t)$ discretisation scheme~~ piece-wise constant elements on a polyhedron:

$$
\begin{aligned}
p^s(\mathbf{r},t) &= -\rho_0 \dot{\varphi}^s(\mathbf{r},t) \\
&= -\rho_0 \sum_{elements} \left[\frac{\theta_{origin}}{4\pi}\frac{z}{|z|}\dot{\varphi}^t\left(\mathbf{r}_{origin}, t - |z|\!\big/\!c\right) - z\oint_{S_n} \frac{\dot{\varphi}^t\left(\mathbf{r}',t - R(\theta)\!\big/\!c\right)}{4\pi R} d\theta\right]
\end{aligned}
$$

<div align="right">3.34</div>

3.2.1.6 Pressure Operator

The pressure operator is defined as the scattered pressure divided by $-\rho_0$ so when $\alpha = 0$ the elements of the interaction matrix are defined according to Equation 3.35. The element self-interaction term (Equation 3.36) is defined by the boundary condition to be the limit as the observer point approaches the surface element from inside the

body; it is encouraging that this statement matches Ergin *et al's* self-interaction statement. Here the contour integral has been replaced by a sum of edge integrals using the identities derived in section 3.2.1.2 so the statements are in a form ready for implementation.

$$
\begin{aligned}
Z_{m,n,l} &= - L_p \left\{ f_n(\mathbf{r}) T_{j-l}(t) \right\}\Big|_{t=t_j;\mathbf{r}=\mathbf{r_m^c}} \\
&= \left[z \sum_{\text{edges}} \int_0^1 \frac{\dot{T}_{j-l}(\tau)}{4\pi R} \frac{d\theta}{d\mu} d\mu - \frac{\theta_{origin}}{4\pi} \frac{z}{|z|} \dot{T}_{j-l}\left(t_j - \frac{|z|}{c} \right) \right]\Bigg|_{\mathbf{r}=\mathbf{r_m^c}}
\end{aligned}
$$
3.35

$$
\begin{aligned}
Z_{n,n,l} &= - L_p \left\{ f_n(\mathbf{r}) T_{j-l}(t) \right\}\Big|_{t=t_j;\mathbf{r}=\mathbf{r_n^c}} \\
&= \lim_{z \to 0_-} \left[z \sum_{\text{edges}} \int_0^1 \frac{\dot{T}_{j-l}(\tau)}{4\pi R} \frac{d\theta}{d\mu} d\mu - \frac{\theta_{origin}}{4\pi} \frac{z}{|z|} \dot{T}_{j-l}\left(t_j - \frac{|z|}{c} \right) \right] \\
&= \frac{\dot{T}_{j-l}(t_j)}{2}
\end{aligned}
$$
3.36

3.2.1.7   Scattered velocity

Scattered velocity is the gradient of scattered velocity potential. In this scenario $\mathbf{r}$ is an off-body point hence the velocity potential field is assumed smooth enough that the gradient operator may be moved inside the integral:

$$
\begin{aligned}
\mathbf{v}^s(\mathbf{r},t) &= \nabla \varphi^s(\mathbf{r},t) \\
&= -\nabla \iint_S \hat{\mathbf{n}}' \cdot \hat{\mathbf{R}} \frac{\partial}{\partial R} \frac{\varphi^t\left(\mathbf{r}', t - \frac{R}{c} \right)}{4\pi R} d\mathbf{r}' \\
&= -\iint_S \nabla \left[\hat{\mathbf{n}}' \cdot \hat{\mathbf{R}} \frac{\partial}{\partial R} \frac{\varphi^t\left(\mathbf{r}', t - \frac{R}{c} \right)}{4\pi R} \right] d\mathbf{r}'
\end{aligned}
$$
3.37

Application of the spatial gradient operator to the bracketed term requires use of the product rule; this is done below where for clarity $q(\mathbf{r}', R, t)$ is introduced according to Equation 3.39.

$$\mathbf{v}^s(\mathbf{r},t) = -\iint_S \nabla\left[\hat{\mathbf{n}}'\cdot\hat{\mathbf{R}}\,\frac{\partial q}{\partial R}\right] d\mathbf{r}'$$

$$= -\iint_S \left[\hat{\mathbf{n}}'\cdot\hat{\mathbf{R}}\nabla\frac{\partial q}{\partial R} + \frac{\partial q}{\partial R}\nabla\hat{\mathbf{n}}'\cdot\hat{\mathbf{R}}\right] d\mathbf{r}' \qquad 3.38$$

$$q(\mathbf{r}',R,t) = \frac{\varphi^t\left(\mathbf{r}',t - R/c\right)}{4\pi R} \qquad\qquad 3.39$$

The gradient is evaluated at the observation point so it is only the dependency of the scattered velocity potential on R that contributes; the local variation of surface velocity potential at the integration point does not. Hence Equation 3.40 holds; there is no minus sign here because at the collocation point $\hat{\mathbf{R}}$ points in the direction of increasing R. Equation 3.41 is proved in section 8.3. Equation 3.42 may be readily proven using the product differentiation rule. These three identities are substituted into Equation 3.38 to produce Equation 3.43.

$$\nabla\frac{\partial q}{\partial R} = \hat{\mathbf{R}}\frac{\partial^2 q}{\partial R^2} \qquad\qquad 3.40$$

$$\nabla\hat{\mathbf{n}}'\cdot\hat{\mathbf{R}} = \frac{\hat{\mathbf{n}}'}{R} - \frac{\hat{\mathbf{n}}'\cdot\hat{\mathbf{R}}}{R}\hat{\mathbf{R}} \qquad\qquad 3.41$$

$$\frac{\partial}{\partial R}\left(\frac{1}{R}\frac{\partial q}{\partial R}\right) = \frac{1}{R}\left(\frac{\partial^2 q}{\partial R^2} - \frac{1}{R}\frac{\partial q}{\partial R}\right) \qquad\qquad 3.42$$

$$\mathbf{v}^s(\mathbf{r},t) = -\iint_S \left[\hat{\mathbf{R}}\hat{\mathbf{n}}'\cdot\hat{\mathbf{R}}\frac{\partial^2 q}{\partial R^2} + \left(\frac{\hat{\mathbf{n}}'}{R} - \frac{\hat{\mathbf{n}}'\cdot\hat{\mathbf{R}}}{R}\hat{\mathbf{R}}\right)\frac{\partial q}{\partial R}\right] d\mathbf{r}'$$

$$= -\iint_S \left[\frac{\hat{\mathbf{n}}}{R}\frac{\partial q}{\partial R} + \hat{\mathbf{R}}\hat{\mathbf{n}}'\cdot\hat{\mathbf{R}}\left(\frac{\partial^2 q}{\partial R^2} - \frac{1}{R}\frac{\partial q}{\partial R}\right)\right] d\mathbf{r}' \qquad 3.43$$

$$= -\iint_S \left[\frac{\hat{\mathbf{n}}}{R}\frac{\partial q}{\partial R} + \hat{\mathbf{R}}\hat{\mathbf{n}}'\cdot\hat{\mathbf{R}}R\frac{\partial}{\partial R}\left(\frac{1}{R}\frac{\partial q}{\partial R}\right)\right] d\mathbf{r}'$$

The geometric identities in Equation 3.30 and Equation 3.44 are valid for each flat surface element. These are substituted to create Equation 3.45 and the surface integrals grouped as polar or Cartesian.

$$\hat{\mathbf{R}} = \frac{\mathbf{R}}{R} = \frac{1}{R}\left(z\hat{\mathbf{n}}' - \left(v\hat{\mathbf{v}} + w\hat{\mathbf{w}}\right)\right) \tag{3.44}$$

$$\mathbf{v}^s(\mathbf{r},t) = -\sum_{\text{elements}} \iint_{S_n} \left[\frac{\hat{\mathbf{n}}'}{R}\frac{\partial q}{\partial R} + \frac{z}{R}\left(z\hat{\mathbf{n}}' - \left(v\hat{\mathbf{v}} + w\hat{\mathbf{w}}\right)\right)\frac{\partial}{\partial R}\left(\frac{1}{R}\frac{\partial q}{\partial R}\right)\right]d\mathbf{r}'$$

$$= -\sum_{\text{elements}} \begin{bmatrix} \hat{\mathbf{n}}'\iint_{S_n}\frac{1}{R}\left[\frac{\partial q}{\partial R} + z^2\frac{\partial}{\partial R}\left(\frac{1}{R}\frac{\partial q}{\partial R}\right)\right]d\mathbf{r}' \\ -\hat{\mathbf{v}}z\iint_{S_n}\frac{v}{R}\frac{\partial}{\partial R}\left(\frac{1}{R}\frac{\partial q}{\partial R}\right)d\mathbf{r}' \\ -\hat{\mathbf{w}}z\iint_{S_n}\frac{w}{R}\frac{\partial}{\partial R}\left(\frac{1}{R}\frac{\partial q}{\partial R}\right)d\mathbf{r}' \end{bmatrix}$$

$$= -\sum_{\text{elements}} \begin{bmatrix} \hat{\mathbf{n}}'\iint_{S_n}\frac{r}{R}\left[\frac{\partial q}{\partial R} + z^2\frac{\partial}{\partial R}\left(\frac{1}{R}\frac{\partial q}{\partial R}\right)\right]drd\theta \\ -\hat{\mathbf{v}}z\iint_{S_n}\frac{v}{R}\frac{\partial}{\partial R}\left(\frac{1}{R}\frac{\partial q}{\partial R}\right)dvdw \\ -\hat{\mathbf{w}}z\iint_{S_n}\frac{w}{R}\frac{\partial}{\partial R}\left(\frac{1}{R}\frac{\partial q}{\partial R}\right)dvdw \end{bmatrix} \tag{3.45}$$

The integration variables are changed to allow analytical integration in R; this requires the derivatives of Equation 3.46. In Equation 3.47 these are substituted, the analytical integration performed, and then conversion to contour integrals is achieved using the appropriate identities from sections 3.2.1.2 and 3.2.1.3.

$$\frac{dR}{dr} = \frac{r}{R}; \qquad \frac{dR}{dv} = \frac{v}{R}; \qquad \frac{dR}{dw} = \frac{w}{R} \tag{3.46}$$

$$
\mathbf{v}^s(\mathbf{r},t) = -\sum_{elements}
\begin{bmatrix}
\hat{\mathbf{n}}' \iint_{S_n} \left[\dfrac{\partial q}{\partial R} + z^2 \dfrac{\partial}{\partial R}\left(\dfrac{1}{R}\dfrac{\partial q}{\partial R} \right) \right] dR\,d\theta \\[2ex]
-\hat{\mathbf{v}}z \iint_{S_n} \dfrac{\partial}{\partial R}\left(\dfrac{1}{R}\dfrac{\partial q}{\partial R} \right) dR\,dw \\[2ex]
-\hat{\mathbf{w}}z \iint_{S_n} \dfrac{\partial}{\partial R}\left(\dfrac{1}{R}\dfrac{\partial q}{\partial R} \right) dv\,dR
\end{bmatrix}
$$

$$
= -\sum_{elements}
\begin{bmatrix}
\hat{\mathbf{n}}' \int_{S_n} \left[q(\mathbf{r}',R,t) + \dfrac{z^2}{R}\dfrac{\partial q}{\partial R} \right]_{R_{\min}(\theta)}^{R_{\max}(\theta)} d\theta \\[2ex]
-\hat{\mathbf{v}}z \int_{S_n} \dfrac{1}{R}\dfrac{\partial q}{\partial R}\Big|_{R(v_{\min})}^{R(v_{\max})} dw \\[2ex]
-\hat{\mathbf{w}}z \int_{S_n} \dfrac{1}{R}\dfrac{\partial q}{\partial R}\Big|_{R(w_{\min})}^{R(w_{\max})} dv
\end{bmatrix}
$$

$$
= -\sum_{elements}
\begin{bmatrix}
\hat{\mathbf{n}}' \oint_{S_n} \left[q(\mathbf{r}',R,t) + \dfrac{z^2}{R}\dfrac{\partial q}{\partial R} \right] d\theta \\[2ex]
-\hat{\mathbf{n}}'\theta_{origin} \left[q(\mathbf{r}_{origin},|z|,t) + |z|\dfrac{\partial q}{\partial R}\Big|_{\mathbf{r}=\mathbf{r}_{origin}} \right] \\[2ex]
-\hat{\mathbf{v}}z \oint_{S_n} \dfrac{1}{R}\dfrac{\partial q}{\partial R} dw \\[2ex]
-\hat{\mathbf{w}}z \oint_{S_n} \dfrac{1}{R}\dfrac{\partial q}{\partial R} dv
\end{bmatrix}
\qquad 3.47
$$

Again this statement is valid for ~~any $\varphi^t(\mathbf{r}',t)$ discretisation scheme~~ piece-wise constant elements on a polyhedron.

3.2.1.8 Velocity Operator

The velocity operator is equal to $-\hat{\mathbf{n}} \cdot \mathbf{v}^s(\mathbf{r},t)$ and is calculated as a contour integral as follows, where the (v, w, z) coordinate system has chosen such that $\hat{\mathbf{n}} \cdot \hat{\mathbf{w}} = 0$. Here the contour integrals have been replaced by a sum of edge integrals using the identities derived in sections 3.2.1.2 and 3.2.1.3 so the statements are in a form ready for implementation:

$$
L_v\left\{\varphi^t\left(\mathbf{r}',t\right)\right\}\Big|_{t=t_j\,;\mathbf{r}=\mathbf{r_m^c}} = \sum_{\text{elements}} \begin{bmatrix} \hat{\mathbf{n}}\cdot\hat{\mathbf{n}}'\sum_{\text{edges}}\int_0^1\left[q(\mathbf{r}',R,t)+\dfrac{z^2}{R}\dfrac{\partial q}{\partial R}\right]\dfrac{d\theta}{d\mu}d\mu \\[2ex] -\hat{\mathbf{n}}\cdot\hat{\mathbf{n}}'\theta_{origin}\left[q\left(\mathbf{r}_{origin},|z|,t\right)+|z|\dfrac{\partial q}{\partial R}\Big|_{\mathbf{r}=\mathbf{r}_{origin}}\right] \\[2ex] -\hat{\mathbf{n}}\cdot\hat{\mathbf{v}}\sum_{\text{edges}}\int_0^1\dfrac{z}{R}\dfrac{\partial q}{\partial R}\dfrac{dw}{d\mu}d\mu \end{bmatrix}_{\substack{t=t_j\\ \mathbf{r}=\mathbf{r_m^c}}}
\qquad 3.48
$$

Still this statement is valid for any discretisation scheme on a polyhedron. It is equivalent to Kawai and Terai's [18] Equation 15, except for a factor of $-\left(4\pi\right)^{-1}$ that occurs due to a difference in definition of the integral operators. A basis representation specific refinement is now introduced: substituting Equation 3.49 into Equation 3.48 gives the following statement for the elements of the interaction matrices when $\alpha = 1$:

$$
\frac{\partial q}{\partial R} = \frac{-1}{4\pi}\left[\frac{\dot{\mathrm{T}}_{j-l}(\tau)}{cR} + \frac{\mathrm{T}_{j-l}(\tau)}{R^2}\right]
\qquad 3.49
$$

$$
Z_{m,n,l} = cL_v\left\{\mathrm{f_n}(\mathbf{r})\mathrm{T}_{j-l}(t)\right\}\Big|_{t=t_j\,;\mathbf{r}=\mathbf{r_m^c}}
$$

$$
= c\begin{bmatrix} \dfrac{\hat{\mathbf{n}}\cdot\hat{\mathbf{n}}'}{4\pi}\sum_{\text{edges}}\int_0^1\left[\dfrac{\mathrm{T}_{j-l}(\tau)}{R}-z^2\dfrac{\dot{\mathrm{T}}_{j-l}(\tau)}{cR^2}-z^2\dfrac{\mathrm{T}_{j-l}(\tau)}{R^3}\right]\dfrac{d\theta}{d\mu}d\mu \\[2ex] +\hat{\mathbf{n}}\cdot\hat{\mathbf{n}}'\dfrac{\theta_{origin}}{4\pi}\dfrac{\dot{\mathrm{T}}_{j-l}\left(t_j-\dfrac{|z|}{c}\right)}{c} \\[2ex] +z\dfrac{\hat{\mathbf{n}}\cdot\hat{\mathbf{v}}}{4\pi}\sum_{\text{edges}}\int_0^1\left[\dfrac{\dot{\mathrm{T}}_{j-l}(\tau)}{cR^2}+\dfrac{\mathrm{T}_{j-l}(\tau)}{R^3}\right]\dfrac{dw}{d\mu}d\mu \end{bmatrix}_{\mathbf{r}=\mathbf{r_m^c}}
\qquad 3.50
$$

$L_v\{...\}$ is continuous across $z = 0$, so the element self-interaction term below is the limit when the observer point approaches the surface element from inside or outside the body. This statement matches Ergin *et al's* self-interaction statement, except for the factor of $\left(4\pi\right)^{-1}$ typographical error mentioned in the section 2.3.4.

$$Z_{n,n,l} = cL_v \left\{ f_n(\mathbf{r}) T_{j-l}(t) \right\} \Big|_{t=t_j ; \mathbf{r}=\mathbf{r}_n^c}$$

$$= c \lim_{z \to 0} \begin{bmatrix} \dfrac{\hat{\mathbf{n}} \cdot \hat{\mathbf{n}}'}{4\pi} \sum_{\text{edges}} \int_0^1 \left[\dfrac{T_{j-l}(\tau)}{R} - z^2 \dfrac{\dot{T}_{j-l}(\tau)}{cR^2} - z^2 \dfrac{T_{j-l}(\tau)}{R^3} \right] \dfrac{d\theta}{d\mu} d\mu \\[2em] + \hat{\mathbf{n}} \cdot \hat{\mathbf{n}}' \dfrac{\theta_{origin}}{4\pi} \dfrac{\dot{T}_{j-l}\left(t_j - \dfrac{|z|}{c}\right)}{c} \\[2em] + z \dfrac{\hat{\mathbf{n}} \cdot \hat{\mathbf{v}}}{4\pi} \sum_{\text{edges}} \int_0^1 \left[\dfrac{\dot{T}_{j-l}(\tau)}{cR^2} + \dfrac{T_{j-l}(\tau)}{R^3} \right] \dfrac{dw}{d\mu} d\mu \end{bmatrix}_{\mathbf{r}=\mathbf{r}_n^c}$$

$$= c \sum_{\text{edges}} \int_0^1 \left[\dfrac{T_{j-l}(\tau)}{4\pi R} \right] \dfrac{d\theta}{d\mu} d\mu + \dfrac{\dot{T}_{j-l}\left(t - \dfrac{|z|}{c}\right)}{2} \qquad\qquad 3.51$$

Equations 3.35 and 3.50 are equivalent to the double integrals that for non-self interactions are evaluated using numerical integration in the Gaussian scheme. These now only contain single integrals as the nested integral has been performed analytically. This reduces the order of algorithmic complexity, as integration is now over a line instead of over a surface, and allows one-dimensional numerical integration methods to be applied. The expressions are also valid for calculating velocity potential, pressure and velocity fields scattered to off-body points.

3.2.1.9 Implementation details

Ergin *et al* write that the contour integral that occurs in their implementation of the self-interaction case of the $L_v\{...\}$ operator may be performed analytically, though similar accuracy was achieved using a seventeen point Gauss-Legendre rule. Here, despite numerous attempts, the author has not been able to replicate this analytical integration, nor is it known if the more general result of completely analytical integration of all non-self interactions is possible. Instead this thesis adopts adaptive integration.

Adaptive integration focuses its effort on the regions with greatest variation, tunnelling into greater detail until an accuracy criterion is met. If integrating a polynomial of

known order it is likely to be less efficient than an appropriate Gaussian integration scheme. However, for an unknown integrand it has the benefit of only applying computational effort where required and guaranteeing a certain accuracy. In the view of the author this is inherently suitable for evaluating the edge integrals derived in the previous section. As long as all terms are brought inside the numerical integration (including constant multipliers such as $(4\pi)^{-1}$) an absolute accuracy termination criterion may be used. This produces greater relative accuracy on larger (and hence more significant) interaction terms, while smaller (less significant) interaction terms receive less effort and relative accuracy.

Another benefit is the subjective property of algorithmic elegance. If Gaussian integration is used, both with or without a coordinate transformation or regularization procedure, then to increase efficiency the order of the rule may be changed according to the expected complexity of the integrand, perhaps dictated by some combination of element separation and orientation; Ergin *et al* increase the order for adjacent elements, others have suggested that a one-point rule is adequate for distant element pairs. While such bespoke schemes may bring a modest increase in computational efficiency, this is likely to be by a fixed factor, unlikely to scale with problem size, and non-physical rifts are created at which different accuracy integration schemes are selected. By comparison the adaptive integration scheme proposed here is continuous and transparent, with the tailoring of computational effort abstracted into an assertion of accuracy. The integrands are weakly singular, with a non-zero line of integration never intersecting a singularity point, and are well conditioned at larger element separations so misbehaviour is not anticipated.

Due to the support of the temporal basis function each element interaction creates non-zero values for a sequence of retardation indices; this is length four or above for the temporal basis function used in this chapter. The new numerical integration scheme carries geometrical overheads both in setting up the coordinate system, and evaluating geometrical terms in the integrands. These overheads are effectively reduced if they can be shared over the sequence of retardation indices. To achieve this, an adaptive integrator has been implemented that can integrate multiple retardations simultaneously;

this was adapted from the standard Matlab function quad.m, which uses adaptive Simpson integration with Romberg extrapolation. The integrand routine was also vectorised to evaluate multiple retardations simultaneously. To ensure maximal efficiency at each recursion the adaptive integrator compares retardations to the termination criterion individually and only the subset that fail have their integration refined.

Thus all retardations for an element pair are evaluated simultaneously. A new storage class was designed that stores these retardation sequences in the order they were generated; this is done efficiently by exploiting the fact that non-zero interactions always occur in adjacent sequences with respect to l (this pattern is depicted in Figure 3.25). The data structure comprises three arrays; the 'values' array is a double precision column vector containing all interaction coefficients stacked below each other. The 'start' and 'length' arrays are square, with number of rows and columns equal to the number of elements, and store the lowest non-zero retardation index (precision int16) and length of the sequence (precision int8) respectively. A Mex ('c' subroutine compiled for Matlab) implementation was created that executed the MOT solver directly from this storage class. Conversion to and from the sparse matrix representation used in the MOT equation was also implemented as M-files for comparison and verification.
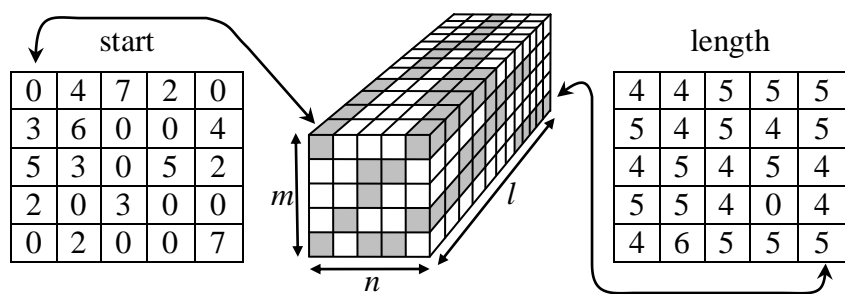
Figure 3.25: Pattern of non-zero interactions

One final issue facing adaptive integration is that the edge integrands in Equations 3.35 and 3.50 contain discontinuities due to the presence of the first derivative of the temporal basis function. The adaptive integrator will expend considerable effort trying

to integrate this discontinuity as if it were a smooth, albeit rapidly varying, quantity. It is more efficient to locate the intersections of discontinuities and edges and integrate each continuous edge section separately and sum the results.

3.2.2 Comparison with Gaussian integrands

The accuracy and correctness of the new integration scheme must now be verified. This is done by examining the convergence of Monte Carlo integration to the contour result.

3.2.2.1 Monte Carlo convergence

Figure 3.26 and Figure 3.27 show the convergence of Monte Carlo integration to the contour integration result for interaction between the same adjacent element pair used in section 1.1.1. Δ_t has been chosen such that $c\Delta_t = 0.16\text{m}$ and no discontinuities intersect S_n. Some retardations have not fully converged, indicating the accuracy of the contour integration is better than the Monte Carlo, but all retardations achieve accuracy significantly better than 1% for both $L_p\{\ldots\}$ and $L_v\{\ldots\}$. This demonstrates the excellent accuracy of the contour integration implementation for elements not intersecting discontinuities.

Figure 3.28 and Figure 3.29 show the same convergence scenario with Δ_t adjusted such that $c\Delta_t = 0.08\text{m}$ so a discontinuity does intersect S_n. For both $L_p\{\ldots\}$ and $L_v\{\ldots\}$ integrands the error of the contour integration is chronic; this must be associated with the presence of the discontinuity as accuracy was excellent in the continuous case. The derivation of the contour integration scheme will now be revisited to establish and cure the source of these errors.
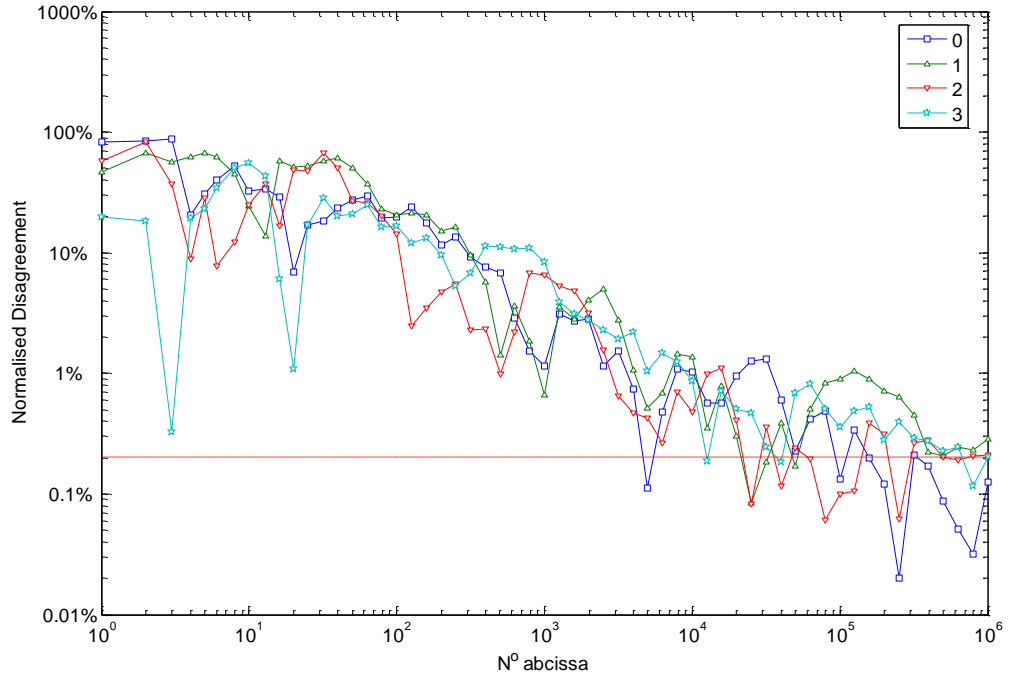
Figure 3.26: $L_p\{...\}$ Monte Carlo convergence to contour result, $c\Delta_t = 0.16\text{m}$.
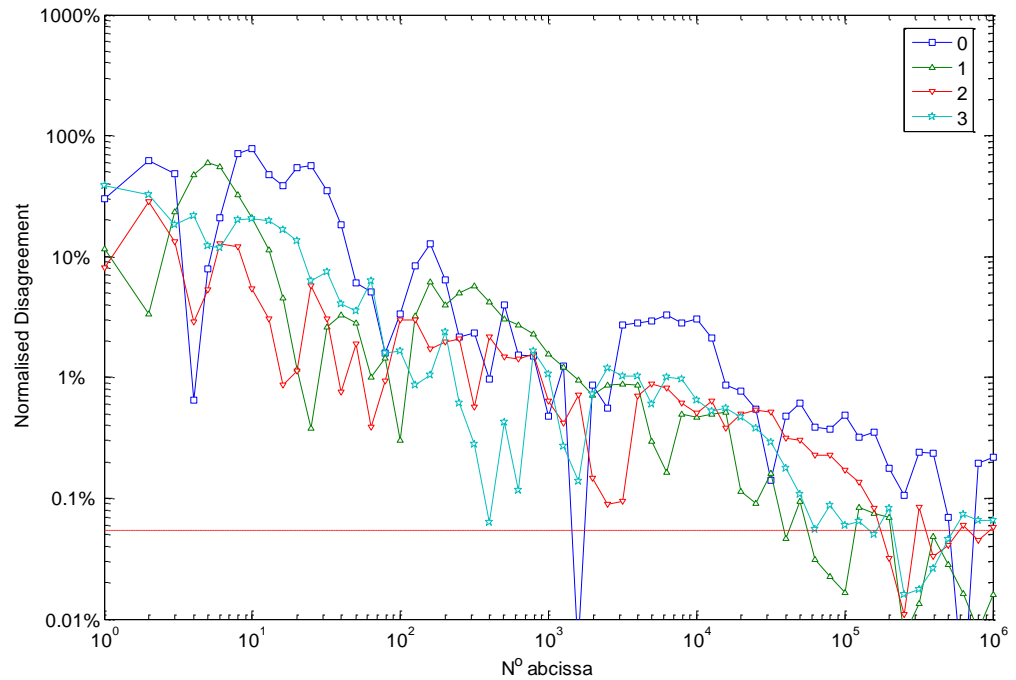
Figure 3.27: $L_v\{...\}$ Monte Carlo convergence to contour result, $c\Delta_t = 0.16\text{m}$.
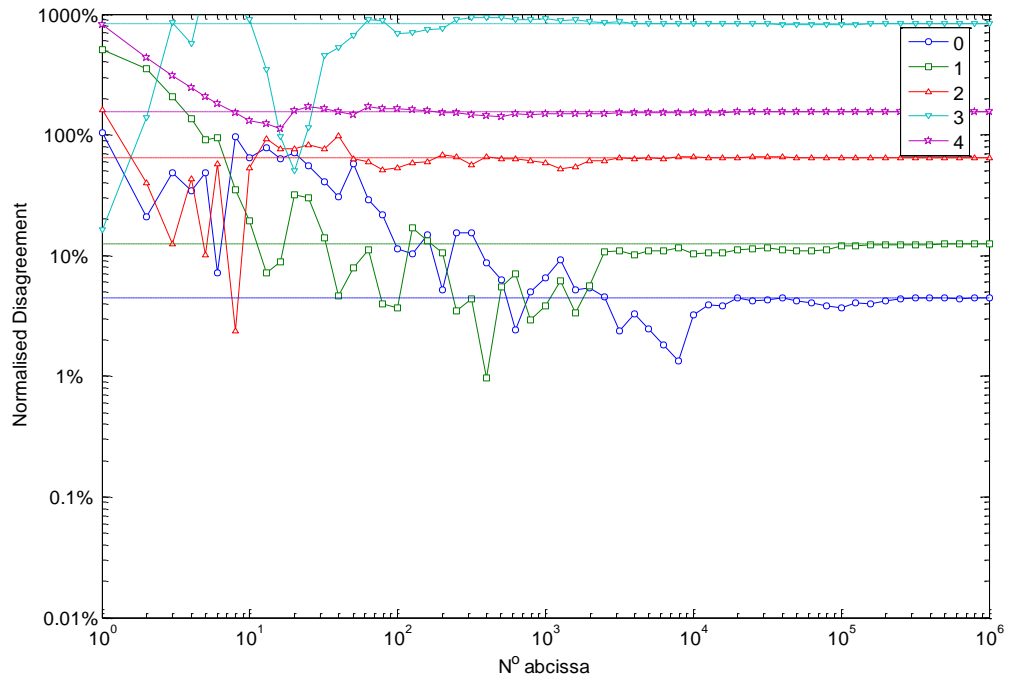
Figure 3.28: $L_p\{...\}$ Monte Carlo convergence to contour result, $c\Delta_t = 0.08$m
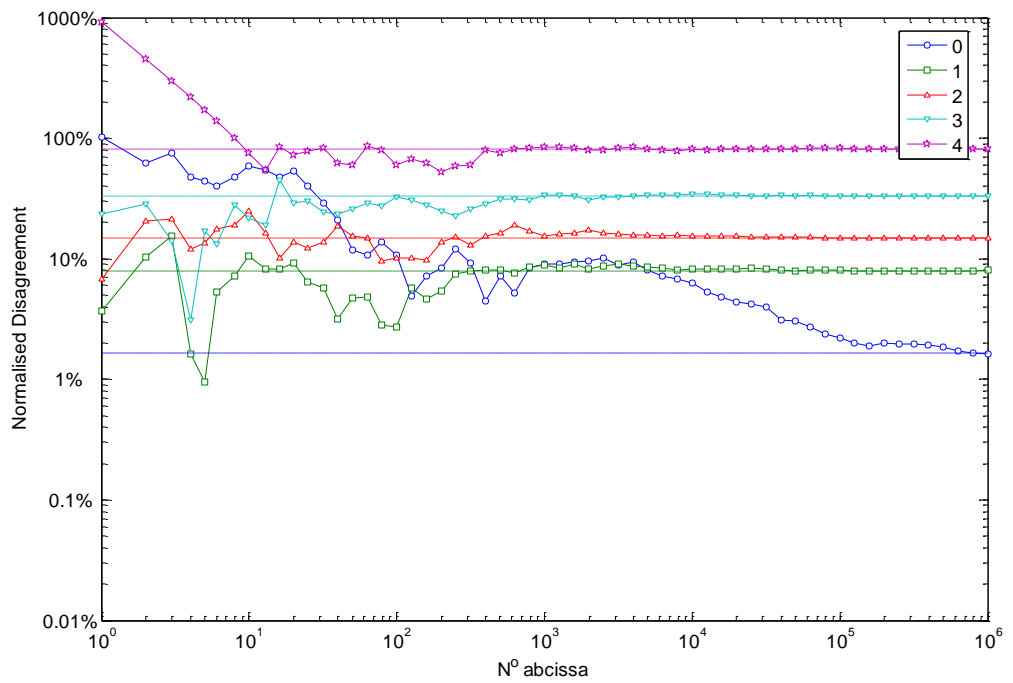
Figure 3.29: $L_v\{...\}$ Monte Carlo convergence to contour result, $c\Delta_t = 0.08$m

3.2.2.2 Modifications to the contour integration derivation

The derivation in section 3.2.1 is correct so some difference between it and the derivation of the Gaussian integrands must be causing the discrepancy in Figure 3.28 and Figure 3.29. One fundamental difference is that in the Gaussian implementation spatial derivatives are evaluated as temporal derivatives, where as in the new scheme they are mostly kept as derivatives with respect to R, the intention being to remove them by analytic integration after a change of coordinates.

If, instead of starting the contour integration derivation from the KIE, it is started from the Gaussian integrands a slightly different algorithm arises. In section 3.2.2.4 it will be shown that Equations 3.52 and 3.53 only hold for continuous regions of the integrand. This means that when they are applied to the Gaussian integrands each continuous region must be converted to a contour integral separately; this is depicted in Figure 3.30 and written in Equations 3.54 and 3.55.

$$\frac{\ddot{\mathrm{T}}_{j-l}(\tau)}{cR} + \frac{\dot{\mathrm{T}}_{j-l}(\tau)}{R^2} = -\frac{\partial}{\partial R}\left[\frac{\dot{\mathrm{T}}_{j-l}(\tau)}{R}\right] \tag{3.52}$$

$$\frac{\ddot{\mathrm{T}}_{j-l}(\tau)}{c^2 R} + 3\frac{\dot{\mathrm{T}}_{j-l}(\tau)}{cR^2} + 3\frac{T_{j-l}(\tau)}{R^3} = -R\frac{\partial}{\partial R}\left[\frac{\dot{\mathrm{T}}_{j-l}(\tau)}{cR^2} + \frac{\mathrm{T}_{j-l}(\tau)}{R^3}\right] \tag{3.53}$$
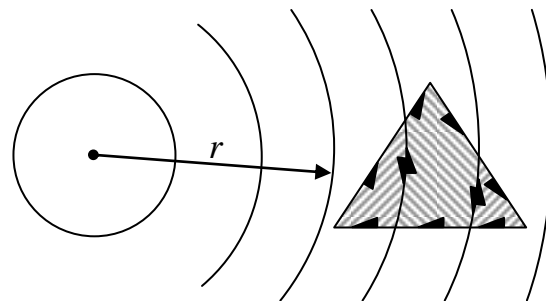
Figure 3.30: Continuous integration regions

$$L_p\{f_n(\mathbf{r})T_{j-l}(t)\}\Big|_{t=t_j;\mathbf{r}=\mathbf{r_m^c}} = \iint_{S_n} \frac{\hat{\mathbf{n}}'\cdot\bar{\mathbf{R}}}{4\pi}\left[\frac{\ddot{T}_{j-l}(\tau)}{cR} + \frac{\dot{T}_{j-l}(\tau)}{R^2}\right]d\mathbf{r}'$$

$$= -\sum_{\substack{\text{contiuous}\\ \text{regions}}} \iint_{\text{region}} \frac{z}{4\pi R}\frac{\partial}{\partial R}\left[\frac{\dot{T}_{j-l}(\tau)}{R}\right]d\mathbf{r}'$$

3.54

$$L_v\{f_n(\mathbf{r})T_{j-l}(t)\} = -\iint_{Sn}\left[\begin{array}{c}\dfrac{\hat{\mathbf{n}}\cdot\hat{\mathbf{n}}'}{4\pi}\left[\dfrac{\dot{T}_{j-l}(\tau)}{cR^2}+\dfrac{T_{j-l}(\tau)}{R^3}\right]\\[4mm] -\dfrac{\hat{\mathbf{n}}'\cdot\hat{\mathbf{R}}\hat{\mathbf{n}}\cdot\hat{\mathbf{R}}}{4\pi}\left[\dfrac{\ddot{T}_{j-l}(\tau)}{c^2R}+3\dfrac{\dot{T}_{j-l}(\tau)}{cR^2}+3\dfrac{T_{j-l}(\tau)}{R^3}\right]\end{array}\right]d\mathbf{r}'$$

$$= \sum_{\substack{\text{continuous}\\ \text{regions}}}\iint_{\text{region}}\left[\begin{array}{c}\dfrac{\hat{\mathbf{n}}\cdot\hat{\mathbf{n}}'}{4\pi R}\dfrac{\partial}{\partial R}\left[\dfrac{T_{j-l}(\tau)}{R}\right]\\[4mm] -R\dfrac{\hat{\mathbf{n}}'\cdot\hat{\mathbf{R}}\hat{\mathbf{n}}\cdot\hat{\mathbf{R}}}{4\pi}\dfrac{\partial}{\partial R}\left[\dfrac{\dot{T}_{j-l}(\tau)}{cR^2}+\dfrac{T_{j-l}(\tau)}{R^3}\right]\end{array}\right]d\mathbf{r}'$$

3.55

The crux of this change is that a contour integral around an element will be replaced by a summation of contour integrals around its continuous regions. The summation over regions is rearranged such that contributions from the region boundary sections lying along the discontinuities are separated from the sections lying on the edges of S_n. Due to there being two regions sharing a boundary along each discontinuity its contribution is the difference between the contour integrand in each region. The net result is the same as that which was derived in sections 3.2.1.2 and 3.2.1.3 plus extra terms contributed by the discontinuities.

$$\sum_{\text{regions}}\left[\int_{\theta_{\min}}^{\theta_{\max}}f(R_{\max}(\theta))d\theta - \int_{\theta_{\min}}^{\theta_{\max}}f(R_{\min}(\theta))d\theta\right]$$

$$= \sum_{\text{edges}}\sum_{\text{regions}}\int_{\mu_{lo}}^{\mu_{hi}}f(R(\mu))\frac{d\theta}{d\mu}d\mu + \sum_{\text{discontinuities}}\left[f_{\substack{\text{inner}\\ \text{region}}}(R) - f_{\substack{\text{outer}\\ \text{region}}}(R)\right]\theta_{included} - \theta_{origin}f(|z|)$$

3.56

The polar case is shown above. All integrands vary spatially with R only and, as R is constant on a discontinuity arc, integration along it with respect to θ is just multiplication by the total angle of the arc intersecting S_n, denoted $\theta_{included}$. $\theta_{included}$ is found by tabulating all angles where an arc crosses an edge. These are automatically in

ascending order due to the definition of the cylindrical polar coordinate system. An arc may enter and exit S_n up to six times if it is triangular, and each angle must be identified as an entry or exit point. In most cases this is straightforward as at least one pair of angles will occur on one edge; the first must be an exit point and the second an entry point, then other angles may be identified as they alternate along the table. In the remaining case where an arc intersects two edges once, $\theta_{included}$ is the acute angle:

$$\theta_{included} = \left|\text{wrap}(\theta_1 - \theta_2)\right| \qquad 3.57$$

Special care must be taken when an arc passes through a vertex as arc / edge intersections may be lost due to finite machine precision. To counteract this issue, the implementation adds extra angles to the table at any vertex that lies on (or very close to) an arc. A sort procedure is used to eliminate duplicate angles in the case that an odd number results. The angle table is implemented in Matlab by a cell array (similar to a hash table) with each cell corresponding to an edge / discontinuity pair and containing zero, one or two angles.

$$\sum_{regions}\left[\int_{w_{min}}^{w_{max}} f(R(v_{max}(w)))dw - \int_{w_{min}}^{w_{max}} f(R(v_{min}(w)))dw\right]$$
$$= \sum_{edges}\sum_{regions}\int_{\mu_{lo}}^{\mu_{hi}} f(R(v(\mu)))\frac{dw}{d\mu}d\mu + \sum_{discontinuities}\left[f_{\substack{lower\\region}}(R) - f_{\substack{upper\\region}}(R)\right]\left|w_{included}\right| \qquad 3.58$$

The Cartesian integral above is rearranged in the same way as Equation 3.56. The lower and upper regions are respectively below and above the discontinuity with respect to v. As all integrands are functions of R only and along a discontinuity arc R is constant, integration with respect to w is just multiplication by the total length with respect to w of the arc intersecting S_n, denoted $w_{included}$ and easily found from the angle table according to Equation 3.59. It is also convenient for implementation that due to the definition of the axis systems Equation 3.60 holds. In the case where an arc intersects two edges once Equation 3.61 is used.

$$w_{included} = \sum_{\substack{arc\ pieces}} [\sin(\theta_{outward}) - \sin(\theta_{inward})] \qquad 3.59$$

$$\left[f_{\substack{lower\\region}}(R) - f_{\substack{upper\\region}}(R) \right] |w_{included}| = \left[f_{\substack{inner\\region}}(R) - f_{\substack{outer\\region}}(R) \right] w_{included} \qquad 3.60$$

$$w_{included} = |\sin(\theta_1) - \sin(\theta_2)| \operatorname{sign}(\cos(\operatorname{mean}(\theta_1, \theta_2))) \qquad 3.61$$

The scattered velocity potential statement is not affected by these complications as its contour integrand is continuous. If the derivation of the contour integrals for $L_p\{...\}$ and $L_v\{...\}$ is repeated for each continuous region separately, application of the identities derived in this section produces Equations 3.62 and 3.63 respectively. Recalling from section 3.2.1.9 that the adaptive integrator was implemented to integrate each continuous region of the edge separately, this modified scheme is identical to the scheme of section 3.2.1 with the addition of contributions from the discontinuities. As it is derived from the point-wise integrands it should agree with them under Monte Carlo integration.

$$L_p\left\{f_n(\mathbf{r})T_{j-l}(t)\right\}\Big|_{t=t_j;\mathbf{r}=\mathbf{r_m^c}} = \begin{bmatrix} -\displaystyle\sum_{\substack{edges}}\sum_{\substack{regions}} \left[\dfrac{z}{4\pi} \int_{\mu_{lo}}^{\mu_{hi}} \dfrac{\dot{T}_{j-l}(\tau)}{R} \dfrac{d\theta}{d\mu} d\mu \right] \\[4mm] -\displaystyle\sum_{\substack{discontinuities}} \dfrac{z}{4\pi R} \left[\dot{T}_{j-l}(\tau)\right]_{\substack{outer\\region}}^{\substack{inner\\region}} \theta_{included} \\[4mm] +\dfrac{\theta_{origin}}{4\pi} \dfrac{z}{|z|} \dot{T}_{j-l}\left(t_j - \dfrac{|z|}{c}\right) \end{bmatrix} \qquad 3.62$$

$$L_v\left\{f_n(\mathbf{r})T_{j-l}(t)\right\} = \left[\begin{array}{l} \displaystyle\sum_{\text{edges}}\sum_{\text{regions}}\left(\begin{array}{l} \dfrac{\hat{\mathbf{n}}\cdot\hat{\mathbf{n}}'}{4\pi}\displaystyle\int_{\mu_{lo}}^{\mu_{hi}}\left[\dfrac{T_{j-l}(\tau)}{R} - z^2\dfrac{\dot{T}_{j-l}(\tau)}{cR^2} - z^2\dfrac{T_{j-l}(\tau)}{R^3}\right]\dfrac{d\theta}{d\mu}d\mu \\[2em] + \dfrac{z\hat{\mathbf{n}}\cdot\hat{\mathbf{v}}}{4\pi}\displaystyle\int_0^1\left[\dfrac{\dot{T}_{j-l}(\tau)}{cR^2} + \dfrac{T_{j-l}(\tau)}{R^3}\right]\dfrac{dw}{d\mu}d\mu \end{array}\right) \\[4em] + \displaystyle\sum_{\text{discontinuities}}\left(\begin{array}{l} \dfrac{z\hat{\mathbf{n}}\cdot\hat{\mathbf{v}}}{4\pi}\left[\dfrac{\dot{T}_{j-l}(\tau)}{cR^2}\right]_{\substack{\text{outer}\\\text{region}}}^{\substack{\text{inner}\\\text{region}}}w_{included} \\[2.5em] - \dfrac{z^2\hat{\mathbf{n}}\cdot\hat{\mathbf{n}}'}{4\pi}\left[\dfrac{\dot{T}_{j-l}(\tau)}{cR^2}\right]_{\substack{\text{outer}\\\text{region}}}^{\substack{\text{inner}\\\text{region}}}\theta_{included} \end{array}\right) \\[4em] + \theta_{included}\dfrac{\hat{\mathbf{n}}\cdot\hat{\mathbf{n}}'}{4\pi c}\dot{T}_{j-l}\left(t_j - \dfrac{|z|}{c}\right) \end{array}\right] \qquad 3.63$$

3.2.2.3 Monte Carlo convergence

The Monte Carlo convergence procedure is performed as sections 1.1.1 and 3.2.2.1 and the results are shown below. Δ_t is chosen such that $c\Delta_t = 0.08\text{m}$ and a discontinuity intersects S_n. Accuracy is excellent with all errors less than 1%. The $L_p\{\ldots\}$ $l = 3$ result is above the trend simply because it contains a large discontinuity that the Monte Carlo integrates very inaccurately. However, the convergence still demonstrates that the modified contour result is performing well. The results for $c\Delta_t = 0.16\text{m}$ are not shown; they are identical to Figure 3.26 and Figure 3.27 because there are no additional terms.

The modified scheme is now verified against point-wise integration. It should be noted that in addition to the shown convergence results, convergence was examined on larger meshes. As the recognition process could not be reliably automated, this was achieved efficiently by identifying element pairs for which the contour scheme disagreed significantly with the Gaussian scheme and examining those manually. As the scheme of section 3.2.1 may be recovered by simply removing the discontinuity contributions introduced in 3.2.2.2, it too may be considered verified against its definition.
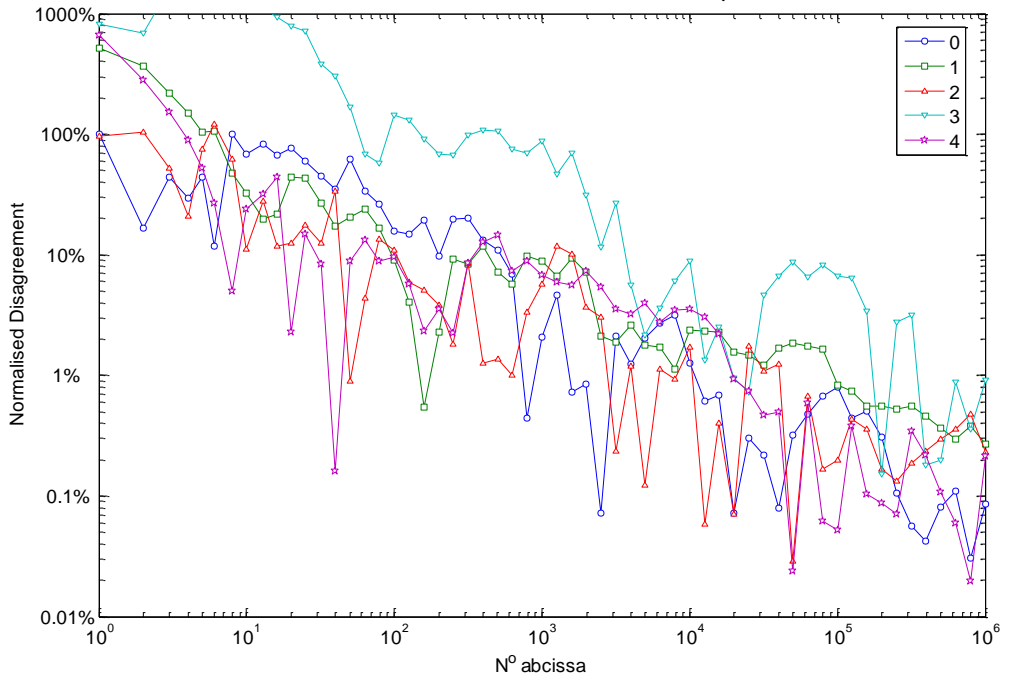
Figure 3.31: $L_p\{\ldots\}$ Monte Carlo convergence to contour result, $c\Delta_t = 0.08$m
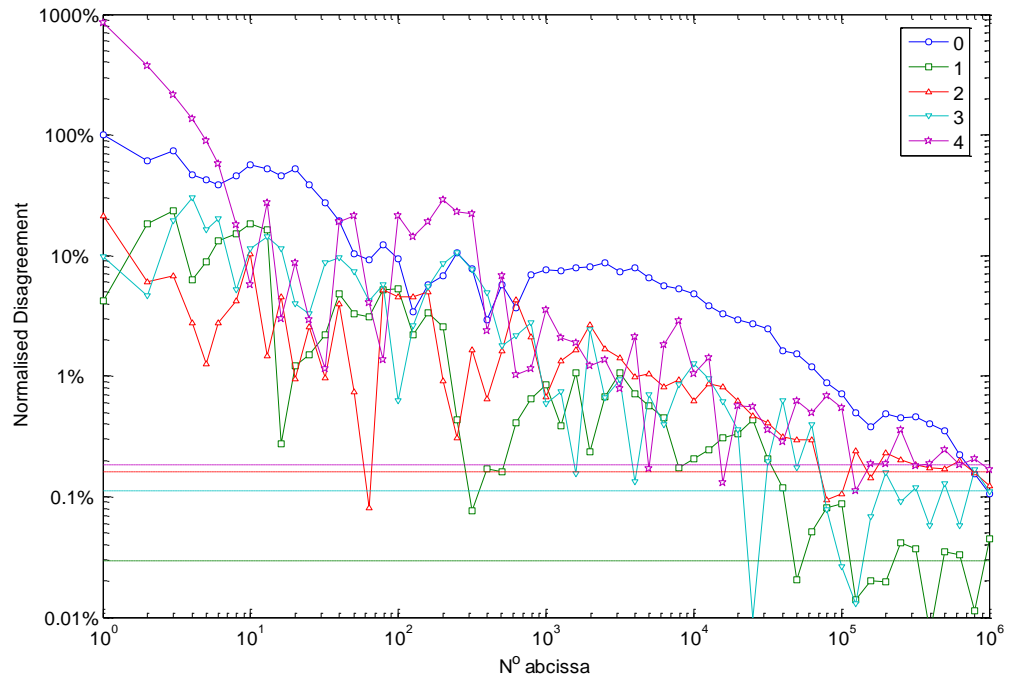
Figure 3.32: $L_v\{\ldots\}$ Monte Carlo convergence to contour result, $c\Delta_t = 0.08$m

Table 3.3 and Table 3.4 respectively give the disagreement between the three integration schemes for $L_p\{\ldots\}$ and $L_v\{\ldots\}$ when the time-step duration is chosen such that $c\Delta_t = 0.08\text{m}$. In each case the disagreement between the schemes is normalised to the contour integration scheme to give relative disagreement as a percentage. Significant disagreement appears between the Gaussian scheme and the contour with discontinuity terms scheme only for $L_p\{\ldots\}$ with $l = 3$ and $L_v\{\ldots\}$ with $l = 0$; both of these disagreements are due to the error of the Gaussian scheme as was discussed in section 1.1.1. Massive disagreement appears between the Gaussian scheme and the contour without discontinuity terms scheme. The effect of these errors on overall system accuracy and stability will be investigated in section 3.3.

Table 3.3: Integration disagreement for $L_p\{\ldots\}$, $c\Delta_t = 0.08\text{m}$

l	Gaussian versus contour with discontinuity terms	Gaussian versus contour without discontinuity terms
0	0.51%	3.82%
1	0.65%	10.75%
2	1.40%	38.34%
3	10.20%	112.26%
4	1.20%	276.01%

Table 3.4: Integration disagreement on $L_v\{\ldots\}$, $c\Delta_t = 0.08\text{m}$

l	Gaussian versus contour with discontinuity terms	Gaussian versus contour without discontinuity terms
0	3.46%	1.93%
1	0.21%	8.86%
2	0.18%	17.46%
3	0.06%	49.80%
4	0.34%	440.63%

3.2.2.4 Inadequacy of point-wise integration

Presently there are two contour integration schemes, one derived directly from KIE and another derived from the point-wise integrands, which disagree and agree with them respectively. The important question is which is a more accurate evaluation of the integrals in the discretised KIE?

The shortcoming lies in the combination of the temporal basis function choice and point-wise integration. The first derivative of the mother temporal basis function (Equation 3.12 and Figure 3.6) contains discontinuities. The upper (+) and lower (-) piece values for each discontinuity are summarised in Table 3.5. This suggests the decomposition of $T'_{mother}(\varsigma)$ into a continuous piecewise polynomial plus a sum of heavy-side functions to encapsulate the discontinuities; this in done in Equation 3.64 and shown in Figure 3.34.

The second derivative may be decomposed in the same way; this is done in Equation 3.65 and shown in Figure 3.33. The piecewise polynomial in Equation 3.64 gives rise to a new piecewise polynomial and a new sum of heavy-side functions. The heavy-side functions become delta functions.

Table 3.5: Discontinuities in first derivative of mother temporal basis function

ς	-1	0	1	2	3
$T'^{+}_{mother}(\varsigma)$	$\frac{1}{3}$	$\frac{1}{2}$	-1	$\frac{1}{6}$	0
$T'^{-}_{mother}(\varsigma)$	0	$1\frac{1}{6}$	-3	$\frac{3}{2}$	$-\frac{1}{3}$
$T'^{+}_{mother}(\varsigma) - T'^{-}_{mother}(\varsigma)$	$\frac{1}{3}$	$-\frac{4}{3}$	2	$-\frac{4}{3}$	$\frac{1}{3}$

$$T'_{mother}(\varsigma) = H_1(\varsigma) + P_1(\varsigma)$$

$$H_1(\varsigma) = \tfrac{1}{3}H(\varsigma+1) - \tfrac{4}{3}H(\varsigma) + 2H(\varsigma-1) - \tfrac{4}{3}H(\varsigma-2) + \tfrac{1}{3}H(\varsigma-3)$$

$$P_1(\varsigma) = \begin{cases} \dfrac{3}{2} + 2\varsigma + \dfrac{1}{2}\varsigma^2 & -1 \le \varsigma \le 0 \\[2mm] \dfrac{3}{2} - 2\varsigma - \dfrac{3}{2}\varsigma^2 & 0 \le \varsigma \le 1 \\[2mm] -\dfrac{3}{2} - 2\varsigma + \dfrac{3}{2}\varsigma^2 & 1 \le \varsigma \le 2 \\[2mm] -\dfrac{3}{2} + 2\varsigma - \dfrac{1}{2}\varsigma^2 & 2 \le \varsigma \le 3 \\[2mm] 0 & \text{elsewhere} \end{cases}$$

3.64

$$T''_{mother}(\varsigma) = \delta_2(\varsigma) + H_2(\varsigma) + P_2(\varsigma)$$

$$\delta_2(\varsigma) = \tfrac{1}{3}\delta(\varsigma+1) - \tfrac{4}{3}\delta(\varsigma) + 2\delta(\varsigma-1) - \tfrac{4}{3}\delta(\varsigma-2) + \tfrac{1}{3}\delta(\varsigma-3)$$

$$H_2(\varsigma) = H(\varsigma+1) - 4H(\varsigma) + 6H(\varsigma-1) - 4H(\varsigma-2) + H(\varsigma-3)$$

$$P_2(\varsigma) = \begin{cases} 1+\varsigma & -1 \le \varsigma \le 0 \\ 1-3\varsigma & 0 \le \varsigma \le 1 \\ -5+3\varsigma & 1 \le \varsigma \le 2 \\ 3-\varsigma & 2 \le \varsigma \le 3 \\ 0 & \text{elsewhere} \end{cases}$$

3.65

These decompositions cast new light on the performance of Gaussian integration on the $L_p\{...\}$ and $L_v\{...\}$ integrands. The piecewise polynomial parts are not the integrand Gaussian integration is optimised for, but they are continuous and low order within each part so error is expected to be low. The sums of heavy-side functions are responsible for the discontinuities seen in the integrands and are very poorly integrated by a Gaussian scheme; where the abscissa fall in relation to the discontinuities massively affects the result.
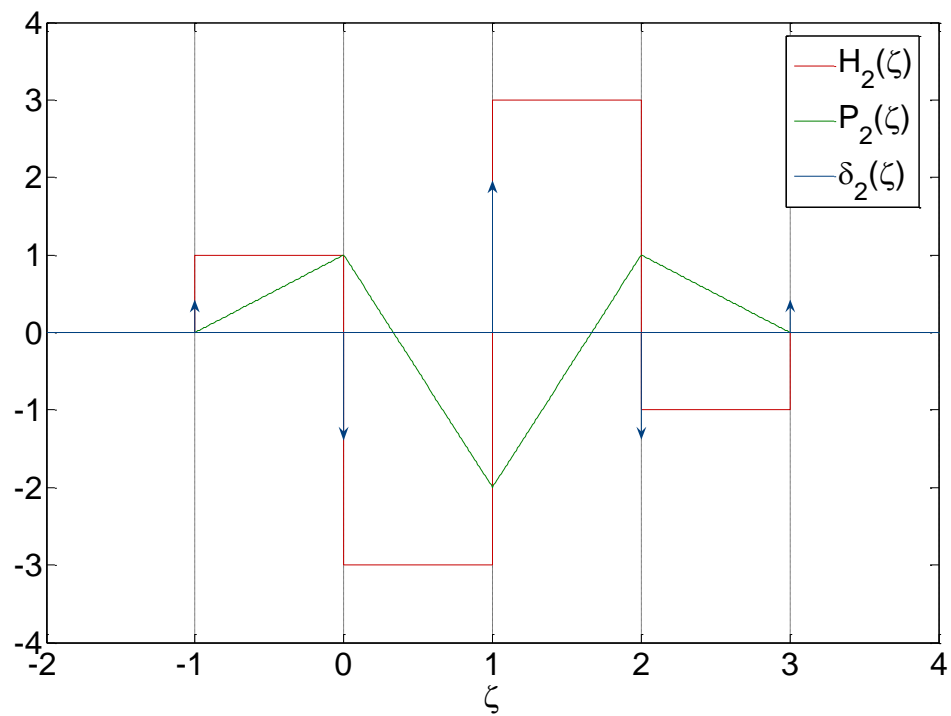
Figure 3.33: Decomposition of $\mathrm{T}''_{mother}(\varsigma)$
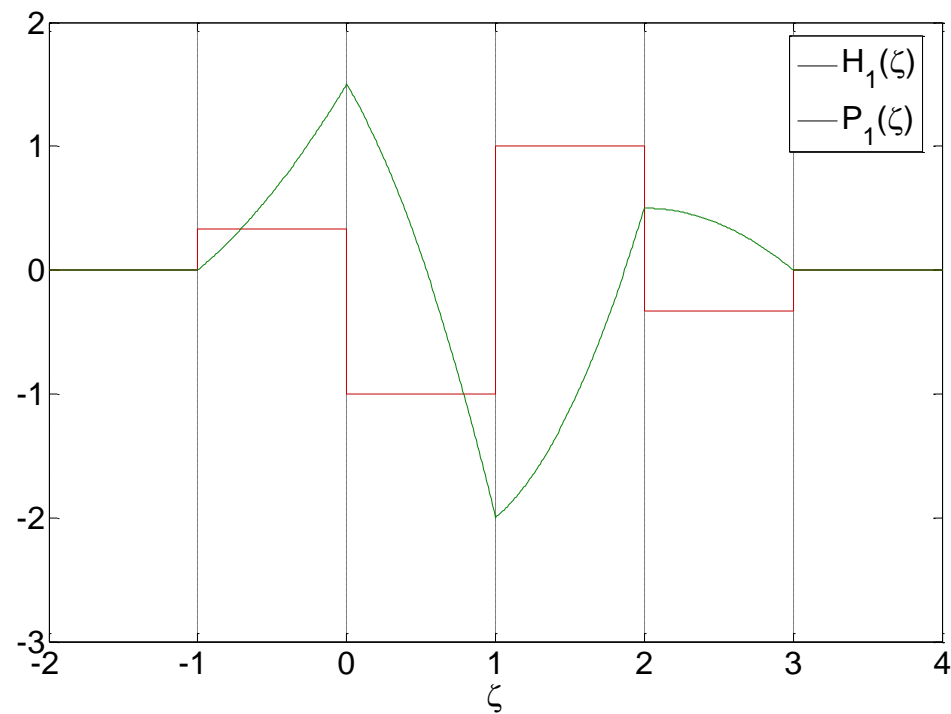
Figure 3.34: Decomposition of $\mathrm{T}'_{mother}(\varsigma)$

The delta functions present in the second derivative have been entirely omitted in previous statements. Their presence indicates that the $L_p\{...\}$ and $L_v\{...\}$ integrands are in fact infinite valued along the discontinuities, as depicted below. Such a function could never be integrated accurately by a point-wise integration scheme, regardless of the number of abscissa, as any abscissa falling near the delta functions will either miss or be infinite valued; both scenarios fail to characterise the step in first derivative from which these delta functions arise. In fact, they cancel out the discontinuity terms added to the contour integration implementation, meaning that it is the original contour integration implementation (without discontinuities) that correctly integrates the discretised KIE.
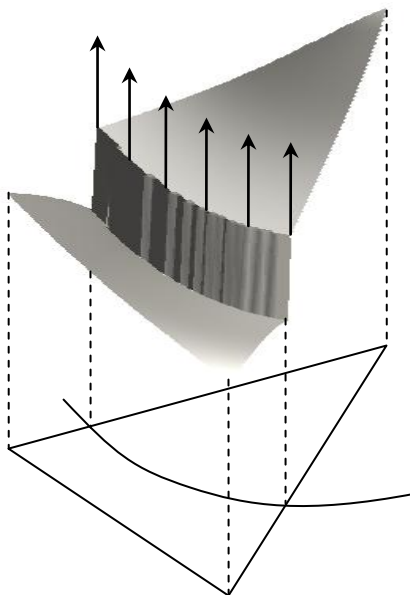
Figure 3.35: Gaussian integrands are infinite at discontinuities

Ergin *et al* do not specify exactly what expressions they used to evaluate these temporal derivatives in their implementation, but given they chose Gaussian integration it is unlikely that these would include the delta functions above. This means their scheme is not integrating the spatial derivatives they say but something subtly different. Evaluation of this erroneous integral by contour integration requires the addition of the discontinuity contributions introduced in section 3.2.2.2. By contrast, the integration scheme derived in section 3.2.1 correctly integrates the discretised KIE and possesses a

simpler implementation. The latter is regarded as the 'correct' integration scheme, and the effects of its use on accuracy and stability will be investigated in the next section.

3.3 Numerical examples

In this section the effect of integration accuracy on solution accuracy and system stability will be investigated for two meshes. These meshes have been chosen with contrasting geometrically complexity; the first is a uniformly meshed sphere, the second is a two-dimensional primitive root diffuser known as skyline. Both meshes have a relatively small number of elements so that the magnitude of the largest pole of the resulting MOT system of equations can be calculated to characterise system stability. Solution accuracy will be calculated by comparison to a previously verified frequency domain BEM (RADDIFF.exe) at the principle frequency of excitation using the DFT. This BEM is implemented according to Terai's [64] 1980 paper.

The time domain BEM model will be executed with a variety of time-step values and excitation signals. Temporal discretisation is characterised by the implicitness of the time-step duration, being the ratio between the distance sound travels in a time-step and the largest element dimension (3.66). This choice, in preference to the CFL parameter (Equation 2.34), is motivated by the phase-change argument in section 2.2.5 and produces a fairer comparison between the two meshes.

$$\frac{c\Delta_t}{\max\limits_{S_n \in mesh} \max\limits_{\mathbf{r},\mathbf{r}' \in \partial S_n} |\mathbf{r} - \mathbf{r}'|} \qquad 3.66$$

The excitation signal will be a sine wave propagated from a point source and the solution duration is chosen such that the system reaches steady state and any instability has the opportunity to appear. This is clearly an inefficient application of the time domain BEM but was found to be necessary to make error between it and the frequency domain implementation small enough that fluctuations due to temporal discretisation could be observed. Additionally, the frequency domain BEM solution is approximate and its inherent error will limit the best model agreement that can be achieved. The

excitation signal has no effect on inherent system stability but the observed stability may differ in accordance with the extent to which the respective resonant mode is excited. The combined field operator ($\alpha = \frac{1}{2}$) was used in all models.

Results are displayed for both meshes as follows. There are three integration types and disagreement will be plotted for two pairs. The first plot will show the disagreement between the contour integration scheme with and without discontinuity terms; this is error caused by omission of the delta function terms from the second derivative of the temporal basis function. The second plot will show the disagreement between the contour integration scheme with discontinuity terms and the Gaussian scheme; this describes the error caused by integrating a discontinuous, singular integrand with a Gauss-Legendre rule. Both plots will comprise histograms for each time-step duration modelled. The height of a bin is the number of element interactions that fall into it as a percentage of the total number of non-zero interactions at that time-step duration. Bin edges are logarithmically spaced, but the error axis is also logarithmically spaced hence the area of each bin represents the percentage of interactions in it. Absolute disagreement magnitude is used as the bin criteria in preference to relative (percentage) disagreement as the former favourably displays larger magnitude interactions which are more significant in the solution, while the latter has the pitfall that errors on insignificant interactions are inflated by the small magnitude of their correct values. When analysing the histograms it should be remembered that both meshes' interaction coefficients typically have magnitudes between 10^3 and 10^{-3},

Stability will be characterised by plots of the two largest SEM poles of the MOT process versus implicitness.

Surface sound error between the time domain BEM and the frequency domain BEM is calculated from the respective source to surface element transfer function at the excitation frequency. In the frequency domain this is simply the element pressure divided by the source monopole pressure (Equation 3.67). In the time domain it is found by division of the DFT of the surface velocity potential by the DFT of the source monopole potential (Equation 3.68); complex conjugates are taken because this thesis

uses $\varphi^t(\mathbf{r},t) = \mathrm{Re}\!\left[\Phi(\mathbf{r})e^{-i\omega t}\right]$ whereas the Matlab implementation of the DFT uses $\varphi^t(\mathbf{r},t) = \mathrm{Re}\!\left[\Phi(\mathbf{r})e^{i\omega t}\right]$. The first 50β (defined below) iterations are omitted from the DFT to allow the time domain solution to reach steady state. The next 100β iterations are chosen for DFT; this length maintains periodicity and eliminates windowing error. The surface sound error is calculated as the spatial mean magnitude of the difference between H_{FD} and H_{TD}, normalised to the spatial mean magnitude of H_{FD} (Equation 3.69) and is written as a percentage. This is displayed for each integration type as a contour plot verses time-step implicitness and temporal resolution $\beta = 2\pi(\Delta_t \omega)^{-1}$.

$$\mathrm{H}_{FD}\!\left(\mathbf{r}_{source}, \mathbf{r}_m^c, \omega\right) = \frac{P\!\left(\mathbf{r}_m^c, \omega\right)}{P_{source}} \qquad\qquad 3.67$$

$$\mathrm{H}_{TD}\!\left(\mathbf{r}_{source}, \mathbf{r}_m^c, \omega\right) = \frac{\overline{F\!\left\{\varphi_t\!\left(\mathbf{r}_m^c, t\right)\right\}(\omega)}}{F\!\left\{\varphi_{source}(t)\right\}(\omega)} \qquad\qquad 3.68$$

$$error = \frac{\displaystyle\sum_{m=1}^{N_S}\left|\mathrm{H}_{TD}\!\left(\mathbf{r}_{source}, \mathbf{r}_m^c, \omega\right) - \mathrm{H}_{FD}\!\left(\mathbf{r}_{source}, \mathbf{r}_m^c, \omega\right)\right|}{\displaystyle\sum_{m=1}^{N_S}\left|\mathrm{H}_{FD}\!\left(\mathbf{r}_{source}, \mathbf{r}_m^c, \omega\right)\right|} \qquad\qquad 3.69$$

3.3.1 Spherical mesh

This mesh is of a 1m radius sphere using 270 flat triangular elements. It can be seen from Figure 3.36 that the mesh is quite regular with no elements having a skewed aspect ratio or being at right angles to a neighbour. As the surface is entirely convex the poles of its physical response are likely to be well damped. The point source is located 100m distant.
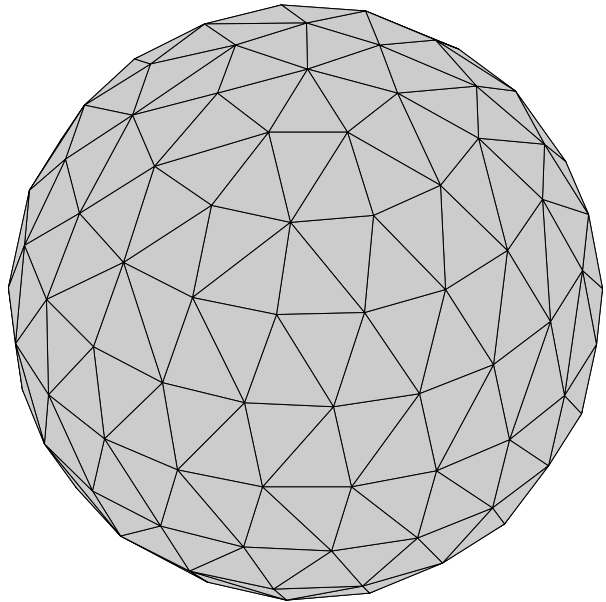
Figure 3.36: The spherical mesh

Figure 3.37 shows the error of the contour integration scheme with discontinuities components compared to the implementation without; this is the error caused by omission of the delta functions from the second derivative of the temporal basis function. These errors are towards the bottom of the figure so are of large magnitude. On the left of the figure where the time-step is most explicit these errors occur for the majority of element interactions due to the density of discontinuities. By contrast, on the right of the figure error is zero as the time-step multiplied by the celerity spans the entire mesh and no discontinuities intersect any element.
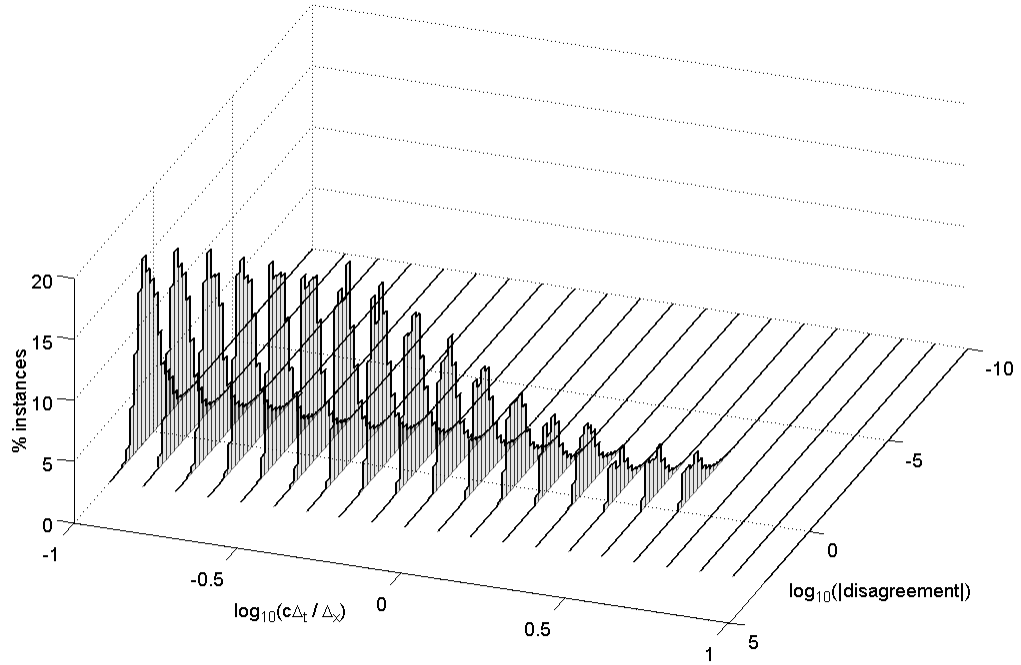
Figure 3.37: Disagreement populations between the spherical mesh interaction coefficients, as calculated by the two contour integration schemes, versus time-step implicitness

Figure 3.38 shows the disagreement between the Gaussian scheme and the contour integration scheme with discontinuity components, which correctly evaluates the numerical integrands of the former; this is error caused by using Gaussian integration to integrate a discontinuous singular integrand. Two error mechanisms with defined ridges can be observed. At explicit time-steps (left) there is a high density of discontinuities intersecting the mesh and error associated with these dominates. Moving to the right the discontinuity density approaches zero revealing the, previously masked, error due to the singularity of the integrand. This latter mechanism is of spatial origin and occurs for all time-step durations. However it predominately results in errors smaller than 10^{-5} hence is deemed insignificant for this mesh.
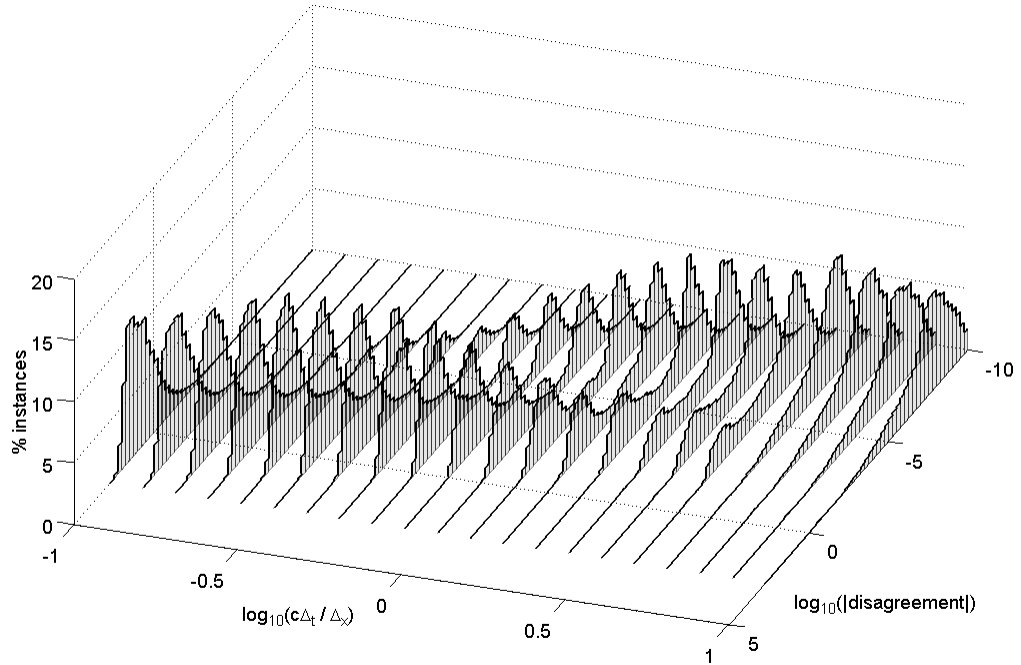
Figure 3.38: Disagreement populations between the spherical mesh interaction coefficients, as calculated by the contour integration scheme without discontinuity terms and the Gaussian scheme, versus time-step implicitness

Figure 3.39 shows the magnitude of the largest two SEM poles versus time-step. The dominant observation is that there always seems to be a pole with magnitude close to one. This characteristic occurs because the scatterer is a passive body: Devoid of excitation the system remains silent. Silence implies zero pressure (relative to atmospheric) and this implies constant velocity potential. Thus the system must be able to exist in a non-zero steady state and this requires the MOT equation to possess an eigenmode with an eigenvalue of unity. Numerical experiments suggest that this eigenmode is primarily associated with the self-interaction coefficients.

The largest poles (solid lines) of the three sets of interaction matrices deviate little with Δ_t, so seem unaffected by the large integration errors seen in the previous figures. The largest pole of the Gaussian implementation reduces marginally at implicit Δ_t but this is dismissed as a numerical quirk. The second largest poles (dashed lines) reduce in magnitude as Δ_t becomes more implicit, supporting those in section 2.2.5 that believe

117

implicitness improves stability. It is encouraging to see the 'correct' contour integration scheme achieving the best stability in the middle of the time-step range.
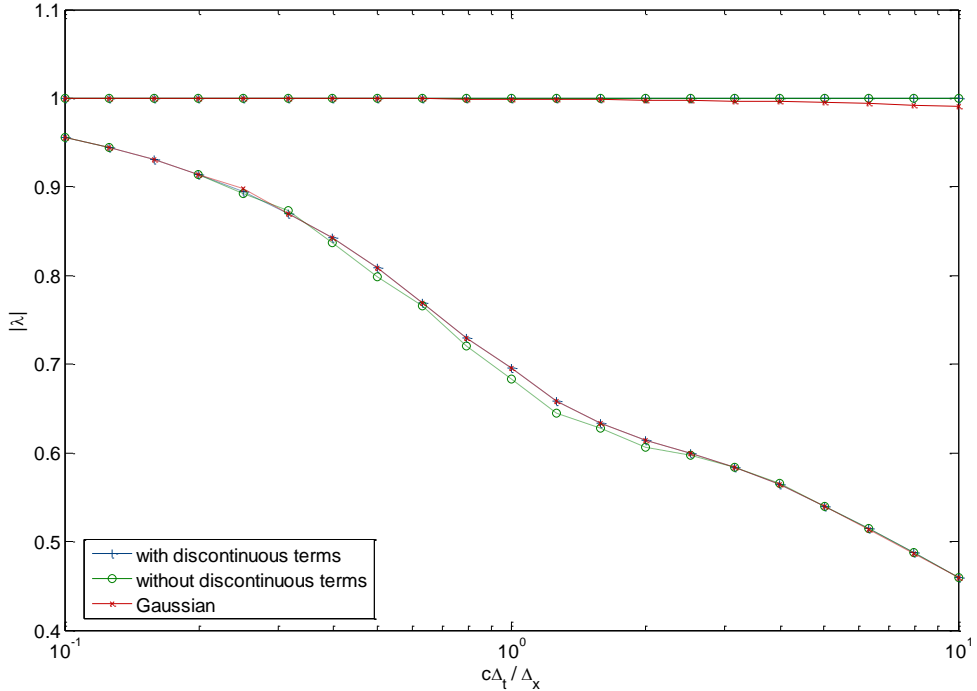
Figure 3.39: Stability trends on the spherical mesh characterised by the largest two poles versus time-step implicitness for each integration scheme

Figure 3.40, Figure 3.41 and Figure 3.42 show the error versus the frequency domain BEM model for contour integration without discontinuities, contour integration with discontinuities, and the Gaussian scheme respectively. The grey shaded area indicates $\Delta_x > \frac{\lambda}{8}$ so spatial discretisation error is expected.

All three figures show the same trend; error reduces with increased β as expected from the discretisation scheme, and also as Δ_t becomes more implicit in harmony with Herman and van den Berg's [36] results. Error seems to hit a floor at around 1%, likely due to error inherent to the numerical implementations or the comparison process. Despite the considerable integration discrepancies shown above there is are no significant differences between the surface error trends, so any time domain errors must be masked by the error floor.
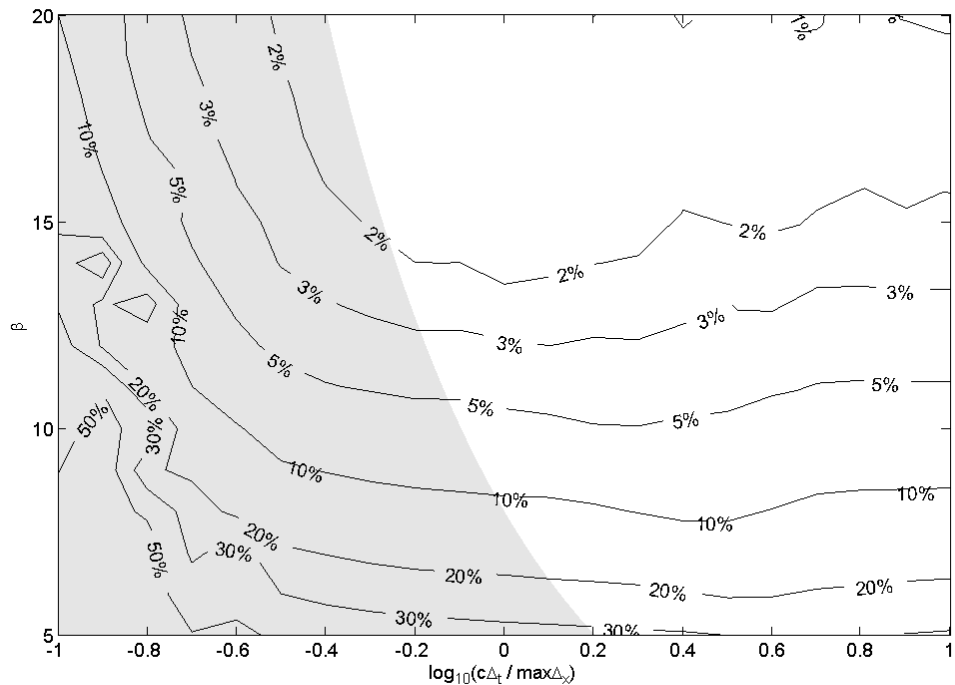
Figure 3.40: Surface error on the spherical mesh versus temporal resolution and implicitness when interactions are calculated by the contour integration scheme without the discontinuity terms
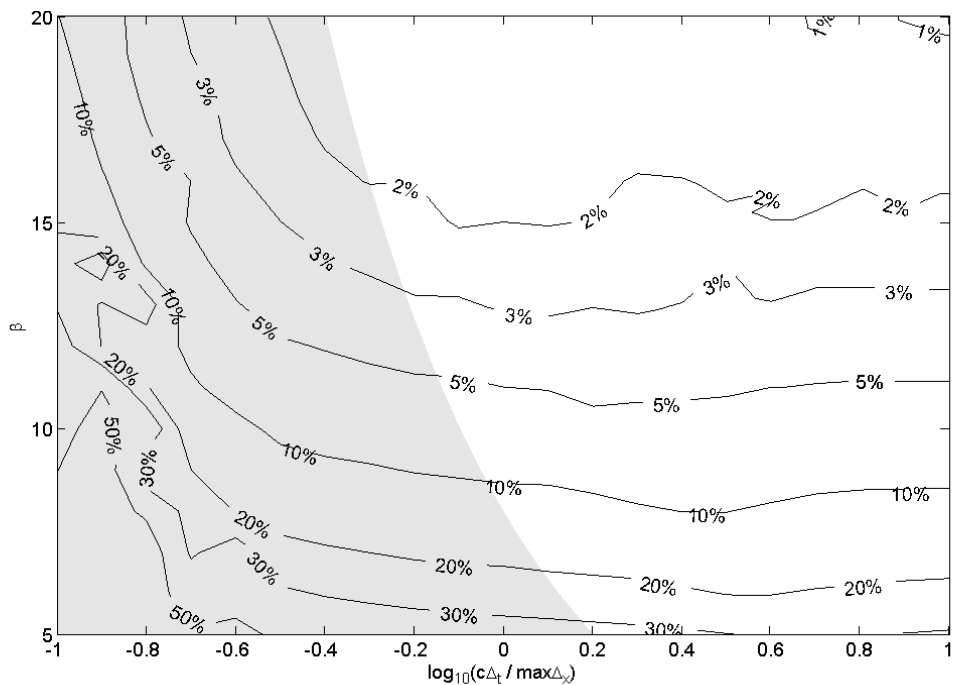
Figure 3.41: Surface error on the spherical mesh versus temporal resolution and implicitness when interactions are calculated by the contour integration scheme with the discontinuity terms
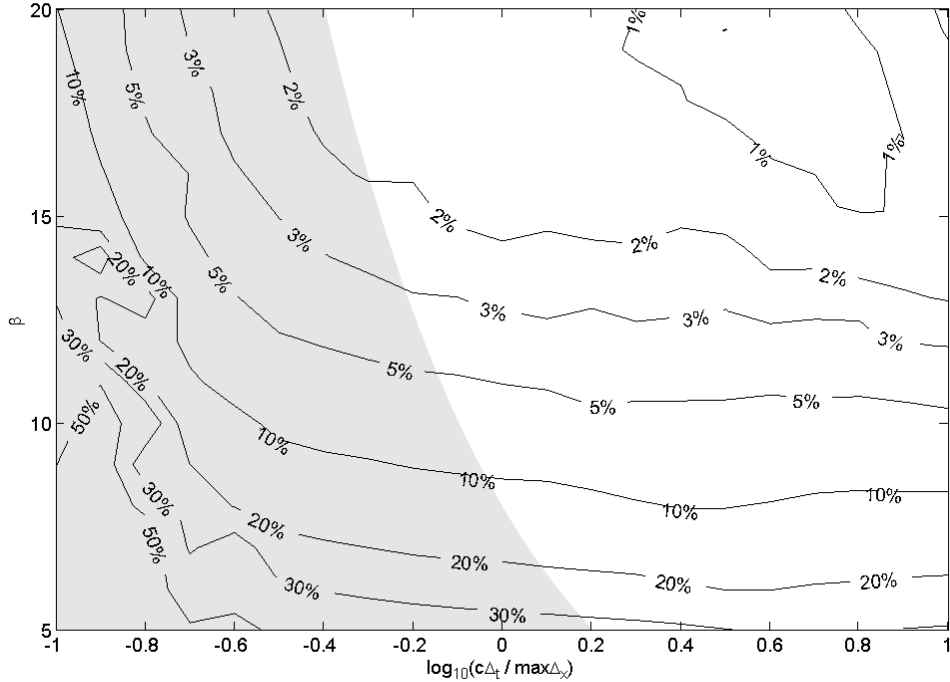
Figure 3.42: Surface error on the spherical mesh versus temporal resolution and implicitness when interactions are calculated by the Gaussian integration scheme

3.3.2 Skyline mesh

This mesh is of a five by six well primitive root diffuser using 266 flat triangular elements and is depicted in Figure 3.43; please note the surface is meshed correctly, graphical anomalies are due to Matlab's rendering engine. Its surface comprises rectangular faces so triangular elements are not a first choice but necessary for comparison with the Gaussian implementation. Due to the small difference in height between some wells, some elements have an extremely irregular aspect ratio, causing collocation points to be very close to adjacent elements, which are often also at right angles to the observer element, resulting in worst case singularities. The surface contains concave parts so may possess physical poles which are more lightly damped than those of the sphere. The point source is located 100m distant.
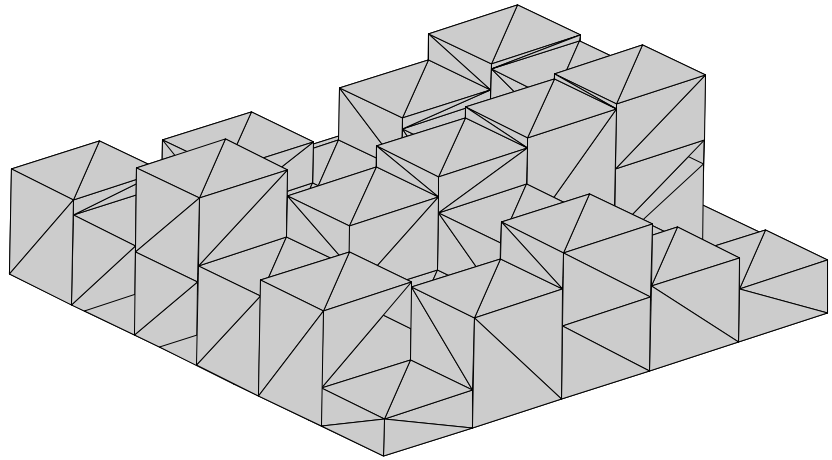
Figure 3.43: The skyline mesh
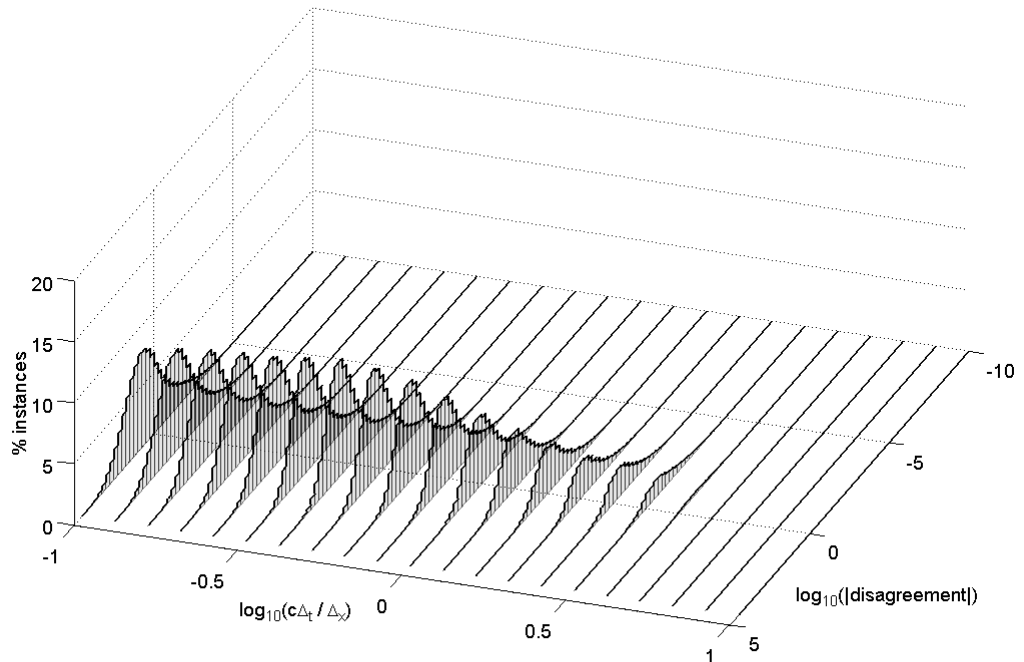
Figure 3.44: Disagreement populations between the skyline mesh interaction coefficients, as calculated by the two contour integration schemes, versus time-step implicitness

Figure 3.44 shows the error of the contour integration scheme with discontinuity components compared to the implementation without; this is the error caused by omission of the delta functions from the second derivative of the temporal basis function. The trend here is the same as Figure 3.37, though the error peaks are wider reflecting the greater variety of element pair geometries that occur in this complex mesh.
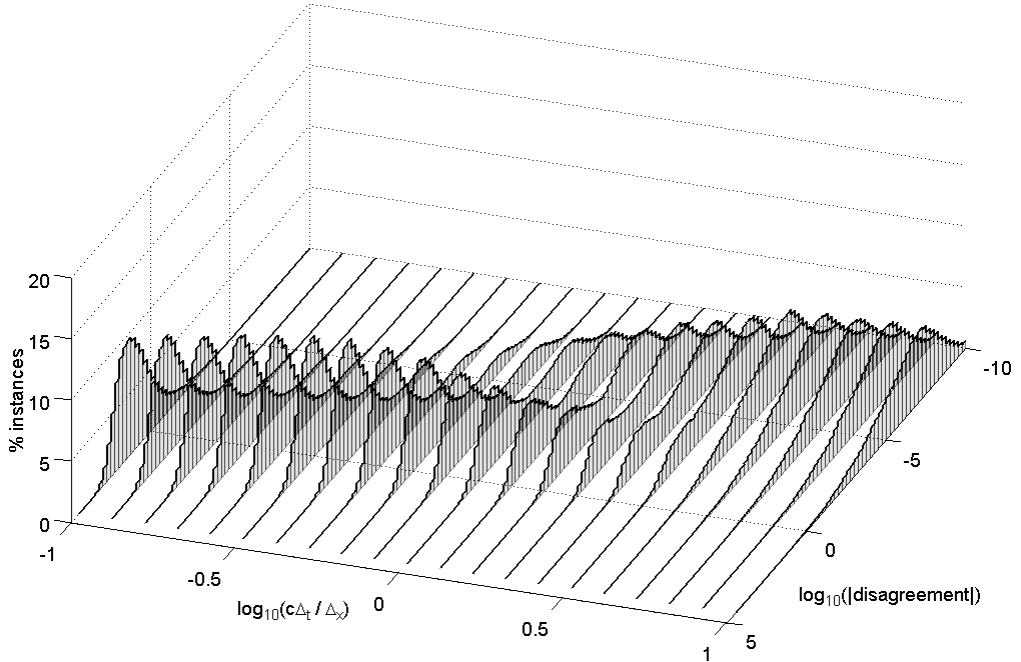
Figure 3.45: Disagreement populations between the skyline mesh interaction coefficients, as calculated by the contour integration scheme with discontinuity terms and the Gaussian scheme, versus time-step implicitness

Figure 3.45 shows the disagreement between the Gaussian scheme and the contour integration scheme with discontinuity components that correctly evaluates the numerical integrands of the former; this error is caused by using Gaussian integration to integrate a discontinuous singular integrand. As in Figure 3.38, two error mechanisms with defined ridges can be observed. At explicit time-steps error associated with discontinuities again dominates though the peaks are wider. Moving to the right the previously masked error due to the singularity of the integrand is revealed. This latter mechanism contributes more error of significant magnitude than it does for the spherical mesh, so may affect the solution.

122

Figure 3.46 shows the magnitude of the largest two SEM poles versus time-step. Again the contour integration models always have a pole with magnitude close to one. However the largest pole of the Gaussian implementation grows non-linearly with implicitness so the system becomes grossly unstable. This is counter-intuitive in light of Figure 3.45, since larger interaction errors are observed at explicit time-steps. Instead instability correlates with dominance of the less significant error mechanism observed above, so it is inferred that the latter may be the cause of the former. That fact that this causes solver divergence for this mesh, whereas none was witnessed for the spherical mesh, is due to more resonant nature of this surface; numerical error perturbs SEM poles, so the less well damped they were physically the more likely they are to stray unstable. The second largest pole is well behaved for all schemes, though significantly more stable when contour integration is used.
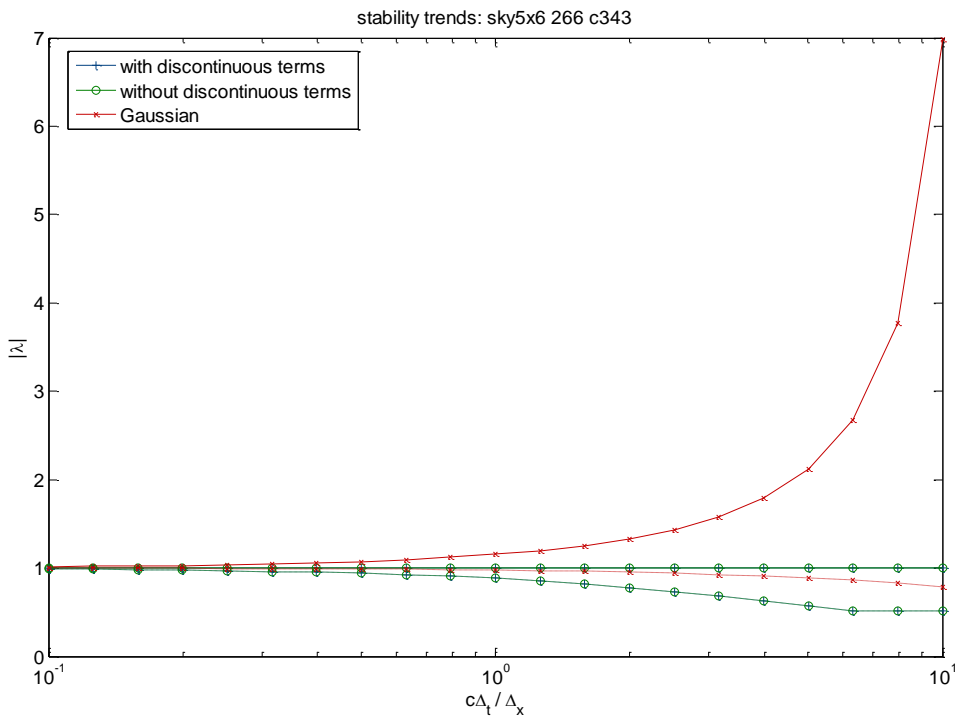
Figure 3.46: Stability trends on the skyline mesh characterised by the largest two poles versus time-step implicitness for each integration scheme

Figure 3.47, Figure 3.48 and Figure 3.49 show the error versus the frequency domain BEM model for contour integration without discontinuities, contour integration with

discontinuities, and Gaussian integration respectively. The two contour integration implementations show the same trend as they did on the spherical mesh, in fact with smoother convergence. The Gaussian scheme is unstable as predicted by Figure 3.46 and even at the most explicit time step, where stability is best, error relative to the frequency domain BEM is close to 100%; it cannot handle the singular nature of the integrals regardless of the time-step duration chosen.
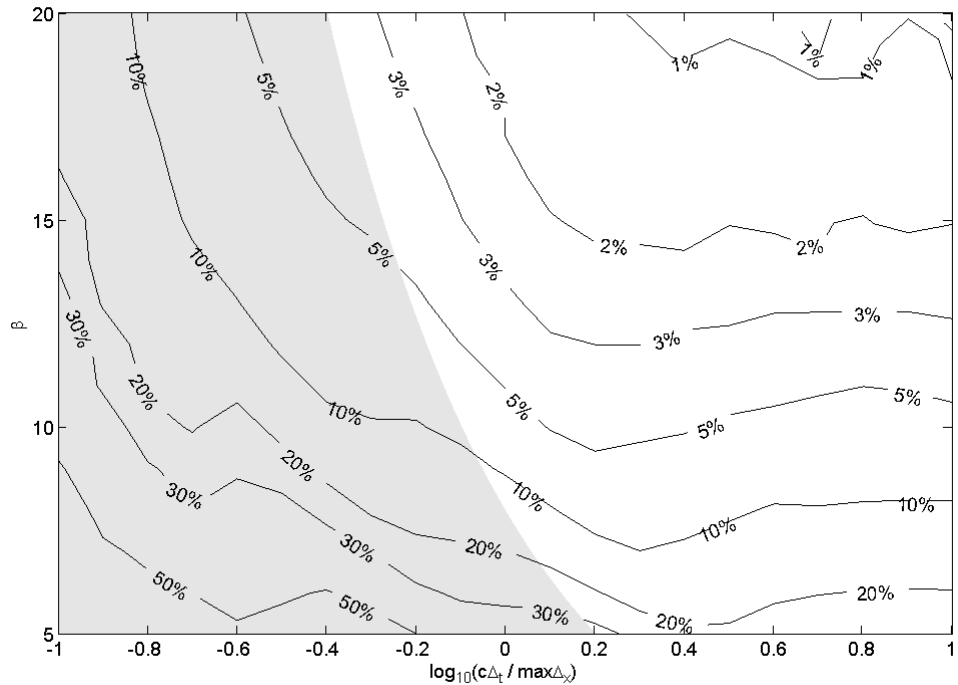
Figure 3.47: Surface error on the skyline mesh versus temporal resolution and implicitness when interactions are calculated by the contour integration scheme without the discontinuity terms
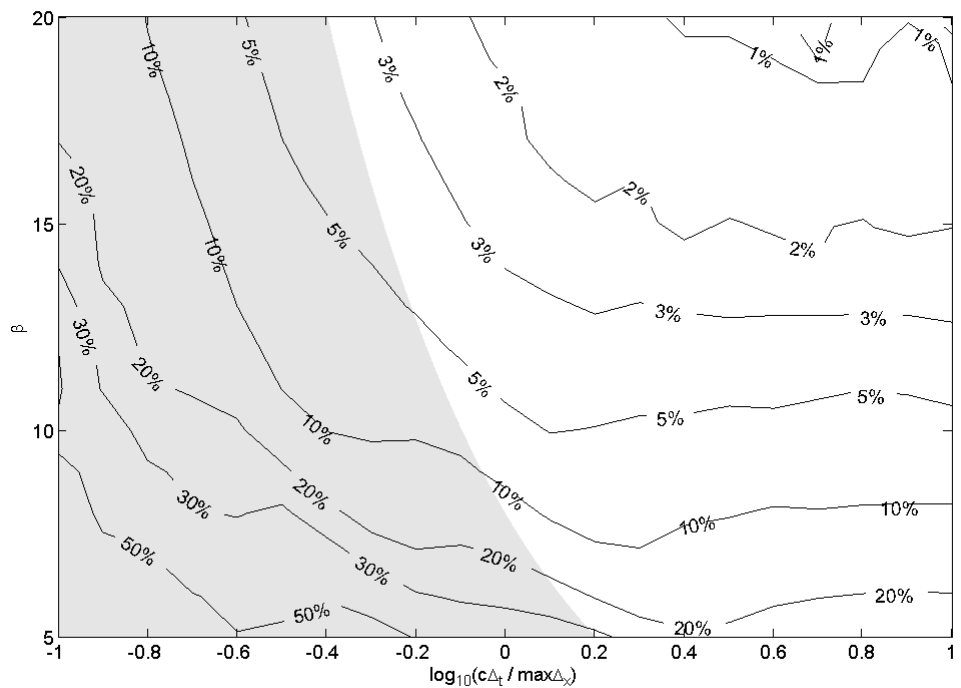
Figure 3.48: Surface error on the skyline mesh versus temporal resolution and implicitness when interactions are calculated by the contour integration scheme with the discontinuity terms
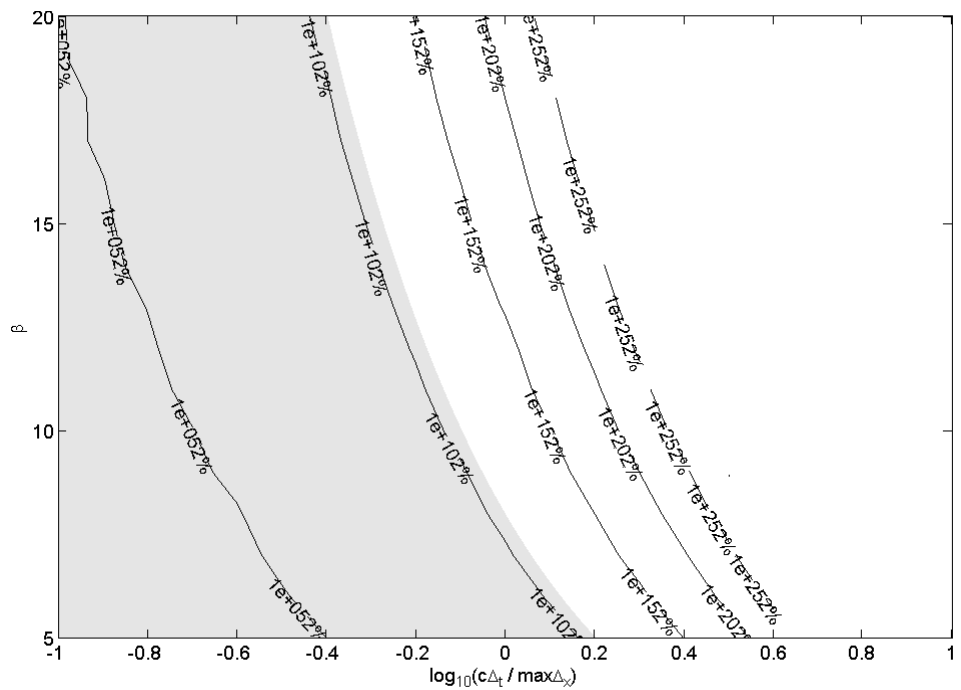
Figure 3.49: Surface error on the skyline mesh versus temporal resolution and implicitness when interactions are calculated by the Gaussian integration scheme

3.3.3 Discussion

Evidence has been presented that integration accuracy can affect system stability. However, further questions have been raised as extremely significant errors have been observed to have had very little effect on the end result.

What is certainly not the case is that off-diagonal terms of the interaction matrices are insignificant and the solution solely due to the incident field and the self-interaction terms. This is readily shown by setting all off-diagonals to zero (equivalent to the Kirchhoff optical boundary condition), running the MOT solver and observing that the resulting surface sound field is very different and does not agree with the frequency domain model.

One possible explanation is that the interaction errors resulting from discontinuities partially cancel out in the MOT solver routine. As retardation l increments, a spatial discontinuity appearing within an integrand will arise from each temporal basis joint in turn. Table 3.6 shows that the summations of the discontinuities in the first and second derivatives of the temporal basis function are zero, suggesting cancellation is possible.

Table 3.6: Cancellation of temporal basis function discontinuities

ς	-1	0	1	2	3	$\sum_{l}$
$\mathrm{T}'^{+}_{mother}(\varsigma) - \mathrm{T}'^{-}_{mother}(\varsigma)$	$\frac{1}{3}$	$-\frac{4}{3}$	2	$-\frac{4}{3}$	$\frac{1}{3}$	0
$\mathrm{T}''^{+}_{mother}(\varsigma) - \mathrm{T}''^{-}_{mother}(\varsigma)$	1	-4	6	-4	1	0

The delta functions appearing in Equation 3.65 are weighted by the middle row of Table 3.6 and are completely omitted by Gaussian integration; these omissions will cancel out in a summation over l. The cancellation of the effect of the sums of heavy-side functions in Equations 3.64 and 3.65 is harder to prove since they do affect the Gaussian

integration results. To do so consider a single abscissa; this is always located at the same point on the element, so always has the same τ value. For each value of l this will correspond to a different piece of $\text{T}_{mother}(\varsigma)$ and a different column in Table 3.7. The cumulative effect of either row of Table 3.7 upon the single abscissa is shown to cancel. Additionally, when an abscissa lies close to a discontinuity Gaussian accuracy appears very poor as a change in Δ_t or numerical error could move the abscissa across the discontinuity and give a very different result. However, in the context of summation of interactions with respect to l, this shift of the abscissa across the discontinuity just shifts the row of terms in Table 3.7 left or right by one; their effect still cancels.

Table 3.7: Cancellation of temporal basis function decomposition heavy-side terms

	$-1 \leq \varsigma < 0$	$0 \leq \varsigma < 1$	$1 \leq \varsigma < 2$	$2 \leq \varsigma < 3$	$\sum_l$
$\text{H}_1(\varsigma)$	⅓	-1	1	$-⅓$	0
$\text{H}_2(\varsigma)$	1	-3	3	1	0

Thus the effect of discontinuities on Gaussian integration is shown to cancel under summation with respect to l. This means that if $\varphi^t(\mathbf{r}, t)$ is constant with respect to time (silence) such integration errors will entirely cancel within the MOT solver, if $\varphi^t(\mathbf{r}, t)$ is slowly varying then they will mostly cancel. Consideration of system stability is more complex as no assumptions can be made about the system state or excitation. However, these cancellations do provide a mechanism for the substantial interactions errors observed to have so little effect on the system response.

There is also the issue of Gaussian integration of the piecewise polynomial parts of Equations 3.64 and 3.65. These are continuous but are still not the class of integrand the Gaussian rule is optimised for, so errors will result. It is inferred that this and spatial

singularity are the source of the less significant error observed in Figure 3.38 and Figure 3.45, to which the instability in Figure 3.46 and Figure 3.49 has been associated.

Above is the beginning of understanding why the Gaussian implementation is so stable in face of its deficiencies. The temporal basis function is a curious choice, but perhaps one that is somehow quasi-optimal for MOT solution of a collocation scheme with piecewise constant spatial basis. Ergin *et al's* lack of commentary on the subject of basis selection suggests that this is by chance rather than design. It has been seen that the bulk of the interaction errors occurring due to use of Gaussian integration cancel to some degree, but there remains error primarily of spatial origin that can cause instability. These deficiencies are overcome by the proposed contour integration scheme, leaving discretisation approximations as the primary source of error.

3.4 Conclusions

The aim of this chapter has been to investigate the effect of integration accuracy on system accuracy and stability. A shortcoming has been identified in Ergin *et al's* implementation in the form of their combination of temporal basis function and integration scheme. A new integration scheme utilising contour integration has been derived to accurately evaluate the necessary integrals. The integration schemes have been compared on two meshes, one geometrically simple and another geometrically complex, the latter typifying those of interest in Room Acoustics. Accurate integration has been shown to improve stability on the more complex mesh. However it has also been seen that a Gaussian integration scheme is remarkably robust in the face of significant interaction errors, and a mechanism has been highlighted that accounts for this.

The following chapter will investigate extending the method such that bodies with thin appendages may be modelled. A common example of such an object occurring within the field of Room Acoustics is the Quadratic Residue Diffuser and the time domain BEM will be applied to model it.

4 Time domain BEM for Finned Closed Surfaces

The purpose of this thesis is application of the time domain BEM to model surface treatments typical to Room Acoustics. In the preceding chapter, a simple surface was contrasted with a complex surface used to diffuse sound, and integration accuracy was concluded to be an important factor for accurate and stable modelling of complex real-world surfaces such as the latter.

The models considered so far have been closed surfaces where S surrounds some interior domain Ω_-. This chapter will consider surfaces that are thin and open (with air on both sides of S), such as an orchestral canopy, and lead onto solid bodies with thin appendages, such as a Quadratic Residue Diffuser (QRD). Both class of surface have been modelled using frequency domain BEMs, but only the former has been investigated using a time domain BEM [18]. This chapter aims to redress this by modelling the latter class of surface using the time domain algorithm.

Section 4.1 discusses the application of BEMs to thin surfaces. Problems that occur as the thickness of Ω_- tends to zero are described and publications analysing this in the frequency domain discussed. The procedure of modelling a thin surface by an open surface is introduced, in particular the concept of jump in velocity potential or pressure across S, and an existing time domain BEM that uses this approach is detailed.

Section 4.2 is concerned with modelling mixed surfaces, that is a closed surface and a thin surface attached to or in proximity of one another. Here it is proposed that the CFIE be used on closed parts of the surface while the open surfaces model is used on the thin parts, and anticipated that this shall improve stability relative to using the open model for the entire surface. Research on the frequency domain BEM is cited as justification for this approach. The formulation of the CFIE is seen to lend itself to modelling mixed surfaces in this way.

Numerical results are presented in the two sections that follow. Section 4.3 models a simple geometry (a cube plus a fin) to establish that the mixed surfaces approach is accurate and that the improvement in stability occurs. Section 4.4 models a real world surface (a QRD) and shows that the improvements still hold, although stability is not universally guaranteed.

Section 4.5 presents conclusions and discusses the significance of the results.

4.1 BEM Thin Shape Breakdown

All thin surfaces occurring in the real world have some finite thickness, so accordingly attempts have been made to use the closed surface BEM to model these with two surfaces, each conformal to a body-air interface. This is a reasonable model of reality, however when the BEM is applied problems occur. These surfaces will be very close with respect to their other dimensions, causing the singularity of the KIE to affect non-self element pairs, leading to very large interaction coefficients and integration accuracy issues. These can in turn lead to breakdown in the numerical solution stage of the algorithm, a phenomena known as Thin Shape Breakdown (TSB).
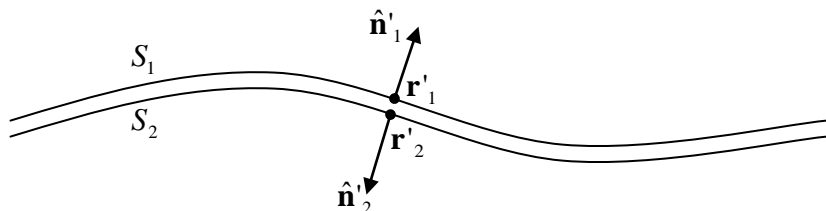
Figure 4.1: A thin body section

TSB can be avoided by taking the limit as thickness approaches zero and approximating the two body-air interfaces by a single surface. Figure 4.1 depicts a thin body whose air-interfaces are the surfaces S_1 and S_2. As the thickness approaches zero S_1 approaches S_2, so $\mathbf{r}'_1$ and $\mathbf{r}'_2$ coalesce. The normal vectors are opposed, meaning the sound radiated by the surface is a function of the jump in velocity potential (or pressure)

across the surface instead of the absolute values on each side; this is shown in Equation 4.1 where jump velocity potential $\tilde{\varphi}^t(\mathbf{r}',t) = \varphi_1^t(\mathbf{r}',t) - \varphi_2^t(\mathbf{r}',t)$. The surface subscripts are dropped as they both refer to the same surface.

$$
\begin{aligned}
\varphi^s(\mathbf{r},t) &= \iint_{S_1} \varphi_1^t(\mathbf{r}',t) * \hat{\mathbf{n}}_1 \cdot \nabla' \frac{\delta\left(t - R/c\right)}{4\pi R} d\mathbf{r}' + \iint_{S_2} \varphi_2^t(\mathbf{r}',t) * \hat{\mathbf{n}}_2 \cdot \nabla' \frac{\delta\left(t - R/c\right)}{4\pi R} d\mathbf{r}' \\
&= \iint_{S_1} \varphi_1^t(\mathbf{r}',t) * \hat{\mathbf{n}}_1 \cdot \nabla' \frac{\delta\left(t - R/c\right)}{4\pi R} d\mathbf{r}' - \iint_{S_1} \varphi_2^t(\mathbf{r}',t) * \hat{\mathbf{n}}_1 \cdot \nabla' \frac{\delta\left(t - R/c\right)}{4\pi R} d\mathbf{r}' \quad 4.1 \\
&= \iint_S \tilde{\varphi}^t(\mathbf{r}',t) * \hat{\mathbf{n}} \cdot \nabla' \frac{\delta\left(t - R/c\right)}{4\pi R} d\mathbf{r}'
\end{aligned}
$$

It is apparent that the equation for jump velocity potential on an open surface is identical to that for velocity potential on a closed surface; this concurs with the discussion in chapter 2. The KIE does not distinguish between Ω_+ and Ω_-; they are both modelled as air filled, so differences only arise because of the source locations and boundary condition. A closed rigid boundary condition typically asserts that $\varphi_2^t(\mathbf{r}',t) = 0$, hence $\tilde{\varphi}^t(\mathbf{r}',t) = \varphi_1^t(\mathbf{r}',t)$. Similarly, the concept of a double layer potential is based on dipoles, which cause a jump in velocity potential (and pressure) across the surface. Accordingly one way of viewing this is that whenever $\varphi^t(\mathbf{r}',t)$ is found for a closed body using a BEM, what is really being found is $\tilde{\varphi}^t(\mathbf{r}',t)$, it just happens to equal $\varphi^t(\mathbf{r}',t)$ as $\varphi_2^t(\mathbf{r}',t) = 0$. This is a minor distinction, but one that improves algorithmic elegance and will be adhered to in the notation of the remainder of this thesis.

Since $\varphi_1^t(\mathbf{r}',t)$ and $\varphi_2^t(\mathbf{r}',t)$ are unknown, no boundary condition of the form $\varphi_2^t(\mathbf{r}',t) = 0$ may be used. However, boundary conditions involving normal velocity are still valid, so the rigid surface boundary condition of Equation 2.64 may be used, producing the BIE below; this is simply $L_v\{...\}$ (Equation 2.65) applied to jump velocity potential.

$$\hat{\mathbf{n}} \cdot \nabla \varphi^i(\mathbf{r},t) = -\hat{\mathbf{n}} \cdot \nabla \varphi^s(\mathbf{r},t)$$

$$= -\hat{\mathbf{n}} \cdot \nabla \iint_S \tilde{\varphi}^t(\mathbf{r}',t) * \hat{\mathbf{n}}' \cdot \nabla' \frac{\delta\left(t - R/c\right)}{4\pi R} d\mathbf{r}' \qquad 4.2$$

$$= \mathrm{L}_v\left\{\tilde{\varphi}^t(\mathbf{r},t)\right\}$$

The scattered sound may be found directly from jump velocity potential by Equation 4.1. If the absolute values on the front and back of the surface are required then these may be found by combining the double layer potential jump property (Equation 4.3) with the definition of jump velocity potential, yielding Equation 4.4.

$$\tfrac{1}{2}\varphi_1^t(\mathbf{r},t) + \tfrac{1}{2}\varphi_2^t(\mathbf{r},t) = \varphi^i(\mathbf{r},t) + \iint_S \tilde{\varphi}^t(\mathbf{r}',t) * \hat{\mathbf{n}}' \cdot \nabla' \frac{\delta\left(t - R/c\right)}{4\pi R} d\mathbf{r}' \qquad 4.3$$

$$\varphi_1^t(\mathbf{r},t) = \varphi^i(\mathbf{r},t) + \tfrac{1}{2}\tilde{\varphi}^t(\mathbf{r},t) + \iint_S \tilde{\varphi}^t(\mathbf{r}',t) * \hat{\mathbf{n}}' \cdot \nabla' \frac{\delta\left(t - R/c\right)}{4\pi R} d\mathbf{r}'$$

$$4.4$$

$$\varphi_2^t(\mathbf{r},t) = \varphi^i(\mathbf{r},t) - \tfrac{1}{2}\tilde{\varphi}^t(\mathbf{r},t) + \iint_S \tilde{\varphi}^t(\mathbf{r}',t) * \hat{\mathbf{n}}' \cdot \nabla' \frac{\delta\left(t - R/c\right)}{4\pi R} d\mathbf{r}'$$

The first time domain BEM to use this formulation was Kawai & Terai's [18] 1990 implementation. Unlike the above, their derivation supported non-rigid surfaces, though these terms were dropped before the implementation stage, which consequentially just supported thin rigid plates. Integration was performed by conversion to contour integrals, resulting in an implementation equivalent to Equation 3.48, placing a further restriction that the surface be comprised of flat elements. A trapezoidal rule was used to integrate the contribution from each element edge, doubling the division repeatedly until relative error became less than 1%; this is a similar approach to that of section 3.2.1.9, but less efficient (not locally adaptive) and devoid of the assertion of absolute accuracy.

The primary weaknesses of the algorithm were due to the definition of discretisation in prose, that jump velocity potential is assumed uniform over an element between time-steps. There is inconsistency in their contour integrand which interpolates this quantity

between time-steps. Due to this imprecision in definition the only place the current velocity potential could be distinguished from its retarded counterpart was at the collocation point; hence the algorithm was restricted to explicit time-step durations. In their implementation the time derivative at the collocation point was replaced by a backward finite-difference approximation; this was substituted into the integral equation and rearranged to find the current jump velocity potential weight for that element:

$$\frac{\partial}{\partial t}\tilde{\varphi}^{\,t}\left(\mathbf{r}_{\mathbf{m}}^{\mathbf{c}},t_j\right) \approx \frac{\tilde{\varphi}_{m,j}-\tilde{\varphi}_{m,j-1}}{\Delta_t}$$

$$\tilde{\varphi}_{m,j}=\tilde{\varphi}_{m,j-1}-\frac{c\Delta_t}{2\pi}\oint_{S_m}\frac{\tilde{\varphi}^{\,t}\left(\mathbf{r}',t-R/c\right)}{R}d\theta-2c\Delta_t\sum_{m\neq n}L_v\left\{\tilde{\varphi}^{\,t}\left(\mathbf{r},t\right)\right\}$$

4.5

While Kawai & Terai's implementation was progressive in its modelling of thin surfaces and use of contour integration, its discretisation scheme was a significant weakness.

Martinez [65] investigated the TSB problem for the frequency domain BEM in depth in his 1991 paper. He shows by Maclaurin expansion that as the thickness of an object approaches zero, the zero'th expansion term of the KIE vanishes and its first derivative with respect to the surface normal vector becomes dominant. This provides a link to those codes that choose to use the normal derivative form of the KIE (as above), and offers explanation as to why some closed body implementations appear to work on thin appendages. His work's scope includes non-rigid compliant fins supporting flapping and breathing modes, whereas this thesis will restrict its investigation to rigid fins. Finally, he contrasted the methods needed to tackle the TSB with those required for the non-uniqueness deficiency and highlighted that the former is not frequency dependent.

4.2 Mixed surfaces

A method for modelling thin plates has been detailed, but there remains the question of what is best when it is desired to model a plate near a solid body, or a solid body with a protruding fin. $L_v\{\ldots\}$ is valid on closed and open surfaces, so one solution is to use it

for both closed and open surface sections; this will be referred to as an all-thin model. However, Ergin *et al* [22] found that $L_v\{\ldots\}$ supports cavity resonances of closed surfaces so is potentially unstable in that application; they promote use of the Combined Field Integral Equation (CFIE, $L_c\{\ldots\}$, Equation 2.66).

Wu [66] (1994) addresses the same concerns in the frequency domain and shows that the non-uniqueness problem occurs if at least one closed body exists in a mixed body environment. He implements a direct BEM that uses different solution strategies on thick and thin surface parts; thin parts are modelled with the normal derivative of the KIE, as above, closed parts are modelled with either the Burton and Miller method or the CHIEF method, both of which inhibit cavity resonances and the associated non-uniqueness issue. The implementation was verified against a multi-domain BEM, which is correct albeit less elegant and efficient. Martinez [65] mentioned all of these aspects, including use of a different integral operator on open and closed surface parts, but stopped short of proposing such an algorithm.

Wu is careful to distinguish between closed and open surfaces, and groups their elements such that the interaction matrix may be partitioned into thick-thick, thick-thin, thin-thin and thin-thick interactions. By contrast, the comments on jump potential in section 4.1 suggest that these surface parts need not be distinguished in this way; they merely have differing boundary conditions. Derivation is further simplified because $L_c\{\ldots\}$ reduces to $L_v\{\ldots\}$ when $\alpha = 1$; this is not the case for the Burton and Miller [6] definition in which the KIE and its normal derivative have a fixed weight of one and a variable weight respectively.

Consequentially the mixed surfaces algorithm proposed here is identical to Ergin *et al's* algorithm, with the replacement of $\varphi^t(\mathbf{r}',t)$ by $\tilde{\varphi}^t(\mathbf{r}',t)$ and the constraint that $\alpha = 1$ on open surface sections. This has the advantage that all the numerical machinery has been verified, so it is merely the above premise that must be tested. The 'correct' (no discontinuity terms) contour integration scheme from chapter 3 will be used.

4.3 Accuracy and Stability

The verification process will comprise two distinct stages; firstly the response of the model to an impulsive source will be examined to detect instability (as the meshes are now too large to calculate SEM poles for all time-step durations), then the steady-state response will be compared to a frequency domain BEM to assess accuracy.

A new source type will be required to create impulsive excitation, the motivation being to provide a broadband excitation that excites all system poles so any that are unstable make their presence known. The model does not support discontinuous excitation, so delta and heavy-side functions cannot be used. Instead a 'sampled' source with defined scalar values φ_j at each time-step is defined. These samples must be interpolated and the surface discretisation temporal basis function is an obvious candidate. The resulting excitation function is given below, where R is the distance from the source to $\mathbf{r}$:

$$\varphi(\mathbf{r},t) = \sum_j \varphi_j T_j(t) * \frac{\delta\left(t - R/c\right)}{4\pi R} \qquad 4.6$$

This source type could represent many possible signals depending on the choice of sample values; these could for instance be the PCM samples of a piece of recorded music. However, to create the required impulsive source the samples will be chosen to be unitary at t = 0 and zero otherwise. Accuracy is not expected to be good as the rapidly varying field is poorly discretised, so (instead of showing redundant data) the spatial maximum of velocity potential at each time-step is shown, as is required to characterise stability. This is plotted for each time-step duration modelled. The source will be located 10m distant normal to the scattering surface.

Solution accuracy will be calculated by the same method as used in section 3.3. A 100m distant normally located harmonic point source will excite the surface, modelled by the time domain BEM with a variety of time-step durations. The temporal resolution is characterised by the number of time-steps per excitation period (β), and its relationship to spatial resolution by the implicitness ($c\Delta_t\Delta_x^{-1}$). The source to surface

element transfer function at each excitation frequency is calculated using the frequency domain BEM (Equation 3.67). The same is calculated from the time domain data by DFT (Equation 3.68); the first 50β iterations are omitted to allow the solution to reach steady state, then the next 100β iterations are chosen for DFT as this length maintains periodicity and eliminates windowing error. The surface sound error is calculated as spatial mean magnitude of the difference between these transfer function estimates, normalised to the spatial mean magnitude of the frequency domain estimate and is written as a percentage (Equation 3.69). In most cases a frequency domain BEM for open surfaces (DIFTHIN.exe) will be used. However at certain frequencies this shows spurious behaviour so a frequency domain BEM for closed surfaces (RADDIFF.exe) will be used for confirmation. Both these implementations are previously verified against experimental results and follow Terai's [64] 1980 derivation.

This section will commence by modelling a simple surface (a cube) and then progress to a complex 'real-world' one (a QRD). In both cases, the closed part of the surface will first be modelled to observe the stabilising effect of the CFIE. Then the thin appendages will be added, and the mixed model compared with the all-thin model.

4.3.1 Cube

This mesh is 0.7m cubed comprising 294 elements. It is an extremely regular mesh; all elements are perfectly square, so no collocation points are unduly close to element edges and integration error is not anticipated to be an issue. It is depicted in Figure 4.2:

Figure 4.3 shows the response of the surface to an impulsive source when a thick surface model has been used (CFIE with $\alpha = \frac{1}{2}$). Each line shows the spatial maximal velocity potential magnitude versus time for models of differing time-step duration. As expected, energy is dissipated away from the scattering surface and the surface velocity potential decays rapidly. In the most implicit time-step durations (top of figure) the decay appears slower; this is due to the longer excitation and the cruder temporal discretisation failing to model the rapid decay. Note that the minimum of the value axis is artificially set to 10^{-6}; data below this magnitude is not shown.
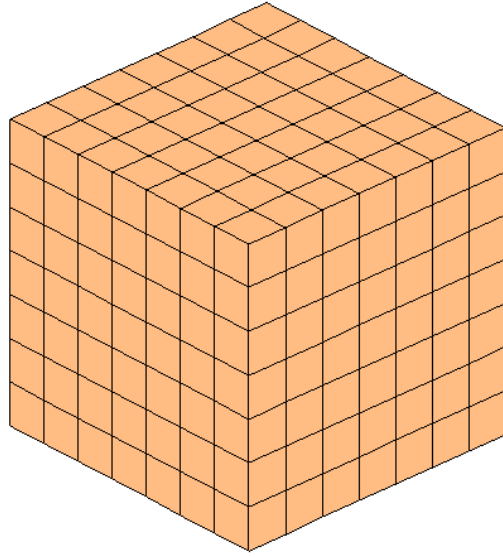
Figure 4.2: Cube mesh
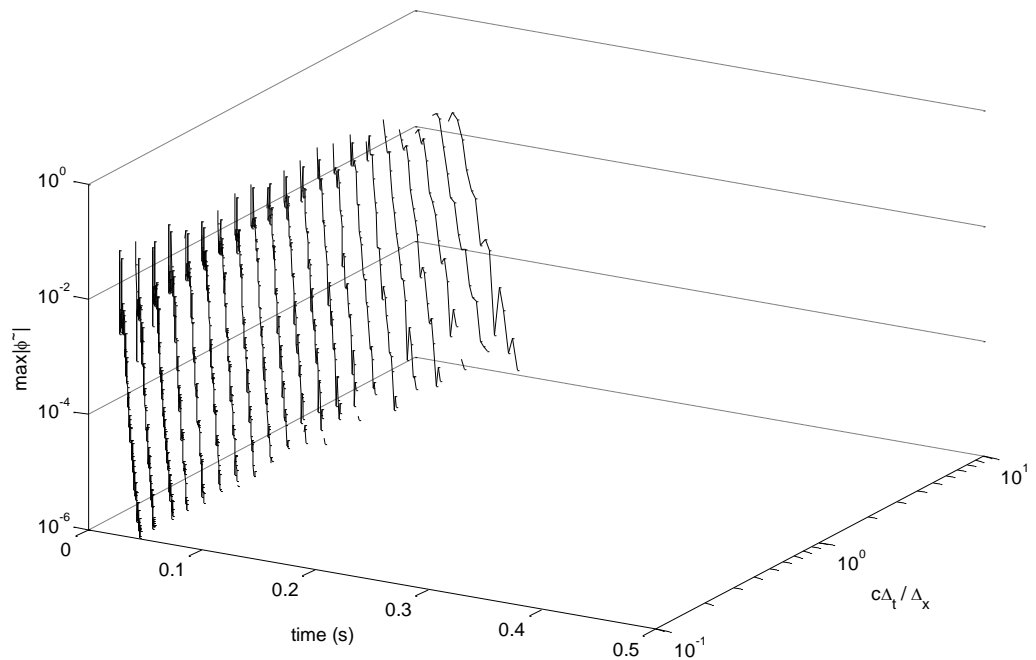
Figure 4.3: Impulse response of the cube closed surface model for various time-step durations

Figure 4.4 shows the response of the surface to an impulsive source when an all-thin surface model has been used (CFIE with $\alpha = 1$). The system still appears to be approaching steady state, but instead of the clear decay of velocity potential seen in Figure 4.3, other artefacts are clearly visible. At the most explicit time-step durations,

high frequency oscillation is observed, which is unlikely to have a physical origin so is considered to be algorithmic error. As time-step durations become more implicit this subsides but velocity potential still converges slowly to a non-zero value. Recalling that it is the derivatives of velocity potential that have physical meaning, any constant value shown here represents silence so the fact that the curves do not tend to zero is not a concern. In fact, terminating with such a non-zero steady state is typical of time domain BEM responses; Figure 4.3 would show such behaviour if the low limit of the value axis were reduced. However, the slow convergence to this value represents a slowly decaying pressure field, indicating that there are some system poles with magnitudes only marginally smaller than unity, which is not expected of a convex scatterer.
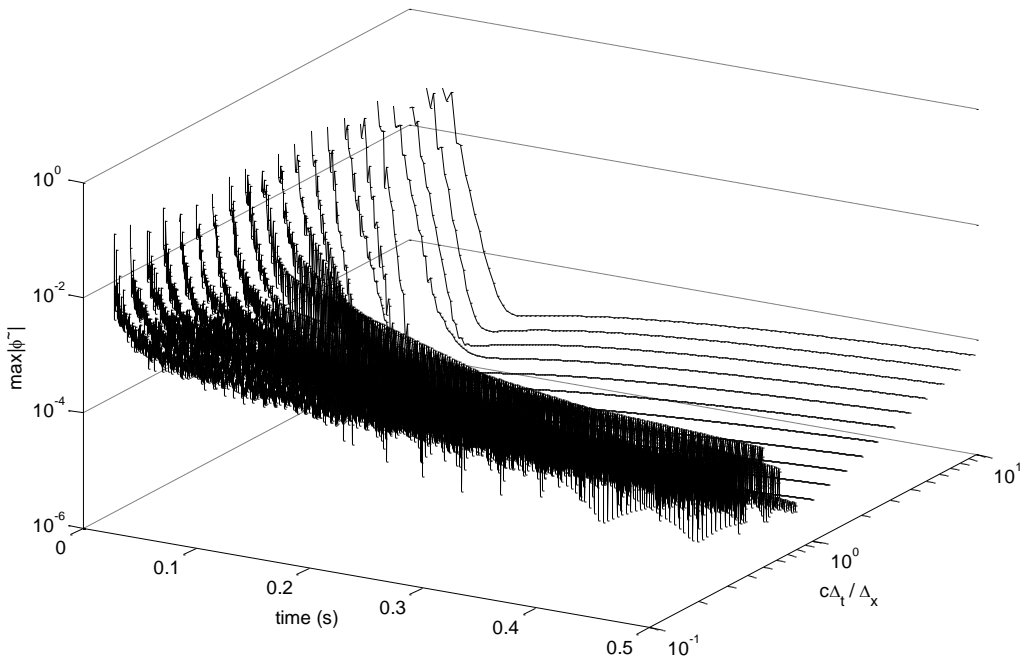
Figure 4.4: Impulse response of the cube open surface model for various time-step durations

Figure 4.5 confirms that the all-thin model has larger magnitude poles than the closed model, even showing one thin pole to have magnitude greater than one, an instability that was not excited in Figure 4.4. To the left of Figure 4.5 few open poles are shown as the sparse matrix eigenvalue solver could not converge to any distinct ones; this is indicative of the problems experienced calculating MOT poles as the number of elements is increased.
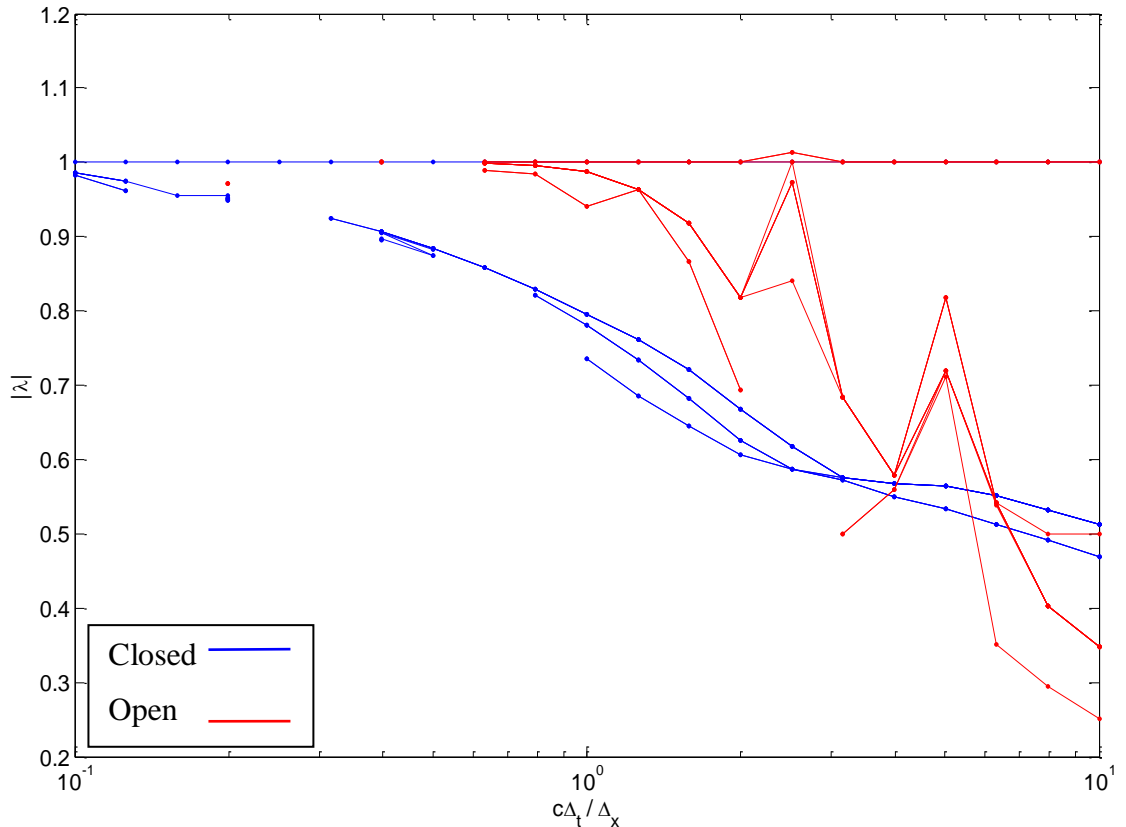
Figure 4.5: Stability trends on the cube mesh characterised by the largest resolvable poles versus time-step implicitness for the open and closed surface models

Although the contour integration derivation of section 3.2 was valid for any polygonal surface, the implementation has not been verified on square elements so here it is first compared to the frequency domain BEM. The results are shown below and show good agreement as seen in section 3.3. The grey shaded area indicates $\Delta_x > \frac{2}{8}$ where spatial discretisation error is anticipated. In the following sections some reference will be made to lines of constant frequency; the curved edge of the shaded area is an example of such and others are envisaged by its horizontal translation.
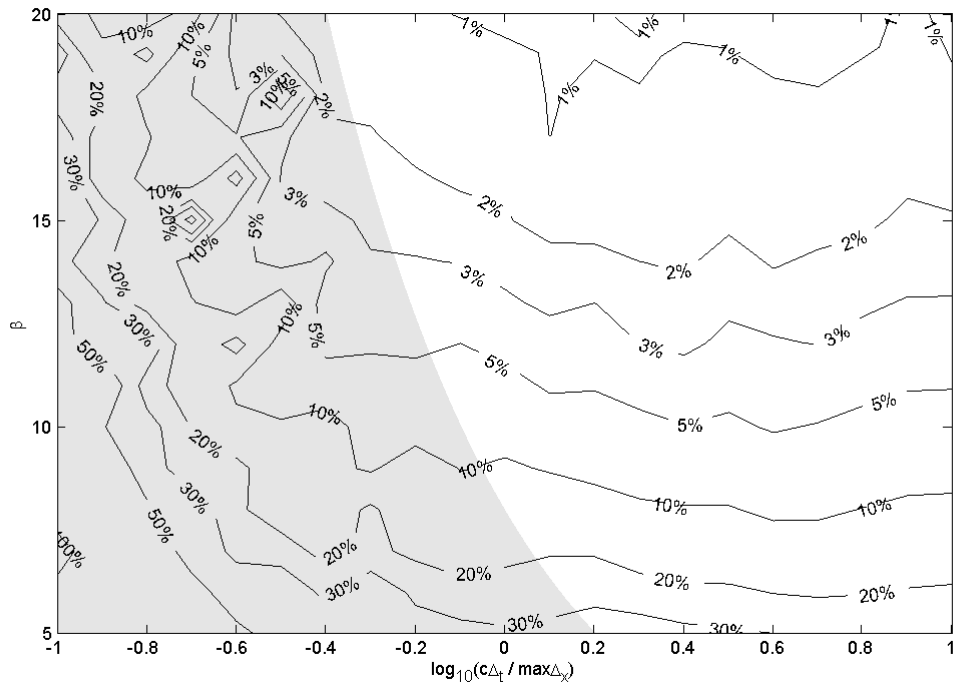
Figure 4.6: Surface error of the time domain BEM for closed surfaces compared to the frequency domain BEM for closed surfaces versus temporal resolution and implicitness on the cube mesh
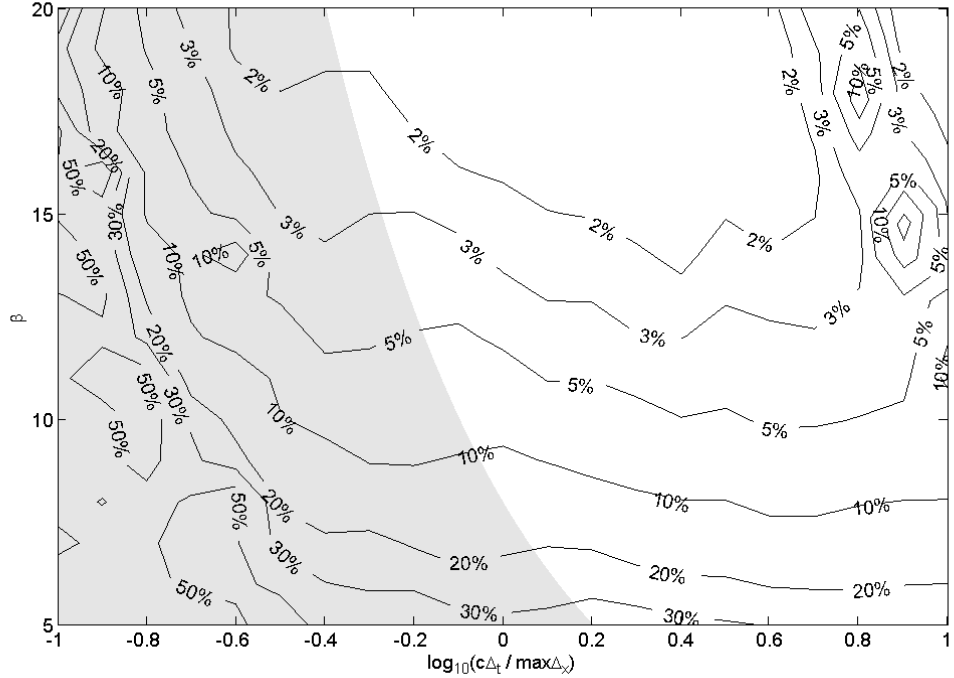
Figure 4.7: Surface error of the time domain BEM for closed surfaces compared to the frequency domain BEM for open surfaces versus temporal resolution and implicitness on the cube mesh

Figure 4.7 shows accuracy of the time domain BEM for closed surfaces versus the frequency domain BEM for open surfaces. Agreement is mostly good, except at a few localised points in the top right of the figure; Figure 4.8 compares the frequency domain BEMs and shows that these errors are associated with the frequency domain BEM for open surfaces rather than the time domain implementation. It is suspected that these could be non-uniqueness symptoms as they lie on a line of roughly constant frequency.

Contrary to the argument favouring jump velocity potential in section 4.2 it has been found that the frequency domain BEM for open surfaces gives lower error if, for closed surface sections, the pressure on the front surface is used. The time domain BEM is still validated on jump velocity potential as proposed and achieves good accuracy versus the frequency domain BEM for closed surfaces. It must therefore be that open surfaces frequency domain implementation supports some spurious interior pressure field that corrupts the jump pressure but that is cancelled out on evaluation of the front pressure. The time domain BEM equipped with the CFIE rejects these interior modes.
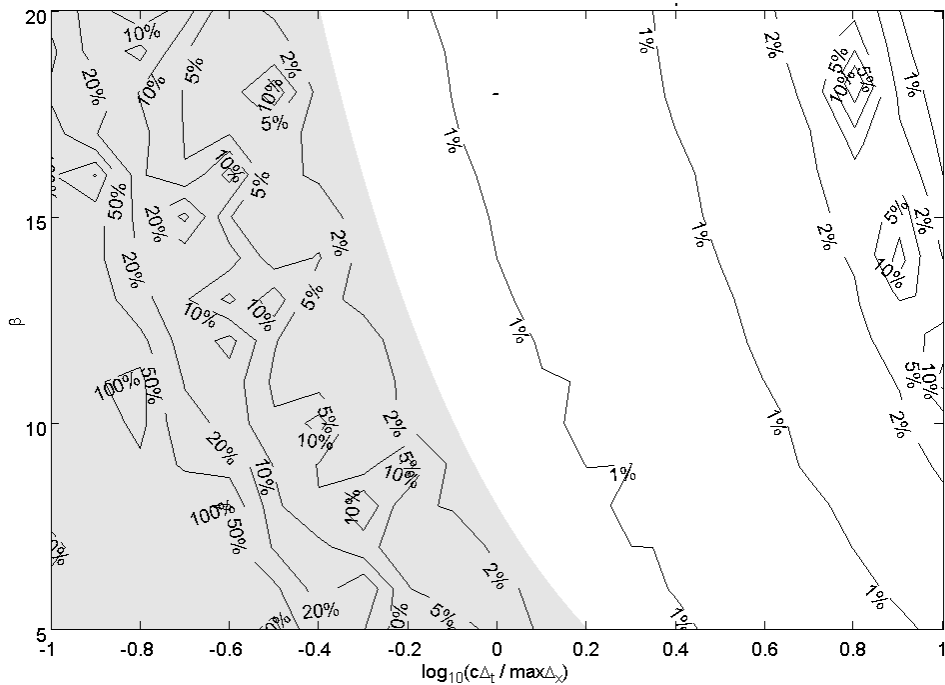
Figure 4.8: Surface disagreement between the frequency domain BEMs versus temporal resolution and implicitness on the cube mesh

141

Figure 4.9 shows accuracy of the time domain BEM for open surfaces versus its frequency domain equivalent. Error appears randomly distributed with a mean value of 80%, demonstrating that the artefacts seen in Figure 4.4 do manifest as error in the solved surface sound, even if only considering the principle frequency of excitation. Comparison of this with Figure 4.6 and Figure 4.7 bolsters the evidence in support of the superiority of the CFIE in comparison to an all-thin model.
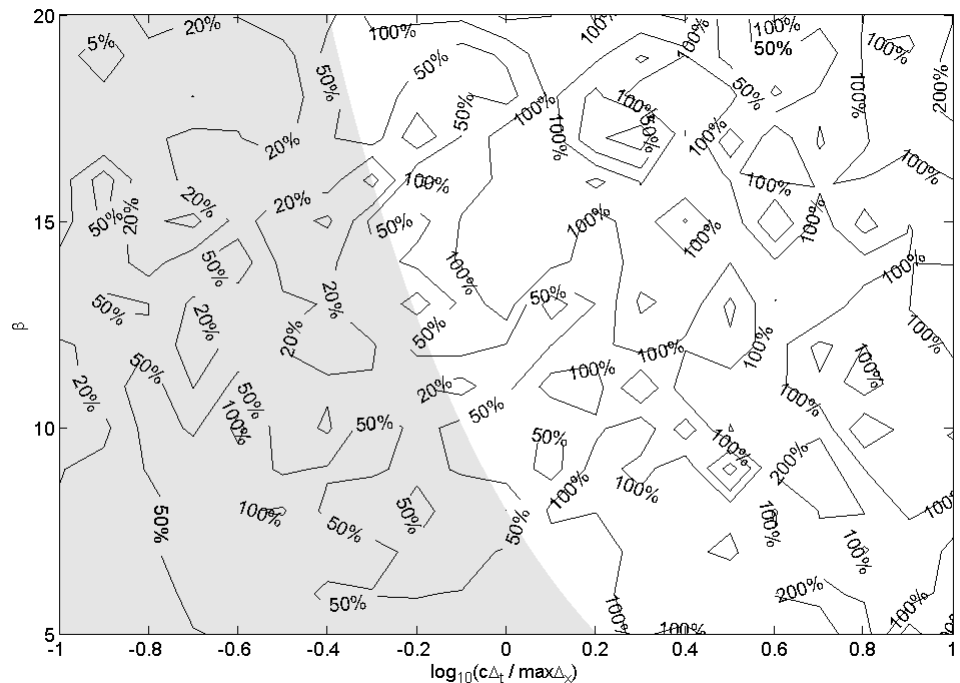
Figure 4.9: Surface error of the time domain BEM for open surfaces compared to the frequency domain BEM for open surfaces versus temporal resolution and implicitness on the cube mesh

4.3.2 Cube with a Thin Appendage

This mesh is the same 0.7m cube modelled above with 0.7m square appendage attached to one edge, increasing the element count to 343. Again it is an extremely regular mesh. It is depicted below, where thin elements are coloured blue, and stability results follow:
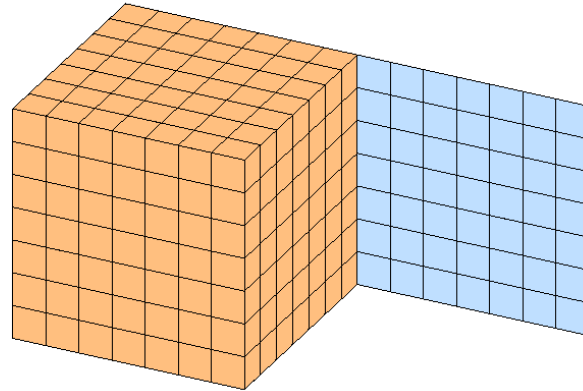
Figure 4.10: Mesh of cube plus fin
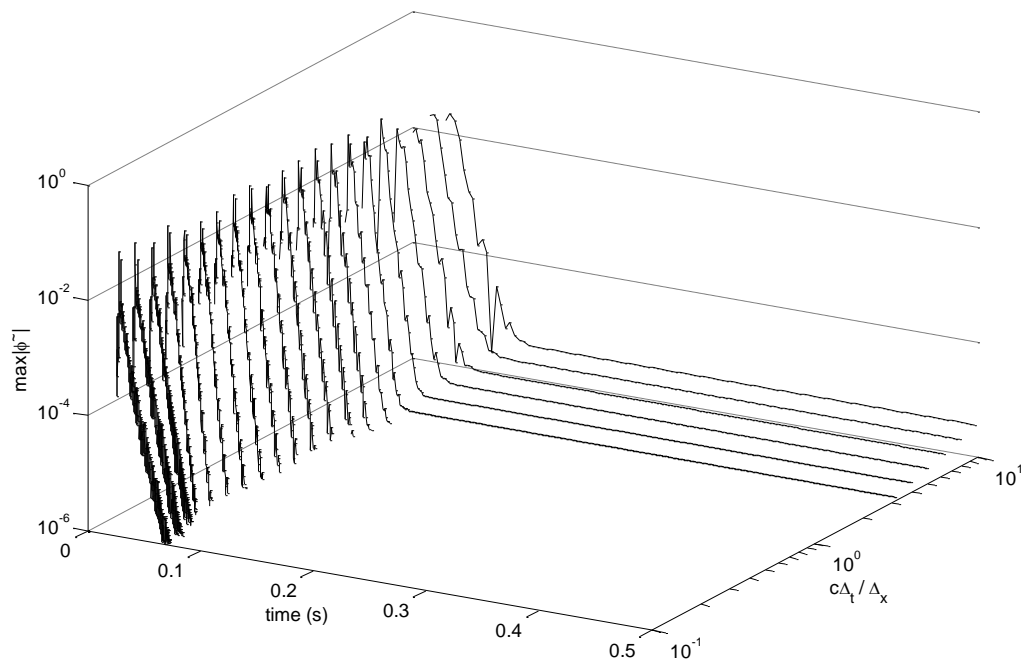
Figure 4.11: Impulse response of the cube plus fin mixed model for various time-step durations
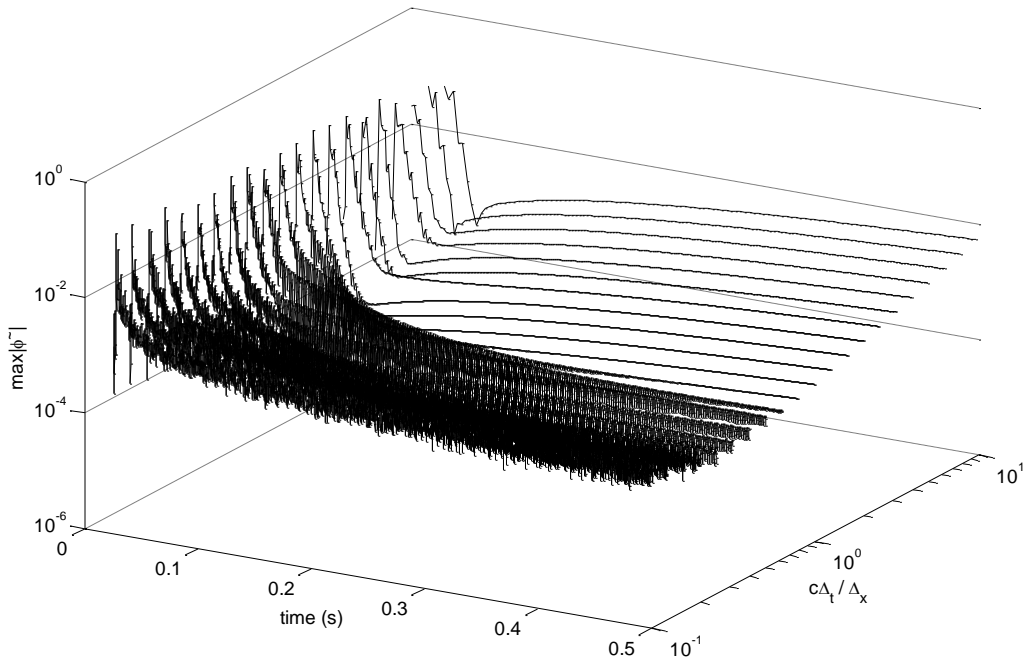
Figure 4.12: Impulse response of the cube plus fin open model for various time-step durations

Figure 4.11 shows the same trends as Figure 4.3, except for a marginally slower decay rate possibly because the surface now has concave parts. The excitation of a steady-state response is now visible for more implicit time-step durations. Similarly, Figure 4.12 shows the same trends as Figure 4.4; in both cases the addition of a fin has not significantly affected model stability. MOT poles are not shown as the results are indistinguishable from Figure 4.5 except that slighter fewer poles are converged to by the solver.

Figure 4.13 shows the same good agreement pattern as Figure 4.7; again this is taken to mean the time domain model is performing accurately and disagreement in the top right corner is due to the frequency domain BEM.

Like Figure 4.9, Figure 4.14 shows poor accuracy from the time domain all-thin model with an average error of 83%. These results demonstrate that, as expected, the superiority of the CFIE is not weakened by the proximity of a thin body, and that the simple implementation change proposed in section 4.2 does indeed improve accuracy on mixed surfaces.
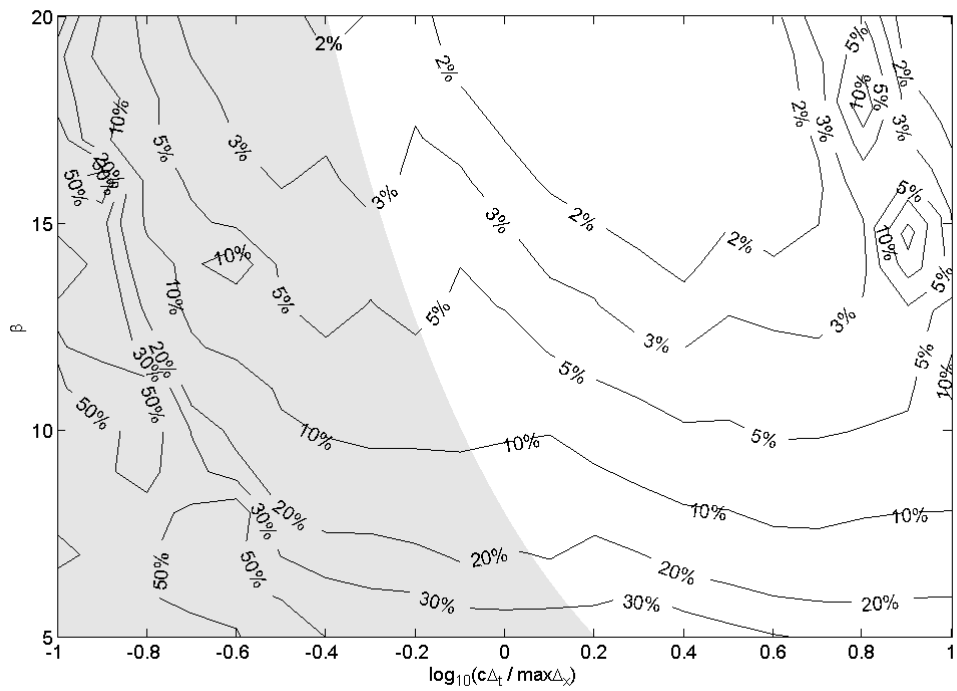
Figure 4.13: Surface error of the time domain BEM for mixed surfaces compared to the frequency domain BEM for open surfaces versus temporal resolution and implicitness on the cube plus fin mesh
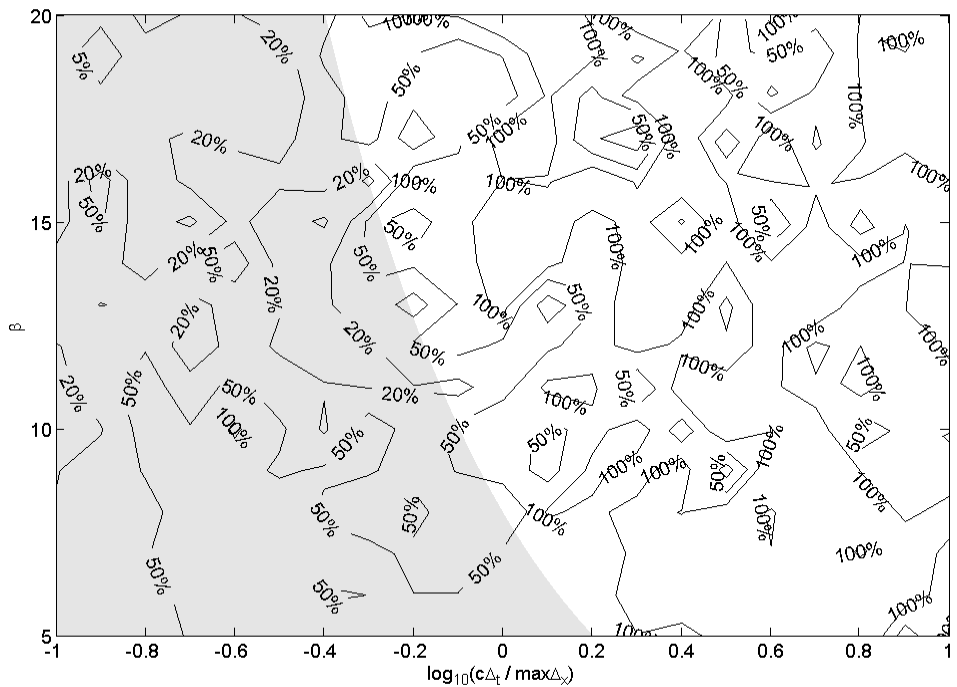
Figure 4.14: Surface error of the time domain BEM for open surfaces compared to the frequency domain BEM for open surfaces versus temporal resolution and implicitness on the cube plus fin mesh

4.4 Application example: Quadratic Residue Diffuser

A Quadratic Residue Diffuser [67] (QRD) is a number-theoretic diffuser popular in Room Acoustics applications. It comprises a series of wells, separated by thin fins, whose depths are dictated by the quadratic residue sequence and a design wavelength. In this thesis only one-dimensional QRDs will considered; these are designed to diffuse in one plane only and take the form of an extruded cross section. The diffuser modelled in this section has a design wavelength of approximately 1.4m, a well width of 0.25m, and a height of 1.0m.

Cox and Lam [68] performed three-dimensional BEM models of QRD in 1994 and concluded that a BEM capable of modelling the thin fins of the diffuser gave the most accurate results compared to scale models, justifying this as an appropriate application of the time domain BEM for mixed surfaces.

4.4.1 QRD Block

Again the closed portion of the surface will be modelled first to demonstrate the effectiveness of the CFIE. This part of the surface is depicted in Figure 4.15 and comprises 726 elements. Dimensions have been chosen such that all elements are close to square, so again integration error is not anticipated to be an issue. This surface has two concave regions which form part of the two deepest wells, and some surface sections are close and parallel, suggesting a disposition toward resonances.

Despite use of the CFIE, the two most explicit time-step durations in Figure 4.16 can be seen to exhibit instability; some poles have been corrupted by discretisation error (at these short time-step durations primarily spatial discretisation error) and their magnitudes perturbed to greater than unity. Otherwise behaviour is as expected from the previous figures, with a slightly slower decay due to the concave parts of the surface.
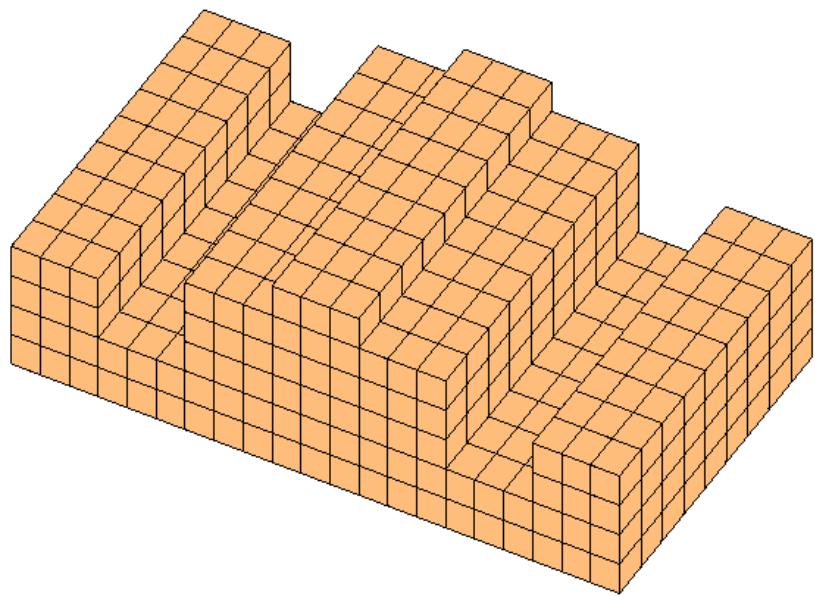
Figure 4.15: Mesh of a QRD without its fins
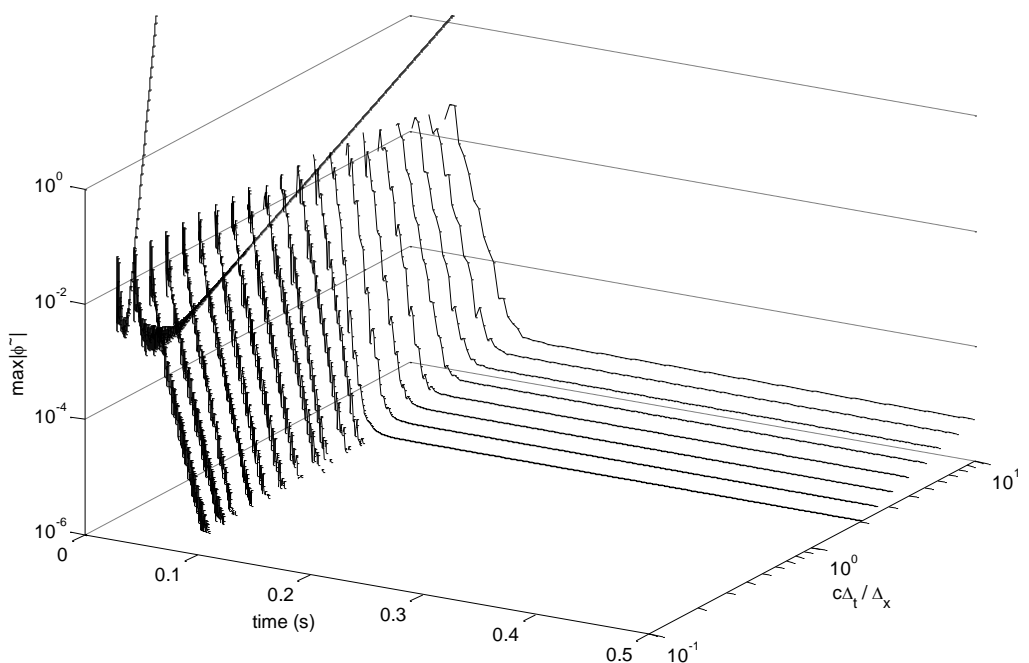
Figure 4.16: Impulse response of the QRD block closed model for various time-step durations
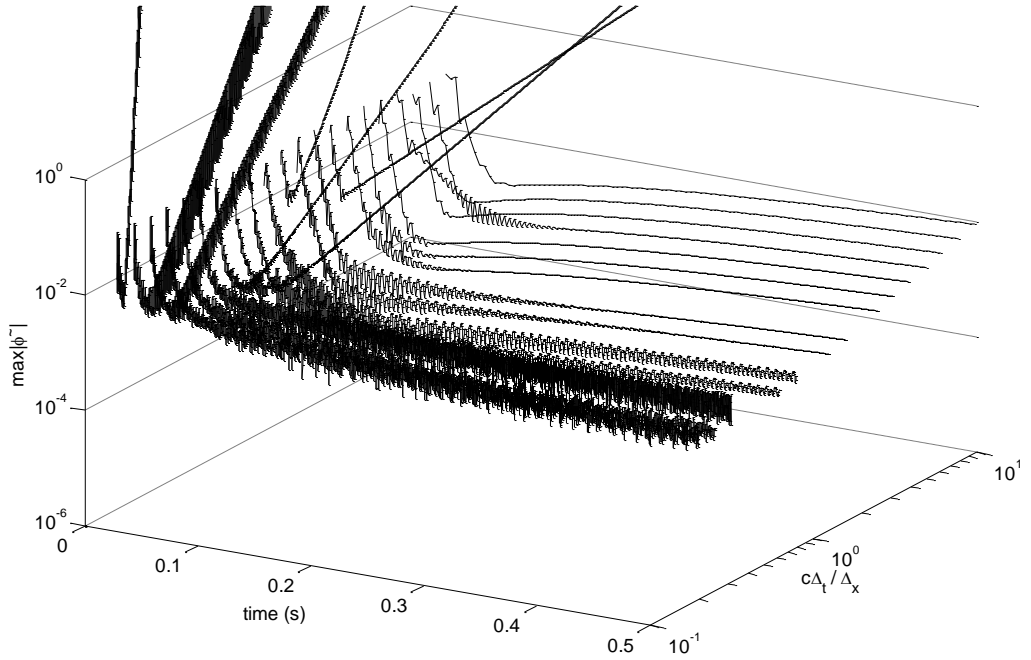
Figure 4.17: Impulse response of the QRD block open surface model for various time-step durations

Figure 4.17 shows the situation is much worse for the time domain BEM for open surfaces. Not only are all the error causing artefacts visible in Figure 4.4 and Figure 4.12 again present, but the solution is clearly unstable at 7 of the 21 time-step durations modelled. It was shown in Figure 4.5 that the open surface model permits more poles with magnitudes close to unity; this result shows how a little discretisation error on a more complex surface may render them unstable.

Figure 4.18 and Figure 4.19 show the error of the time domain closed model compared to the open and closed surface BEMs respectively. The instability seen in Figure 4.16 at the most explicit time-step durations is evident in the error. There is a localised error maxima where $c\Delta_t \approx \Delta_x$ which is common to both figures so must originate from the time domain BEM. That this runs along a line of constant frequency (so occurs for multiple time-step durations) suggests that it is associated with a resonance of the surface geometry. Accuracy is poorer than in section 4.3, however the low minimum error is encouraging.

148
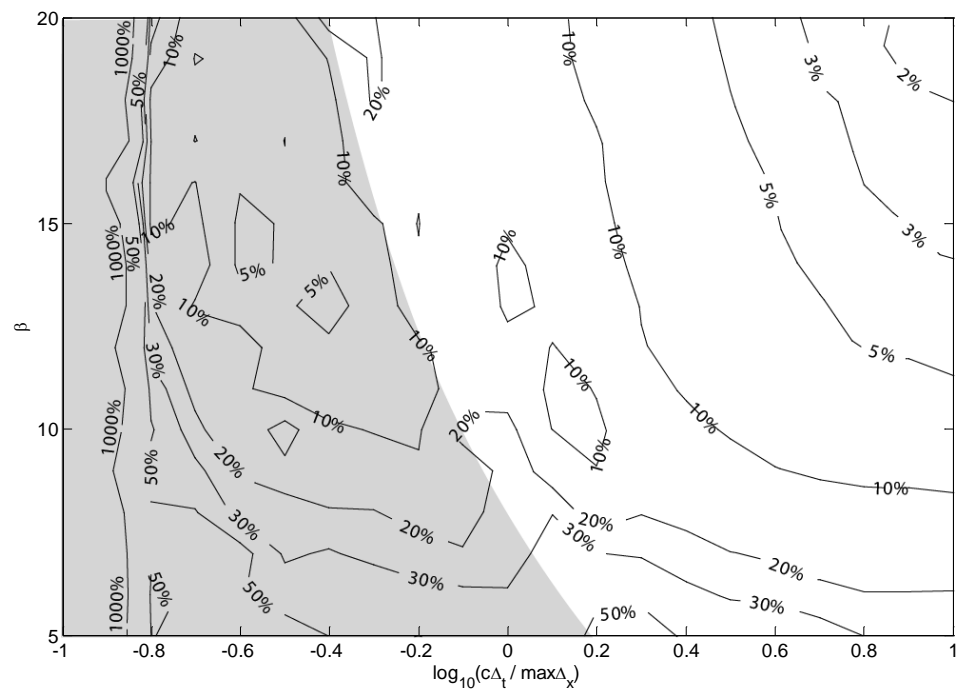
Figure 4.18: Surface error of the time domain BEM for closed surfaces compared to frequency domain
BEM for open surfaces versus temporal resolution and implicitness on the QRD block mesh
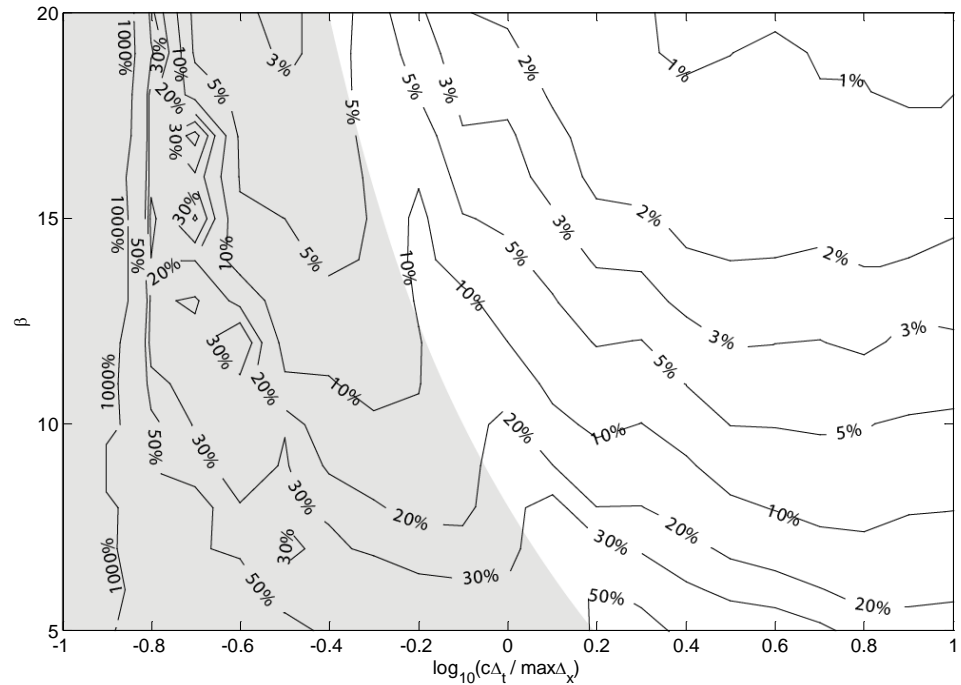

Figure 4.19: Surface error of the time domain BEM for closed surfaces compared to the frequency
domain BEM for closed surfaces versus temporal resolution and implicitness on the QRD block mesh

Error of the open surface time domain model compared to the frequency domain is not shown as no trends can be observed beyond the fact that accuracy is very poor. Omitting the unstable time-step durations, average error for the stable results is still approximately 300%. This result again reinforces the superiority of the CFIE.

4.4.2 Quadratic Residue Diffuser

Here the diffuser is modelled with its fins, shown in translucent blue, increasing the element count to 900. Again all elements are close to square, so integration error is not anticipated to be an issue. The surface now contains a wealth of exterior convex parts and parallel surfaces, whose presence suggests a disposition toward resonances. This is unsurprising since each well may be considered to be a ¼ wave resonator, albeit damped by energy leaving through its mouth. Energy trapped in these is not suppressed by the CFIE as they as physically relevant external features of the problem; their response is part of the desired solution. It will be seen if discretisation errors push these physical lightly damped poles into instability.
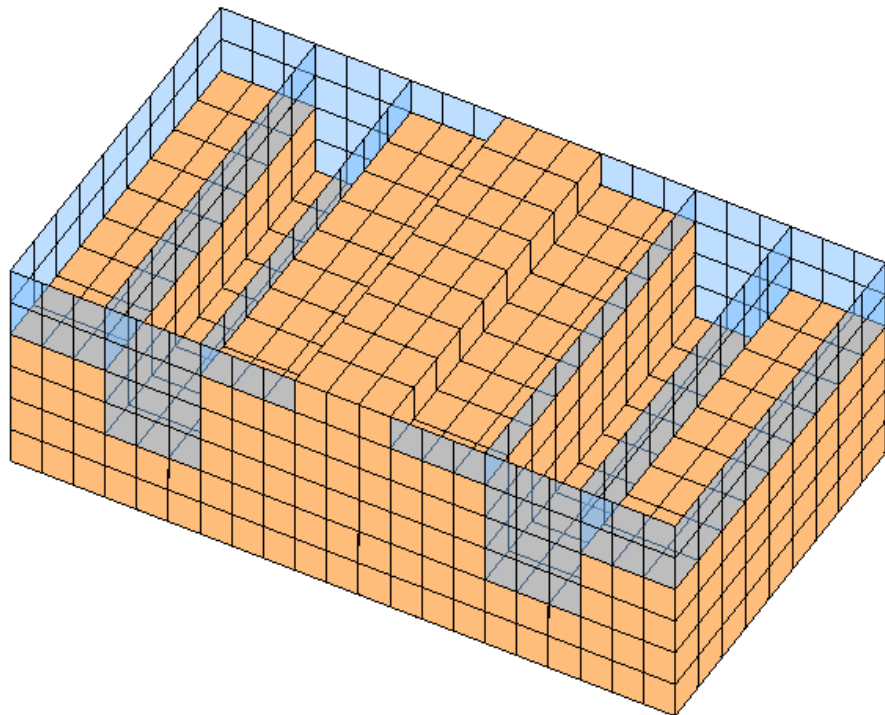
Figure 4.20: Mesh of a QRD

Figure 4.21 shows that addition of the fins has clearly had a negative effect on model stability. In addition to instability of the two most explicit time-step durations observed in Figure 4.16 there are now an additional three that are divergent, plus other artefacts previously restricted to the open model. However, stability is good for most of the more implicit time-step durations, apart from a slowly decaying pole at the fourth most implicit.

The effect of these phenomena on solution accuracy is shown in Figure 4.22. Some instabilities seem to affect all frequencies ($c\Delta_t = 0.1\Delta_x$ and $c\Delta_t = \Delta_x$) while others only seem to become significant at higher frequencies (top of the figure). Error at the most implicit time-step durations is better, though still poorer than has been achieved for other problems.
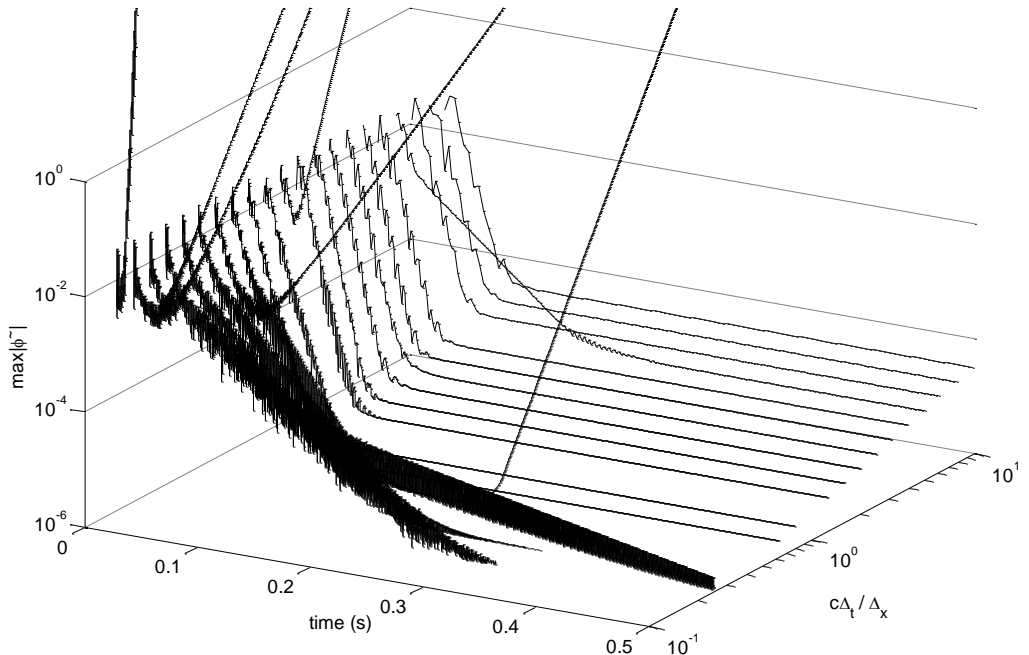
Figure 4.21: Impulse response of the QRD closed model for various time-step durations
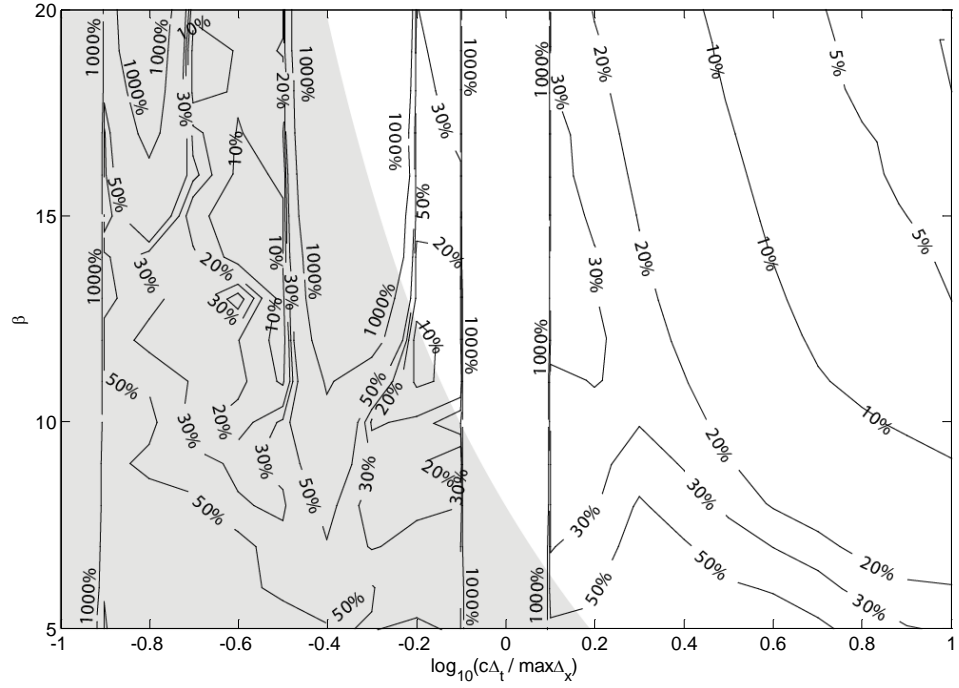
Figure 4.22: Surface error of the time domain BEM for mixed surfaces compared to frequency domain BEM for open surfaces versus temporal resolution and implicitness on the QRD mesh

The model of the QRD by the time domain BEM for open surfaces is unstable for the majority of time-step durations, with the remaining showing poorly damped behaviour. These phenomena have a devastating effect on solution accuracy with error lower than 100% rarely being achieved. Again it can be concluded that the CFIE makes a significant improvement to stability on real world mixed surfaces, however this example has shown that it cannot guarantee it.

4.5 Discussion and Conclusions

This chapter proposed a new time domain BEM variation to model mixed surfaces. This applied the CFIE to the closed part of the surface and the velocity operator to the open part. It was suggested that this should improve stability relative to an all-thin model. Research on the frequency domain BEM was cited in justification of this approach.

The numerical results in sections 4.3 and 4.4 have proven these notions. The mixed surface model has been shown to be more stable and more accurate than an all-thin model. In addition, evidence is shown in support of the stance taken in chapter 2, that implicitness and use of the CFIE increase accuracy and stability.

However, the numerical results also highlight the well known shortcoming of the time domain BEM that stability cannot generally be guaranteed. The instabilities observed for the mixed model of the QRD with an implicit time-step duration result from spatial discretisation error corrupting physical poles, such that their magnitudes become greater than one. The closer to unity magnitude the poles originally were, the greater the likelihood of this occurring, hence the contrast in stability witnessed between the simple surfaces of section 4.3 and the more complex resonant structures of section 4.4.

A finer mesh would improve spatial discretisation so should lower the associated error and improve stability, albeit at a higher computational cost. An argument against implicitness is that it returns a smaller bandwidth for a given spatial resolution than an explicit model would, or equivalently that implicitness demands higher spatial resolution for given temporal resolution. This view suggests higher computational cost for an implicit scheme, although better accuracy and stability result. There is clearly a compromise to be found, and the range of time-step duration and temporal accuracy modelled in the above figures is intended to show trends and not all locations are efficient. For example, in the top right corner of the accuracy figures $c\Delta_t = 10\Delta_x$ and β = 20, which for the QRD mesh ($\Delta_x = 0.15$m) result in a maximum frequency of only 12.5Hz! It is suggested that for efficiency and accuracy $c\Delta_x$ should be the order of Δ_t and that β should be 10 to 15; this region lies central to the above figure and for the QRD mesh gives a maximum frequency of the order of 250Hz.

The following chapter will extend the time domain BEM further by investigating compliant surfaces. In particular, an implementation is developed that allows the well of a QRD to be abstracted to a compliant surface at its mouth. Implications for accuracy and stability are considered.

5 Time Domain BEM for Compliant Surfaces

So far this thesis has concentrated on rigid surfaces which are themselves approximations as no real scatterer has a surface that is truly rigid and impenetrable to sound waves. This is not a bad approximation in certain cases; the diffusers modelled hitherto are effectively rigid within their operational frequency range so were appropriately modelled. However, many materials such as porous absorbers and membrane absorbers are used specifically because of their compliant nature so a rigid model entirely fails to characterise their behaviour. A model of the material of the scatterer is required that can be coupled to the BEM through its unknown surface quantities pressure and normal velocity.

Acoustics is a science whose significant dimensions span orders of magnitude, and there is a need to reconcile models applicable for each. The KIE and resulting BEM models are detailed to the order of wavelength and hence able to describe diffractive effects. However, the interaction of air with a surface such as a porous absorbent is on a much smaller scale, not described by the KIE, where viscous boundary layer and thermal conduction effects are significant. It would be inefficient to couple such models; better to use a material model that is of the same abstraction level as the BEM used to model the scattering. One such suitable model is Finite Element Method and many such coupled algorithms have been published.

However, in the acoustics discipline it is preferred to abstract the properties of the material further so just its interface with the air is modelled. In the frequency domain it is convenient to do this using the concept of surface impedance, which integrates easily into a BEM framework. An equivalent time domain model is sought.

In this chapter a novel time domain BEM algorithm is devised to model compliant surfaces. A simplified version that models surfaces that have absorbing welled regions is implemented and verified. In section 5.1 frequency domain impedance models are discussed along with publications that transfer their meaning to the time domain. The surface reflection coefficient is identified as a more robust candidate for time domain

conversion than impedance. In section 5.2, the time domain boundary integral model for compliant surfaces is developed. This begins with a simple model of a well with a rigid piston at its mouth and is abstracted to include any arbitrary compliant surface where propagation inside the material may be regarded as normal to its surface. The model relies on distinction between sound propagating into and out of the surface. The incoming sound is discretised and the outgoing sound expressed casually from it by convolution. This is believed to be a novel approach.

In section 5.3, the boundary integrals defined in section 5.2 are converted to sums of contour integrals valid for any piecewise flat compliant surface. A simplified surface model allowing the outgoing wave to be delayed and attenuated is introduced in section 5.4 to simulate the behaviour of the mouth of a well containing a hypothetical broadband absorbent. The contour integral formulations are refined to create a numerical integration implementation of this BEM for absorbing welled surfaces. An equivalent frequency domain impedance boundary condition is derived for verification purposes. Verification is presented in section 5.5, including two surfaces typical of diffusing treatments applied in Room Acoustics. Finally conclusions are drawn in section 5.6.

5.1 Surface Impedance

Surface impedance $Z(\mathbf{r},\omega)$ abstracts the behaviour of any locally reacting material to a frequency dependent complex ratio between pressure $P(\mathbf{r},\omega)$ and the inward normal component of particle velocity $V_{in}(\mathbf{r},\omega)$ (Equation 5.1). Its meaning is analogous to its use in Electronics, where it relates voltage and current, again being a potential variable and a flow variable. Its real part is termed resistance and signifies energy that is removed from the system. Its imaginary part is termed reactance and signifies energy that is stored and returned later in the cycle. Because there is an underlying assumption of periodic excitation it does not directly distinguish between energy that is stored for different numbers of periods, only phase is known.

$$Z(\mathbf{r},\omega) = \frac{P(\mathbf{r},\omega)}{V_{in}(\mathbf{r},\omega)} \qquad\qquad 5.1$$

Surface impedance is an ideal notion for the frequency domain BEM as it is a frequency dependent quantity and the scattering body has already been abstracted to a surface. The frequency domain KIE was given in Equation 2.15, and the relationships between velocity potential, pressure and velocity in Equations 2.12 and 2.13. In a direct BEM, Equation 5.2 is substituted into the KIE at the integration point and gives normal velocity in terms of pressure such that there remains only one unknown field on the surface. In an indirect BEM the surface impedance is evaluated as a boundary condition at an observation point approaching the boundary, allowing solution for the single and double layer potential distributions.

$$\hat{\mathbf{n}}.\nabla \Phi^t(\mathbf{r},\omega) = -V_{inward}(\mathbf{r},\omega) = -\frac{P(\mathbf{r},\omega)}{Z(\mathbf{r},\omega)} = -i\omega\rho_0\,\frac{\Phi^t(\mathbf{r},\omega)}{Z(\mathbf{r},\omega)} \qquad\qquad 5.2$$

In contrast time domain non-rigid boundary conditions are usually less straightforward to apply. They usually take a derivative form, as Equations 2.56 and 2.57, so require numerical differentiation or, if possible, analytical differentiation of the discretisation scheme. To arrive at such a form from frequency domain surface impedance requires consideration of its variation with frequency. Measured data is usually in a discreet form, so some form of interpolation with frequency is necessary, and the inverse Fourier transform of the interpolation scheme will form the time domain boundary condition.

Tam and Auriault's [55] 1996 publication is a good example of such a scheme. They first give two single-frequency time domain boundary conditions derived directly from Equation 5.2 and show by Laplace transform that each is unstable for a range of surface reactance values so unsuitable for broadband application. They then progress to interpolate measured impedance data; resistance is assumed to be constant with frequency, and reactance is approximated by the sum of frequency and its reciprocal, each with a scalar weight which is found by a least-squares fit. This leads to a new boundary condition through the association of ω with differentiation and ω^{-1} with integration; stability is proved by Laplace transform.

As was stated in section 2.2.8, the time domain equivalent of Equation 5.2 involves convolution. In accord with Tam and Auriault's two direct boundary conditions, there is immediately ambiguity as two possible convolutions can be implemented; one arises from the impedance (Equation 5.3) and one from its reciprocal the admittance (Equation 5.4). From this it is apparent that $z(\mathbf{r},t)$ and $\beta(\mathbf{r},t)$ are matched filters. However, neither of them represents a causal relationship; both $\dot{\varphi}^t(\mathbf{r},t)$ and $v_n(\mathbf{r},t)$ contain the excitation and scattered waves. Accordingly, it is difficult to clarify by examining $z(\mathbf{r},t)$ or $\beta(\mathbf{r},t)$ whether they represent causal behaviour by the surface; that scattered sound cannot precede incident sound. Fung, Ju and Tallanpragada [56] (2000) write that all roots of $Z(\mathbf{r},\omega)+1$ must have positive imaginary parts to guarantee causality, and that a polynomial fit in frequency cannot generally achieve this; Tam and Auriault's success appears to be a special case.

$$-i\omega\rho_0\Phi^t(\mathbf{r},\omega)=Z(\mathbf{r},\omega)V_n(\mathbf{r},\omega) \quad \rightarrow \quad \rho_0\dot{\varphi}^t(\mathbf{r},t)=z(\mathbf{r},t)*v_n(\mathbf{r},t) \qquad 5.3$$

$$V_n(\mathbf{r},\omega)=-i\omega\rho_0\beta(\mathbf{r},\omega)\Phi^t(\mathbf{r},\omega) \quad \rightarrow \quad v_n(\mathbf{r},t)=\rho_0\beta(\mathbf{r},t)*\dot{\varphi}^t(\mathbf{r},t) \qquad 5.4$$

Instead of interpolating surface impedance or admittance, Fung, Ju and Tallanpragada propose interpolating the surface reflection coefficient. This is the frequency dependent complex ratio between magnitudes of harmonic plane waves travelling into and out of a flat sample of the material, as would occur in an impedance tube, and is related to impedance by the bilinear mapping in Equation 5.5. They write: *"... a direct inversion of $Z(\mathbf{r},\omega)$ generally results in an unstable system of temporal operators. If instead, the equivalent temporal system is derived from the corresponding reflection coefficient $W(\mathbf{r},\omega)$, its stability and convergence are ensured."* This leads to the convolution form of boundary condition in Equation 5.6, where sound into and out of the surface must be distinguished. It is commented that this form is less sensitive to numerical error than the differential based form. $r(\mathbf{r},t)$ is the inverse Fourier Transform of the surface reflection coefficient and will be denoted "surface reflection response" in this thesis, motivated by its form as an impulse response that defines reflection. Causality of the surface response may be easily established by observing that the poles of $W(\mathbf{r},\omega)$ are damped,

and that $w(\mathbf{r},t)$ is zero for negative time. In their 2004 publication, Fung and Ju [58] have migrated to using "wall softness" (Equation 5.7), so named as a value of zero indicates a rigid surface, but the spirit is much the same.

$$W(\mathbf{r},\omega) = \frac{1 - Z(\mathbf{r},\omega)}{1 + Z(\mathbf{r},\omega)} \qquad\qquad 5.5$$

$$\varphi^{out}(\mathbf{r},t) = \varphi^{in}(\mathbf{r},t) * w(\mathbf{r},t) \qquad\qquad 5.6$$

$$\widetilde{W}(\mathbf{r},\omega) = 1 + W(\mathbf{r},\omega) \qquad\qquad 5.7$$

There is a further issue that measured data is discreet and unlikely to cover the entire audible frequency range, so an inverse Fourier transform cannot be used to calculate any of the convolution kernels mentioned above. In particular low frequency information is required to unwrap the phase of the higher frequency behaviour but this is rarely measured. In this thesis only simple surfaces with palpable surface reflection responses will be considered so this is not an immediate issue. However it has the potential to be a serious restriction on the method, and as such has been tackled in the literature.

Fung, Ju and Tallapragada [56] and Fung and Ju [57,58] all decompose surface reflection response into a sum of pole responses, the characteristics of which are found from the complex residues of the interpolation of $W(\mathbf{r},\omega)$. This has the advantages that a representation may be produced when only a finite bandwidth of discrete impedance data is available, and that causality and boundedness are explicitly known. It also replaces the need to store surface history with storage of the most recent contribution by each pole; this is convenient for methods such as FDTD [2] which do not store surface history, less useful for time domain BEM. Modelling the surface as a sum of damped oscillators is also suggested as a future implementation.

These authors, motivated by a variety of research interests, have investigated the concept of impedance in the time domain. The primary contribution which will be carried over into this thesis is the use of surface reflection response to represent surface impedance (Equation 5.6). Crucially for a time marching algorithm this guarantees a

causal surface response if the poles of $W(\mathbf{r},\omega)$ are damped and $w(\mathbf{r},t)$ is zero for negative time. The implementation optimisations for arbitrary surface reflection responses proposed above will not be considered in what follows, not least because it is not clear that these hold any benefit in the time domain BEM framework where the surface history is readily available.

5.2 Incoming and Outgoing Sound Wave Model

The surface reflection response model requires distinction between sound that is propagating into the surface and sound that is propagating out. In order to cast this into a BIE framework the model in Figure 5.1 proved enlightening. This represents a light rigid piston in a rigid baffle, where the piston is coupled to a well of depth d. The properties of the piston are consistent with the assumption of constant velocity potential over an element (piecewise constant spatial basis) implemented in this thesis. The piston does not excite any cross modes in the well so all activity can be described by plane waves propagating vertically. These reflect from the well floor hence the outward wave is simply the inward wave with a change of direction and a delay of $2dc^{-1}$; this is consistent with Schroeder's model of wells in a Quadratic Residue Diffuser [67] (QRD). Total velocity potential at the piston is the sum of the incoming wave and the outgoing wave.
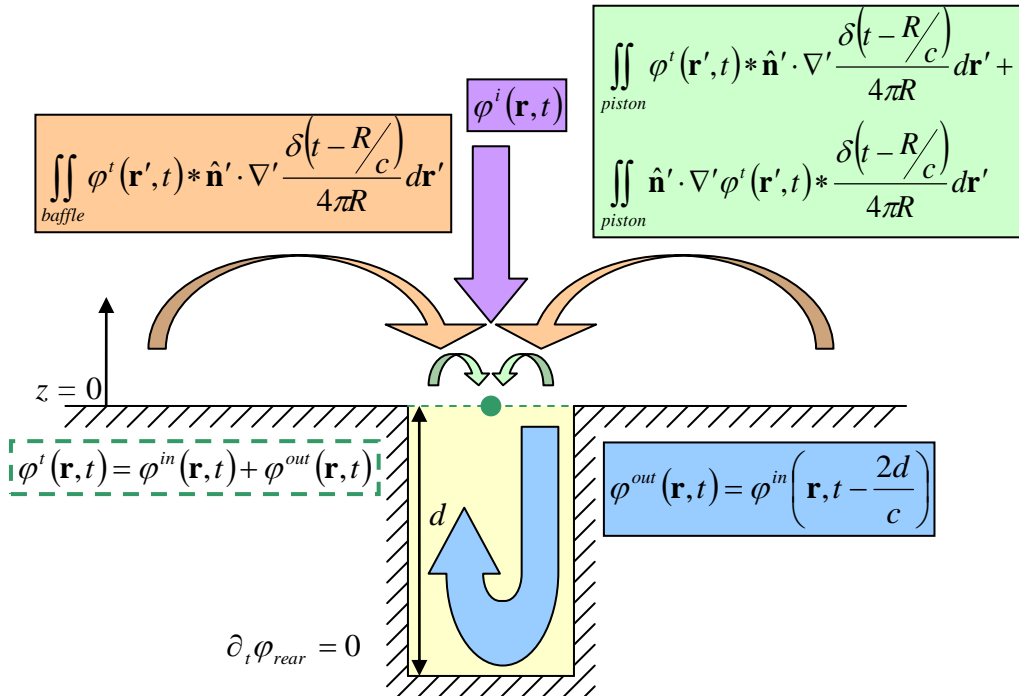
Figure 5.1: Model of a light rigid piston above a well

The arrows, and their correspondingly coloured equations, represent the flow of sound to a collocation point in the centre of the piston. An early conceptual barrier was how to account for reflection back into the well due to radiation impedance of the piston. This turns out to be accounted for directly in the BIEs, indeed it is exactly these equations that are approximated to in the classical model of radiation by a piston [69].

Realising that the BIEs in the figure above express the entirety of the problem and that a well model has limited applicability the above model is generalised. The delayed reflection from the bottom of the well is superseded by a statement that the outgoing wave is found from the incoming wave by convolution with a surface reflection response. If the area of the well is reduced it can be imagined that the surface becomes like an extruded honeycomb material, where each pore has its own surface reflection response. If this area reduction is taken to the limit, the piston becomes irrelevant and what is left is a continuously varying surface reflection response over the surface. However the well analogy still states that each point on the surface behaves independently; the surface is locally reacting. This means that the incoming and outgoing waves are better imagined not as plane waves, but one-dimensional waves

travelling down infinitesimally thin pores perpendicular to the surface. Such a model is appropriate where sound propagates into a material in a direction close to perpendicular to the surface, as may occur due to refraction if the speed of sound in the material is substantially lower than that in air. This is a subclass of the locally reacting impedance surface. What is behind the surface is abstracted; its influence on the surrounding media is completely encapsulated by its surface reflection response. With this in mind, the model depicted above is simply a physical interpretation of the surface reflection response model where piecewise constant spatial basis have been used and the surface reflection response is a delta function delayed by $2dc^{-1}$. The generalised model will now be formalised and discretisation considered.

The outward sound is a causal function of inward sound, defined by convolution with the surface reflection response (Equation 5.6). The total velocity potential on the surface is assumed to be the sum of an inwardly propagating wave and an outwardly propagating wave (Equation 5.8). The propagation directions defined for these waves connect their normal velocities with their temporal derivatives (Equations 5.9 and 5.10). Combining Equations 5.6, 5.8 and 5.10 gives normal velocity in terms of the inward wave (Equation 5.11). These statements for normal velocity are dependent on the local reaction assumption; sound propagating through a point in the surface does so independently of its neighbours and normal velocity is completely defined by the gradient of the incoming and outgoing waves.

$$\varphi^t(\mathbf{r},t) = \varphi^{in}(\mathbf{r},t) + \varphi^{out}(\mathbf{r},t)$$
$$= \varphi^{in}(\mathbf{r},t) * [\delta(t) + w(\mathbf{r},t)] \qquad \qquad 5.8$$

$$\hat{\mathbf{n}} \cdot \nabla \varphi^{in}(\mathbf{r},t) = \hat{\mathbf{n}} \cdot \nabla \varphi^{in}\left(\mathbf{r},t + \frac{z}{c}\right)\bigg|_{z=0} = \frac{\partial}{\partial z} \varphi^{in}\left(\mathbf{r},t + \frac{z}{c}\right)\bigg|_{z=0} = \frac{\dot{\varphi}^{in}(\mathbf{r},t)}{c} \qquad 5.9$$

$$\hat{\mathbf{n}} \cdot \nabla \varphi^{out}(\mathbf{r},t) = \hat{\mathbf{n}} \cdot \nabla \varphi^{out}\left(\mathbf{r},t - \frac{z}{c}\right)\bigg|_{z=0} = \frac{\partial}{\partial z} \varphi^{out}\left(\mathbf{r},t - \frac{z}{c}\right)\bigg|_{z=0} = -\frac{\dot{\varphi}^{out}(\mathbf{r},t)}{c} \qquad 5.10$$

$$\hat{\mathbf{n}} \cdot \nabla \varphi^t(\mathbf{r},t) = \hat{\mathbf{n}} \cdot \nabla \varphi^{in}(\mathbf{r},t) + \hat{\mathbf{n}} \cdot \nabla \varphi^{out}(\mathbf{r},t) = \frac{1}{c}\frac{\partial}{\partial t}\big[\varphi^{in}(\mathbf{r},t) * [\delta(t) - w(\mathbf{r},t)]\big] \qquad 5.11$$

Equations 5.8 and 5.11 wholly define the properties of the surface sound required by the KIE in terms of the inwardly propagating wave. It is therefore natural to discretise the inwardly propagating wave as the unknown surface quantity (Equation 5.12); here the discretisation weights have reverted to being named $w_{j,n}$ since they do not represent instantaneous total surface velocity potential.

$$\varphi^{in}(\mathbf{r},t) = \sum_{n=1}^{N_s}\sum_{j=1}^{N_t} w_{j,n}\, f_n(\mathbf{r}) T_j(t) \qquad \qquad 5.12$$

The above set of equations is believed to be a novel approach to discretisation of a compliant surface. The inwardly propagating wave has been identified as the fundamentally unknown quantity, discretised, and had the total surface sound evaluated from it. Use of surface reflection response to characterise a surface is also believed to be new within the context of time domain BIE. In what follows these equations will be transformed into a time domain BEM.

Surface normal velocity is non-zero, so the boundary conditions associated with $L_v\{...\}$, and therefore $L_c\{...\}$, cannot be used on a compliant surface; $L_p\{...\}$ must be used exclusively. However, as section 4.2 states, the boundary condition is a local restriction and other operators may be used on other parts of the surface. A surface can be

conceived that contains rigid thick parts on which $L_c\{...\}$ is used, rigid fins on which $L_v\{...\}$ is used, and thick compliant parts on which $L_p\{...\}$ is used. Again no special problem partitioning is required as long as the integration routine can handle all surface types. Note that the well in Figure 5.1 has now been abstracted to an infinitesimally thin surface that behaves in accordance with its surface reflection response, so the comments on jump potential in section 4.2 still hold. Care will be taken in the following section to show that sound is not simply allowed to flow into Ω_-.

5.3 Derivation of contour integrals for compliant surfaces

This section extends the contour integration scheme of section 3.2 to support compliant surfaces and the surface reflection response discretisation model. Many definitions are carried across and conclusions cross referenced. The coordinate system of section 3.2.1 will be used; individual terms are described in the glossary but a brief recap of section 3.2.1.1 might be advisable. Again the derivation will be pursued such that it is valid for ~~an arbitrary~~ a piece-wise constant discretisation scheme on a piecewise flat surface.

5.3.1 Scattered velocity potential

Scattered velocity potential is described by the KIE (Equation 2.6). Section 3.2.1.4 evaluates the scattering due to the double layer potential part of the KIE as a contour integral (Equation 3.33) so here the focus will be on evaluating the single layer potential. Below the sifting property of the delta function is applied:

$$\iint_S \hat{\mathbf{n}}'\cdot\nabla'\varphi^t(\mathbf{r}',t) * \frac{\delta\left(t-R/c\right)}{4\pi R}d\mathbf{r}' = \iint_S \frac{\hat{\mathbf{n}}'\cdot\nabla'\varphi^t\left(\mathbf{r}',t-R/c\right)}{4\pi R}d\mathbf{r}'$$
5.13

The incoming and outgoing wave model provides a convenient link between normal velocity and the temporal derivative of velocity potential (Equation 5.11). The retarded nature of the integrand allows the temporal derivative to be converted to a spatial derivative with respect to R by application of the chain rule:

$$\hat{\mathbf{n}} \cdot \nabla \varphi^t \left(\mathbf{r}', t - R/_c \right) = \frac{1}{c} \left[\dot{\varphi}^{in} \left(\mathbf{r}', t - R/_c \right) - \dot{\varphi}^{out} \left(\mathbf{r}', t - R/_c \right) \right]$$

$$= -\frac{\partial}{\partial R} \left[\varphi^{in} \left(\mathbf{r}', t - R/_c \right) - \varphi^{out} \left(\mathbf{r}', t - R/_c \right) \right]$$

5.14

Equation 5.14 is substituted into Equation 5.13 below. As in section 3.2.1.4, the integral over each flat surface section (element) is converted to polar form then the integration variables are changed so that analytical integration may be performed with respect to R. This requires the derivative of Equation 5.15. The angular integral is converted to a contour integral as defined in section 3.2.1.2.

$$\frac{dR}{dr} = \frac{r}{R}$$

5.15

$$\iint_S \frac{\hat{\mathbf{n}}' \cdot \nabla' \varphi^t \left(\mathbf{r}', t - R/_c \right)}{4\pi R} d\mathbf{r}' = -\frac{1}{4\pi} \iint_S \frac{1}{R} \frac{\partial}{\partial R} \left[\varphi^{in} \left(\mathbf{r}', t - R/_c \right) - \varphi^{out} \left(\mathbf{r}', t - R/_c \right) \right] d\mathbf{r}'$$

$$= -\frac{1}{4\pi} \sum_{elements} \int_0^{2\pi} \int_{r_{min}(\theta)}^{r_{max}(\theta)} \frac{r}{R} \frac{\partial}{\partial R} \left[\varphi^{in} \left(\mathbf{r}', t - R/_c \right) - \varphi^{out} \left(\mathbf{r}', t - R/_c \right) \right] dr d\theta$$

$$= -\frac{1}{4\pi} \sum_{elements} \int_0^{2\pi} \int_{R_{min}(\theta)}^{R_{max}(\theta)} \frac{\partial}{\partial R} \left[\varphi^{in} \left(\mathbf{r}', t - R/_c \right) - \varphi^{out} \left(\mathbf{r}', t - R/_c \right) \right] dR d\theta$$

$$= -\frac{1}{4\pi} \sum_{elements} \int_0^{2\pi} \left[\varphi^{in} \left(\mathbf{r}', t - R/_c \right) - \varphi^{out} \left(\mathbf{r}', t - R/_c \right) \right]_{R_{min}(\theta)}^{R_{max}(\theta)} d\theta$$

$$= \frac{1}{4\pi} \sum_{elements} \left[\begin{array}{l} \theta_{origin} \left[\varphi^{in} \left(\mathbf{r}', t - |z|/_c \right) - \varphi^{out} \left(\mathbf{r}', t - |z|/_c \right) \right] \\ - \oint_{S_n} \left[\varphi^{in} \left(\mathbf{r}', t - R/_c \right) - \varphi^{out} \left(\mathbf{r}', t - R/_c \right) \right] d\theta \end{array} \right]$$

5.16

Equation 3.33 gives the contour integral resulting from the double layer potential as follows. The surface reflection response discretisation model is substituted:

$$\iint_S \varphi^t(\mathbf{r}',t) * \hat{\mathbf{n}}'\cdot\nabla' \frac{\delta\!\left(t - R/c\right)}{4\pi R} d\mathbf{r}' = \sum_{elements} \left[\begin{array}{c} \dfrac{\theta_{origin}}{4\pi} \dfrac{z}{|z|} \varphi^t\!\left(\mathbf{r}',t - |z|/c\right) \\[2mm] - z \displaystyle\oint_{S_n} \dfrac{\varphi^t\!\left(\mathbf{r}',t - R/c\right)}{4\pi R} d\theta \end{array} \right]$$

$$= \sum_{elements} \left[\begin{array}{c} \dfrac{\theta_{origin}}{4\pi} \dfrac{z}{|z|}\left[\varphi^{in}\!\left(\mathbf{r}',t - |z|/c\right) + \varphi^{out}\!\left(\mathbf{r}',t - |z|/c\right)\right] \\[2mm] - z \displaystyle\oint_{S_n} \dfrac{1}{4\pi R}\left[\varphi^{in}\!\left(\mathbf{r}',t - R/c\right) + \varphi^{out}\!\left(\mathbf{r}',t - R/c\right)\right] d\theta \end{array} \right]$$

5.17

Equations 5.16 and 5.17 substituted into the KIE to give the statement for scattered velocity potential below. Terms are grouped according to their association with either the incoming or outgoing waves. This statement is valid for any discretisation scheme on a polyhedron.

$$\varphi^s(\mathbf{r},t) = \iint_S \varphi^t(\mathbf{r}',t) * \hat{\mathbf{n}}'\cdot\nabla' \frac{\delta\!\left(t - R/c\right)}{4\pi R} d\mathbf{r}' - \iint_S \hat{\mathbf{n}}'\cdot\nabla'\varphi^t(\mathbf{r}',t) * \frac{\delta\!\left(t - R/c\right)}{4\pi R} d\mathbf{r}'$$

$$= \sum_{elements} \left[\begin{array}{c} \dfrac{\theta_{origin}}{4\pi}\left(\dfrac{z}{|z|} - 1\right)\varphi^{in}\!\left(\mathbf{r}',t - |z|/c\right) - \dfrac{1}{4\pi}\displaystyle\oint_{S_n}\left(\dfrac{z}{R} - 1\right)\varphi^{in}\!\left(\mathbf{r}',t - R/c\right) d\theta \\[3mm] + \dfrac{\theta_{origin}}{4\pi}\left(\dfrac{z}{|z|} + 1\right)\varphi^{out}\!\left(\mathbf{r}',t - |z|/c\right) - \dfrac{1}{4\pi}\displaystyle\oint_{S_n}\left(\dfrac{z}{R} + 1\right)\varphi^{out}\!\left(\mathbf{r}',t - R/c\right) d\theta \end{array} \right]$$

5.18

The meaning of the various terms in Equation 5.18 with respect to their interaction with the incoming wave and its annihilation within Ω_- is summarised in Table 5.1. The existence of an immediate scattered wave that attempts to cancel the incoming wave implies that, as desired, incoming sound is not allowed to flow into Ω_-. The double and single layer potentials ally to create an anechoic termination for incoming waves plus a means of radiation of outgoing waves.

Table 5.1: Interpretation of scattered wave terms

Term	Value	Interpretation
$\dfrac{\theta_{origin}}{4\pi}\left(\dfrac{z}{|z|}-1\right)$	0 in Ω_+ -1 in Ω_-	Describes a plane wave propagating into Ω_- cancelling the incoming plane wave.
$\left(\dfrac{z}{R}-1\right)$	$\widehat{\mathbf{n}}'\cdot\widehat{\mathbf{R}}-1$	Describes the diffraction of the above cancelling wave due to the finite size of S_n. Cardoid pattern below S.
$\dfrac{\theta_{origin}}{4\pi}\left(\dfrac{z}{|z|}+1\right)$	1 in Ω_+ 0 in Ω_-	Describes the outgoing plane wave propagating into Ω_+ .
$\left(\dfrac{z}{R}+1\right)$	$\widehat{\mathbf{n}}'\cdot\widehat{\mathbf{R}}+1$	Describes the diffraction of the outgoing wave due to the finite size of S_n. Cardoid pattern above S.

For a rigid surface $w(\mathbf{r},t)=\delta(t)$ so $\varphi^{out}(\mathbf{r},t)=\varphi^{in}(\mathbf{r},t)$; it is reassuring that in this case the scattered velocity potential resumes the form of the rigid surface model:

$$\varphi^s(\mathbf{r},t)=\sum_{elements}\left[\begin{array}{l}\dfrac{\theta_{origin}}{4\pi}\left(\dfrac{z}{|z|}-1\right)\varphi^{in}\left(\mathbf{r}',t-|z|/c\right)-\dfrac{1}{4\pi}\oint_{S_n}\left(\dfrac{z}{R}-1\right)\varphi^{in}\left(\mathbf{r}',t-R/c\right)d\theta\\[2mm]+\dfrac{\theta_{origin}}{4\pi}\left(\dfrac{z}{|z|}+1\right)\varphi^{in}\left(\mathbf{r}',t-|z|/c\right)-\dfrac{1}{4\pi}\oint_{S_n}\left(\dfrac{z}{R}+1\right)\varphi^{in}\left(\mathbf{r}',t-R/c\right)d\theta\end{array}\right] \quad 5.19$$

$$=\sum_{elements}\left[\dfrac{\theta_{origin}}{4\pi}\dfrac{z}{|z|}\varphi^t\left(\mathbf{r}',t-|z|/c\right)-\dfrac{1}{4\pi}\oint_{S_n}\dfrac{z}{R}\varphi^t\left(\mathbf{r}',t-R/c\right)d\theta\right]$$

5.3.2 Scattered Pressure

The scattered pressure is readily found by temporal differentiation of Equation 5.18. This statement is valid for ~~any discretisation scheme~~ piece-wise constant elements on a polyhedron:

$$p^s(\mathbf{r},t)=-\rho_0\dot{\varphi}^s(\mathbf{r},t)$$

$$=-\rho_0\sum_{elements}\left[\begin{array}{l}\dfrac{\theta_{origin}}{4\pi}\left(\dfrac{z}{|z|}-1\right)\dot{\varphi}^{in}\left(\mathbf{r}',t-|z|/c\right)-\dfrac{1}{4\pi}\oint_{S_n}\left(\dfrac{z}{R}-1\right)\dot{\varphi}^{in}\left(\mathbf{r}',t-R/c\right)d\theta\\[2mm]+\dfrac{\theta_{origin}}{4\pi}\left(\dfrac{z}{|z|}+1\right)\dot{\varphi}^{out}\left(\mathbf{r}',t-|z|/c\right)-\dfrac{1}{4\pi}\oint_{S_n}\left(\dfrac{z}{R}+1\right)\dot{\varphi}^{out}\left(\mathbf{r}',t-R/c\right)d\theta\end{array}\right] \quad 5.20$$

5.3.3 Scattered Velocity

The scattered velocity is the gradient of scattered velocity potential. Section 3.2.1.7 evaluates the scattered velocity due to the double layer potential part of the KIE as a contour integral (Equation 3.47) so here the focus will be on evaluating the velocity scattered by the single layer potential. First the incoming and outgoing wave model is exploited to express the normal velocity at the integration point as a temporal derivative of velocity potential (Equation 5.11). Then, the gradient operator is moved inside the integral under the assumption that $\mathbf{r}$ is an off-body point so the velocity potential field is smooth:

$$\nabla \iint_S \hat{\mathbf{n}}'\cdot\nabla'\varphi^t\left(\mathbf{r}',t\right) * \frac{\delta\left(t-R/c\right)}{4\pi R} d\mathbf{r}' = \nabla \iint_S \frac{\hat{\mathbf{n}}'\cdot\nabla'\varphi^t\left(\mathbf{r}',t-R/c\right)}{4\pi R} d\mathbf{r}'$$

$$= \nabla \iint_S \frac{\dot{\varphi}^{in}\left(\mathbf{r}',t-R/c\right)-\dot{\varphi}^{out}\left(\mathbf{r}',t-R/c\right)}{4\pi c R} d\mathbf{r}' \quad 5.21$$

$$= \iint_S \nabla \frac{\dot{\varphi}^{in}\left(\mathbf{r}',t-R/c\right)-\dot{\varphi}^{out}\left(\mathbf{r}',t-R/c\right)}{4\pi c R} d\mathbf{r}'$$

The gradient operator is evaluated at $\mathbf{r}$ so it is only the dependency of the scattered velocity potential on R that contributes; the local variation of surface velocity potential at the integration point does not. At $\mathbf{r}$ the direction of increasing R is $\hat{\mathbf{R}}$:

$$\nabla \iint_S \hat{\mathbf{n}}'\cdot\nabla'\varphi^t\left(\mathbf{r}',t\right) * \frac{\delta\left(t-R/c\right)}{4\pi R} d\mathbf{r}' = \iint_S \nabla \frac{\dot{\varphi}^{in}\left(\mathbf{r}',t-R/c\right)-\dot{\varphi}^{out}\left(\mathbf{r}',t-R/c\right)}{4\pi c R} d\mathbf{r}'$$

$$= \iint_S \hat{\mathbf{R}} \frac{\partial}{\partial R} \frac{\dot{\varphi}^{in}\left(\mathbf{r}',t-R/c\right)-\dot{\varphi}^{out}\left(\mathbf{r}',t-R/c\right)}{4\pi c R} d\mathbf{r}'$$

$$5.22$$

In order to match the numerical integration framework used in section 3.2.1.7 it is useful to replace $\hat{\mathbf{R}}$ with an equivalent statement in terms of the cartesian unit vectors of Figure 3.21 (Equation 5.24). The surface integrals are decomposed as polar or cartesian below. To aid succinctness $s\left(\mathbf{r}',R,t\right)$ is defined:

$$s(\mathbf{r}',R,t) = \frac{\dot{\varphi}^{in}(\mathbf{r}',t - R/c) - \dot{\varphi}^{out}(\mathbf{r}',t - R/c)}{4\pi cR}$$ 5.23

$$\hat{\mathbf{R}} = \frac{\mathbf{R}}{R} = \frac{z}{R}\hat{\mathbf{n}}' - \frac{v}{R}\hat{\mathbf{v}} - \frac{w}{R}\hat{\mathbf{w}}$$ 5.24

$$\iint_S \hat{\mathbf{R}}\frac{\partial s}{\partial R}d\mathbf{r}' = \sum_{elements}\left[\hat{\mathbf{n}}\iint_{S_n}\frac{z}{R}\frac{\partial s}{\partial R}d\mathbf{r}' - \hat{\mathbf{v}}\iint_{S_n}\frac{v}{R}\frac{\partial s}{\partial R}d\mathbf{r}' - \hat{\mathbf{w}}\iint_{S_n}\frac{w}{R}\frac{\partial s}{\partial R}d\mathbf{r}'\right]$$
$$= \sum_{elements}\left[\hat{\mathbf{n}}z\iint_{S_n}\frac{r}{R}\frac{\partial s}{\partial R}drd\theta - \hat{\mathbf{v}}\iint_{S_n}\frac{v}{R}\frac{\partial s}{\partial R}dvdw - \hat{\mathbf{w}}\iint_{S_n}\frac{w}{R}\frac{\partial s}{\partial R}dvdw\right]$$ 5.25

The integration variables are changed to allow analytical integration in R; this requires the derivatives of Equation 5.26. In Equation 5.27 these are substituted and then the analytical integration performed.

$$\frac{dR}{dr} = \frac{r}{R}; \qquad \frac{dR}{dv} = \frac{v}{R}; \qquad \frac{dR}{dw} = \frac{w}{R}$$ 5.26

$$\iint_S \hat{\mathbf{R}}\frac{\partial q}{\partial R}d\mathbf{r}' = \sum_{elements}\left[\hat{\mathbf{n}}z\iint_{S_n}\frac{r}{R}\frac{\partial s}{\partial R}drd\theta - \hat{\mathbf{v}}\iint_{S_n}\frac{v}{R}\frac{\partial s}{\partial R}dvdw - \hat{\mathbf{w}}\iint_{S_n}\frac{w}{R}\frac{\partial s}{\partial R}dvdw\right]$$
$$= \sum_{elements}\left[\hat{\mathbf{n}}z\iint_{S_n}\frac{\partial s}{\partial R}dRd\theta - \hat{\mathbf{v}}\iint_{S_n}\frac{\partial s}{\partial R}dRdw - \hat{\mathbf{w}}\iint_{S_n}\frac{\partial s}{\partial R}dRdw\right]$$ 5.27
$$= \sum_{elements}\begin{bmatrix}\hat{\mathbf{n}}'z\int_{S_n}[s(\mathbf{r}',R,t)]_{R_{min}(\theta)}^{R_{max}(\theta)}d\theta \\ -\hat{\mathbf{v}}\int_{S_n}[s(\mathbf{r}',R,t)]_{R(v_{min})}^{R(v_{max})}dw \\ -\hat{\mathbf{w}}\int_{S_n}[s(\mathbf{r}',R,t)]_{R(w_{min})}^{R(w_{max})}dv\end{bmatrix}$$

The velocity scattered by the double layer potential term is derived in Equation 3.47 and recapped below. The definitions of $q(\mathbf{r}',R,t)$ and its derivative with respect to R follow:

168

$$\nabla \iint_S \varphi^t(\mathbf{r}',t) * \hat{\mathbf{n}}' \cdot \nabla' \frac{\delta\left(t - R/c\right)}{4\pi R} d\mathbf{r}' = -\sum_{elements} \begin{bmatrix} \hat{\mathbf{n}}' \int_{S_n} \left[q(\mathbf{r}',R,t) + \frac{z^2}{R}\frac{\partial q}{\partial R} \right]_{R_{min}(\theta)}^{R_{max}(\theta)} d\theta \\ -\hat{\mathbf{v}}z \int_{S_n} \left[\frac{1}{R}\frac{\partial q}{\partial R} \right]_{R(v_{min})}^{R(v_{max})} dw \\ -\hat{\mathbf{w}}z \int_{S_n} \left[\frac{1}{R}\frac{\partial q}{\partial R} \right]_{R(w_{min})}^{R(w_{max})} dv \end{bmatrix} \qquad 5.28$$

$$q(\mathbf{r}',R,t) = \frac{\varphi^t\left(\mathbf{r}', t - R/c\right)}{4\pi R} \qquad 5.29$$

$$\frac{dq}{dR} = -\frac{\dot{\varphi}^t\left(\mathbf{r}', t - R/c\right)}{4\pi c R} - \frac{\varphi^t\left(\mathbf{r}', t - R/c\right)}{4\pi R^2} \qquad 5.30$$

Equations 5.27 and 5.28 are combined to give a statement for the velocity scattered from a compliant surface:

$$\mathbf{v}(\mathbf{r},t) = \nabla \iint_S \varphi^t(\mathbf{r}',t) * \hat{\mathbf{n}}' \cdot \nabla' \frac{\delta\left(t - R/c\right)}{4\pi R} d\mathbf{r}' - \nabla \iint_S \hat{\mathbf{n}}' \cdot \nabla' \varphi^t(\mathbf{r}',t) * \frac{\delta\left(t - R/c\right)}{4\pi R} d\mathbf{r}'$$

$$= -\sum_{elements} \begin{bmatrix} \hat{\mathbf{n}}' \int_{S_n} \left[q(\mathbf{r}',R,t) + \frac{z^2}{R}\frac{\partial q}{\partial R} + z\,s(\mathbf{r}',R,t) \right]_{R_{min}(\theta)}^{R_{max}(\theta)} d\theta \\ -\hat{\mathbf{v}} \int_{S_n} \left[\frac{z}{R}\frac{\partial q}{\partial R} + s(\mathbf{r}',R,t) \right]_{R(v_{min})}^{R(v_{max})} dw \\ -\hat{\mathbf{w}} \int_{S_n} \left[\frac{z}{R}\frac{\partial q}{\partial R} + s(\mathbf{r}',R,t) \right]_{R(w_{min})}^{R(w_{max})} dv \end{bmatrix} \qquad 5.31$$

Expanding the terms defined in Equations 5.23, 5.29 and 5.30 and gathering inward and outward terms together results in the following expression for scattered velocity. The integrals have been converted to contour integrals using the equivalences derived in sections 3.2.1.2 and 3.2.1.3. This statement is valid for ~~any discretisation scheme~~ <u>piecewise constant elements</u> on a piecewise flat surface.

$$
\mathbf{v}(\mathbf{r},t) = -\sum_{\text{elements}} \left[
\begin{array}{l}
\hat{\mathbf{n}}' \oint_{S_n} \left[\left(1 - \frac{z^2}{R^2}\right) \frac{\varphi^{in}\left(\mathbf{r}', t - R/c\right)}{4\pi R} - \left(\frac{z^2}{R} - z\right) \frac{\dot{\varphi}^{in}\left(\mathbf{r}', t - R/c\right)}{4\pi c R} \right] d\theta \\[3mm]
+ \hat{\mathbf{n}}' \oint_{S_n} \left[\left(1 - \frac{z^2}{R^2}\right) \frac{\varphi^{out}\left(\mathbf{r}', t - R/c\right)}{4\pi R} - \left(\frac{z^2}{R} + z\right) \frac{\dot{\varphi}^{out}\left(\mathbf{r}', t - R/c\right)}{4\pi c R} \right] d\theta \\[3mm]
+ \hat{\mathbf{n}}' \theta_{origin} \left[\left(1 - \frac{z}{|z|}\right) \frac{\dot{\varphi}^{in}\left(\mathbf{r}_{origin}, t - |z|/c\right)}{4\pi c} \right] \\[3mm]
+ \hat{\mathbf{n}}' \theta_{origin} \left[\left(1 + \frac{z}{|z|}\right) \frac{\dot{\varphi}^{out}\left(\mathbf{r}_{origin}, t - |z|/c\right)}{4\pi c} \right] \\[3mm]
+ \hat{\mathbf{v}} \oint_{S_n} \left[\frac{z}{R^2} \frac{\varphi^{in}\left(\mathbf{r}', t - R/c\right)}{4\pi R} + \left(\frac{z}{R} - 1\right) \frac{\dot{\varphi}^{in}\left(\mathbf{r}', t - R/c\right)}{4\pi c R} \right] dw \\[3mm]
+ \hat{\mathbf{v}} \oint_{S_n} \left[\frac{z}{R^2} \frac{\varphi^{out}\left(\mathbf{r}', t - R/c\right)}{4\pi R} + \left(\frac{z}{R} + 1\right) \frac{\dot{\varphi}^{out}\left(\mathbf{r}', t - R/c\right)}{4\pi c R} \right] dw \\[3mm]
+ \hat{\mathbf{w}} \oint_{S_n} \left[\frac{z}{R^2} \frac{\varphi^{in}\left(\mathbf{r}', t - R/c\right)}{4\pi R} + \left(\frac{z}{R} - 1\right) \frac{\dot{\varphi}^{in}\left(\mathbf{r}', t - R/c\right)}{4\pi c R} \right] dv \\[3mm]
+ \hat{\mathbf{w}} \oint_{S_n} \left[\frac{z}{R^2} \frac{\varphi^{out}\left(\mathbf{r}', t - R/c\right)}{4\pi R} + \left(\frac{z}{R} + 1\right) \frac{\dot{\varphi}^{out}\left(\mathbf{r}', t - R/c\right)}{4\pi c R} \right] dv
\end{array}
\right] \qquad 5.32
$$

5.4 Derivation of a time domain BEM for absorbing welled surfaces

Care has been taken to derive the preceding contour integrals for any surface discretisation and surface reflection response to maximise potential application. However, the remainder of this chapter will concern itself with verifying the derivation for a simpler boundary condition. This shall be that of the well elements depicted in Figure 5.1 plus frequency independent absorption. The surface reflection response is given in Equation 5.33, where d_n is the depth of the well behind S_n and $0 \le r_n \le 1$ is

the ratio of sound that is reflected. The discretisation scheme previously used for $\varphi^t(\mathbf{r},t)$ (piecewise constant spatial basis according to Equation 2.17, piecewise polynomial temporal basis according to Equations 2.19 and 2.60) shall be used for $\varphi^{in}(\mathbf{r},t)$.

$$
w(\mathbf{r},t) = r_n \delta\left(t - \frac{2d_n}{c}\right)\Bigg|_{\mathbf{r}\in S_n}
$$

5.33

5.4.1 Pressure Operator

The pressure operator is defined as the scattered pressure (Equation 5.20) divided by $-\rho_0$, so when $\alpha = 0$ the elements of the interaction matrix are defined according to Equation 3.35. The element self-interaction term (Equation 3.36) is defined by the boundary condition to be the limit as the observer point approaches the surface element from inside the body. Here the contour integral has been replaced by a sum of edge integrals using the identities derived in section 3.2.1.2 so the statements are in a form ready for numerical implementation.

$$
\begin{aligned}
Z_{m,n,l} &= -L_p\left\{f_n(\mathbf{r})T_{j-l}(t)\right\}\Big|_{t=t_j;\mathbf{r}=\mathbf{r_m^c}} \\
&= \frac{1}{4\pi}\sum_{edges}\int_0^1\left[\left(\frac{z}{R}-1\right)\dot{T}_{j-l}\left(t-\frac{R}{c}\right)+\left(\frac{z}{R}+1\right)r_n\,\dot{T}_{j-l}\left(t-\frac{R+2d_n}{c}\right)\right]\frac{d\theta}{d\mu}d\mu \\
&\quad -\frac{\theta_{origin}}{4\pi}\left[\left(\frac{z}{|z|}-1\right)\dot{T}_{j-l}\left(t_j-\frac{|z|}{c}\right)+\left(\frac{z}{|z|}+1\right)r_n\,\dot{T}_{j-l}\left(t-\frac{|z|+2d_n}{c}\right)\right]
\end{aligned}
$$

5.34

$$
\begin{aligned}
Z_{n,n,l} &= -L_p\left\{f_n(\mathbf{r})T_{j-l}(t)\right\}\Big|_{t=t_j;\mathbf{r}=\mathbf{r_n^c}} \\
&= \lim_{z\to 0_-}\left[\begin{array}{l}\frac{1}{4\pi}\sum_{edges}\int_0^1\left[\left(\frac{z}{R}-1\right)\dot{T}_{j-l}\left(t_j-\frac{R}{c}\right)+\left(\frac{z}{R}+1\right)r_n\,\dot{T}_{j-l}\left(t_j-\frac{R+2d_n}{c}\right)\right]\frac{d\theta}{d\mu}d\mu \\ -\frac{\theta_{origin}}{4\pi}\left[\left(\frac{z}{|z|}-1\right)\dot{T}_{j-l}\left(t_j-\frac{|z|}{c}\right)+\left(\frac{z}{|z|}+1\right)r_n\,\dot{T}_{j-l}\left(t_j-\frac{|z|+2d_n}{c}\right)\right]\end{array}\right] \\
&= \frac{1}{4\pi}\sum_{edges}\int_0^1\left[-\dot{T}_{j-l}\left(t_j-\frac{R}{c}\right)+r_n\,\dot{T}_{j-l}\left(t_j-\frac{R+2d_n}{c}\right)\right]\frac{d\theta}{d\mu}d\mu+\frac{\theta_{origin}}{4\pi}\dot{T}_{j-l}(t_j)
\end{aligned}
$$

5.35

5.4.2 Velocity Operator

The velocity operator is equal to $-\hat{\mathbf{n}} \cdot \mathbf{v}^s(\mathbf{r}, t)$ and is calculated as follows, where the (v, w, z) coordinate system has been chosen such that $\hat{\mathbf{n}} \cdot \hat{\mathbf{w}} = 0$. Here the contour integrals have been replaced by a sum of the edge integrals using the identities derived in sections 3.2.1.2 and 3.2.1.3 so the statements are in a form ready for numerical implementation. Equation 5.36 evaluates the elements of the interaction matrices for rows where $\alpha = 1$. $L_v\{..\}$ will never be used for self-interaction since its boundary condition is at odds with the compliancy of the surface, hence no limit as $\mathbf{r}$ approaches S is taken.

$$
Z_{m,n,l} = cL_v\left\{ f_n(\mathbf{r}) T_{j-l}(t) \right\}\Big|_{t=t_j;\, \mathbf{r}=\mathbf{r}_m^c}
$$

$$
= \begin{bmatrix}
\dfrac{\hat{\mathbf{n}} \cdot \hat{\mathbf{n}}'}{4\pi} \sum_{\text{edges}} \int_0^1 \left[\left(1 - \dfrac{z^2}{R^2}\right)\dfrac{c}{R} T_{j-l}\left(t_j - \dfrac{R}{c}\right) - \left(\dfrac{z^2}{R^2} - \dfrac{z}{R}\right)\dot{T}_{j-l}\left(t_j - \dfrac{R}{c}\right) \right]\dfrac{d\theta}{d\mu}\,d\mu \\[2em]
+ \dfrac{\hat{\mathbf{n}} \cdot \hat{\mathbf{n}}'}{4\pi} \sum_{\text{edges}} \int_0^1 \begin{bmatrix} \left(1 - \dfrac{z^2}{R^2}\right)\dfrac{c}{R} r_n T_{j-l}\left(t_j - \dfrac{R + 2d_n}{c}\right) \\[1em] -\left(\dfrac{z^2}{R^2} + \dfrac{z}{R}\right) r_n \dot{T}_{j-l}\left(t_j - \dfrac{R + 2d_n}{c}\right) \end{bmatrix} \dfrac{d\theta}{d\mu}\,d\mu \\[2em]
+ \dfrac{\hat{\mathbf{n}} \cdot \hat{\mathbf{n}}'}{4\pi}\theta_{origin}\left[\left(1 - \dfrac{z}{|z|}\right)\dot{T}_{j-l}\left(t_j - \dfrac{R}{c}\right) \right] \\[2em]
+ \dfrac{\hat{\mathbf{n}} \cdot \hat{\mathbf{n}}'}{4\pi}\theta_{origin}\left[\left(1 + \dfrac{z}{|z|}\right) r_n \dot{T}_{j-l}\left(t_j - \dfrac{R + 2d_n}{c}\right) \right] \\[2em]
+ \dfrac{\hat{\mathbf{n}} \cdot \hat{\mathbf{v}}}{4\pi} \sum_{\text{edges}} \int_0^1 \left[\dfrac{zc}{R^3} T_{j-l}\left(t_j - \dfrac{R}{c}\right) + \left(\dfrac{z}{R^2} - \dfrac{1}{R}\right)\dot{T}_{j-l}\left(t_j - \dfrac{R}{c}\right) \right]\dfrac{dw}{d\mu}\,d\mu \\[2em]
+ \dfrac{\hat{\mathbf{n}} \cdot \hat{\mathbf{v}}}{4\pi} \sum_{\text{edges}} \int_0^1 \begin{bmatrix} \dfrac{zc}{R^3} r_n T_{j-l}\left(t_j - \dfrac{R + 2d_n}{c}\right) \\[1em] +\left(\dfrac{z}{R^2} + \dfrac{1}{R}\right) r_n \dot{T}_{j-l}\left(t_j - \dfrac{R + 2d_n}{c}\right) \end{bmatrix} \dfrac{dw}{d\mu}\,d\mu
\end{bmatrix} \quad 5.36
$$

5.4.3 Constructing the total surface sound from the discretisation weights

In the preceding chapters, the discretisation weights were denoted $\varphi_{j,n}$ to reflect that fact that, due to the temporal basis function chosen, their values gave instantaneous surface velocity potential. For the compliant surfaces model this is not the case. In order to compare the BEM for welled surfaces with a frequency domain BEM instantaneous surface velocity potential must be recovered. Combining Equations 5.8 and 5.12 produces the following relationship for compliant surfaces:

$$\varphi^t(\mathbf{r},t) = \sum_{n=1}^{N_s}\sum_{j=1}^{N_t} w_{j,n}\, \mathrm{f}_\mathrm{n}(\mathbf{r})\big[\mathrm{T}_j(t) + \mathrm{T}_j(t) * w(\mathbf{r},t)\big] \qquad 5.37$$

For the welled surface sections the surface reflection response is defined by Equation 5.33. This is substituted below to find instantaneous velocity potential on an element S_n at $t_j = j\Delta_t$. This may be calculate by discrete convolution with the sequence $T_{j,n} = \mathrm{T}_0\big(t_j - 2d_n c^{-1}\big)$:

$$\begin{aligned}
\varphi_{j,n} &= \varphi^t(\mathbf{r},t_j)\big|_{\mathbf{r}\in S_n} \\
&= \sum_{i=1}^{N_t} w_{i,n}\bigg[\mathrm{T}_i(t_j) + r_n\,\mathrm{T}_i\Big(t_j - \frac{2d_n}{c}\Big)\bigg] \\
&= w_{j,n} + r_n\sum_{i=1}^{N_t} w_{i,n}\,\mathrm{T}_i\Big(t_j - \frac{2d_n}{c}\Big) \\
&= w_{j,n} + r_n\, w_{j,n}\, \underset{j}{*}\, T_{j,n}
\end{aligned} \qquad 5.38$$

5.4.4 Impedance equivalent to absorbing wells

In order to verify the welled time domain BEM against a frequency domain BEM the impedance equivalent of the boundary condition for the absorbing wells must be found. This is readily done analytically by considering the absorbing well depicted in Figure 5.2. For convenience x has been chosen to be zero at the base of the well.
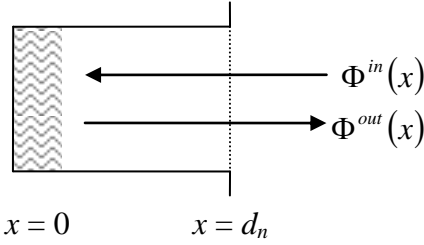
Figure 5.2: An absorbing well

The complex harmonic incoming and outgoing waves are defined as follows where $k = \omega c^{-1}$ is the wavenumber. At the base of the well they are in phase:

$$
\begin{aligned}
\Phi^{in}(x) &= e^{-ikx} \\
\Phi^{out}(x) &= r_n e^{ikx} \\
\Phi^{out}(0) &= r_n \Phi^{in}(0)
\end{aligned}
$$

5.39

The impedance at the mouth of the well is the ratio of the surface pressure to inward velocity and is found below. When $r_n = 0$ and $r_n = 1$ this reduces to $Z(x) = \rho_0 c$ and $Z(x) = i\rho_0 c \cot(kd_n)$ respectively.

$$
Z(x) = \frac{P^t(x)}{V^t_{in}(x)} = \frac{i\omega\rho_0 \Phi^t(x)}{-\dfrac{d\Phi^t}{dx}} = \frac{i\omega\rho_0\left(r_n e^{ikx} + e^{-ikx}\right)}{-ik\left(r_n e^{ikx} - e^{-ikx}\right)} = -\rho_0 c\, \frac{r_n e^{ikx} + e^{-ikx}}{r_n e^{ikx} - e^{-ikx}}
$$

5.40

This completes the BEM framework for absorbing wells. The necessary refinements of the integration scheme of section 5.3 have been derived along with a frequency domain equivalent boundary condition for verification purposes, which shall be performed in the next section.

5.5 Numerical Examples and Verification

In this section the BEM for absorbing wells will be verified on four surfaces. Two are simple surfaces designed to show verification trends in receiver pressure and two are models of diffusing treatments typically used in Room Acoustics applications. On all

four surfaces solution accuracy will be calculated compared to the closed surfaces frequency domain BEM using the impedance boundary condition derived in section 5.4.4. Interference effects between the incident and scattered waves at external points are inspected for the simple surfaces using both the time and frequency domain BEMs. Polar plots of scattered sound are shown for the diffusing surfaces using both the time and frequency domain BEMs. For the surfaces including wells but no absorption, results from the open surfaces frequency domain BEM on equivalent meshes are also shown. Surface sections using the absorbing wells boundary condition are usually referred to as impedance surfaces for brevity.

Solution accuracy will be calculated by the same method used in sections 3.3, 4.3 and 4.4. The time domain BEM will be verified with a range of time-step durations defined by their relationship to spatial resolution by their implicitness ($c\Delta_t \Delta_x^{-1}$). For each of these a harmonic point source excites the surface such that the number of time-steps per excitation period (β) assumes a range of predetermined values. For each combination the source to surface element transfer function is calculated at the excitation frequency using the frequency domain BEM (Equation 3.67). The same is calculated from the time domain data by DFT (Equation 3.68); the first 50β iterations are omitted to allow the solution to reach steady state, then the next 100β iterations are chosen for DFT as this length maintains periodicity and eliminates windowing error. The surface sound error is calculated as spatial mean magnitude of the difference between these transfer function estimates, normalised to the spatial mean magnitude of the frequency domain estimate and is written as a percentage (Equation 3.69). Both the frequency domain BEM implementations for open surfaces (DIFTHIN.exe) and for closed surfaces (RADDIFF.exe) are previously verified against experimental results and follow Terai's 1980 derivation[64].

For the receiver results $c\Delta_t$ is chosen to be equal to Δ_x, as suggested on the grounds of efficiency and accuracy in section 4.5 and by Dodson, Bluck and Walker [35]. Source to receiver transfer functions are calculated in the same manner as the source to surface type defined above. For all meshes the source is located 100m distant normal to the surface, to approximate plane wave incidence.

In section 4.4.2, the mixed surface Quadratic Residue Diffuser model encountered stability problems and these were attributed to the complexity of the surface and its many concave sections. By contrast, an equivalent impedance surface mesh is much simpler so it is anticipated that it might be more stable. The wells mimic the concave, resonant parts of the surface, but in a way that is defined as causal, so it is hoped their presence will not lead to instability.

5.5.1 Uniform welled surface

This mesh is 1.0m square and 0.5m deep comprising 400 elements. The front face comprises 100 well elements all with a depth of 0.1m. It is an extremely regular mesh so integration error is not anticipated to be an issue. It is depicted in Figure 5.3 where the well elements are coloured purple. Non-welled elements have the CFIE boundary condition.
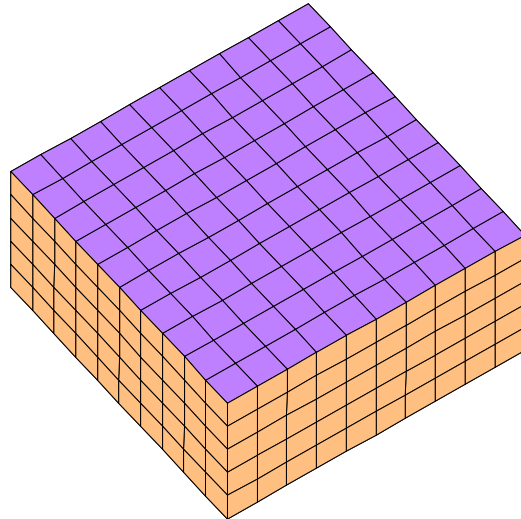
Figure 5.3: Impedance model of a surface with uniform depth wells on its front face

Accuracy is characterised below by error compared to the closed surface frequency domain BEM. The time domain BEM is unstable for 3 of the 21 time-step durations modelled. The same mesh was modelled with zero well depth on the front face and was unanimously stable hence the instability arises from the well elements. This is disappointing but not entirely surprising since a well is a quarter-wave resonator so will

176

possess poles with magnitudes very close to unity. Very small errors, arising from integration, discretisation or finite numerical precision (truncation), may be enough to corrupt these poles so they become unstable.

Aside from the instability, the trends match that which has been observed in chapters 3 and 4. To the left of the figure spatial resolution is poor with respect to excitation wavelength so the accuracy of all BEM suffers. The grey shaded area indicates $\Delta_x > \frac{\lambda}{8}$, its right hand boundary a recommended lower limit in spatial resolution for the frequency domain BEMs. Toward the bottom of the figure temporal resolution of the excitation frequency is poor; error here primarily originates from the time domain BEM. However, in the middle to upper right quadrant of the figure discretisation error is low and good agreement occurs.
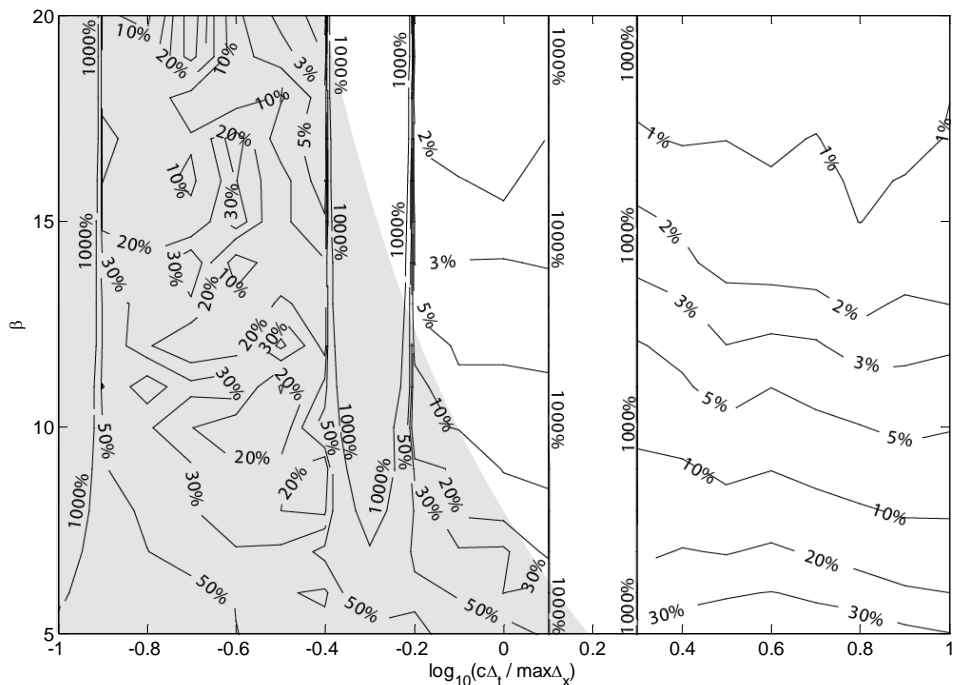
Figure 5.4: Error of the time domain BEM compared to the frequency domain BEM for closed surfaces both modelling the uniform welled surface

An equivalent mixed mesh is depicted in Figure 5.5 where the virtual wells of Figure 5.3 have been meshed explicitly using thin elements (shown in translucent blue) increasing the element count to 580. The presence of this honeycomb of thin elements separating the wells ensures they act in a locally reacting manner. A receiver is placed in the mouth of each mixed mesh well corresponding to the centre of a well element (collocation point). The total velocity potential at each of these should match the surface velocity potential of the well elements in the welled mesh.
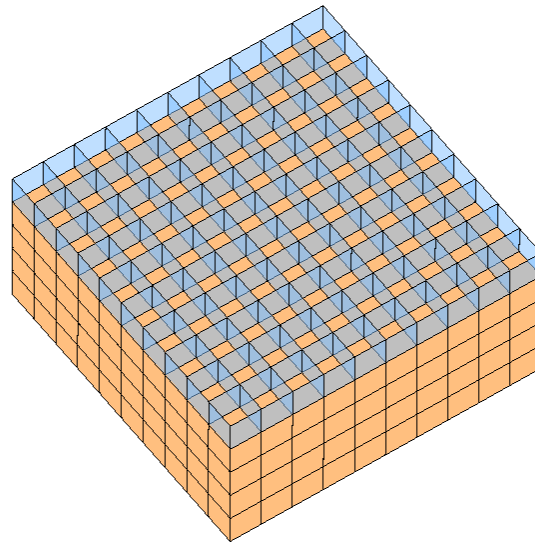
Figure 5.5: Mixed model of a surface with uniform depth wells on its front face

Figure 5.6 may be interpreted as showing how well the impedance surface mesh of Figure 5.3 approximates the behaviour of the mixed mesh of Figure 5.5. The error is calculated as outlined in section 5.5 except that only the well elements and their corresponding mixed mesh receivers have been included in the spatial average. As anticipated, error is greater than Figure 5.4 because the models are not identical, in particular the mixed mesh model does not force velocity potential and normal velocity to be uniform across the well mouth. Disparity to the top right of Figure 5.6 originates from the open surface frequency domain BEM implementation as was the case in Figure 4.7 and Figure 4.13. However, the generally good level of agreement supports this chapter's notion that each well element is an approximation to a rigid walled well of equal mouth dimensions.

178
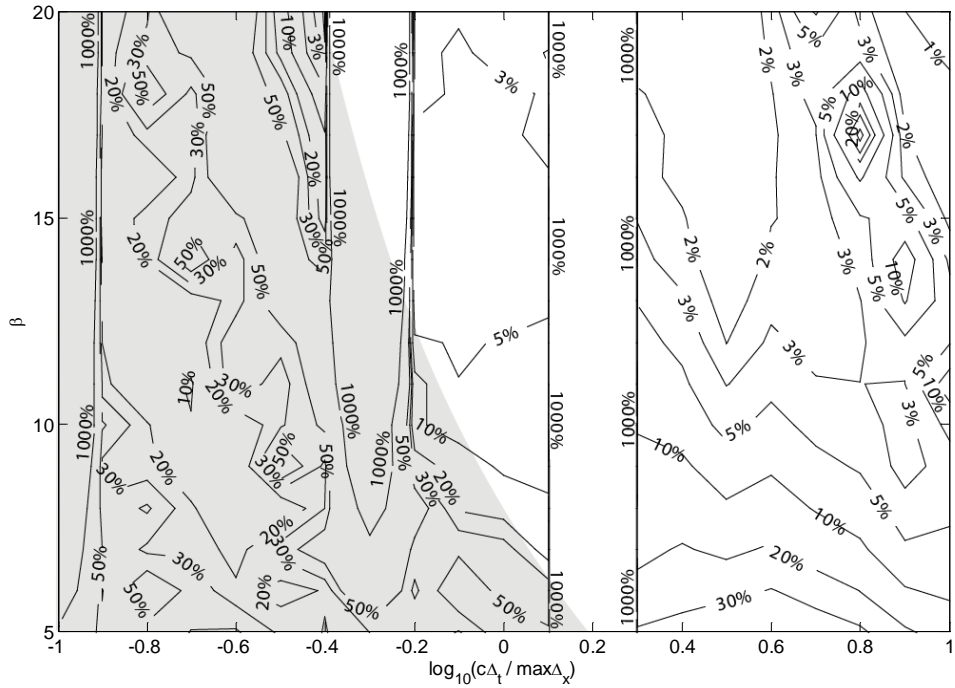
Figure 5.6: Error in total velocity potential between the well elements modelled by the time domain BEM, compared to the well mouth receivers modelled by the frequency domain BEM for open surfaces, both for the uniform welled surface

The following figures show the interference patterns that occur between incident and scattered sound. The receivers are arranged in a vertical line that starts behind the scatterer, passes through its centre and emerges at the front. They are spaced such that none touch the surface. Magnitude of the source to receiver total sound transfer function is plotted in dB versus the receiver z coordinate; incident sound approaches from the right of the figures. Data series are shown for the welled mesh modelled by the time domain BEM (TD Well) and the frequency domain BEM (FD Well) for closed surfaces and for the mixed mesh modelled by the frequency domain BEM for open surfaces (FD Mixed). The vertical lines at $z = 0.0$ and $z = -0.5$ indicated the front and back of the scatterer, and the shaded area indicates the wells of the mixed mesh. A few frequencies are shown so that the variation of the trends with frequency can be recognised.
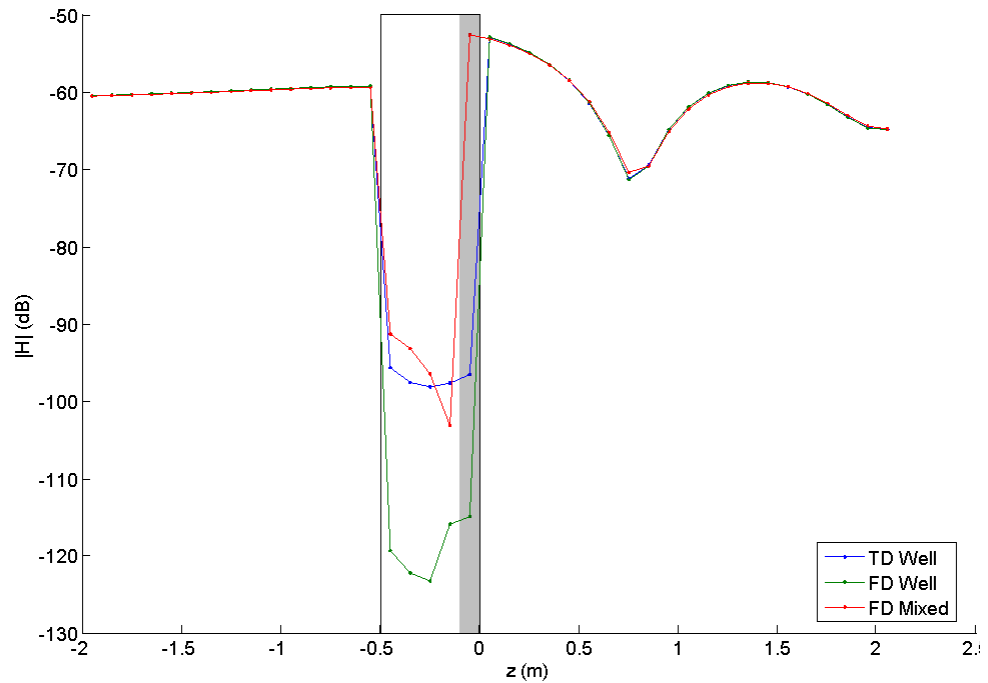
Figure 5.7: Total receiver sound though the uniform welled surface at 142Hz $\equiv \beta = 17$
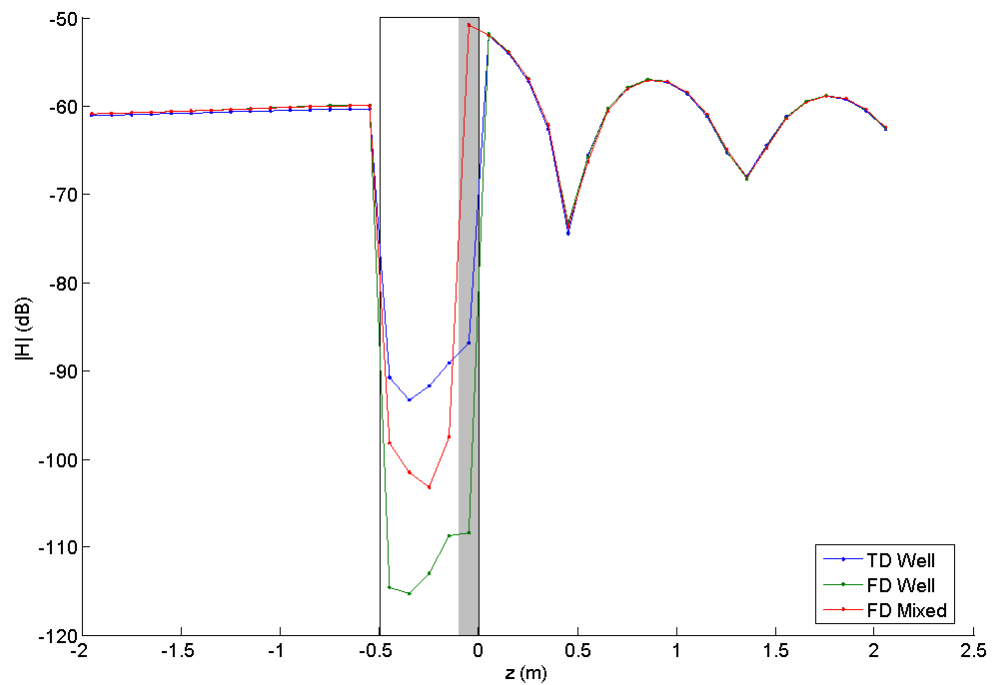
Figure 5.8: Total receiver sound though the uniform welled surface at 202Hz $\equiv \beta = 12$

180

Figure 5.7 and Figure 5.8 both show interference effects between the incident and scattered waves in front of the surface and in this region there is excellent agreement between the time and frequency domains. The BEM for open surfaces is seen to extend the interference patterns into the welled region and its surface normal gradient approaches zero as expected from the rigid well floors. Inside the surface the frequency domain BEM for closed surfaces achieves the best cancellation, but this figure still confirms that the time domain compliant surfaces boundary condition does not permit sound to flow into the cavity. In the shadow region behind the surface all models roughly agree but there is no apparent interference behaviour.
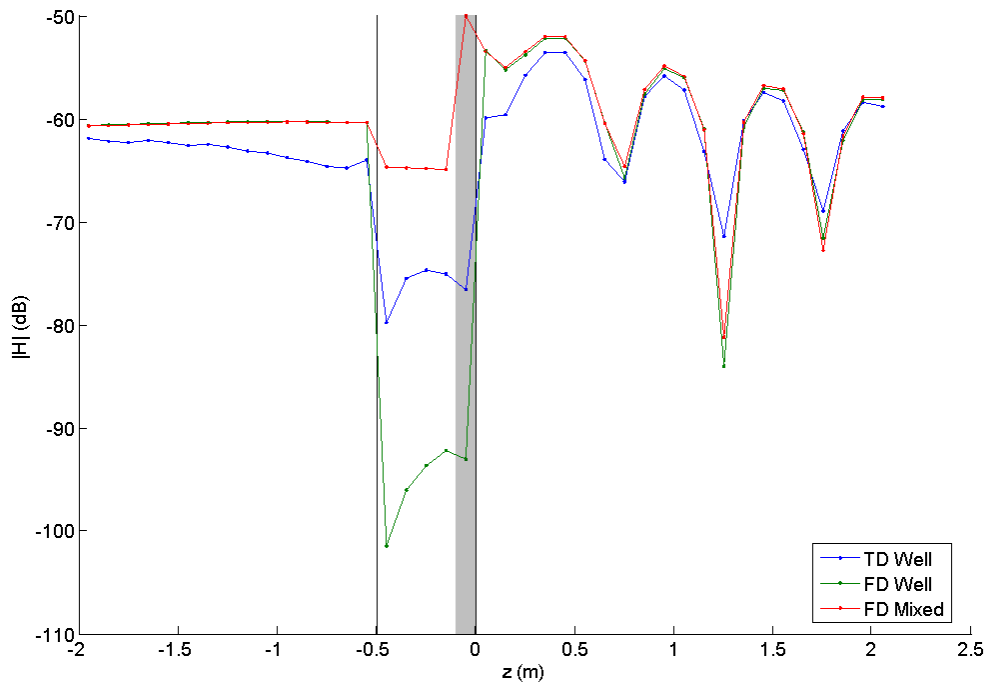
Figure 5.9: Total receiver sound though the uniform welled surface at 346Hz $\equiv \beta = 7$

If the excitation frequency is increased the accuracy of the time domain model solution suffers. This trend is clearly visible in Figure 5.9 and is predictable since $\beta = 7$ is below the $\beta = 10$ limit suggested by Ergin *et al*[22]. The interference patterns are still observed albeit with significant error, but it is inside the surface and in the shadow zone that error is greatest, as in these regions accurate cancellation between the incident and scattered waves is critical. The frequency domain BEM for open surfaces also shows poor cancellation inside the surface. Ergin *et al's* temporal discretisation criterion for rigid

surfaces clearly also applies to welled surfaces with the incoming sound discretisation scheme.

This model has shown agreement between the time and frequency domain BEMs for surfaces with welled sections. Agreement with an equivalent frequency domain mixed model has also been good. However it has been seen that use of well elements can result in instability as they possess the same lightly damped poles as the physical surface they approximate and these are easily corrupted. The well boundary condition is clearly one whose surface reflection response is borderline stable, so this misbehaviour is probably not typical of the compliant surfaces model. The interference trends in total receiver sound shows that the model behaves as expected.

5.5.2 Uniform absorbing surface

This mesh is identical to the uniform welled surface except that the front face is now absorbing instead of welled. The rigid elements on other faces have the CFIE boundary condition. The surfaced is modelled with four different reflection ratios: 1.00 (100% reflection $\equiv$ rigid surface), 0.50, 0.25 and 0.00 (0% reflection $\equiv$ anechoic termination). The frequency domain BEM for open surfaces cannot be used for comparison since no equivalent rigid mesh exists.

The error compared to the frequency domain BEM for closed surfaces is shown in Figure 5.10 for reflection ratio = 0.00. Excellent agreement is seen for this case and the other cases show very similar performance and universal stability.

The following figures show the interference patterns that occur between the incident and scattered sound for receivers behind, within and in front of the surface. The receivers are arranged as for the uniform welled mesh in section 5.5.1, again $c\Delta_t \approx \Delta_x$ and the results are plotted equivalently. Data series are shown for the time domain BEM (TD) and the frequency domain BEM for closed surfaces (FD) for all reflection ratios modelled as indicated by the legend.
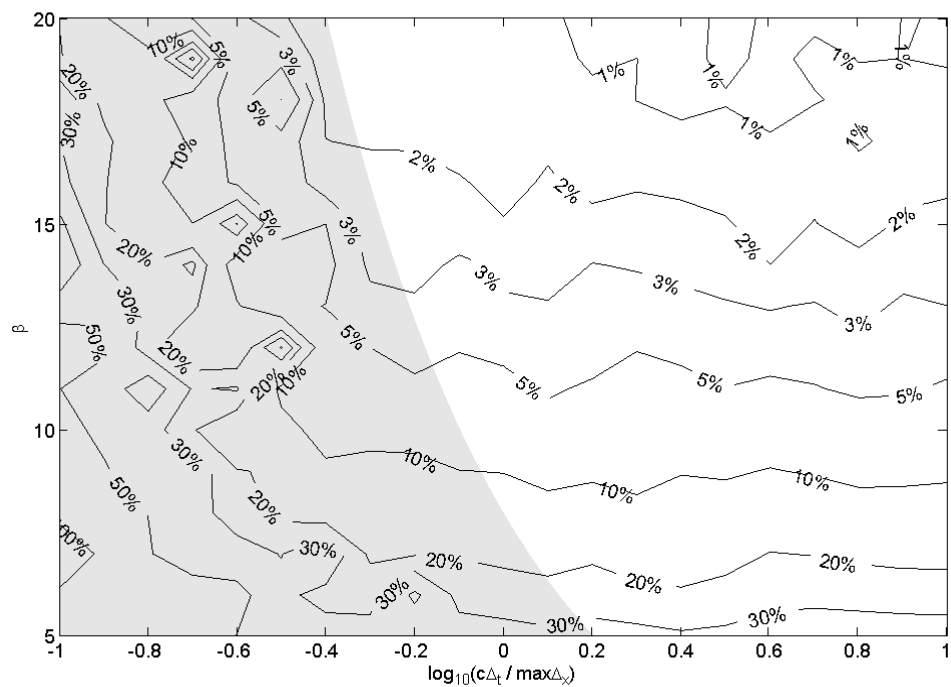
Figure 5.10: Error of the time domain BEM compared to the frequency domain BEM for closed surfaces both modelling the uniform absorbing surface with surface reflection ratio = 0.00.
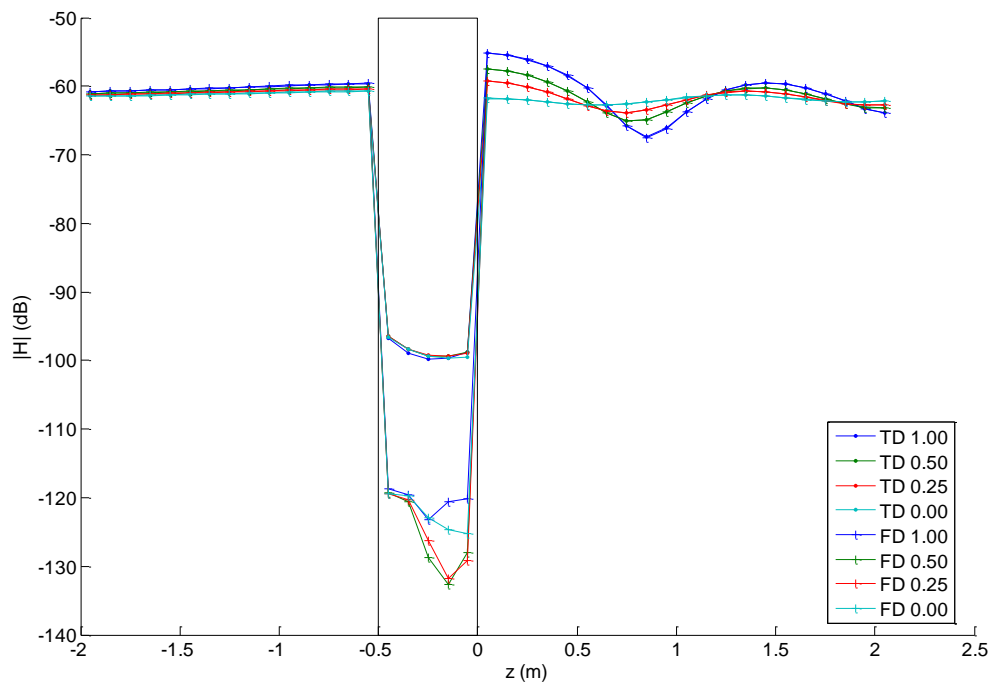
Figure 5.11: Total sound at the receivers though the uniform absorbing surface 142Hz $\equiv \beta = 17$
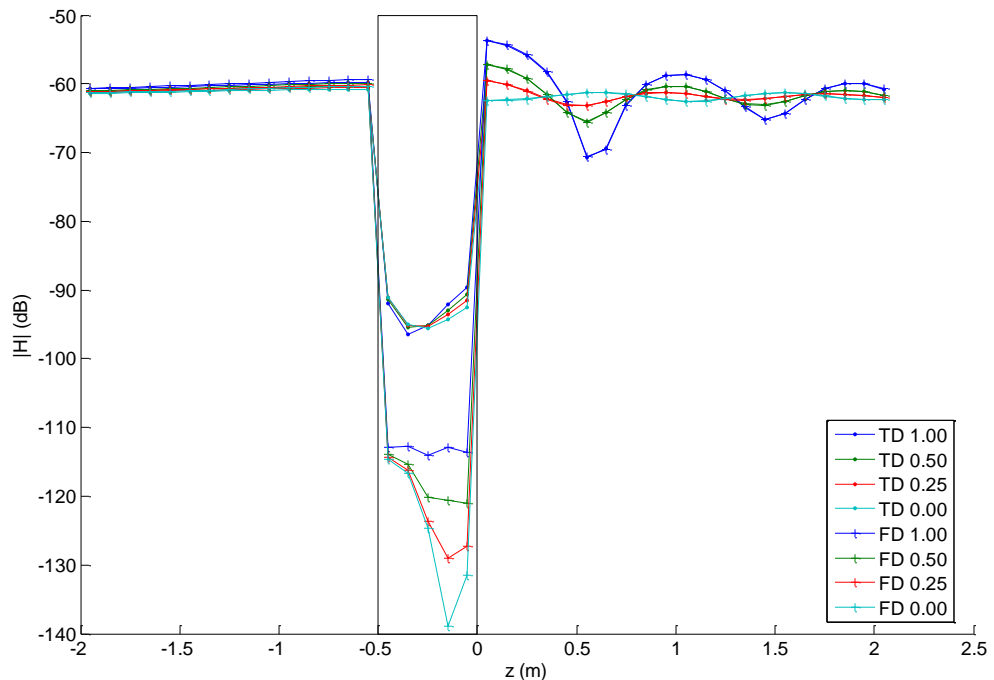
Figure 5.12: Total sound at receivers though the uniform absorbing surface 202Hz $\equiv \beta = 12$
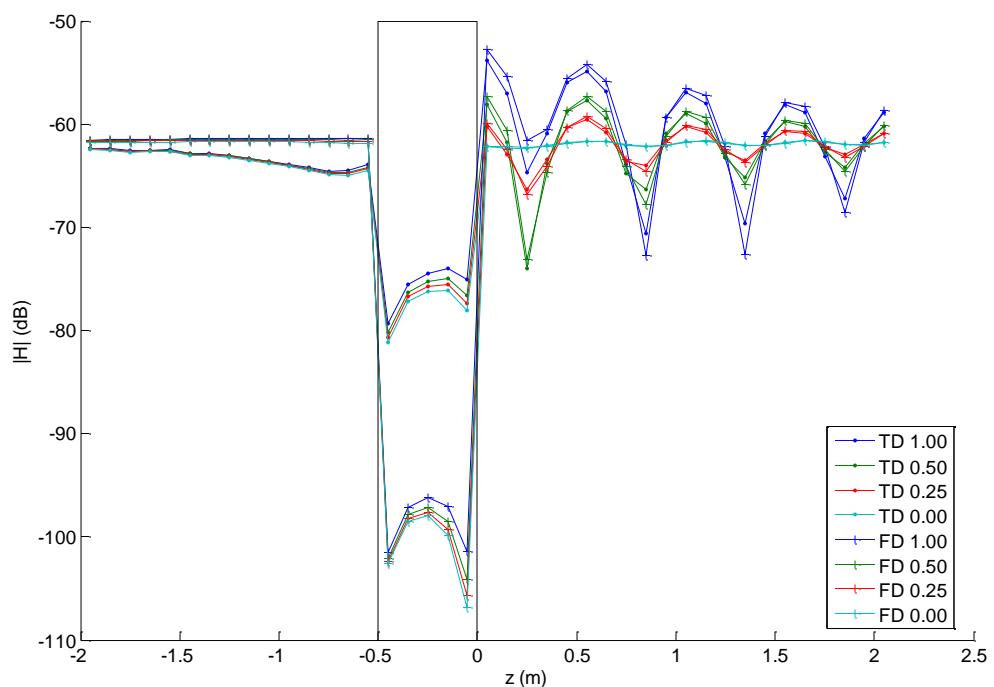
Figure 5.13: Total sound at the receivers though the uniform absorbing surface 346Hz $\equiv \beta = 7$

In both Figure 5.11 and Figure 5.12 the model with unity reflection ratio provides the strongest reflection hence the strongest interference pattern which clearly tends towards zero normal gradient close to the rigid surface. These patterns are proportionally reduced for the 0.5 and 0.25 cases, showing less sound is reflected, down to the zero reflection ratio series which produces only slight fluctuation due to the finite size of the anechoic termination. The pressure in the shadow region seems slightly affected by the front face absorption but here, as in front of the surface, good agreement is present between the time and frequency domains. Inside the surface the frequency domain BEM for closed surfaces again achieves the best cancellation.

As for the uniform welled surface, the accuracy of the time domain model solution worsens as excitation frequency is increased and β reduced. In Figure 5.13 the interference patterns are still observed with time domain error proportional to the strength of the reflection; the weaker reflections cause smaller error as the total sound is dominated by the incident sound which is calculated analytically. Again it is inside the surface and in the shadow zone, where cancellation is most critical, that the error is largest.

This model has shown excellent agreement between the time and frequency domain BEMs for surfaces with absorbing sections and the MOT solver has been universally stable. The trends in total received sound show that the absorbing surface model is behaving as expected.

5.5.3 Quadratic Residue Diffuser

The Quadratic Residue Diffuser [67] (QRD) is the first of the realistic Room Acoustics treatments to be modelled using the time domain BEM for absorbing welled surfaces. It comprises a series of wells, whose depths are defined by a quadratic residue sequence and a design wavelength, separated by thin rigid fins. Its diffusion mechanism is the interference patterns created by the delayed sound re-radiating from each of these wells. The specific diffuser modelled in this section has a design wavelength of approximately 1.4m, a well width of 0.25m, and a height of 1.0m.
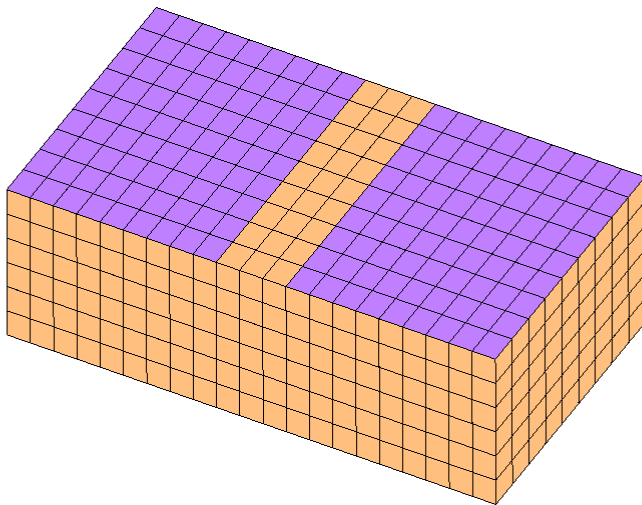
Figure 5.14: Impedance surface model of a Quadratic Residue Diffuser

The welled mesh (738 elements) is depicted above, though as it is simply a box whose front surface has the impedance boundary condition necessary to mimic the QRD it is more informative to review Figure 4.20 which depicts the mixed surface version (900 elements). On comparison of the two Figures it is apparent that their relationship does not exactly mirror the relationship between the two meshes of the uniform welled surface of section 5.5.1 (Figure 5.3 and Figure 5.5). In particular, the wells of the mixed surface QRD mesh, like the real device, are not subdivided by thin rigid surfaces into the honeycomb structure that is equivalent to the welled surface model. This means the mixed surface model allows modal behaviour in the well prohibited by the welled model, hence the latter, as a poorer approximation of reality, may show increased error. This issue was investigated by Cox and Lam [68] in the frequency domain. They concluded that a BEM capable of modelling the thin fins of the diffuser gives the most accurate results compared to scale models, but that an impedance surface model gives good results and is more efficient due to the smaller number of elements. This conclusion justifies this application of the time domain BEM for absorbing welled surfaces though the model disparity remains.

The error for the time domain BEM compared to the frequency domain BEM for closed surfaces is shown below. The time domain BEM is unstable for 2 of the 21 time-step durations modelled. Unlike the instability observed in chapter 4, none occurs at the

shortest most explicit time-step durations; instead it occurs in the middle of the time-step range tested. The instability seen for the mesh with uniform depth wells (section 5.5.1) was shown to result from the well elements, and so it is likely that here it is of the same origin. Where the time domain BEM is stable its accuracy is good, much improved over that seen for the QRD mixed mesh in Figure 4.22.
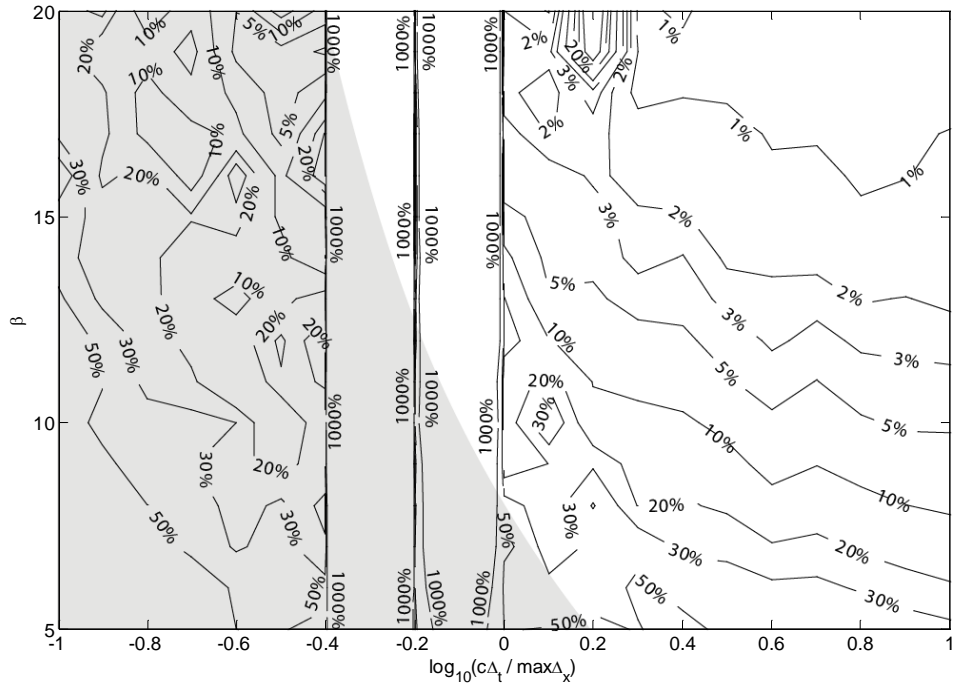
Figure 5.15: Error of the time domain BEM compared to the frequency domain BEM for closed surfaces both modelling a QRD as an impedance surface.

Receivers are placed in the mouth of each mixed mesh well such that each lies at the centre of a well element (collocation point); the total velocity potential at each of these should match the surface velocity potential of the corresponding well element in the welled mesh. The error is calculated as for Figure 5.6; only the well elements and their corresponding mixed mesh receivers are included in the spatial average:
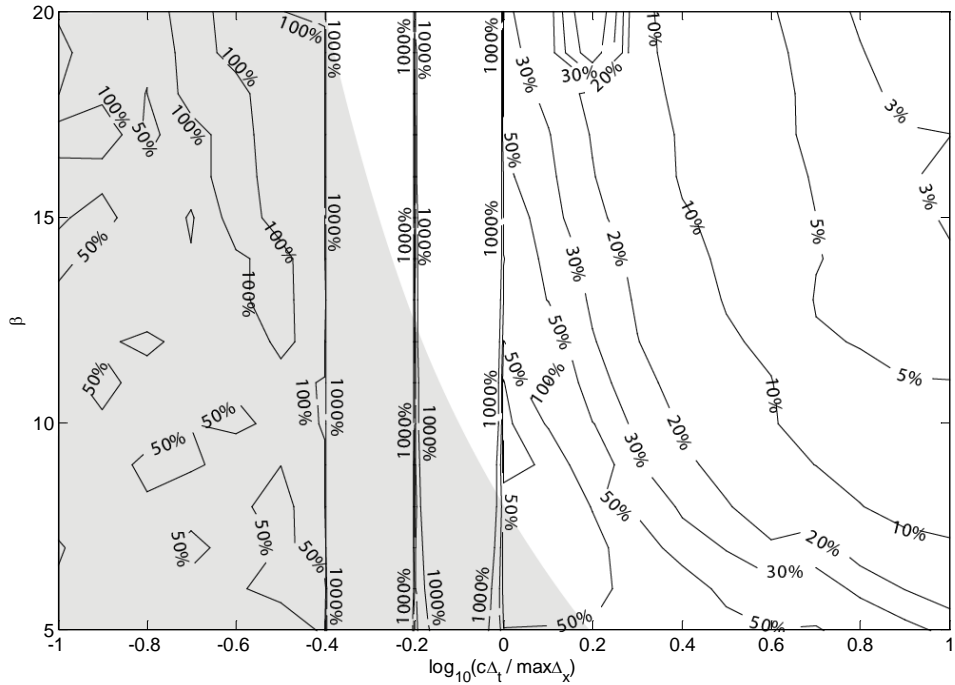
Figure 5.16: Error in total velocity potential between the well elements modelled by the time domain BEM, compared to the well mouth receivers modelled by the frequency domain BEM for open surfaces, both for the QRD

Figure 5.16 may be interpreted as showing how well the impedance surface mesh of Figure 5.14 approximates the behaviour of the QRD mixed mesh of Figure 4.20. The instabilities are of course again apparent. The underlying error is greater than Figure 5.15 because the models are not identical, in particular the mixed mesh model permits sound transmission paths in the well that are forbidden in the locally reacting impedance surface model. Coincidentally the error trend here is similar to that obtained with the mixed surface model in Figure 4.22, suggesting that modelling a QRD with the time domain BEM results in similar error whether it be using a mixed surface model or an impedance surface model.

The following figures are polar plots of the source to receiver scattered sound transfer function magnitude in dB versus receiver angle relative to the surface normal. The 91 receivers are uniformly spaced in a 5m arc located in the primary scattering plane of the diffuser. Data series are shown for the welled mesh modelled by the time domain BEM (TD Well) and the frequency domain BEM for closed surfaces (FD Well) and for the

mixed mesh modelled by the frequency domain BEM for open surfaces (FD Mixed). Again $c\Delta_t \approx \Delta_x$, the optimal compromise between spatial and temporal resolution, though the different value of Δ_x for this mesh results in a slightly different set of frequencies for the same choices of β compared to the previous two sections. Neither of the frequency domain implementations output receiver scattered pressure so it has been calculated by subtracting the incident pressure from the total pressure.
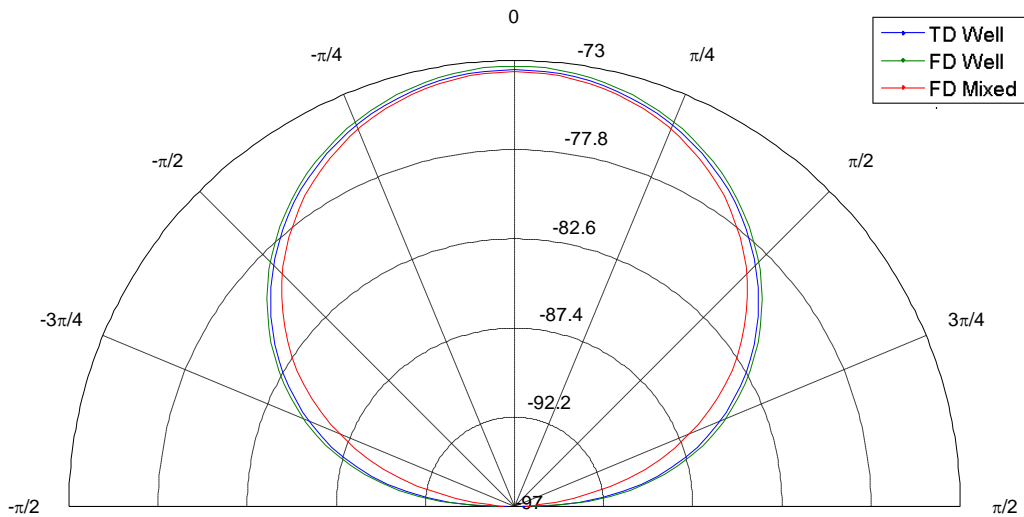
Figure 5.17: Sound scattered from the QRD at 5m. 134Hz $\equiv \beta = 17$
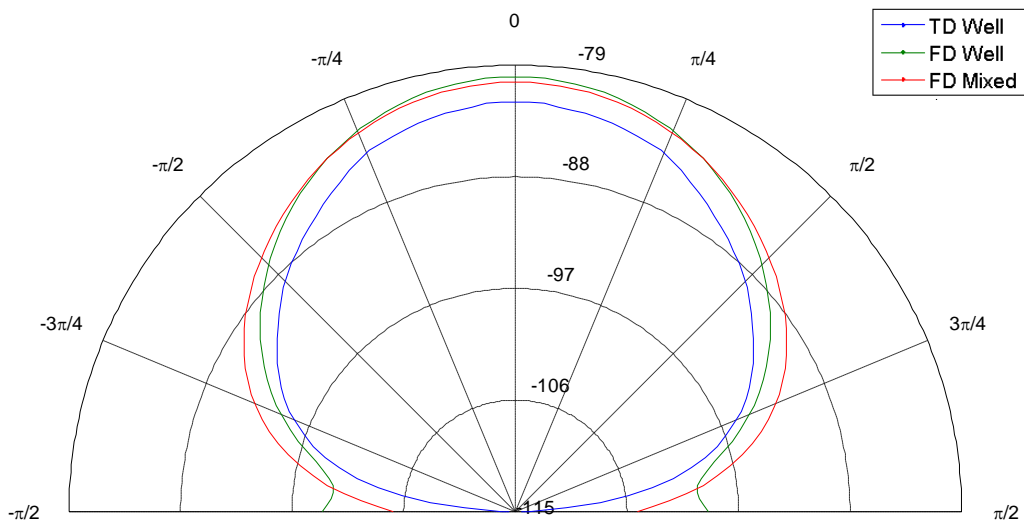
Figure 5.18: Sound scattered from the QRD at 5m.190Hz $\equiv \beta = 12$

In Figure 5.17 and Figure 5.18 the frequency is below that at which the diffuser produces grating lobes so scattering is fairly uniform. Agreement between the time domain and frequency domain impedance surface models is good in Figure 5.17, but in Figure 5.18 there is significant discrepancy. The frequency domain mixed model shows significant discrepancy at both frequencies.
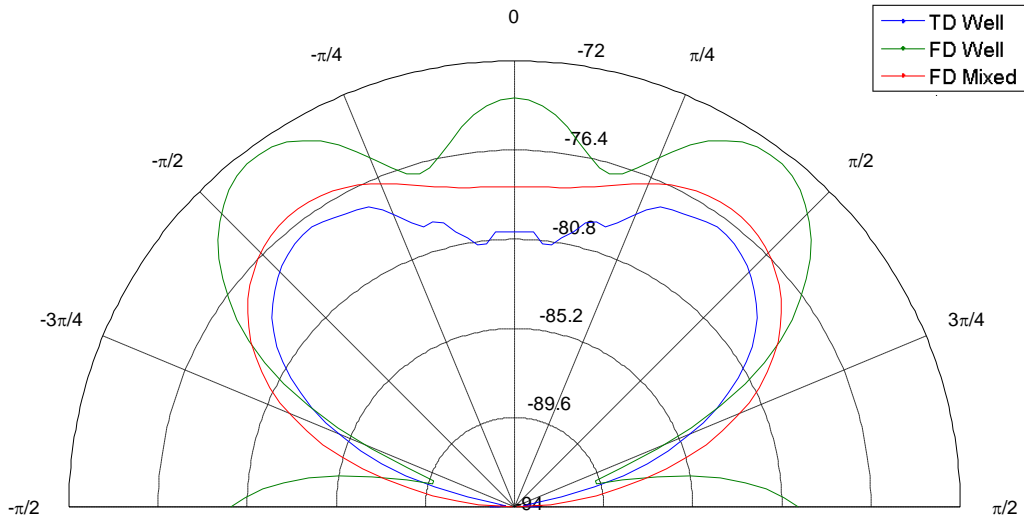
Figure 5.19: Sound scattered from the QRD at 5m. $326Hz \equiv \beta = 7$

In Figure 5.19 grating lobes are apparent; however agreement between the three models is poor. For the time domain model, poor temporal resolution is a factor at this frequency, although accuracy was also poor in Figure 5.18, suggesting other error sources also contribute. Figure 5.15 shows that this time-step duration is close to one which is unstable and surface error here is greater than it was for this implicitness in sections 5.5.1 and 5.5.2. Again agreement between the frequency domain models is poor.

In this section instability originating from the well elements has again been witnessed. Accuracy has generally been as good as or better than the mixed surface QRD model in section 4.4.2, but the robust alternative hoped for has not emerged. Scattered sound has not seen good agreement, though this could be due to borderline stability at the chosen time-step duration.

5.5.4 Idealised Binary Amplitude Diffuser

An idealised Binary Amplitude Diffuser [70] (BAD) is a surface comprising an array of patches that alternate between 0% and 100% absorption, hence the term binary amplitude. The arrangement of these patches is critical. Individually each patch scatters sound widely as it is small with respect to wavelength at typical frequencies of operation. However, if there is a recurring pattern in the arrangement, the uniformity of the scattering will be reduced as certain scattering angles will experience constructive interference and other destructive interference due to the pattern periodicity. Diffusion quality is defined as the uniformity of scattering so any such recurring pattern will reduce the diffuser's effectiveness.

Consequentially the arrangement of patches should have minimal similarity to a shifted version of itself (be optimally spatially auto-decorrelated). This is achieved by starting with a Maximum Length Sequence (MLS), which has optimal auto-correlation properties, and folding it into a surface using a process called the Chinese Remainder Theorem [71]. This process requires the resulting array to have dimensions specified by a pair of co-primes, and MLSs always have $2^n - 1$ bits (where n is a real number), so only certain sizes are possible. Commercial implementations typically comprise a 31 by 33 array of $2^{10} - 1 = 1023$ patches. This section has opted for a smaller diffuser comprising a 15 by 17 array of $2^8 - 1 = 255$ patches depicted below.

It should be noted here that what is being modelled is an idealised BAD and behaviour of the real device differs, particularly at low frequencies. The construction is usually a perforated mask of steel or wood in front of a slab of mineral wool, all wrapped in cloth. At low frequencies this mineral wool is unlikely to be thick enough to create significant absorption, although the sound propagating through it will still experience a phase change meaning diffusion may still occur though not as predicted by the idealised model herein. Other mechanisms arise that are not considered here such as compliance of the mask as it is supported by the compressible mineral wool. What follows should be considered a model of the diffusing principle rather than the real device.
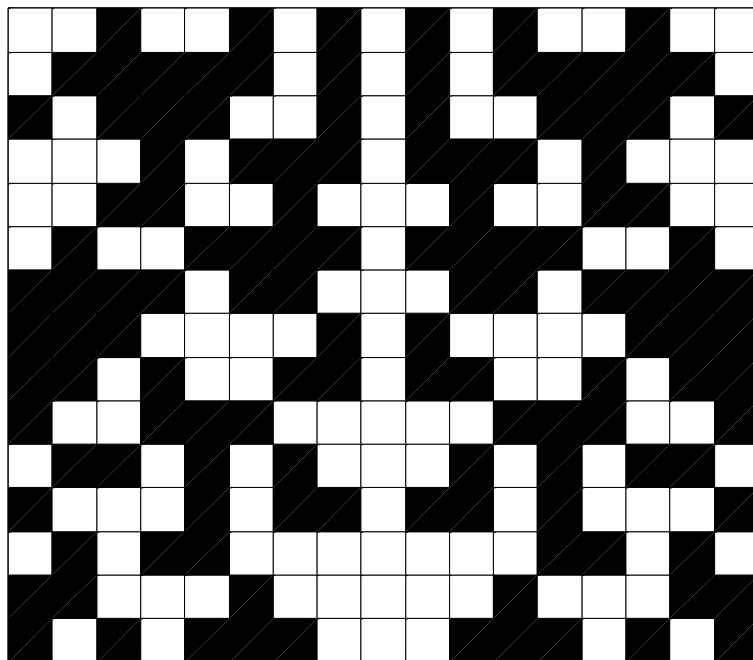
Figure 5.20: Chinese Remainder Folding of a 255 bit MLS to a 15 by 17 array
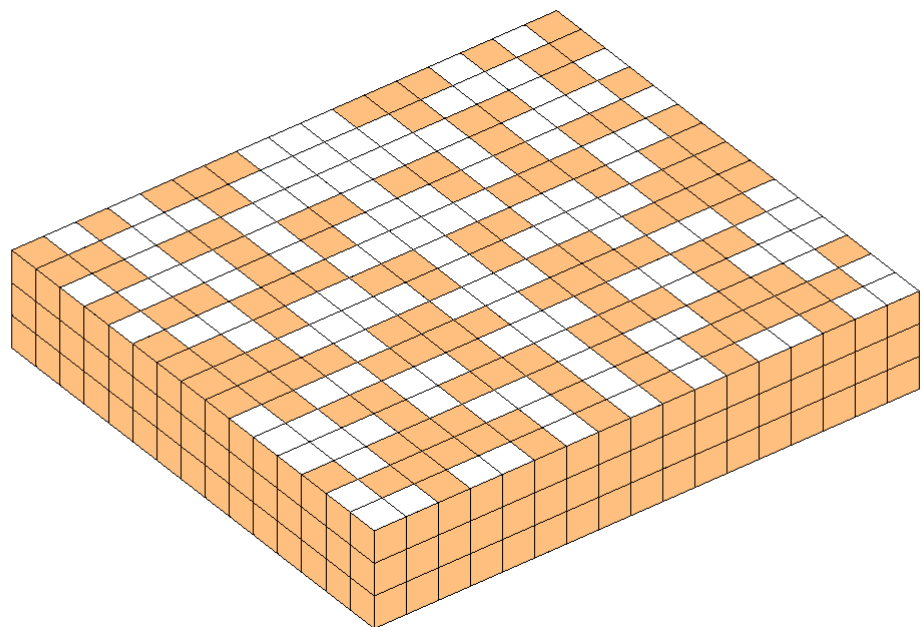
Figure 5.21: Binary Amplitude Diffuser Mesh

The BAD mesh (Figure 5.21) is 0.15m by 0.17m by 0.03m and comprises 702 elements. Δ_x is one tenth of that used in the models in sections 5.5.1 to 5.5.3 so time-step durations are proportionally shorter and frequencies inverse proportionally higher. The

white elements are 100% absorbing and the coloured elements are rigid. The CFIE boundary condition is used on the rigid elements of the non-front face.

The error compared to the frequency domain BEM for closed surfaces with an equivalent impedance boundary condition is shown in Figure 5.22 and excellent agreement occurs with no instability evident.
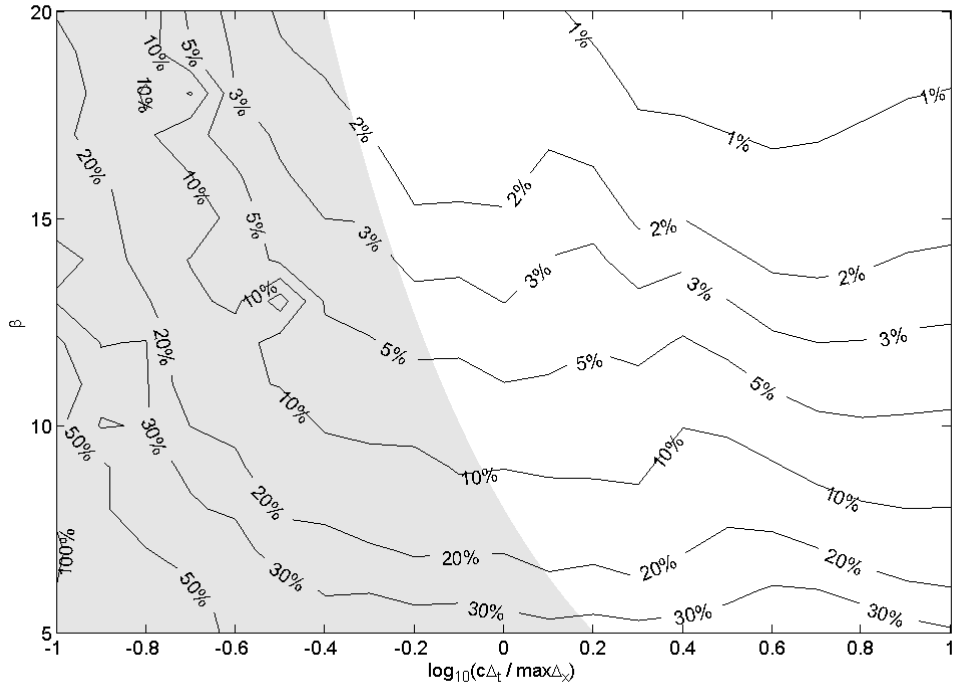
Figure 5.22: Error of the time domain BEM compared to the frequency domain BEM for closed surfaces both modelling a BAD as an impedance surface.

91 receivers are arranged in a 5m radius arc as was the case for the QRD. Unlike the QRD, the BAD is designed to scatter hemispherically so what is shown is a cross-section through its scattering. Polar plots follow displaying the magnitude of the source to receiver scattered sound transfer function in dB versus receiver angle relative to the surface normal. Data series are shown for time domain (TD) and frequency domain (FD) BEMs and again $c\Delta_t \approx \Delta_x$:
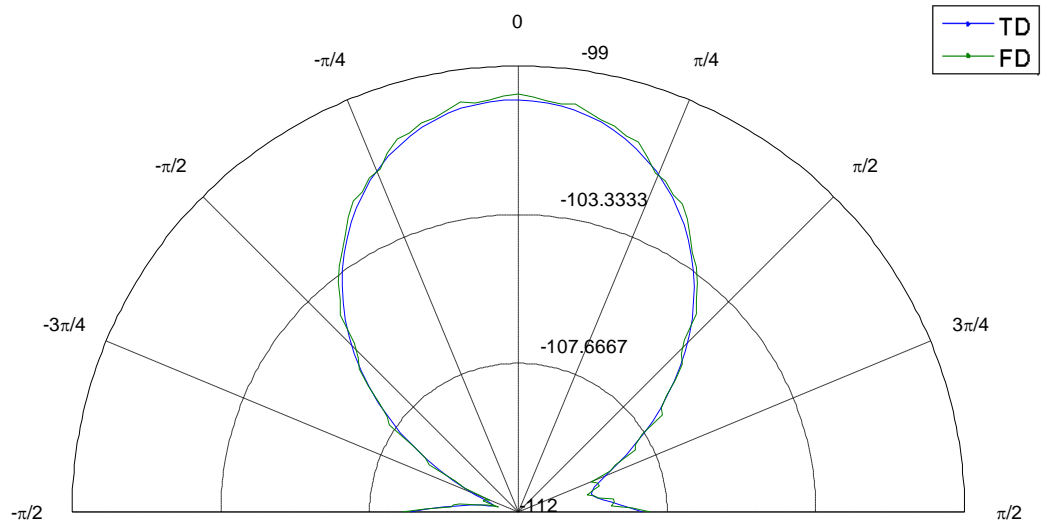
Figure 5.23: Sound scattered from the BAD at 5m. $1426\text{Hz} \equiv \beta = 17$
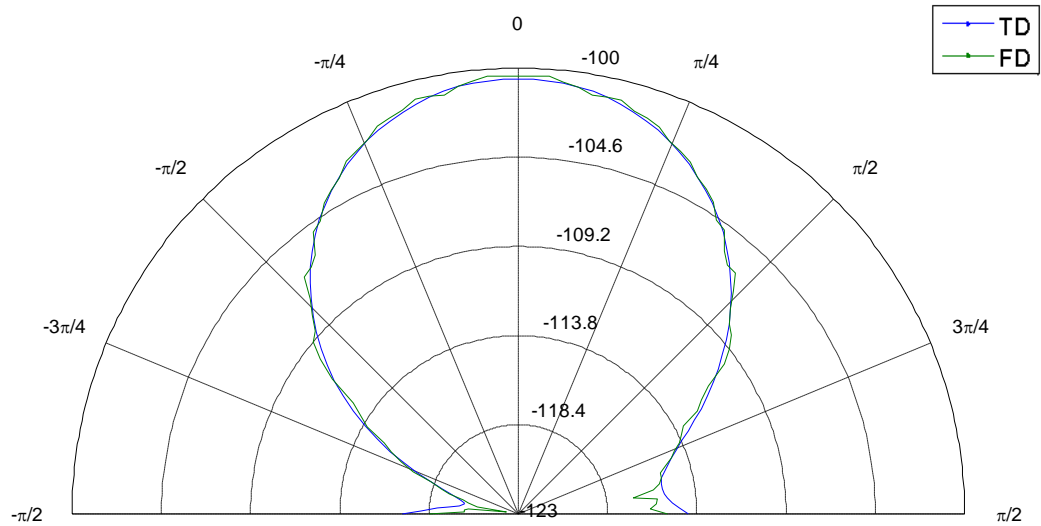
Figure 5.24: Sound scattered from the BAD at 5m. $2021\text{Hz} \equiv \beta = 12$

In the above figures, the frequency is below that at which the diffuser produces grating lobes, so scattering is fairly uniform. Agreement between the time and frequency domain impedance surface models is excellent. (The wiggle in the frequency domain line is due to truncation error in the process of extracting scattered pressure.) Grating lobes are apparent in both results in Figure 5.25, but the poor temporal resolution of the time domain model at this frequency has compromised its accuracy somewhat.
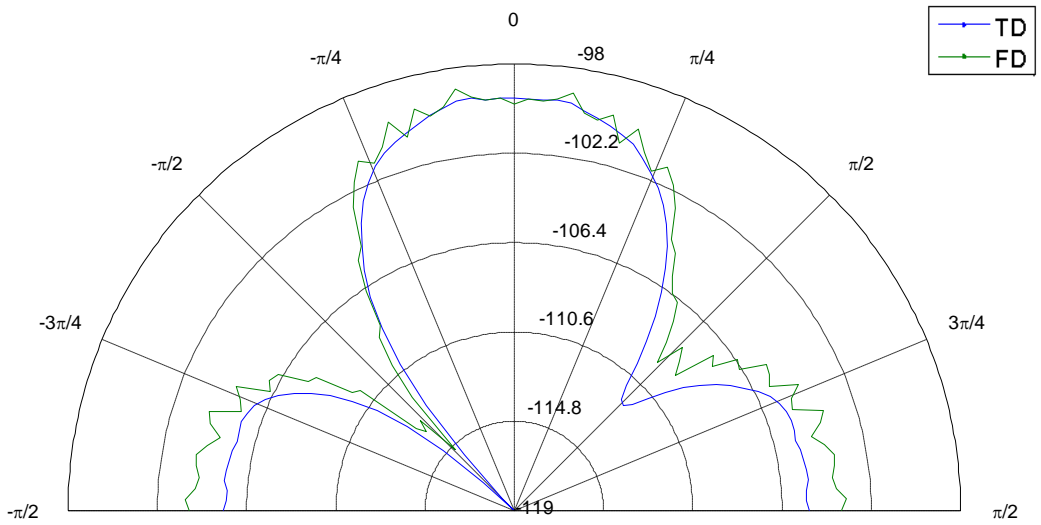
Figure 5.25: Sound scattered from the BAD at 5m 3464Hz $\equiv \beta = 7$

In this section, the time domain BEM has been applied to an idealised model of a Binary Amplitude Diffuser. Excellent agreement has been seen with the equivalent frequency domain model and no instability has been witnessed.

5.6 Conclusions

This chapter has sought a representation for abstracting a non-rigid material into a compliant surface suitable for incorporation into a time domain BEM. Differential and impedance representations were deemed unsuitable as their stability and causality are hard to prove. Instead, the inverse Fourier transform of the surface reflection coefficient was adopted as it explicitly defines the surface response to an incident impulse so is easy to characterise and is said to be robust in the presence of numerical error; this quantity was termed surface reflection response.

Application of the surface reflection response requires the ability to distinguish between sound travelling into and out of the surface. This concept gave rise to a new surface model. The outgoing sound is found by convolution of the incoming sound with the surface reflection response. Crucially this model allows surface normal velocity to be found from surface pressure for each of these waves, as for plane waves in free space. The combination of these insights allows the integrands of the KIE to be written solely

in terms of the incoming wave, thus it is natural to discretise incoming sound in preference to total sound. This model was cast into a time domain BEM framework and contour integrals were derived valid for an arbitrary compliant surface without restriction on the surface reflection response or discretisation, the only one being that the surface be piecewise flat. These novel statements are the time domain equivalent of a frequency domain BEM that supports impedance boundary conditions so have wide potential application.

A simpler model was implemented and verified. In this each piecewise constant surface element represents the mouth of a well containing some hypothetical broadband absorbent, thus the outgoing wave is a scaled and delayed copy of the incoming wave. This simplified scheme is verified on two simple surfaces and two diffuser models. The models with absorbing and rigid sections demonstrate excellent accuracy and stability properties. The models with welled and rigid sections demonstrate excellent accuracy but aggravate some stability issues with the MOT solver. This agrees with the corruption of poles model, as a well is a quarter wave resonator so possesses lightly damped poles. A well is therefore concluded to be a borderline stable example of a compliant surface and the stability issues encountered not expected to be inherent to the model proposed in sections 5.2 and 5.3. The Quadratic Residue Diffuser model showed similar accuracy and stability performance to the equivalent mixed surface time domain model in section 4.4.2 so no particular advantage is seen there beyond the reduced computational cost of the simpler mesh. Overall the results are encouraging and suggest viability of the full time domain BEM for compliant surfaces proposed.

In the following chapter the contributions of the thesis will be discussed and avenues for future research identified.

6 Discussion and Future Research

Many publications in the field of time domain BEM study are quite abstract and have a similar structure. Firstly some aspect of the algorithm is analysed and arguments made for why proposed criteria are desirable, for example improving accuracy, efficiency or stability. Secondly an algorithm is presented that contains modifications such that it excels according to the proposed criteria. This generalisation is not meant critically; the analysis and criteria may be lucid and revealing, enlightening the research community, and the modifications novel and progressive, maturing the algorithm. Instead its purpose is to contrast the structure of this thesis which, while essential effort has been made to retain generality and rigour, is motivated by the application of modelling surface treatments typical to Room Acoustics. Hence focus has more been toward extending the scope of the time domain BEM rather than modifying the trends of its computational cost or stability.

The original goal of this investigation was naïvely stated to be application of the time domain BEM to modelling Room Acoustics surface treatments, under the misconception that the algorithm was sufficiently mature to allow this. Once investigations commenced inadequacies emerged and it became apparent that a deeper understanding was required, so the purpose shifted to developing the algorithm.

The purpose of this chapter is to examine the contribution of this thesis and identify where future research should be focussed. It is organised thematically, as was the literature review in section 2.2, but the section boundaries will be drawn differently in response to the different significance and priority this thesis gives to subjects and their future research.

6.1 Stability and the MOT solver

A popular goal in published algorithms has been unconditional stability of the MOT solver and many properties have been correlated with this. These include: discretisation (particularly temporal basis and time-step choice), underlying integral equation formulation, bespoke stabilisation and averaging, and heuristic mesh criteria. In

contrast this thesis has considered stability but not pursued it as a primary goal. Partly this was because the thesis's primary goal lay elsewhere, but more fundamental reasons were also influential.

Ergin *et al* [22] showed that both the KIE and its surface normal derivative permit non-physical cavity resonances, as do their frequency domain equivalents, but that the CFIE does not. This was a fundamental failing of the integral equation representation of the physical problem so must be redressed in the interests of model correctness. Remaining model error originates from a number of sources, primarily discretisation. However, the fact that this may manifest as instability is a property of the MOT solver rather than the underlying integral equations. The dominant analysis of this phenomenon has stemmed from the work of Rynne [38] and has been embraced herein, being the concept of corruption of stable physical poles into instability.

In this thesis stability has been analysed and where possible quantified by extraction of the maximum discreet pole magnitude. These results have been used as supporting evidence for algorithmic modifications that can be considered good practice anyway, but the algorithm has not been modified in the sole pursuit of stability. An example of good practice that aids stability is the improvement in integration accuracy achieved in chapter 3. The instability that occurred for the Quadratic Residue Diffuser model in chapters 4 and 5 was disappointing but no attempt was made to eradicate it by heuristic means, instead an explanation for its origin was suggested.

Stability is clearly a prerequisite for a mature algorithm, so if a solution does not lie with the integral equations, discretisation and boundary conditions considered in this thesis, then hope must be placed elsewhere. Discretisation and computational errors will always exist to some extent, but it is the solution strategy that dictates whether these manifest as modest solution inaccuracy or overwhelming error due to solver divergence. Rynne [38] suggested that simultaneous solvers such as Herman and van den Berg's [36] steep descent algorithm may be more resilient than the MOT scheme. Although the divergent poles may still permitted be by the matrix equations, they are its homogeneous solutions so tend to be disregarded as they do not affect the residual the aim is to minimise. Such solvers superficially have very bad cost scaling, so an acceleration strategy is necessary, but do lift restrictions on temporal discretisation

placed by the MOT solver. Acceleration could involve compression of the interaction matrix [51], exploitation of orthogonal basis functions [26, 52, 53], or perhaps some aggregation matrix solution strategy similar to fast multipole method [48-50]. Such a simultaneous solver may still require a method of managing non-physical cavity resonances else it is conceivable that the non-uniqueness issues that plagued the frequency domain BEM may emerge. This could utilise the CFIE, or a time domain equivalent of the CHIEF [5] algorithm may be possible. Future research into improving stability would be better focussed on establishing the behaviour of such algorithms rather than persisting with the MOT solver. To an extent this comment also applies to accelerated versions of the MOT solver, such as the PWTD [46, 47] algorithm, though the possibility that aspects of their implementations may aid stability is not denied.

6.2 Discretisation

This thesis has not specifically investigated discretisation, though a stance emerged from the discussion in section 2.2.2. This was that the discretisation scheme should be chosen on the grounds of required accuracy, rather than ensuing effects such as stability, and that a basis function representation has advantages in precision of definition yet the ability to be carried through integral derivations without refinement. The ability to choose an implicit time-step duration is an example of liberation that is brought about by careful derivation with a temporal basis function representation. Ha-Duong, Ludwig and Terrasse's [25] 2003 paper demonstrates basis function choice made according to the expected variation of the quantities they interpolate.

The MOT solver places two restrictions on the temporal basis function family; it must comprise regularly delayed copies of a mother basis function and that must be zero for $t \le -\Delta_t$. Another property fundamental of a basis function family is that the sum of its members should be one over the interpolation domain; such a family is called a partition of unity. There are many conceivable mother temporal basis functions who fulfil the MOT criteria and whose delayed copies form a partition of unity. The element interaction integrands place a further restriction by the evaluation of $\dot{T}_{mother}(0)$ at the collocation point; the mother temporal basis function cannot be smooth and symmetrical about $\varsigma = 0$ else sufficiently explicit time-step durations would result in an entirely zero

$\mathbf{Z}_0$ matrix so the MOT equation could not be solved. This criterion prohibits various choices such as the raised cosine (Hanning) function and Hu, Chan and Xu's [23, 24] optimised basis functions, however it is worth noting that it is specific to temporal collocation as for temporal Galerkin testing it is the basis function's autocorrelation that is significant.

Contrary to the perspective of this thesis, much influence on stability has been ascribed to the temporal basis function. Both the temporal basis function used in this thesis, and its predecessor by Manara *et al* [21], have been cited as possessing stabilising properties. Hu, Chan and Xu [23, 24] took such notions further and optimise their temporal basis function against an instability cost function to achieve maximal stability for their electromagnetic algorithm. Above it was stated that discretisation should be dictated by desired accuracy and stability should be a separate issue, however for the MOT solver this is not the case. Because the temporal basis function typically has support longer than Δ_t, element self-interactions coefficients will be non-zero for past time-steps in addition to the current one. Anti-intuitively this allows a lone element to be unstable, regardless of integration accuracy or the properties of the rest of the mesh.

Consider the state transition matrix of Equations 2.43 and 2.44. If there is only a single element in the mesh then each of the sub-matrices on the top rows of $\mathbf{M}$ becomes a scalar (Equation 6.1) and its eigenvalues are readily found as the roots of its characteristic polynomial (Equation 6.2). l_{max} is the support of $T_0(t)$ divided by Δ_t.

$$\mathbf{M} = \begin{bmatrix} m_1 & m_2 & \cdots & m_{l_{max}-1} & m_{l_{max}} \\ 1 & & & & \\ & 1 & & & \\ & & \ddots & & \\ & & & 1 & \end{bmatrix} \qquad 6.1$$

$$\sum_{l=0}^{l_{max}} m_l \lambda^l = 0 \qquad 6.2$$

Calculation of interaction by the pressure operator $L_p\{...\}$ ($\alpha = 0$) is the simplest case as only the collocation point contributes so element shape and time-step duration do not affect the result. The elements of $\mathbf{M}$ and its characteristic polynomial are given as follows, providing a direct analytical link between the temporal basis function and its effect on MOT solver stability:

$$m_l = -\frac{\dot{T}_l(0)}{\dot{T}_0(0)} \qquad\qquad 6.3$$

$$\sum_{l=0}^{l_{max}} \dot{T}_l(0)\lambda^l = 0 \qquad\qquad 6.4$$

Any temporal basis function whose delayed copies form a partition of unity also has the property that the sum of the derivatives of its delayed copies sum to zero. This causes the coefficients of the pressure operator's characteristic polynomial (Equation 6.4) to sum to zero resulting in a trivial pole at unity, as has been a feature of all pole magnitude plots (Figure 3.39, Figure 3.46 and Figure 4.5). The physical explanation of this pole is that it carries the current system state to the next system iteration so that, when there is no excitation, the time derivative of the surface velocity potential is zero representing zero pressure.

Self-interaction poles are more complicated for the combined operator $L_c\{...\}$ due to the contribution from the edge of element, hence are dependent on element geometry and Δ_t. Due to the definition of $L_c\{...\}$, the immediate self interaction coefficients are unchanged by the blend coefficient α for CFL < 1. If CFL $\geq$ 1 and α > 0, the element edges contribute extra terms to the immediate self interaction coefficients that shift the poles of $\mathbf{M}$. With Ergin *et al's* temporal basis function these extra terms usually act to reduce the magnitude of the largest pole as shown below, however other temporal basis candidates exist where this is not the case.
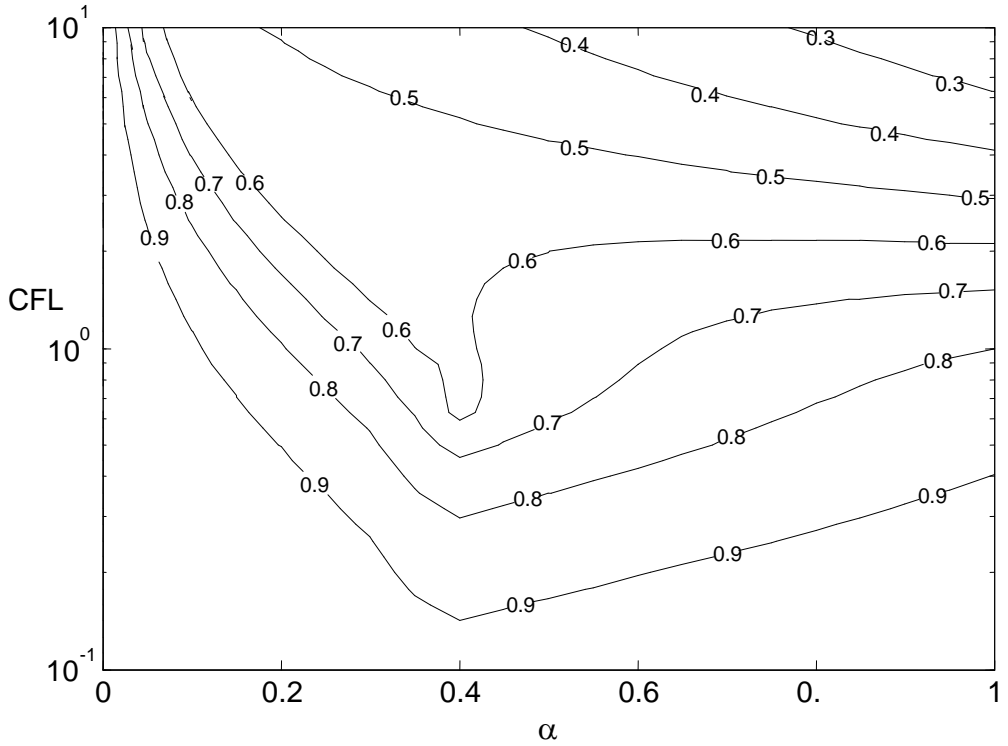
Figure 6.1: Self-interaction poles of an equilateral triangular element with a piecewise constant spatial basis function and Ergin *et al's* temporal basis function.

While it cannot be denied that the basis function used herein does provide accurate and mostly stable results, it seems likely that there should be other possibilities that also achieve this and whose mathematical properties are better known. If such could be found that had a continuous first derivative then the integration implementation would be simplified. One candidate family of such functions are the uniform B-splines [72]. These come in various orders matching their underlying polynomials, starting with the commonly used top hat and triangle functions then subsequently becoming more complex and having greater overlap. Early investigations suggest they produce stable self-interaction poles with collocation and the MOT solver.

The more mathematically elegant alternative to collocation is Gallerkin testing. This was described in section 2.2.4 and is mentioned here because of its influence on basis function choice. Essentially it replaces the aim of satisfying the boundary condition at a set of points in space time by satisfying it in a weighted average sense as defined by a set of testing functions. This averaging requires extra integration so immediately appears computationally expensive. However, unlike its spatial counterpart, little

increased cost is seen for temporal Gallerkin testing as the testing integral may be moved inside the spatial integral to only enclose the retarded temporal basis function term. This temporal integral is an inner product or cross-correlation between the testing and basis functions and, for such as are considered herein, may be computed analytically. Assuming the testing and basis functions are both retarded copies of the same mother basis function, what is achieved is equivalent to the collocation integrands herein but with the mother basis function replaced by its auto-correlation.

This is of modest interest in itself, although it permits impulse excitation as the cross-correlation of the incident wave with the testing function will be finite; a simpler and more elegant solution than the early algorithms [10-13, 17] that modelled shockwaves. However it has great impact if the MOT solver's restrictions on temporal basis choice are lifted and a family is used that has orthogonal members whose inner product is zero. A solver can be constructed that predicts and exploits the resulting pattern of zero interactions to achieve excellent efficiency. Such algorithms have been published within the Electromagnetics community that exploit Laguerre polynomials [52, 53] and multi-resolution basis [51] and it would make sense for these ideas to be transferred to acoustic modelling. This approach could accelerate the simultaneous solvers described in section 6.1; hopefully an efficient and stable algorithm would result.

Temporal Gallerkin testing also highlights the symmetry between the time domain and frequency domain BEMs. If a complex exponential is used as the temporal basis function and its complex conjugate as a testing function, then inner product between the two resembles a Fourier transform and the frequency domain integral equations are recovered. In acoustics applications, data averaged for a third of an octave is often desired but cannot be calculated by a frequency domain BEM except by averaging of discreet frequencies. It is possible that this data could be calculated directly using a time domain BEM with appropriately band limited basis functions.

In this section it has been shown that temporal basis function choice is inextricably linked with stability of the MOT solver. Alternative temporal discretisations have been discussed plus some cost aspects of Gallerkin temporal testing. The latter is identified as a means of accelerating the simultaneous solvers discussed in section 6.1 plus permits modelling of impulse excitation and possibly third octave analysis.

6.3 Integration Accuracy

The research presented in chapter 3 initially appears slightly at odds with the earlier comment that this thesis has been focused on extending the scope of the algorithm, as it examines the effect of integration accuracy on solution accuracy and solver stability rather than propose an algorithmic extension. However it arose from the same motivation as the other chapters; that of applying the time domain BEM to modelling typical Room Acoustics surface treatments. Having selected an algorithm to replicate as a starting point for investigation, it quickly became apparent that the Gaussian numerical integration employed was inadequate, especially for complex real world surfaces, so further investigation was necessary.

Gaussian integration is a popular method of evaluating discretised boundary integrals because of its efficiency and simplicity. It is generally recognised that the self-interaction integral must be treated as a special case and regularised in some way, but the potential unsuitability of Gaussian schemes for other interactions seems to often be ignored. By contrast the contour integration scheme derived herein regularises all integrals and treats them in a consistent and appropriate way. Use of an adaptive numerical integration scheme with an absolute accuracy criterion on each edge abstracts tailoring of numerical effort to an assertion of accuracy so that the same integration implementation can be used for all element pairs without loss of efficiency. It was recognised that such algorithmic modifications create maximum impact if derived in a general manner, so the pre-conditions were relaxed to be only that the surface is rigid and piece-wise flat (polygonal). This coordinate transform had been applied to these integrals before [18, 25], but this derivation's generality gives it potential for wider impact on this matter than either of these publications. Tomes [64] exist on integral methods suitable for BEM but this one is omitted, a frustration to this investigation for which integration accuracy is a secondary objective.

The contour integration scheme was shown to be more stable than the Gaussian integration scheme. Ironically the dominant error in the Gaussian results, originating from derivatives of the temporal basis function, was shown to cancel within the MOT solver while the spatial singularity error caused the instability. The latter conclusion is evidence that regularisation of some non-self element interactions is necessary.

The contour integration scheme was carried forward to subsequent chapters. In chapter 5 significant developments were performed embedding the surface reflection response model and deriving a contour integral implementation of the single layer potential term of the KIE. Again it was possible to achieve this without restriction on discretisation, just that the surface be piecewise flat, so generality and impact were maximised. The compliant surfaces model encompasses rigid surfaces so it was possible to retain a single integration routine that calculated all interactions in an elegant way.

It is felt that the current scheme is exceptionally well suited to calculating interactions on a piecewise flat surface; it is this geometric restriction that is its primary weakness. An implementation that was valid for curvilinear surfaces or surfaces of revolution would have significant application, though it is unclear whether it would retain the same brevity. It is anticipated that any such transformation would be derived by Stokes theorem [63], which is valid for any bounded surface. Obtaining a Stokes theorem based derivation equivalent to the current scheme is a likely first step toward this.

A pre-requisite to adopting spatial Galerkin testing would be a scheme for evaluating its double surface integrals. In principle the testing integral should be less singular than that of the KIE since its integrand is total sound radiated from the integration element to a point on the observation element; this is closely related to total surface velocity potential which is assumed smooth so Gaussian integration may suffice. However, the work of Bonnet *et al* [33] suggests that this is a naive viewpoint and more careful consideration of the arising singularities is required, especially where the elements share an edge or vertex. Conversion to a double contour integral appears attractive based on the conclusions of this thesis, but may prove excessively complex.

6.4 Scope & Applications

The primary aim of this thesis was development of the time domain BEM to better suit the needs of Room Acoustics modelling. There are many surface treatments of interest that cannot be modelled by a rigid closed surface BEM so accordingly chapters 4 and 5 focused on extending the algorithm's scope.

Predicting the scattering from a Schroeder Diffuser was an application of particular interest. These comprise a sequence of wells, separated by thin fins, whose depths are dictated by a number theoretic sequence and a design wavelength. Modelling these devices in the time domain is of interest as their wells are resonators so store energy and potentially produce transient effects not predicted by the diffusion mechanism model. The Schroeder Diffuser is modelled using two approaches: one involves meshing its entire geometry, the other replacing the wells by surfaces across their mouths that mimic their behaviour.

The time domain BEM implemented in chapter 3 cannot model objects with thin fins as the proximity of the surfaces at each solid / air interface causes singular behaviour in the underlying integral equations, a phenomena known as Thin Shape Breakdown [65]. Chapter 4 tackles this by adopting an open surfaces model where a single surface models the fin as a rigid air / air interface, an approach previously used with the time domain BEM [18] so not itself new. However, Ergin *et al* [22] showed that such a model of a closed surface permits cavity resonances so is often unstable. In light of this it was proposed herein that the open surfaces model be applied solely to the thin surface sections (the fins), the CFIE be applied to the remaining closed sections and that an improvement in stability will result relative to universal application of the open surfaces model. This mixed surface approach is analogous to an approach used for the frequency domain BEM [66] but is novel for the time domain algorithm. The observation that jump in velocity potential across the surface is the dictating factor in scattering by the entire rigid body, not just the thin sections, allows the same integral formulation to be applied to the entire surface and only the CFIE's blend parameter varied, thus algorithmic elegance is maintained.

The other strategy to model a Schroeder diffuser is as a box with properties on its front face that mimic the wells of the real device. In the frequency domain this property would be surface impedance, which encapsulates the fixed phase change between sound travelling into and out of the well as a relationship between total surface pressure and total surface normal velocity. Chapter 5 achieves an equivalent model as an application example of a new time domain BEM for compliant surfaces.

A Quadratic Residue Diffuser [67] is a class of Schroeder Diffuser and a single period of the device was modelled using the two methods outline above. Both approaches were successful, achieving similar accuracy compared to an open surfaces frequency domain BEM, but universal stability can be ensured for neither. As postulated, the mixed surface model of chapter 4 does achieve superior stability compared to a purely open surface model, but instability still occurs for some time-step durations. It is suggested that this occurs because the wells possess lightly damped poles, not suppressed by the CFIE as they are physical and external to the body, and that these are easily corrupted into instability. The impedance surface model in chapter 5 suffers from instability, but this is not due to the mesh which is a simple convex box. Instead it is the well elements themselves that possess lightly damped poles in likeness to the physical structure they represent. Again the light damping of the poles means the system readily becomes unstable if corrupted by numerical error. Both models fail for the fundamental reason that the Schroeder diffuser contains wells which are lightly damped resonators. Obviously the real device does not become unstable so the behaviour of the time domain BEM is erroneous. However, Rynne [38] showed that divergent poles should be forbidden by the system initial condition, so it is the way error accumulates in the MOT solver, rather than a fundamental property of the integral equations, that allows the solution to diverge

There are many materials used by Acousticians that are not well approximated by a rigid surface model, the most extreme examples being ones used specifically for their sound absorbing properties, thus the scope of the time domain BEM would be increased if it could model compliant surfaces. Compliant surfaces have been modelled by frequency domain BEMs for some time. It is achieved by coupling the BEM to a material model through the surface unknowns of pressure and normal velocity. This material model could be a volumetric model of the interior of the scattering body, but more commonly it is abstracted to surface impedance, a frequency dependent complex valued scalar relating pressure and inward normal velocity. The absence of a time domain equivalent to the impedance boundary condition is sometimes remarked upon as a limitation of the time domain BEM for Room Acoustics modelling applications, but in chapter 5 that is redressed.

Surface impedance is a convenient quantity for use in a frequency domain BEM as it relates pressure and normal velocity by a fixed complex scalar so only one unknown surface quantity need be solved for. However this representation is not convenient for the time domain BEM with an MOT solver. The frequency dependent multiplication by a scalar becomes a convolution under inverse Fourier transform. Total surface pressure is not a causal function of total normal velocity, or vice versa, so a convolution to find one from the other will include future sound, thus is incompatible with the time marching MOT solver. The surface reflection coefficient provides a solution to this issue as it relates inward and outward propagating sound, the latter being a causal function of the former, so its time domain equivalent includes convolution with past sound only. Its convolution kernel is the inverse Fourier transform of surface reflection coefficient, the frequency dependent complex ratio between magnitudes of harmonic plane waves travelling into and out of a flat sample of the material as would occur in an impedance tube, and is denoted the surface reflection response. This representation is cited[56] as being more robust to numerical error than differential boundary conditions and allows the causality and stability of the boundary condition to be examined in a straightforward way not possible for impedance.

A crucial and novel step to allow the surface reflection response model to be efficiently integrated into a time domain BEM framework was made in section 5.2. This observed that the inward and outward wave model allowed normal velocity and pressure to be related by a scalar for the incoming and outgoing waves independently, as for plane waves in free space. This highlights that it is not the relating of pressure and normal velocity by a scalar that causes impedance to yield convolutions that include future sound, rather it is its aggregation of incoming and outgoing sound. The resulting time domain algorithm shares the convenience of only possessing one surface unknown, the incoming sound wave, but to find the total pressure and normal velocity values convolution with the surface reflection response is required. It was identified that incoming velocity potential should be discretised, and that the basis function representation allowed the convolution necessary to evaluate total sound to be embedded into the temporal convolution of the MOT solver, both novel approaches. The interaction coefficients for such were derived as contour integrals, valid for a piecewise-flat surface of arbitrary compliance without refinement to a particular

discretisation scheme or surface reflection response. These statements are hoped to have significant impact on state of the art time domain BEM research.

At this early stage a full compliant surface time domain BEM was not implemented, instead the statements were refined for a simpler boundary condition. In this each piecewise constant surface element represents the mouth of a well containing some hypothetical broadband absorbent, thus the outgoing wave is a scaled and delayed copy of the incoming wave. This simplified scheme was verified on surfaces containing either welled or absorbent surface sections, including the Quadratic Residue Diffuser discussed above. Accuracy compared to a frequency domain BEM modelling an equivalent impedance surfaces was excellent. Interference effects between incident and scattered sound were examined close to box shaped scatterers with one source orientated face of uniform welled or absorbing elements; trends were seen to make physical sense and agree with both frequency domain BEMs. The surfaces with welled elements experienced some instability; this was interpreted as corruption of the lightly damped physical poles of the real device manifesting as divergence of the MOT solver, rather than failure of the compliant surface boundary condition. In contrast the surfaces with absorbing sections were universally stable. These did not represent an increase in algorithm scope since absorbing surfaces have been modelled before [19, 25], but they served to further verify the principle of the compliant surfaces BEM.

As regards future research directions, the compliant surfaces BEM has been derived for arbitrary surface reflection responses but not implemented, so this should be pursued. However, obtaining suitable surface reflection response data is a serious impediment. A direct approach would involve applying the inverse discrete Fourier transform to discrete measured frequency domain data. Adequate temporal resolution and length of the surface reflection response could be ensured by including suitably high frequency domain measurements and interpolating their data respectively, but the extremely low frequency data necessary to unwrap phase is unlikely to be available. Literature cited [23-25] in chapter 5 attempts to overcome this obstacle by decomposing the convolution into the individual responses of the poles of the surface reflection coefficient within the frequency band of interest and may provide a solution. Further research is required to establish for exactly what class of surface the surface model proposed herein holds.

An alternative to the surface impedance equivalent model proposed herein is coupling to a volumetric material model though the physical surface unknowns of pressure and normal velocity. This could be a BEM [33, 36] if the material were homogeneous; otherwise a Finite Element Method would be more suitable and may be more efficient if vibrations are known to not penetrate far into the scatterer. This approach would likely have higher computational cost than a surface impedance type model, but could simulate additional phenomena: The local reaction assumption is invalid for certain materials in cases of grazing incident sound and this could be correctly modelled. The motion and consequential absorption of thin surfaces, such as the fins of a Schroeder diffuser or an orchestral canopy, in response to the pressure differential across them could be simulated. In addition there are potential applications that are not readily modelled by other means: If the material model supports non-linear effects then the coupled system could model their audible response, such as far-field radiated components of loudspeaker distortion.

A remaining enhancement of algorithm scope that was discussed in section 2.2.3 but has not received further attention is modelling in two dimensions. Cox [27] found this was a good approximation for frequency domain modelling of extruded shapes, such as the Quadratic Residue Diffuser modelled in chapters 4 and 5, accompanied by excellent cost scaling due to the reduced number of elements. These cost savings do not translate directly to the time domain as its two dimensional Greens function is not compact. However methods such as the PWTD [29] algorithm or calculation of discrete convolutions by Fourier transform may redress this and are worthy of further research.

All future research suggested so far has focussed on enhancing the time domain BEM rather than applying it, a reflection on the immaturity of the method. However, it is application that gives meaning to modelling so a research question the time domain BEM could answer is pertinent. This regards the transient nature of scattering from diffusers as mentioned in the discussion of Schroeder diffusers at the beginning of this section. The two diffusers modelled in this thesis have different diffusing mechanisms. Fundamentally they both rely on being partitioned into sections that are small with respect to wavelength so individually scatter widely. The impedances of these surface sections are varied so that instead of constructive interference occurring for one angle only, as would happen for a uniform flat surface, it occurs at many angles so the total

reflected wave is diffuse. The Quadratic Residue Diffuser achieves this by changing the phase of reflections. The Binary Amplitude Diffuser modulates which parts of the surface reflect and which absorb. The former diffuser has resonant wells capable of storing energy while the latter does not; hence it is likely their transient responses will be very different. To what extent theses differences propagate to the far-field and are audible is of interest to diffuser designers. This data could be calculated through many frequency domain BEM models and inverse DFT, but this would be computationally expensive and the time domain BEM is well suited to this type of transient analysis.

6.5 Conclusions

This thesis achieves its original goal of modelling surface treatments typical to Room Acoustics. In particular, two classes of diffuser have been modelled that previously were not possible. These are a two-dimensional Primitive Root Diffuser, which was unstable due to poor integration accuracy, and a Quadratic Residue Diffuser, which required the mixed surfaces model to achieve any useful stability. An idealised Binary Amplitude Diffuser was also modelled requiring absorbing surfaces; technically this was previously possible using other published algorithms but had not been attempted. A more realistic Binary Amplitude Diffuser model would be possible with a full implementation of the BEM for compliant surfaces.

In addition to the primary goal, the field of time domain BEM research has been given two new surface models, one for finned closed surface and the other for compliant surfaces, plus an efficient and accurate integration scheme valid for arbitrary discretisation of a piecewise-flat scatterer. More so than the above modelling results, these are the primary contributions of this thesis.

However, the time domain BEM still requires significant development before it can be considered a mature method. In particular stability issues persist, albeit to a lesser extent, and computational cost is still high. These two critical issues preclude the algorithm from widespread application given that alternate modelling methods exist. Nonetheless the algorithm has potential applications that are not readily modelled by other means, particularly if coupled to a non-linear model of the scattering or radiating

surface. If stability and computational cost can be overcome then in such applications the algorithm will have the opportunity to shine.

7 Conclusions

This thesis has attempted to improve the suitability of the time domain BEM for modelling the scattering of sound by surface treatments typical to Room Acoustics. Such numerical predictions aid treatment design by accelerating prototyping and allowing optimisation to be performed.

Unlike the frequency domain BEM, the time domain algorithm discretises the surface sound in time as well as space. The solution is solved iteratively in time from known initial conditions, a process named Marching On in Time (MOT), so the algorithm has the potential to be unstable and diverge from the correct solution. This behaviour and high computational cost currently prohibit the algorithm from widespread application.

The time domain BEM also finds application in Electromagnetics and Elastodynamics, and between these fields and Acoustics much research has been published. The research on stability falls into two main camps: those that analyse the stability of the MOT solver, and those that consider the fundamental behaviour of the underlying boundary integral equations. This thesis has adopted the prominent stability analysis of the former, being the concept of the corruption into instability of damped physical poles then excited by numerical truncation error, and the cures of the latter, for example the Combined Field Integral Equation which inhibits non-physical surface cavity resonances. It was identified that representation of the discretisation scheme using basis functions has advantages in maintaining generality when deriving numerical integrands, such as permitting implicit time-step durations. As a starting point for this research an algorithm that included these features was replicated.

It was observed that the numerical integrands of the replicated algorithm are discontinuous because they contain the derivatives of the temporal basis function, and that this caused significant integration error. The algorithm was not universally stable so it was inferred that these two aspects were connected. The purpose of chapter 3 was to investigate this connection and develop a solution. A method of quantifying integration error was required and was found in the guise of Monte Carlo integration.

This showed that the Gaussian integration scheme gave errors worse than 10% on some element interactions, so an alternative integration scheme was developed.

The superior numerical integration scheme proposed is based on conversion to contour integrals by analytical integration following a change of coordinates. This regularises the integrals so the same routine may be used for self and non-self interactions. Adaptive numerical integration with an absolute accuracy criterion is applied to each contour to tailor numerical effort as required in a transparent and continuous way.

The contour integration scheme and the Gaussian scheme were compared on simple and realistic surface meshes to investigate the effect that integration errors have on solution accuracy and stability. The contour integration scheme yielded interaction matrices that were universally stable on both meshes. The interaction discrepancies originating from the presence of the derivatives of the temporal basis function in the integrands were shown to largely cancel within the MOT solver and not significantly affect the solution. The remaining error of the Gaussian scheme was due to its unsuitability for the spatially singular numerical integrands and rendered it unstable on the realistic surface mesh. The superiority of the contour integration implementation was confirmed.

Chapter 4 aimed to expand the modelling scope of the time domain BEM while maintaining the state-of-the-art in stability control. Objects with thin fins, in particular Schroeder diffusers, were considered because these cannot be modelled naïvely by surfaces at each solid / air interface as their proximity causes singular behaviour in the underlying integral equations. Instead the fins were modelled as rigid air / air interfaces and the rest of the body using the CFIE, the latter necessary to inhibit resonances of the enclosed cavity. This approach is analogous to an approach used for the frequency domain BEM but is novel for the time domain algorithm. The observation that jump in velocity potential is the dictating factor in scattering by the entire surface, not just the thin sections, allows the same integral formulation to be applied to the entire surface and only the CFIE's blend parameter varied, thus algorithmic elegance is maintained.

This mixed surfaces model is extensively verified, and there is unanimous evidence that use of the CFIE improves accuracy for any surface with closed sections. However,

results also show that, even with the CFIE and contour integration, stability is not guaranteed, especially on complex surfaces with concave parts.

In chapter 5 a new time domain BEM capable of modelling certain compliant surfaces is developed. For the frequency domain BEM this is usually achieved using the concept of a surface impedance boundary condition, which relates total surface pressure and normal velocity. This is unsuitable for a time domain BEM with a time marching solver as neither of these quantities is a causal function of the other, so evaluating the boundary condition will require future data which is not yet known to the solver. Instead the time domain impedance equivalent boundary condition is derived from the surface reflection coefficient; this relates sound propagating into and out of the surface, a causal relationship so involves past data only. The inverse Fourier transform of surface reflection coefficient is denoted surface reflection response and its convolution with the incoming sound wave gives the outgoing sound wave.

This boundary condition requires the incoming and outgoing sound waves to be distinguished within the boundary integral equations. The surface model allows the normal velocity of each wave to be found by scalar multiplication of its pressure, so only the velocity potential of the incoming wave is unknown and need be discretised. The resulting boundary integral equations are expressed as contour integrals, derived for a piecewise flat surface without refinement to a particular discretisation scheme or surface reflection response.

A full compliant surface time domain BEM is not implemented; instead the statements are refined for a simpler boundary condition. In this, each piecewise constant surface element represents the mouth of a well containing some hypothetical broadband absorbent, thus the outgoing wave is a scaled and delayed copy of the incoming wave. This simplified scheme is verified on simple surfaces and two diffuser models. Accuracy compared to a frequency domain BEM is good, confirming the principles of the model; however instability is evident for surfaces including welled elements.

The three algorithm extensions (contour integration, mixed and compliant surfaces) are considered to be the primary contributions to knowledge by this thesis, as the modelling

that was performed was primarily for verification purposes and the analysis followed the thoughts of others.

Much further research and development is required of the time domain BEM before it can be considered a mature method and put to widespread use. The association of instability with the way error accumulates in the MOT solver and the connection created between temporal discretisation and stability suggests an alternative solver should be sought. This could be some type of simultaneous solver as these are said to less favour divergent solutions and relieve restrictions on choice of temporal discretisation. However, they have potentially poor computational cost scaling so an acceleration strategy is required; this could exploit element interaction aggregation and / or orthogonality of the discretisation basis functions under Galerkin testing.

The full compliant surfaces BEM was not implemented in chapter 5 so this is an obvious avenue of future work. However, there are issues surrounding obtaining suitable surface reflection response data that need to be resolved. Coupling to a material model of the scatterer is more computationally expensive but circumvents this issue and widens the modelling scope.

This thesis has investigated the time domain BEM and its applicability to modelling of Room Acoustics surface treatments. Despite improving the algorithm, it is still insufficiently mature to permit this. One source of numerical error is integration accuracy and this has been addressed by derivation of a contour integration scheme valid for any discretisation of a piecewise flat surface. Unless treated carefully the underlying boundary integral equations become singular on thin bodies and support non-physical cavity resonances inside larger bodies; an algorithm was developed that manages both these phenomenon. Many surface treatments used in Room Acoustics are not rigid so an impedance equivalent surface model was developed, cast into the BEM framework and implemented for surfaces with welled and absorbing sections. Some instability was observed on surfaces with lightly damped physical resonances; this is thought to be due to the behaviour of the MOT solver and it is suggested that an alternative be sought.

8 Appendix

8.1 Temporal convolution with spatial derivative of the Greens function

The Kirchhoff Integral Equation (KIE) for rigid surfaces contains the following boundary integral which it is desired to solve numerically. Currently this is not in an amenable form as it contains the spatial derivative of a generalised function, which cannot be tackled numerically. It is also in an inefficient form containing three nested integrations; a double spatial integral and the temporal integration of the convolution operator. The purpose of this section is to exploit the sifting characteristics of the delta function to remove the temporal integral and handle the spatial derivative.

$$\iint_S \varphi^t(\mathbf{r}',t) * \hat{\mathbf{n}}' \cdot \nabla' \frac{\delta\left(t - R/c\right)}{4\pi R} d\mathbf{r}' \qquad\qquad 8.1$$

Ergin *et al*[22] tackled this hurdle in the derivation of their numerical integrands; they use the equivalence below. It will be seen later that this equivalence only holds for rigid surfaces; this was not an issue for them as they only considered such. However, Equation 8.1 is the double layer potential which forms part of the KIE for non-rigid surfaces (Equation 2.6), therefore the scope of any integration implementation derived from it will be widened if care is taken to not assume the surface is rigid. The change will be seen to be subtle, but significant given that this thesis aims to maximise generality and considers non-rigid surfaces.

$$\iint_S \varphi^t(\mathbf{r}',t) * \hat{\mathbf{n}}' \cdot \nabla' \frac{\delta\left(t - R/c\right)}{4\pi R} d\mathbf{r}' = \iint_S \hat{\mathbf{n}}' \cdot \nabla' \frac{\varphi^t\left(\mathbf{r}', t - R/c\right)}{4\pi R} d\mathbf{r}' \qquad\qquad 8.2$$

First the spatial derivative of the Greens function will be considered. As this is a function solely in R and t its spatial gradient may be expressed as a derivative with respect to R, yielding a scalar, and a unit vector to indicate direction. The minus sign

appears because at the integration point $\hat{\mathbf{R}}$ points away from the direction of increasing R. The quotient rule is then applied:

$$\nabla' \frac{\delta\left(t - R/c\right)}{4\pi R} = -\hat{\mathbf{R}} \frac{\partial}{\partial R} \frac{\delta\left(t - R/c\right)}{4\pi R}$$
$$= \frac{-\hat{\mathbf{R}}}{4\pi R^2}\left[R \frac{\partial}{\partial R}\delta\left(t - R/c\right) - \delta\left(t - R/c\right)\right]$$

8.3

This is substituted into the temporal convolution and all possible terms are moved outside the convolution. The derivative of the delta function with respect to R is substituted by a derivative with respect to t by observing the chain rule:

$$\varphi^t\left(\mathbf{r}',t\right) * \hat{\mathbf{n}}'{\cdot}\nabla' \frac{\delta\left(t - R/c\right)}{4\pi R}$$
$$= \frac{-\hat{\mathbf{n}}'{\cdot}\hat{\mathbf{R}}}{4\pi R^2}\left[R\left[\varphi^t\left(\mathbf{r}',t\right) * \frac{\partial}{\partial R}\delta\left(t - R/c\right)\right] - \varphi^t\left(\mathbf{r}',t\right) * \delta\left(t - R/c\right)\right]$$
$$= \frac{-\hat{\mathbf{n}}'{\cdot}\hat{\mathbf{R}}}{4\pi R^2}\left[-cR\left[\varphi^t\left(\mathbf{r}',t\right) * \frac{\partial}{\partial t}\delta\left(t - R/c\right)\right] - \varphi^t\left(\mathbf{r}',t\right) * \delta\left(t - R/c\right)\right]$$

8.4

The sifting property of the delta function under convolution (below) is now exploited. As this is not especially well known for derivatives of the delta function, it is derived in section 8.2. In Equation 8.6 this is substituted into Equation 8.4, and the process of expanding the spatial derivative is reversed.

$$\varphi^t\left(\mathbf{r}',t\right) * \frac{\partial^n}{\partial t^n}\delta\left(t - R/c\right) = \frac{\partial^n}{\partial t^n}\varphi^t\left(\mathbf{r}',t - R/c\right)$$

8.5

$$\varphi^t\left(\mathbf{r}',t\right) * \hat{\mathbf{n}}'{\cdot}\nabla' \frac{\delta\left(t - R/c\right)}{4\pi R} = \frac{-\hat{\mathbf{n}}'{\cdot}\hat{\mathbf{R}}}{4\pi R^2}\left[-cR\frac{\partial}{\partial t}\varphi^t\left(\mathbf{r}',t - R/c\right) - \varphi^t\left(\mathbf{r}',t - R/c\right)\right]$$
$$= \frac{-\hat{\mathbf{n}}'{\cdot}\hat{\mathbf{R}}}{4\pi R^2}\left[R\frac{\partial}{\partial R}\varphi^t\left(\mathbf{r}',t - R/c\right) - \varphi^t\left(\mathbf{r}',t - R/c\right)\right]$$
$$= -\hat{\mathbf{n}}'{\cdot}\hat{\mathbf{R}} \frac{\partial}{\partial R} \frac{\varphi^t\left(\mathbf{r}',t - R/c\right)}{4\pi R}$$

8.6

Equation 8.7 gives the integral of the KIE for a rigid surface in a form amenable to numerical evaluation. The delta function has been extracted and the order of integration reduced. To see that this that this is equivalent to Ergin *et al's* statement on a rigid surface, consider under what circumstances Equation 8.8 holds; this asserts that all surface normal variation in the quotient term is due to the dependence on R, or conversely that $\hat{\mathbf{n}}' \cdot \nabla' \varphi^t(\mathbf{r}',t) = 0$. This is the rigid boundary condition, so 8.2 holds only for a rigid surface. By contrast, 8.7 also holds for non-rigid surfaces so may be used to evaluate the double layer potential within the full KIE.

$$\iint_S \varphi^t(\mathbf{r}',t) * \hat{\mathbf{n}}' \cdot \nabla' \frac{\delta\left(t - R/c\right)}{4\pi R} d\mathbf{r}' = -\iint_S \hat{\mathbf{n}}' \cdot \hat{\mathbf{R}} \frac{\partial}{\partial R} \frac{\varphi^t\left(\mathbf{r}', t - R/c\right)}{4\pi R} d\mathbf{r}' \qquad 8.7$$

$$-\hat{\mathbf{n}}' \cdot \hat{\mathbf{R}} \frac{\partial}{\partial R} \frac{\varphi^t\left(\mathbf{r}', t - R/c\right)}{4\pi R} = \hat{\mathbf{n}}' \cdot \nabla' \frac{\varphi^t\left(\mathbf{r}', t - R/c\right)}{4\pi R} \qquad 8.8$$

ERROR – It has been implicitly assumed in this section that all spatial variation in the retarded surface velocity potential is due to the convolution with the retarded delta function. Hence this statement only holds when there is no spatial variation in the surface velocity potential, which requires the use of piece-wise constant spatial elements.

8.2 Sifting properties of the delta function

The sifting property of the delta function under convolution (below) is well known, but the properties of its temporal derivatives are less so, hence this explanation appears here. $f(t)$ is an arbitrary function of time, and a is a constant scalar.

$$f(t) * \delta(t - a) = f(t - a) \qquad 8.9$$

What is of interest is the convolution of $f(t)$ with the nth temporal derivative of a retarded delta function. This is written below, and the convolution is expanded into its integral form. Note that τ is being used here as an integration variable, rather than to represent retarded time. The derivative with respect to t is substituted by a derivative

with respect to τ by observing the chain rule; the $(-1)^n$ term arises due to the opposite signs of t and τ in the argument of $\delta(\ldots)$. Flipping the sign of the argument cancels this term.

$$
\begin{aligned}
f(t) * \frac{d^n}{dt^n} \delta(t-a) &= \int_{-\infty}^{\infty} f(\tau) \frac{d^n}{dt^n} \delta(t-a-\tau) d\tau \\
&= (-1)^n \int_{-\infty}^{\infty} f(\tau) \frac{d^n}{d\tau^n} \delta(t-a-\tau) d\tau \\
&= \int_{-\infty}^{\infty} f(\tau) \frac{d^n}{d\tau^n} \delta(\tau-(t-a)) d\tau
\end{aligned}
\qquad 8.10
$$

The sifting property of derivatives of the delta function[73] is usually written as follows. It has the effect of applying the derivative and delay to $f(\ldots)$, plus a change of sign if the order of differentiation is odd:

$$
\int_{-\infty}^{\infty} f(t) \frac{d^n}{dt^n} \delta(t-a) dt = (-1)^n \frac{d^n}{dt^n} f(a)
\qquad 8.11
$$

This is substituted into Equation 8.10 and the derivative with respect to τ changed back to one with respect to t. This statement extends the well known sifting property (Equation 8.9) to temporal derivatives of the delta function as required by section 8.1.

$$
f(t) * \frac{d^n}{dt^n} \delta(t-a) = (-1)^n \frac{d^n}{d\tau^n} f(t-a) = \frac{d^n}{dt^n} f(t-a)
\qquad 8.12
$$

8.3 Gradient of dot product term

This section focuses on evaluating $\nabla \hat{\mathbf{n}}' \cdot \hat{\mathbf{R}}$. A cylindrical polar coordinate system is defined centred on $\mathbf{r}'$, depicted below. This is the same as that which is used in section 3.2.1, except for a translation of the origin and that it is specific to the current choice of $\mathbf{r}'$; the later point means this derivation applies to any shape surface.
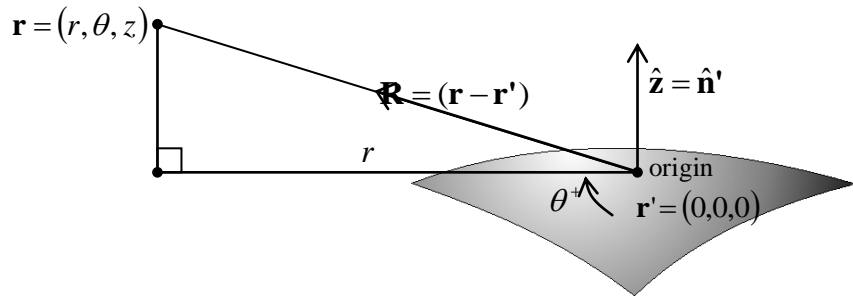
Figure 8.1: Cylindrical Polar Coordinate System

The gradient is evaluated in cylindrical polar form as follows, where $f(\mathbf{r}) = \hat{\mathbf{n}}' \cdot \hat{\mathbf{R}}$:

$$\nabla f(\mathbf{r}) = \hat{\mathbf{r}}\frac{\partial f}{\partial r} + \frac{1}{r}\hat{\boldsymbol{\theta}}\frac{\partial f}{\partial \theta} + \hat{\mathbf{z}}\frac{\partial f}{\partial z} \qquad 8.13$$

$f(\mathbf{r})$ is re-written as an explicit function of the position of $\mathbf{r}$:

$$f(\mathbf{r}) = \hat{\mathbf{n}}' \cdot \hat{\mathbf{R}} = \frac{\hat{\mathbf{n}}' \cdot \mathbf{R}}{R} = \frac{z}{R} = \frac{z}{\sqrt{r^2 + z^2}} = \left[\left(\frac{r}{z}\right)^2 + 1 \right]^{-\frac{1}{2}} \qquad 8.14$$

Immediately it is clear that the angular derivative of f is zero. In calculating the remaining derivatives it will prove convenient to define $x = rz^{-1}$, so the derivative of $f(\mathbf{r})$ with respect to x may be found. The remaining derivatives are found by chain rule:

$$f(\mathbf{r}) = \left[x^2 + 1\right]^{-\frac{1}{2}}$$
$$\frac{df}{dx} = -x\left[x^2 + 1\right]^{-\frac{3}{2}} = -\left(\frac{r}{z}\right)\frac{z^3}{\left(r^2 + z^2\right)^{\frac{3}{2}}} = -\frac{rz^2}{R^3} \qquad 8.15$$

$$\frac{\partial f}{\partial r} = \frac{\partial x}{\partial r}\frac{df}{dx} = \frac{1}{z}\left(-\frac{rz^2}{R^3}\right) = -\frac{rz}{R^3} \qquad 8.16$$

$$\frac{\partial f}{\partial z} = \frac{\partial x}{\partial z}\frac{df}{dx} = -\frac{r}{z^2}\left(-\frac{rz^2}{R^3}\right) = \frac{r^2}{R^3} = \frac{R^2 - z^2}{R^3} = \frac{1}{R} - \frac{z^2}{R^3} \qquad 8.17$$

221

Equations 8.16 and 8.17 are substituted into Equation 8.13 to evaluate the gradient. The terms are manipulated such that the end result is written using only quantities directly found from the surface geometry, rather than via the coordinate system of Figure 8.1. This equality applies to any smooth surface.

$$
\begin{aligned}
\nabla \hat{\mathbf{n}}'\cdot\hat{\mathbf{R}} &= -\hat{\mathbf{r}}\frac{rz}{R^3} + \hat{\mathbf{z}}\left(\frac{1}{R} - \frac{z^2}{R^3}\right) \\
&= \frac{\hat{\mathbf{z}}}{R} - \frac{z}{R^3}\left(r\hat{\mathbf{r}} + z\hat{\mathbf{z}}\right) \\
&= \frac{\hat{\mathbf{z}}}{R} - \frac{z\mathbf{R}}{R^3} \\
&= \frac{\hat{\mathbf{n}}'}{R} - \frac{\hat{\mathbf{n}}'\cdot\hat{\mathbf{R}}}{R}\hat{\mathbf{R}}
\end{aligned}
$$

8.18

9 References

1. T. J. Cox and P. D'Antonio, *Acoustic Absorbers and Diffusers*, Spon Press (2004)

2. J. G. Meloney and K. E. Cummings, "Adaption of FDTD techniques to acoustic modelling", *11th Annu. Rev. Prog. Appl. Comput. Electromagnet.* **2**: 724 (1995)

3. A. D. Pierce, *Acoustics: an introduction to its physical principles and application*, McGraw-Hill 1981

4. P. H. L. Groenenboom, "Wave Propagation Phenomena", *Progress in Boundary Element Methods 2*, Pentech Press (1983)

5. H. A. Schenck, "Improved integral formulation for acoustic radiation problems", *J. Acoust. Soc. Am.* **44** (1) $41 - 58$ (1968)

6. A. J. Burton and G. F. Miller, "The application of integral equation methods to the numerical solution of some exterior boundary-value problems", *P. Roy. Soc. Lond. A. Mat.* **323**: $201 - 210$ (1971)

7. J. Keller and A. Blank, "Diffraction and Reflection of Pulses by Wedges and Corners", *Commun. Pur. Appl. Math.* **4** (1): $75 - 94$ (1951)

8. R. D. Mindlin and H. H. Bleich, "Response of an Elastic Cylindrical Shell to a Transverse Step Shock Wave", *J. Appl. Mech.* **75**: 189 (1953)

9. Richard G. Barakat, "Transient Diffraction of Scalar Waves by a Fixed Sphere", *J. Acoust. Soc. Am.* **32** (1): $61 - 66$ (1960)

10. M. B. Friedman and R. P. Shaw, "Diffraction of Pulses by Cylindrical Obstacles of Arbitrary Cross Section", *J. Appl. Mech.* **29**: $40 - 46$ (1962)

11. R. P. Shaw, "Diffraction of Acoustic Pulses by Obstacles of Arbitrary Shape with a Robin Boundary Condition", *J. Acoust. Soc. Am.* **41** (4A): $855 - 859$ (1967)

12. R. P. Shaw and J. A. English, "Transient Acoustic Scattering by a Free (Pressure Release) Sphere", *J. Sound. Vib.* **20** (3): 321 – 331 (1972)

13. R. P. Shaw, "Transient Scattering by a Circular Cylinder", *J. Sound. Vib.* **42** (3): 295 – 304 (1975)

14. K. M. Mitzner, "Numerical Scattering for Transient Scattering from a Hard Surface of Arbitrary Shape – Retarded Potential Technique", *J. Acoust. Soc. Am.* **42** (2): 391 – 397 (1967)

15. R. P. Shaw, "Comments on "Numerical Scattering for Transient Scattering from a Hard Surface of Arbitrary Shape – Retarded Potential Technique"", *J. Acoust. Soc. Am.* **43** (3): 638 – 639 (1968)

16. O. D. Kellogg, *Foundations of Potential Theory*, Dover Publications Inc (1953)

17. H. C. Neilson, Y. P. Lu and Y. F. Wang, "Transient Scattering by Arbitrary Axisymmetric Surfaces", *J. Acoust. Soc. Am.* **63** (6): 1719 – 1726 (1978)

18. Y. Kawai and T. Terai, "A Numerical Method for the Calculation of Transient Acoustic Scattering from Thin Rigid Plates", *J. Sound Vib.* **141** (1): 83 – 96 (1990)

19. P. H. L. Gronenboom, "The applications of boundary elements to steady and unsteady potential fluid flow problems in two and three dimensions", *Appl. Math. Modelling* **6**: 35 – 40 (1982)

20. M. J. Bluck and S. P. Walker, "Analysis of Three-Dimansional Transient Acoustic Wave Propagation using the Boundary Integral Equation Method", *Int. J. Numer. Meth. Eng.* **39**: 1419 – 1431 (1996)

21. G. Manara, A. Monorchio and R. Regginannini, "A Space-Time Discretisation Criterion for a Stable Time-Marching Solution of the Electric Field Integral Equation", *IEEE T. Antenn. Propag.* **45** (3): 527 – 532 (1997)

22. A. A. Ergin, B. Shanker and E. Michielssen, "Analysis of transient wave scattering from rigid bodies using a Burton-Miller approach", *J. Acoust. Soc. Am.* **106** (5): 2396 – 2404 (1999)

23. J. L. Hu and C. H. Chan, "Improved temporal basis function for time domain electric field integral equation method.", *Electronics Letters* **35** (11): 883 – 885 (1999)

24. J. L. Hu, C. H. Chan and Y. A. Xu, "A new temporal basis function for the time-domain integral equation method", *IEEE Microw. Wirel. Co.* **11** (11): 465 – 466 (2001)

25. T. Ha-Duong, B. Ludwig and I.Terrasse, "A Galerkin BEM for transient acoustic scattering by an absorbing obstacle", *Int. J. Numer. Meth. Engng.* **57**: 1845 – 1882 (2003)

26. S. Amini and S. P. Nixon, "Multiwavelet Galerkin boundary element solution of Laplace's equation", *Eng. Anal. Bound. Elem.* **30**: 116 – 123 (2006)

27. T. J. Cox, "Predicting the scattering from reflectors and diffusers using 2D BEM", *J. Acoust. Soc. Am.* **96** (2): 874 – 878 (1994)

28. P. M. Morse and K.U. Ingard, *Theoretical Acoustics*, Princeton University Press (1968)

29. M. Lu, J. Wang, A. A. Ergin and E. Michielssen, "Fast Evaluation of Two-Dimensional Transient Wave Fields", *J. Comput. Phys.* **158**: 161 – 185 (2000)

30. D. A. Vechinski and S. M. Rao, "Transient Scattering from dielectric cylinders: E-field, h-field and combined-field solutions", *Radio Sci.* **27** (5): 611 – 622 (1992)

31. A. A. Ergin, "Plane-Wave Time-Domain Algorithms For Efficient Analysis of Three-Dimensional Transient Wave Phenomena", PhD Thesis, University of Illinois at Urbana-Champaign (2000)

32. Y. Ding, A. Forestier and T. Ha-Duong, "A Galerkin scheme for the time domain integral equation of acoustic scattering from a hard surface", *J. Acoust. Soc. Am.* **86** (4): 1566 – 1572, (1989)

33. M. Bonnet, G. Maiera and C. Polizzotto, "Symmetric Galerkin Boundary Element Methods", *Appl. Mech. Rev.* **51** (11): 669 – 703 (1998)

34. T. Ha-Duong, "On Retarded Potential Boundary Integral Equations and their Discretisation", Lecture Notes in Computational Science and Engineering 31: Topics in Computational Wave Propagation, Direct and Inverse Problems, Springer (2003)

35. S. J. Dodson, S. P. Walker, M. J. Bluck, "Implicitness and stability of time domain integral equation scattering analysis", *ACES. J.* **13**: 291 – 301 (1998)

36. G. C. Herman and P. M. van den Berg, "A Least Squares Iteratively Technique for solving Time-Domain Scattering Problems", *J. Acoust. Soc. Am.* **72** (6): 1947 – 1953 (1982)

37. C. T. Dyka and R. P. Ingel, "Transient fluid-structure interaction in naval applications using the retarded potential technique", *Eng. Anal. Bound. Elem.* 21 (3): 245 – 251 (1998)

38. B. P. Rynne, "Instabilities in Time Marching Methods for Scattering Problems", *Electromagnetics* **6**: 129 – 144 (1986)

39. B. P. Rynne and P. D. Smith, "Stability of Time Marching Algorithms for the Electric Field Integral Equation", *J. Electromagnet. Wave.* **4** (12): 1181 – 1205 (1990)

40. P. D. Smith, "Instabilities in Time Marching Methods for Scattering: Cause and Rectification", *Electromagnetics* **10**: 439 – 451 (1990)

41. P. J. Harris, H. Wang, R. Chakrabarti and R. Henwood, "Stability analysis of a collocation method for solving the retarded potential integral equation", *J. Comput. Acoust.* **13** (2): 287 – 299 (2005)

42. B. Shanker, A A. Ergin, K. Aygün and E. Michielssen, "Analysis of Transient Electromagnetic Scattering from Closed Surfaces Using a Combined Field Integral Equation", *IEEE T. Antenn. Propag.* **48** (7): 1064 – 1074 (2000)

43. D. J. Chappell, P. J. Harris, D. Henwood and R. Chakrabarti, "A stable boundary integral equation method for modelling transient acoustic radiation", *J. Acoust. Soc. Am.* **120** (1): 74 – 80 (2006)

44. S. P. Walker and M. J. Vartiainen, "Hybridisation of curvilinear time domains integral equations and time domain optical methods for electromagnetic scattering analysis.", *IEEE T. Antenn. Propag.* **46**: 318 – 324 (1998)

45. A. E. Yilmaz, J.-M. Jina and E. Michielssen, "A Fast Fourier Transform Accelerated Marching-on-in-Time Algorithm for Electromagnetic Analysis", *Electromagnetics* **21**: 181 – 197 (2001)

46. A. A. Ergin, B. Shanker and E. Michielssen, "Fast Transient analysis of acoustic wave scattering from rigid bodies using a two-level plane wave time domain algorithm", *J. Acoust. Soc. Am.* **106** (5): 2405 – 2416 (1999)

47. A. A. Ergin, B. Shanker and E. Michielssen, "Fast analysis of transient acoustic wave scattering from rigid bodies using the multilevel plane wave time domain algorithm", *J. Acoust. Soc. Am.* **107** (3): 1168 – 1178 (2000)

48. R. Coifman, V. Rokhlin, and S. Wandzura, "The Fast Multipole Method: A Pedestrian Description", *IEEE Antenn. Propag. M.* **35** (3): 7 – 12 (1993)

49. M. F. Gyure and M. A. Stalzer, "A prescription for the multilevel Helmholtz FMM", *IEEE Comput. Sci. Eng.* **5** (3): 39 (1998)

50. S. Amini and A. T. J. Profit, "Multi-level fast multipole solution of the scattering problem", *Eng. Anal. Bound. Elem.* **27**: 547 – 564 (2003)

51. Y. Shifman and Y. Leviatan, "On the Use of Spatio-Temporal Multiresolution Analysis in Method of Moments Solutions of Transient Electromagnetic Scattering", *IEEE T. Antenn. Propag.* **49** (8): 1123 – 1129 (2001)

52. Y. K. Chung, T. K. Sarkar, B. H. Jung, M. Salazar-Palma, Z. Ji, S. Jang and K. Kim, "Solution of Time Domain Electric Field Integral Equations Using the Laguerre Polynomials", *IEEE T. Antenn. Propag.* **52** (9): 2319 – 2328 (2004)

53. Z. Ji, T. K. Sarkar, B. H. Jung, M. Yuan and M. Salazar-Palma, "Solving Time Domain Electric Field Integral Equation without the Time Variable", *IEEE T. Antenn. Propag.* **54** (1): 258 – 262 (2006)

54. G. C. Herman, "Scattering of Transient Acoustic Waves by an Inhomogeneous Obstacle", *J. Acoust. Soc. Am.* **69** (4): 909 – 915 (1981)

55. C. K. W. Tam and L. Auriault, "Time-Domain Impedance Boundary Conditions for Computational Aeroacoustics", *AIAA J.* **34** (5): 917 – 923 (1996)

56. K.-Y. Fung, H. Ju, B.-P. Tallapragada, "Impedance and Its Time-Domain Extensions", *AIAA J.* **38** (1): 30 – 38 (2000)

57. K.-Y. Fung and H. Ju, "Broadband Time-Domain Impedance Models", *AIAA J.* **39** (8): 1449 – 1454 (2001)

58. K.-Y. Fung and H. Ju, "Time-domain Impedance Boundary Conditions for Computational Acoustics and Aeroacoustics", *Int. J. Comput. Fluid. D.* **18** (6): 503 – 511 (2004)

59. E. W. Weisstein, *Monte Carlo Integration*, http://mathworld.wolfram.com/MonteCarloIntegration.html

60. M. Abramowitz and I. A. Stegun, Handbook of mathematical functions: with formulas, graphs and mathematical tables, Dover (1965)

61. S. Wandzura and H. Xiao, "Symmetric Quadrature Rules on a Triangle", Comput. Math. Appl. **45**: 1829 – 1840 (2003)

62. J. Burkardt, STROUD N-Dimensional Quadrature, http://people.scs.fsu.edu/~burkardt/m_src/stroud/stroud.html

63. E. W. Weisstein, *Curl Theorem*, http://mathworld.wolfram.com/CurlTheorem.html

64. T. Terai, "On The Calculation of fields around three-dimensional objects by integral equation method", *J. Sound Vib.* **69** (1): 71 – 100 (1980)

65. R. Martinez, "The thin-shape breakdown (TSB) of the Helmholtz integral equation", *J. Acoust. Soc. Am.* **90** (5): 2728 – 2738 (1991)

66. T. W. Wu, "A direct boundary element method for acoustic radiation and scattering from mixed regular and thin bodies", *J. Acoust. Soc. Am.* **97** (1): 84 – 91 (1995)

67. M. R. Schroeder, "Binaural dissimilarity and optimum ceilings for concert halls: More lateral sound diffusion", *J. Acoust. Soc. Am.* **65** (4): 958 – 963 (1979)

68. T. J. Cox and Y. W. Lam, "Prediction and Evaluation of the Scattering from Quadratic Residue Diffusers", *J. Acoust. Soc. Am.* **95** (1): 297 – 305 (1994)

69. L. E. Kinsler, A. R. Frey, A. B. Coppens and J. V. Sanders, *Fundamentals of Acoustics*, John Wiley & Sons (2000)

70. J. A. S. Angus and P. D'Antonio, "Two dimensional Binary Amplitude Diffusers", *Proc. Audio. Eng. Soc.* Preprint 5061 (D-5) (1999)

71. M. R. Schroeder, "Diffuse sound reflection by maximum-length sequences", *J. Acoust. Soc. Am.* **57** (1): 149 – 150 (1975)

72. E. W. Weisstein, *B-Spline*, http://mathworld.wolfram.com/B-Spline.html

73. E. W. Weisstein, *Delta Function*, http://mathworld.wolfram.com/DeltaFunction.html